GEOLOGICA ULTRAIECTINA

Mededelingen van de
Faculteit Aardwetenschappen der
Rijksuniversiteit te Utrecht

No. 99

Porous Structure and Particle Size of Silica and Hydrotalcite Catalyst Precursors

a thermoporometric study

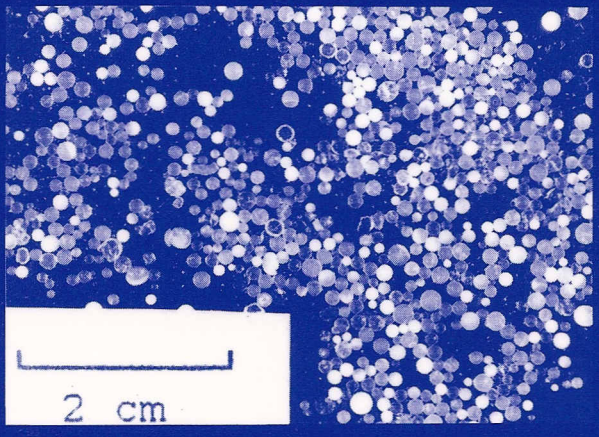

Mark Titulaer

GEOLOGICA ULTRAIECTINA

Mededelingen van de
Faculteit Aardwetenschappen der
Rijksuniversiteit te Utrecht

No. 99

Porous Structure and Particle Size of Silica and Hydrotalcite Catalyst Precursors

a thermoporometric study

24-015

CIP-DATA KONINKLIJKE BIBLIOTHEEK, DEN HAAG

Titulaer, Mark Kurt

Porous structure and particle size of silica and
hydrotalcite catalyst precursors / Mark Kurt Titulaer.-
Utrecht : Faculteit Aardwetenschappen der
Rijksuniversiteit Utrecht.-(Geologica Ultraiectina,
ISSN 0072-1026; No.99)
Thesis Rijksuniversiteit Utrecht.-With ref.-With
summary in Dutch
ISBN 90-71577-53-8
Subject headings: silica / hydrotalcite / thermoporometry

Porous Structure and Particle Size of Silica and Hydrotalcite Catalyst Precursors

De Poreuze Structuur en Deeltjesgrootte van Silica en Hydrotalcite Katalysator Precursors

(Met een samenvatting in het Nederlands)

PROEFSCHRIFT

TER VERKRIJGING VAN DE GRAAD VAN DOCTOR AAN DE RIJKSUNIVERSITEIT TE UTRECHT, OP GEZAG VAN DE RECTOR MAGNIFICUS, PROF. DR. J.A. VAN GINKEL, VOLGENS BESLUIT VAN HET COLLEGE VAN DEKANEN IN HET OPENBAAR TE VERDEDIGEN OP WOENSDAG 24 MAART 1993 DES NAMIDDAGS OM 12.45 UUR

DOOR

Mark Kurt Titulaer

geboren op 29 juli 1964 te Hilversum

PROMOTOR : PROF. IR. J.W. GEUS
associated with the Faculty Chemistry of the Rijksuniversiteit Utrecht

PROMOTOR : PROF. DR. R.D. SCHUILING
CO-PROMOTOR : DR. J.B.H. JANSEN
associated with the Department of Geochemistry of the Rijksuniversiteit Utrecht

To my parents
To Jean, Caroline, Yord, and Suzanne

Table of Contents

PROLOGUE		8
Chapter 1	General introduction	9
Chapter 2	The preparation and characterization of sol-gel silica spheres	15
Chapter 3	The differences in the elementary processes proceeding during ageing of hydrogels and xerogels	37
Chapter 4	The rise in pH during ageing of porous sol-gel silica spheres	59
Chapter 5	The shrinkage of hydrothermally aged porous silica spheres measured by thermoporometry	77

Chapter 6 Control of the porous structure of silica gel by the preparation pH and drying 107

Chapter 7 The effect of drying on the pore dimensions of electrodialyzed silica sol gels 133

Chapter 8 Characterization of tubular chrysotile by thermoporometry, nitrogen sorption, DRIFTS and TEM 175

Chapter 9 The shrinkage and swelling of differently pillared hydrotalcite investigated by thermoporometry 207

Chapter 10 The quantity of reduced nickel in synthetic takovite ; effects of preparation conditions and calcination temperature 243

SAMENVATTING 263

CURRICULUM VITAE

Prologue

In this thesis, experimental work is described, which is done in the period 1-7-1987 till 1-7-1991. Without the help of many, it had never been accomplished. I wish to thank for their support the staff members, colleagues, students, supporting divisions, librarians of the Institute for Earth Sciences, Department of Inorganic Chemistry (employees of the former Analytical Chemical Laboratory), Department of Practical Pharmacy, Chemical Thermodynamics Group, who have contributed to parts of the thesis. Especially I wish to mention Ad van der Eerden for technical assistance, Ineke Kalt and Rikky van Zelst of the secretary's offices, Willem Nieuwenhuizen and Herman Trommar of the glass-works, Lou Louwerse and Henk Erkelens of electronics, Fred Quint, Fred Trappenburg, Izaak Santoe, and Jacco Bergehenegouwe of the audio-visual department of the IVAU, and Jan den Boesterd of the audio-visual department of the faculty Chemistry for making illustrations and photographs, Dr. Ben Dekker and Piet Elberse for their technical assistance with the N_2 adsorption and desorption experiments, Marjan Versluis for XRD-, Paul Anten for ICP-AES- , and Ton Zalm for TGA-DTA analysis, and Jan Ebskamp providing me the most unusual equipment. Dr. Jos van Dillen, and Jos Kock of the practicum "Maken II", thank you, for your assistance with coaching the students.

My roommates and colleagues ; Ronald Bakker, Jan van Beek, Paul Buining, Peter Dirken, Theo Kloprogge, Jack Voncken, Ronald Vogels, thank you, for your cooperation and pleasant lunch times in the canteen of the IVAU.

Dr. Ben Jansen and prof. ir. John Geus, thank you, for your enthusiasm, ideas, and patience with the correction of the first manuscripts. Finally, I wish to thank my parents, giving my the opportunity to study, and, of course, my brother for the 'computer facilities'.

Chapter 1

General Introduction

Industrial utilization of heterogeneous catalysts has continuously increased during this century. The nineteenth century had shown the development of catalysts for the production of sulphuric acid and for the oxidation of hydrochloric acid to elemental chlorine. At the beginning of the twentieth century the catalytic oxidation of ammonia over platinum gauze to nitrogen oxide, which is subsequently reacted with water to nitric acid, has been developed. After the introduction of the ammonia and the methanol synthesis, processes based on solid catalysts, the use of catalysts in the production of fuels rapidly rose during the thirties and forties with the development of processes, such as, the Fischer-Tropsch synthesis and catalytic cracking. The Fischer-Tropsch synthesis involves the production of hydrocarbons to be used as gasoline substituents from carbon monoxide and hydrogen. The reaction of carbon monoxide and hydrogen to hydrocarbons is carried out over supported cobalt and iron catalysts. Catalytic cracking is one of the most successful catalytic developments. Heavier hydrocarbons are catalytically reacted to hydrocarbons of a lower boiling point and to carbon. Combustion of the carbon deposited on the catalyst provides the thermal energy for the endothermic cracking reaction. Hydrogenation of coal aimed also at the production of gasoline substituents. The hydrogenation of coal led to the development of sulphur-resistant catalysts containing molybdenum or tungsten. Later on catalytic reforming based on platinum and subsequently on platinum-rhenium catalysts was introduced. Abatement of environmental pollution brought about the need for removing impurities, such as, sulphur, nitrogen, nickel, and vanadium out of crude oil fractions. The above catalysts for coal hydrogenation were adapted for hydrodesulphurization, hydronitrification, and hydrodemetallization, and are presently used on a very large scale. These processes are used to purify fuels from sulphur, nitrogen, and metals, and thus considerably decrease the air pollution caused by the combustion of the fuels produced from crude oil. Hydrogen sulphide released during the hydrodesulfurization of fossil fuels is catalytically processed in large units to elemental sulphur according to the Claus process. Recently catalysts, based on Pt, Pd, and Rh, for the purification of automotive exhaust gases have to be installed in almost every new car. Finally, catalysts for the selective catalytic reduction of nitrogen oxides present in flue gases with ammonia are increasingly being used.

With most solid catalysts the active surface area per unit volume is decisive; a large active surface area per unit volume of catalyst is a prerequisite for industrial application. With precious metals, such as, platinum or rhodium, a maximum active surface per atom of precious metal is required in view of the high price of precious

metals. Almost all catalytically active solids severely sinter under the conditions of the thermal pretreatment or the catalytic reactions. Sintering first of all decreases the active surface area per unit volume, which usually is unacceptable. Moreover, the pressure drop of sintered fixed bed catalysts may be too high, while the gas flow through a sintered catalyst bed may be very non-uniform and strongly deviating from the required plug flow. Sintering may lead to the formation of more open regions within the catalyst bed through which slip of the gas flow proceeds.

To suppress effectively the sintering of catalytically active solids, the active components are generally applied onto a suitable support. The support must be sufficiently thermostable and generally must exhibit an elevated surface area per unit volume. Though the support can display catalytic activity, usually the activity of the support is either not important or even not attractive. An instance of an undesired activity is the presence of acid sites at the surface of a methanol synthesis catalyst. The acid sites catalyzing the reaction to dimethylether adversely affect the selectivity of the catalytic reaction. The opposite is observed with catalytic reforming. Catalytic reforming rises the octane number of gasoline fractions by passing the gasoline vapor through a catalyst bed in which Pt, Pt-Re, or Pt-Ir has been deposited onto an acid support. Besides isomerization of linear to branched hydrocarbons, dehydrogenation and cyclization to aromatic compounds proceeds. The support must contain suitable acid sites, that together with the platinum or platinum alloy particles accelerate the dehydrocyclization reactions without exhibiting carbon deposition.

The mechanical strength of the bodies of supported catalysts as well as the porous structure of the support is highly important. Disintegration of catalyst bodies in fixed bed reactors leads to high pressure drops over the catalyst bed that cannot be tolerated. With fluidized catalyst beds a high resistance of the catalyst bodies against attrition is a prerequisite. The porous structure of solid catalysts is, especially with fixed catalyst beds, important. To achieve acceptable pressure drops over the reactor the catalyst bodies must have dimensions of at least some mm's. Often the transport of reactants and reaction products through the pores within the catalyst bodies cannot keep up with the rate of the catalytic reaction proceeding at the catalytically active surface. As a result the performance of a catalyst in a technical reactor is often significantly less than suggested by the rate of the chemical reaction. Transport limitations thus often lower the overall rate of catalytic reactions in technical installations. Most important, however, is the effect of transport limitations on the selectivity of catalytic reactions. When reactions products liable to subsequent undesired reactions cannot leave the catalyst bodies sufficiently rapidly, the selectivity may drop considerably. Instances are the hydrogenation of fatty oils, where reaction to completely saturated hydrocarbon chains has to be prevented, and the oxidation of hydrogen sulphide to elemental sulphur, where oxidation to sulphur dioxide must be avoided. Plugging of the pore mouths of catalyst bodies can rapidly deactivate solid catalysts. Important is to prevent plugging of pore mouths with hydrodemetallization catalysts, where mainly nickel and vanadium are deposited on or within the catalyst bodies, and with catalytic reactions where carbon can be deposited, such as, catalytic

reforming.

Procedures for the technical production of solid catalysts can be divided into two main groups. The first group of procedures involves preparation of a, generally non-porous, solid in which the precursor of the active component and of the support are thoroughly mixed. With the subsequent thermal treatment some components are selectively removed from the solid providing a, generally highly, porous solid containing the supported active component. With the ammonia synthesis catalyst magnetite (Fe_3O_4), alumina, and potassium oxide are melted to a homogeneous melt in an electrical furnace. After cooling the melt is ground to bodies of some mm's size. Reduction of the non-porous solid selectively removes the oxygen of the iron oxide, leading to highly porous metallic iron stabilized by the remaining alumina.

The porous structure of the final supported catalyst is difficult to control with this procedure, which is used for technically important catalysts, such as the ammonia synthesis catalyst, and the high- and low-temperature carbon monoxide shift conversion catalysts. With the CO shift conversion, which involves the reaction of carbon monoxide with steam to carbon dioxide and hydrogen, a hydrotalcite containing Zn, Cu, and Al is precipitated. Drying and calcination selectively remove the water and carbon monoxide, and the subsequent reduction removes the oxygen bonded to copper from the catalyst.

The second production procedure involves the application of the precursor of the active component onto a separately produced support. Often a relatively finely divided, powdered support is used with the procedure involving a separately produced support. Finally a shaping procedure must be applied to produce the desired catalyst bodies. Again the porous structure of the catalyst bodies eventually produced is difficult to control. When the porous structure of the catalyst is of decisive importance, the best procedure is to start from pre-shaped bodies of the support having the required porous structure, mechanical strength, and physical dimensions. Commercially a wide range of, mainly alumina and silica, support bodies of different size, shape, and porous structure is available. Procedures to apply active precursors into pre-shaped support bodies, such as, incipient wetness impregnation, have been developed. It is therefore highly important to be able to control the porous structure of catalyst supports. Especially combination of shaping of support bodies with establishment of the desired porous structure is very attractive.

Often catalyst supports are produced by reactions in aqueous solutions. Separation of the support from the liquid and drying severely affect the porous structure of the final solid. The high surface energy of water causes the formation of a xerogel, in which the elementary particles are tightly connected, out of the original, much less dense, hydrogel. Though the structure of porous solids after removal of water can be accurately determined by adsorption and desorption of nitrogen at 77 K and by mercury penetration, the porous structure of hydrogels is more difficult to assess. Nevertheless establishment of the porous structure of hydrogels is essential, since the structure of the hydrogel determines the porous structure of the final xerogel obtained after separation from the liquid and drying. Thermoporometry allows one to assess

accurately the porous structure of hydrogels.

The subject of this thesis is the control of the porous structure of catalyst bodies. The first part deals with silica, that can be utilized as catalyst support with many industrially important catalytic reactions. The second part of the thesis deals with the preparation and characterization of solid catalysts having a tubular or a platelet microstructure. The success of zeolites in catalytic reactions is due to the fact that the shape of the porous structure can be controlled on an atomic scale. The possibility to adapt also the surface composition of zeolites has led to important catalytic possibilities. Besides zeolites other minerals have structures that are interesting for catalytic applications. Natural minerals usually are contaminated, which renders utilization for catalytic purposes difficult, in spite of the favourable price. As with zeolites synthetic minerals therefore have to be preferred. Synthetic chrysotile will be studied, mainly to calibrate the porometric technique. The preparation and characterization of layered structures will subsequently be dealt with. Structures of platelets the separation of which can be controlled by insertion of suitable charged clusters ("pillaring") are presenting interesting catalytic properties.

The first part of this thesis deals with the determination of the porous structure of hydrogels and the change of the porous structure during the transition to the xerogel. First of all the preparation of suitable silica bodies will be studied. A procedure that can also be used on a large scale is the preparation of sol-gel spheres. The spheres are attractive catalyst support bodies, since pneumatic loading and emptying of industrial reactor is viable with the easily flowing and mechanically strong silica spheres prepared by a sol-gel process. Furthermore the spheres exhibit a relatively low pressure drop to a liquid or gas flow passed through a fixed bed. Chapter 2 deals with the preparation and characterization of silica sol-gel spheres. The porous structure of the silica spheres can be well controlled by hydrothermal treatment. Usually wider pores result from hydrothermal treatment, while the pore volume does not decrease significantly. With most supports it is difficult or impossible to control the porous structure. Since the transport of reactants and reaction products within catalyst bodies is determining often the performance of solid catalysts, control of the porous structure is highly important. Transport limitations often cause the performance of solid catalysts in liquid phase reactions to be less favourable than that of homogeneous catalysts, in which transport limitations do not arise easily. It is therefore interesting to investigate thoroughly the effects of drying and of hydrothermal treatment of silica sol-gel spheres. Chapter 3 describes hydrothermal treatment of hydrogel and xerogel spheres, and Chapter 4 considers the increase in pH during hydrothermal treatment of silica sol-gel spheres. The amount of sodium adsorbed on the silica surface, which affects subsequent application of catalytically active precursors and the catalytic properties of the final catalysts, is also dealt with in Chapter 4. The shrinkage of sol-gel spheres during hydrothermal treatment is described in Chapter 5.

Usually silica sol-gel bodies are produced from elementary silica particles of a size of 5 nm. The size of the elementary silica particles is difficult to control and the sodium content of the thus produced silica may present problems during application of the

active precursor or adversely affect the catalytic performance. Chapters 6 and 7 therefore deal with alternative procedures to produce silica gels. Chapter 6 describes a pH static preparation and the effect of the pH on the size of the elementary silica particles. Chapter 7 presents an interesting procedure to produce gels of silica by means of electrodialysis.

Measurement of the porous structure of chrysotile tubes is described in Chapter 8. Since the dimensions of the diameter of the chrysotile tubes can be assessed electronmicroscopically, the tubes are very appropriate to calibrate the thermoporometric technique. Preparation and pillaring of hydrotalcite is dealt with in Chapter 9. Again thermoporometry is a very useful technique to characterize the porous structure of the tiny plates. Finally the reduction of a nickel containing hydrotalcite structure, takovite, and the effect of the reduction on the particle size is described in Chapter 10.

Chapter 2

The preparation and characterization of sol-gel silica spheres*

M.K. Titulaer, J.B.H. Jansen and J.W. Geus[1]

Department of Geochemistry, Institute of Earth Sciences, University of Utrecht, Budapestlaan 4, P.O. Box 80.021, 3508 TA Utrecht, The Netherlands.
[1]Department of Inorganic Chemistry, University of Utrecht, Sorbonnelaan 16, P.O. Box 80.083, 3508 TB Utrecht, The Netherlands.

*This paper is a contribution of the Debye Institute, University of Utrecht, The Netherlands.

ABSTRACT

Silica sol-gel spherical bodies are prepared containing 2 to 13 wt% SiO_2 in water. The silica sol is prepared by addition of a sodium silicate solution to a dilute nitric acid solution. The silica sol thus obtained is introduced dropwise into hot paraffin oil, which results in spherical hydrogel bodies. The pore volume of the spheres is varied between 0.16 and 1.4 ml/g, and the pore radii between 0.8 and 60 nm. The pore structure of the hydrogels is investigated by thermoporometry.

The hydrogels are washed and dried at 293, 333, and 393 K. The pore structure of the dried spheres is determined by nitrogen adsorption and desorption at 77 K. Drying causes a considerable shrinkage of the pore dimensions. The pore radius of the sample containing 2 wt% SiO_2 in water diminishes from 10.2 to 2.9 nm, while the pore volume decreases from 0.9 to 0.5 ml/g. Drying the gelled spheres at temperatures above 293 K leads to a lower shrinkage, and consequently to a higher pore volume of the dried spheres. The pore structure of both xerogel and hydrogel spheres is modified by means of a hydrothermal treatment. Hydrothermal treatment of the hydrogel spheres increases the pore volume, whereas that of the of the xerogel spheres remains constant. Differences observed with the hydrothermally aged hydrogel and xerogel spheres are attributed to the ripening mechanism being dependent on the initial pore structure.

INTRODUCTION

Amorphous silica is used as a catalyst support [1], a glass precursor [2], a paint thickener, or a coating film [3]. With all applications the pore structure and size of the powder have to be controlled, especially when the silica is used as a catalyst support, since the pore structure and the specific surface area of the support may determine the performance and deactivation of the catalyst [4]. The pore structure comprises pore size distribution, pore volume, pore shape, and the (internal) surface area. The pore structure of silica gels critically depends on the preparation conditions [5,6]. Furthermore, the increase of the solubility of silica in water at high temperatures allows modification of the pore structure of the silica gels by hydrothermal ageing [5,7-9].

Porous silica bodies can be prepared by a sol-gel process [9-11]. The silica source may be either a siliciumalcoxide, such as, tetraethyl or tetramethyl orthosilicate (TEOS and TMOS), or a concentrated sodium silicate solution (waterglass). The alcoxide, dissolved in alcohol, can be hydrolyzed by addition of water. The primary silica sol particles, which are generated during the hydrolysis, link together and build a monolithic reticulated alcogel [12]. The gel network resulting from the hydrolysis of alcoxides is very soft and fragile. Removal of the alcohol is accompanied by an undesired shrinkage. The silica density of the dried xerogel is evidently higher than of the previous hydrogel. The shrinkage of the alcogel can be reduced by hypercritical drying. To that end the sample is placed in a steel vessel and the alcohol is evacuated above its critical temperature. This treatment results in an aerogel of a low density [13].

The aim of the present work is to investigate the effect of the preparation conditions and of the hydrothermal treatment on the pore structure of spherical silica gel bodies prepared from sodium silicate. The spheres consist of small primary particles. The influence of the pH on the primary particle size will be dealt with first. Secondly, the effects of the silica concentration in the sol and of the drying temperature on the pore structure of the xerogel will be investigated. Finally, the change in pore structure of hydrogels and of xerogels as affected by the duration of the hydrothermal treatment will be compared. As coalescence of the silica spheres proceeds above the critical temperature of water, thermal treatment at a temperature below the critical temperature is chosen [14].

The sodium silicate solution is analyzed by inductively coupled plasma atomic emission spectrophotometry (ICP-AES), and atomic absorption spectrophotometry (AAS). The textural analysis of the gel samples is performed by transmission electron microscopy (TEM), thermoporometry, N_2 adsorption and desorption at 77 K, and mercury penetration.

Thermoporometry

The pore structure of hydrogels and xerogels in water is examined by thermoporometry.

This recently developed technique is based on the lowering of the solidification or fusion point of a suitable compound (usually water), which is present within the pores of a solid material [15,16]. The advantage of this technique is the fact that the sample does not have to be dried first. By measuring the endothermic heat flux due to fusion, and subsequently, the exothermic heat flux with solidification of the fluid in the material, information is obtained about the pore size distribution, the pore volume, the pore shape, and the internal surface area of the sample. The depression of the freezing point of water is caused by the high surface energy of the critical nucleus of ice, the radius R_n (in nm), of which is approximately equal to the pore radius R_p (in nm) :

$$R_n = -64.67/dT-0.23 \quad \text{(nm)} \quad (1)$$

R_n is related to the temperature difference dT (in K) between the experimental solidification temperature T_s and 273 K. Since freezing and melting proceeds at temperatures lower than 273 K, dT is always negative. The technique is appropriate to measure pore radii in the range of 1 to 150 nm, according to the theory in [15-20].

The pore volume, V_n (in ml/g), of the wet samples, which corresponds to the volume of the ice present within the pores of the silica divided by the weight, W, of the silica (in g) is estimated by integration of the heat flux-versus-time plot using Eqn. 2. Division of this value by the solid-liquid enthalpy change H (J/g) and the density D of ice (g/ml) provides the pore volume V_n :

$$V_n = \int (P*dt)/H*W*D \quad \text{(ml/g)} \quad (2)$$

$$H = 332 + 3.3*dT \quad \text{(J/g)} \quad (3)$$

The surface area, A_n, of the ice crystals (in m^2) divided by the weight, W, of the silica (in g) is calculated from V_n, R_n, and the shape factor F according to the empirically determined Eqn. 4 :

$$A_n = (1+2/F) * V_n/R_n \quad \text{(m}^2\text{/g)} \quad (4)$$

The shape factor, F, is calculated from the fusion hysteresis [16,17], and has a theoretical value of unity for a pure spherical, two for a cylindrical, and infinite for an open slit pore shape. In practice, an infinite shape factor can never be found. The expressions (3) and (4) deviate from the expressions in the literature [18,19]. This discrepancy will be addressed in the discussion.

EXPERIMENTAL

Formation of the silica gel spheres

The solution of silica sol particles in water is formed by lowering the pH of a sodium silicate solution according to a procedure based upon the method of Plank and Drake [21]. The final pH must be between 3 and 9.35. Above the value of 9.35, which is the first ionization constant of monosilicic acid (MSA) in 1 M NaCl [22], the supersaturation of MSA decreases and the sol particles dissolve. Additionally, below the point of zero charge of silica, which is at a pH level of about 3, there are few ionized silanol groups on the silica surface. The presence of ionized surface silanol groups is required for the growth and gelling of the sol particles. Above the pH of 3 the silica surface is negatively charged [23].

The formation of an aqueous hydrogel involves two stages, viz., (i) addition of the sodium silicate solution to an acid solution and formation of the sol, and (ii) increase of the pH of the acid solution above 3 during the addition and gelling of the sol particles.

Two solutions A and B are prepared. The stock sodium silicate solution A is prepared by mixing commercially available waterglass (Merck Natronwasserglas, Art. 5621) with an equal volume of doubly distilled water. The composition of the stock solution A is listed in Tab. 1. The total silicon content is determined by ICP-AES [24], the sodium content both by ICP-AES and AAS. The MSA is reacted with ammonium heptamolybdate, and the yellow β-silicomolybdate complex is determined colorimetrically at 410 nm, according to the procedure of Iler [25]. With colorimetry, standard silicon and sodium solutions in the range of 1 to 100 mg/l SiO_2 and of 1 to 10 mg/l Na_2O are prepared.

The nitric acid solution B is prepared by diluting 65 wt% nitric acid (Merck, art. 456) with water.

Stable sols of two different weight concentrations of silica are prepared, viz., sample 1a containing 5 wt%, and sample 2a containing 13 wt% of silica in water (Tab. 2). In practice, the weight concentration of silica can be varied between 2 and 13 wt% SiO_2 in water. Above 13 wt%, rapid gelling of the sol proceeds before the spherical bodies are formed, and below 2 wt% SiO_2, no significant gelling of the silica sol occurs.

The sodium silicate solution A is slowly added to 50 ml of a stirred diluted nitric acid solution B (present in a plastic cup in an ice-water bath). The nitric acid solution B is kept at 273 K to avoid premature gelling. The rate of addition of A is kept constant at 60 ml/h with a Gilson Minipuls 2 pump. Two different nitric acid solutions of 0.4 and 2 M HNO_3 are used to prepare the samples 1a and 2a (Tab. 2), respectively. The added volume of the waterglass solution A is expressed by the empirically determined Eqn. 5.

$$V_{Si} \equiv 50 * [HNO_3]/[Na^+] \approx 2.4 + 36.7\,[HNO_3] \quad \text{(ml)} \quad (5)$$

with V_{Si}, the volume of added sodium silicate A (in ml), $[HNO_3]$ the initial nitric acid concentration (in mole/l) of B, and $[Na^+]$ the sodium concentration (in mole/l) of A.

When a pH of 5 is reached, the sol is quickly introduced through a hollow vibrating needle into a double walled vessel (length 70 cm, diameter 9.5 cm) containing a cylinder of 5 l hot paraffin oil. The temperature of the oil is kept at 363 K by means of a water thermostatic bath (Tamson). The sol-gel conversion of the spherical sol droplets in the paraffin oil is accelerated by the high temperature. The formation of siloxane bonds between the primary sol particles calls for an activation energy between 50 and 84 kJ/mole depending on the silica structure [7,26,27]. Even higher values up to 100 kJ/mole have been reported [28]. The spherical hydrogel bodies of few mm's are caught in 2 l demineralized water under the paraffin cylinder and subsequently washed with 1.5 l demineralized water.

TEM and thermoporometry of hydrogel spheres

Samples 1a and 2a are not dried (hydrogel). The microstructure of the spheres of sample 2a (13 wt% silica in water) is investigated within a Philips EM 420 transmission electron microscope (TEM) operated at 100 kV. A suspension of the hydrogel spheres in ethanol is therefore prepared. A droplet of the suspension is brought on a holey carbon film applied onto a copper specimen grid and dried.

The hydrogels 1a and 2a are characterized by thermoporometry, which is performed with a Setaram DSC 111 microcalorimeter. Two different cooling rates of the wet samples, 2 and 30 K/h, respectively, are applied.

Drying of hydrogel spheres

Samples 1b and 2b, with 5 and 13 wt% silica, respectively, are dried at 393 K (Tab. 2). A second batch is prepared with 2 M HNO_3 to check the reproducibility of the sol-gel processes. This batch containing 13 wt% silica, is dried at 393, 333, and 293 K (samples 3-5). A third batch, containing 13 wt% silica, is dried at 293 K (sample 6). No hydrogels of samples 3 to 6 are investigated. Subsequently, the xerogels 1b, 2b, 3-6 are calcined at 723 K, where no significant sintering occurs [29].

Characterization of the dried spheres

The six samples 1b, 2b, and 3 to 6 are evacuated for 6 h at 473 K for N_2 adsorption and desorption within a Carlo Erba Sorptomatic 1800. The BET surface area and related pore volume can be calculated from the extent of N_2 adsorption. The pore size distribution is calculated from the desorption isotherm [31]. The xerogel spheres of sample 1b and 2b are impregnated with distilled water at a reduced pressure of about 0.03 hecto Pa. The impregnated wet samples are measured by thermoporometry and the textural data thus obtained are compared with those calculated from N_2 adsorption and desorption (Tab. 2).

Hydrothermal ageing of hydrogel and xerogel spheres

Strengthening of the gel structure is achieved by hydrothermal ageing of the gel spheres at 473 K. The pore radius, pore volume, and surface area are assessed as a function of the period of time of the hydrothermal treatment, which amounts to 2, 4, 7, 23, and 47 h. The change in pore structure of xerogel spheres in 1 M NaCl is compared with that of hydrogel spheres of an equal silica concentration after hydrothermal treatment at the above temperature of 473 K.

The xerogel spheres of sample 2b, dried at 393 K, are divided into five fractions for hydrothermal treatment for the above five periods of time. The xerogel fractions (3.15 g each) are treated with 20.85 ml 1 M NaCl. The same treatment is performed on the hydrogel spheres of sample 2a, which have not been previously dried. The hydrogel spheres are washed with 1 M NaCl solution. In each experiment 24 g of the hydrogel spheres, and the impregnated xerogel spheres with 1 M NaCl are placed in Teflon cups in steel pressure vessels of 48 ml.

After hydrothermal treatment, the spheres of both sample 2a and b are washed with distilled water and dried at 393 K. The hydrothermally aged samples are characterized by Hg penetration, because Hg penetration is applicable for pore sizes larger than 4 nm [31]. The pore size distribution and pore volume are calculated with the Washburn equation and the volume of Hg intruded at different pressures [31]. The internal surface area is estimated from the pore volume and pore radius, assuming a cylindrical pore shape.

Examination of the shape factor F in thermoporometric characterization

A commercial silica xerogel sample 7 is impregnated with water and measured by thermoporometry. Sample 7 has a pore radius of 7.7 nm and a specific pore volume of 1.8 ml/g, determined from N_2 adsorption and desorption data.

Thermoporometry of sample 7 is performed using a Netzsch DSC controller 200 and a model 43 measuring cell. The calorimeter has been calibrated for the 'relative calorimetric sensitivity', the 'time-lag', and the 'thermal heat resistance' (THR). Due to the calibration the position of the peak in the DSC profile does not depend on the rate of cooling or heating. The following measuring sequence is used :

1. a cooling step from 293 to 213 K, rate -2 K/min
2. a heating step from 293 to 271.5 K, rate 1 K/min
3. a cooling step from 271.5 to 213 K, rate -1 K/min
4. a heating step from 213 to 293 K, rate 1 K/min

RESULTS

Sodium silicate solution

Otterstedt et al. [33] determined the size of the silica particles within the sodium silicate solution to be 2 nm. Alexander [31] derived the relationship between the colloidal particle size and the monosilicic acid concentration. The particle size is a function of the sodium-to-silica ratio in the stock sodium silicate solution [32,33]. The ionized surface is believed to be covered with a monolayer of hydrated sodium ions. A high sodium content increases the surface area and reduces the particle size. A large part of the silica is expected to be present as monosilicic acid, but not as large as the 63 mole% of the silicon present as soluble silica (MSA), as determined with the silicomolybdate method (Tab. 1).

Table 1 Composition and properties of the stock sodium silicate solution.

pH	11.3[1]	
[Si]	3 M	0.18 g SiO_2/ml
[Na]	1.5 M	0.047 g Na_2O/ml
[MSA]	1.9 M	
density	1.19 g/ml	

1) below the second ionization constant pK_a of $H_3SiO_4^-$ [43]

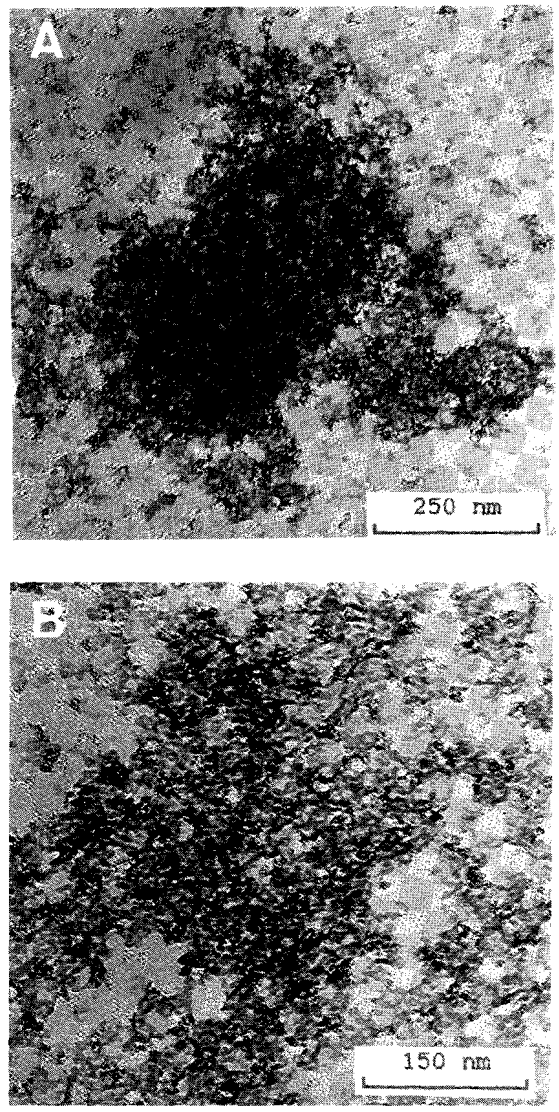

Figure 1 TEM micrographs of fragmented hydrogel spheres gelled at a pH of 5, with initial magnifications of 32,000 x (a) and 54,000 x (b). The sol particle size is 5 nm.
(c) spherical silica sol gel bodies of few mm's size. The spheres are dried at 393 K.

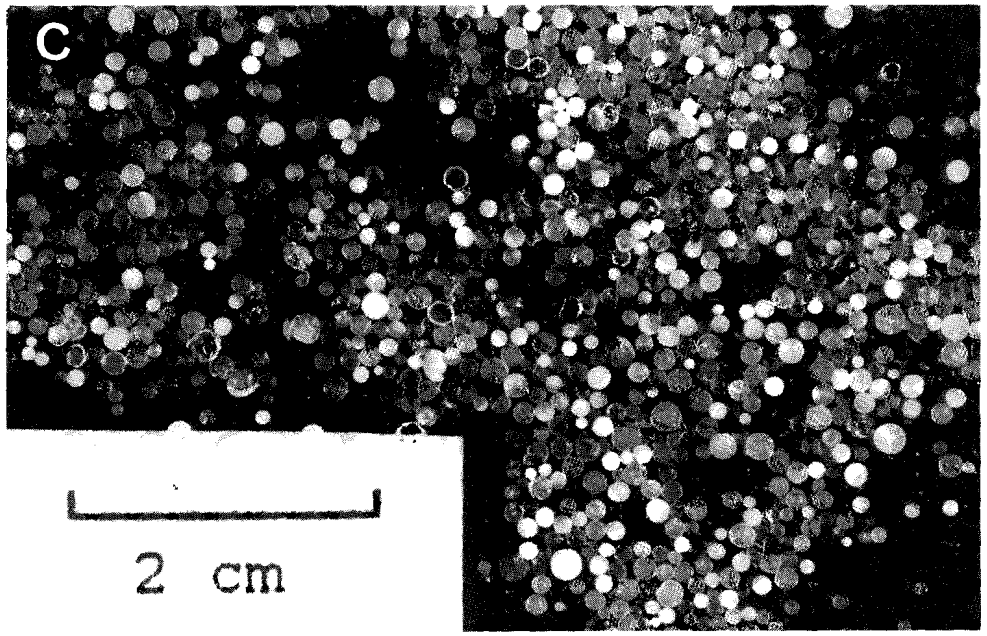

TEM of hydrogel spheres

TEM photographs of fragmented hydrogel spheres of sample 2a (Fig. 1) show that the sol primary particles in the hydrogel have a size of about 5 nm. Accordingly the small primary silica particles of a diameter of 2 nm present in the sodium silicate solution react to particles of 5 nm during formation of the hydrogel. Small particle sizes of sol solutions of silica prepared at low pH levels without any ripening have been reported by Okkerse and de Boer [34].

Gel spheres of 5 and 13 wt% silica

The solid weight concentration of silica in the hydrogel is calculated from the weight after drying :

$$wt\% = (\text{wt xerogel} / \text{wt hydrogel}) * 100 \quad (\%) \quad (6)$$

The weight concentration of silica to be expected from the silica content of the added

stock sodium silicate solutions, can be evaluated from the empirical Eqn. 7.

$$wt\% = 100 * V_{Si} * 0.18/(50+V_{Si}*1.19) \quad (\%) \quad (7)$$

with V_{Si}, the volume of added sodium silicate solution A (in ml), 0.18 the silica concentration in A (in g/ml), 50 the volume of B (in ml) with a density of 1 g/ml, and 1.19 the density of A (in g/ml) (Tab. 1).

The pore structure parameters of the hydrogel spheres of samples 1a and 2a and the xerogel spheres 1b and 2b are given in Tab. 2. The solid weight concentration according to Eqn. 6 appears to be slightly higher than the theoretical silica concentration according to Eqn. 7 (see Tab. 2). The apparent pore radius, R_n, of 10.2 nm of hydrogel sample 1a of a low silica content is slightly larger than the radius of 8.4 nm of sample 2a, while the meso pore volume, V_n, of both samples is equal (0.9 ml/g).

Dried silica spheres

A photograph of the sol-gel xerogel spheres dried at 393 K, which have a size of few mm's size, is shown in Fig. 1c. Drying of the hydrogel samples leads to a reduction of the pore radius to about 33 % of the original size, regardless of the silica concentration, which ranges from 5 to 13 wt%. The thermoporometric shape factor F changes from 2.6 for the hydrogel to 1.7 for the xerogel, indicating a more spherical pore shape after drying. The pore radius, R_p, (2.5 nm), the pore volume, V_p, (0.8 ml/g), and the BET surface area (455 m^2/g) of the xerogels samples 1b and 2b as measured by N_2 adsorption and desorption are equal within the experimental accuracy. The pore radius, R_n, of the xerogel spheres 1b and 2b determined by thermoporometry is larger than that obtained by N_2 adsorption and desorption (Tab. 2). The fact that thermoporometry yields the pocket size instead of the size of the pore necks may explain the difference of the pore radii determined by thermoporometry and nitrogen sorption.

The thermoporometric pore volume, V_n, is lower than the liquid N_2 pore volume, V_p, owing to a non-freezing layer of at least a thickness, t, of 0.9 nm at the silica-water interface ($R_p = R_n + 0.9$ nm) [35]. The pore volume of the samples can (roughly) be corrected for this layer and the ice surface area, A_n, following Eqn. 8.

$$V_p = V_n + A_n * t \quad (ml/g) \quad (8)$$

Table 2 Texture of hydrogel and xerogel spheres of various weight content of silica. The xerogel spheres are dried at 393 K. R_n, V_n and A_n obtained by thermoporometry involve only the physical values of ice and not the pore characteristics.

	hydrogel			xerogel	
Sample	1a	2a		1b	2b
$[HNO_3]$ (mole/l)	0.4	2			
wt% SiO_2 (Eqn.6)	5	13		idem 1a	idem 2a
wt% SiO_2 (Eqn.7)	4	10			
thermoporometry					
cooling branch					
rate (K/h)	-2	-2	-30	-4	-5
R_n (nm)	10.2	8.4[1]	6.4	2.9	3.5
V_n (ml/g)	0.9	0.9	-	0.5	0.5
heating branch					
rate (K/h)	-	2	30	2	-
shape factor F	-	2.6	2.8	1.7	-
A_n (m^2/g)	200[2]	240	-	308	280[2]
V_n	-	1.5	-	-	-
N_2 adsorption and desorption of xerogel					
R_p (nm)				2.5	2.3
V_p (ml/g)				0.81	0.76
BET surface area (m^2/g)				459	455

1) average of 8.2 and 8.6 nm. 2) assumption of a cylindrical pore shape

Drying temperatures 273, 333, and 393 K

The effect of the drying temperature, viz., 293, 333 and 393 K, for the samples 5, 4 and 3, respectively, on the pore structure of the xerogel is illustrated in Tab. 3 and in Fig. 2, where the extent of N_2 adsorption of the samples is plotted as a function of the relative N_2 pressure. Reduction of shrinkage is observed at drying temperatures above 293 K, since the samples dried at 333 and 393 K exhibit a high pore volume.

The sigmoid shape of the curves of Fig. 2 exhibited by the samples dried at 393 and 333 K indicate the occurrence of multilayer adsorption. Xerogel spheres dried at 293 K have narrow pores. An isotherm displaying the shape of a Langmuir isotherm is observed. The BET surface area values of samples 5 and 6 are maybe smaller than the real surface areas.

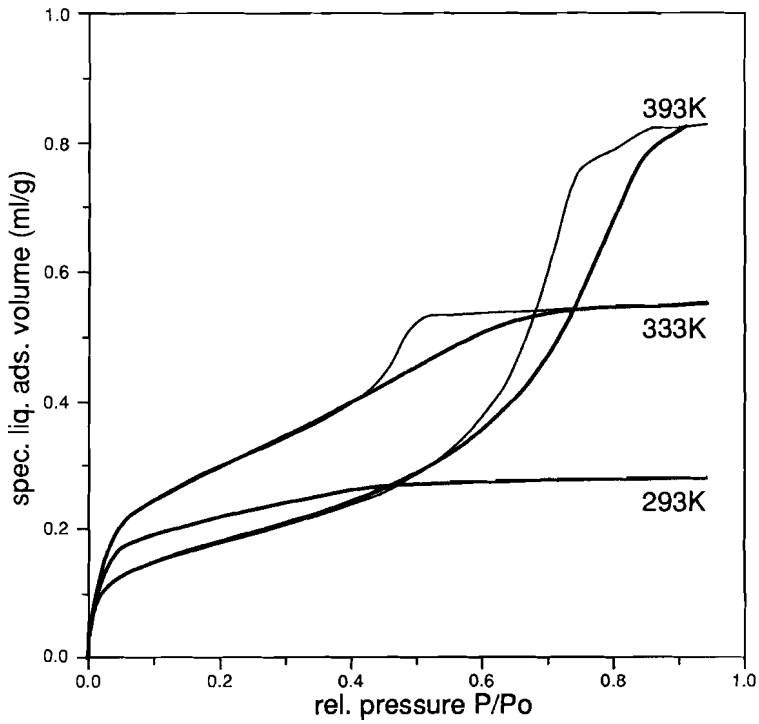

Figure 2 Adsorption isotherms of N_2 at 77 K on xerogel spheres dried at various temperatures. The thick lines represent adsorption and the thin lines the desorption isotherms.

Hydrothermal ageing of hydrogel and xerogel spheres

The growth of the mean pore size with ageing time of the samples 2a and b is represented in Fig. 3. A close relationship exists between the particle size of the initial sol and the pore radius. Between large particles large pore radii are expected. The driving force (Ostwald ripening) drops when the sol particles in the silica gel grow, which explains the gradual decline in pore growth.

Fig. 4 displays the change of the pore volume with the period of time of hydrothermal treatment for hydrogel 2a and xerogel 2b. Only the pore volume of the hydrogel samples significantly increases. The pore volume of the xerogel samples, already submitted to

shrinkage upon drying, remains at a constant low level [7,29]. In Fig. 5 the surface area is plotted as a function of the period of time of hydrothermal treatment of hydrogel and xerogel spheres, samples 2a and 2b, respectively. The decrease in surface area is accompanied by pore growth as evident from Figs. 3 and 5.

Table 3 Influence of the drying temperature on the texture of xerogel spheres determined by measuring the N_2 adsorption and desorption isotherm.

sample	T(K)	R_p(nm)	V_p(ml/g)	BET surface area (m^2/g)
1b	393	2.5	0.81	459
2b	393	2.3	0.76	455
3	393	3.5	0.83	424
4	333	2.1	0.55	689
5	293	<2	0.28	486
6	293	0.8	0.16	621

The shape factor F in thermoporometric characterization

Fig. 6 shows the thermogram of sample 7, which comprises the cooling step (3) and the heating step (4). The two endotherm peaks plotted in the positive direction of step (4) represent water in the pores at -3 °C and bulk water at 0 °C. The exotherm peak plotted in the negative direction at -7 °C of cooling step (3) represents water in the pores of the silica gel. The shape factor F of sample 7 is the ratio of A and B, which is A/B = 7/3 = 2.3 in Fig. 6.

DISCUSSION

The silica concentration calculated according to Eqn. 6 appears to be slightly higher than the theoretical value calculated from Eqn. 7 (Tab. 2). The difference is attributed to sodium and water captured in the cavities of the gel structure in combination with not fully condensed, adsorbed MSA at the silica-water interface [7,29,31,36]. Chertov [7]

reports the release of interglobular water from hydrothermally sintered silica as assessed by means of ignition and differential thermogravimetric measurement up to 1273 K. The release of sodium and condensation of silanol groups during hydrothermal treatment causes a dramatic change in pH of the hydrothermal ageing fluid ; the pH level rises from 6 to 10.

In the literature [6,7,34,37] the silica concentration is assumed to affect the pore structure of hydrogel and xerogel spheres only slightly. Plank and Drake have reported differences in pore structure for samples of various silica concentrations ranging from 1.5 to 10 wt% [21]. Subjecting the gels to an exchange of the sodium ions before drying [21] may initiate a variation in pH with drying [9]. In our experiments sodium exchange has not been performed, and, therefore, the pore structure of the xerogel is not a function of the silica concentration, but depends on the pH and the primary particle size [38].

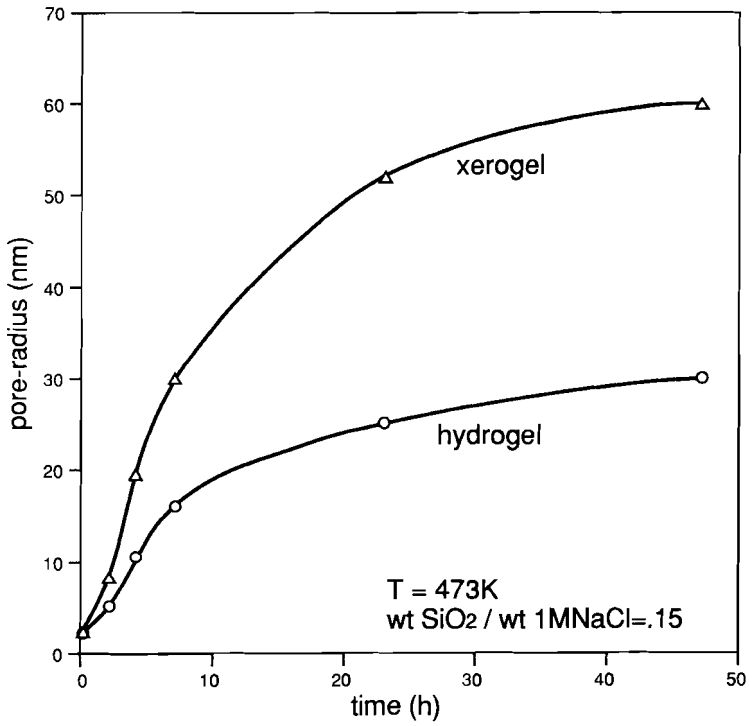

Figure 3 Pore growth of aged hydrogel and xerogel spheres with increasing duration of the hydrothermal treatment. The pore radius of the silica spheres has been plotted as a function of the period of time of the hydrothermal treatment. The pore radius has been measured by Hg intrusion.

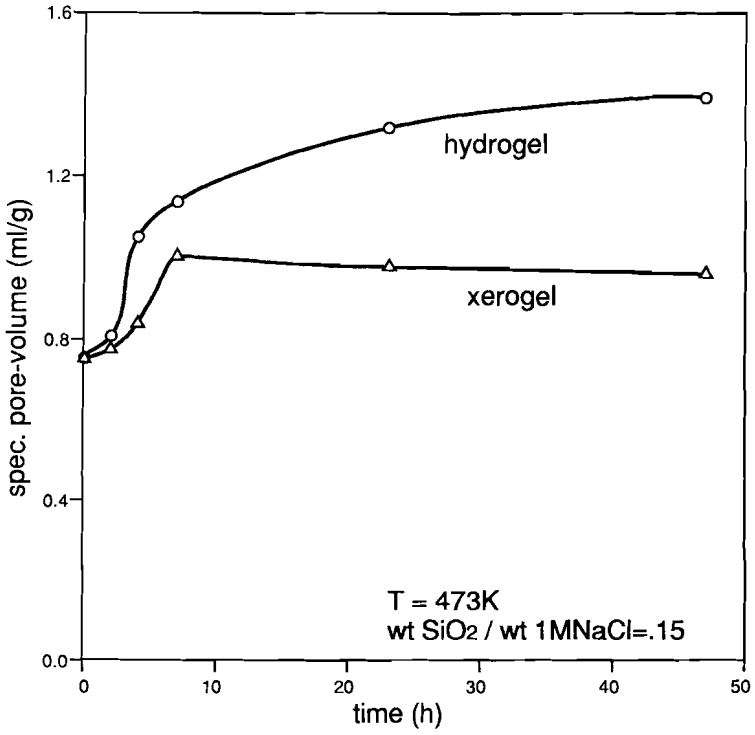

Figure 4 Influence of hydrothermal gel ripening on the pore volume of hydrogel and xerogel spheres. The pore volume has been calculated from the Hg intrusion results.

Silica xerogels prepared by Okkerse and de Boer [34] at a static pH level of 3 and dried at 393 K have a high specific surface area (820 m^2/g), a small primary particle size, and a low pore volume (0.3 ml/g). Silica xerogel prepared at a static pH level above 5.5 has a low specific surface area (440 m^2/g), large primary particles, and a high pore volume (0.8 ml/g). The pH in solution B varies from 0 to 5 during preparation of the sol, but the final pH level of 5 seems to be most important, because the pore structure of our samples resembles that of the silica gels of Okkerse and de Boer prepared at a static pH level of 5.5 [34].

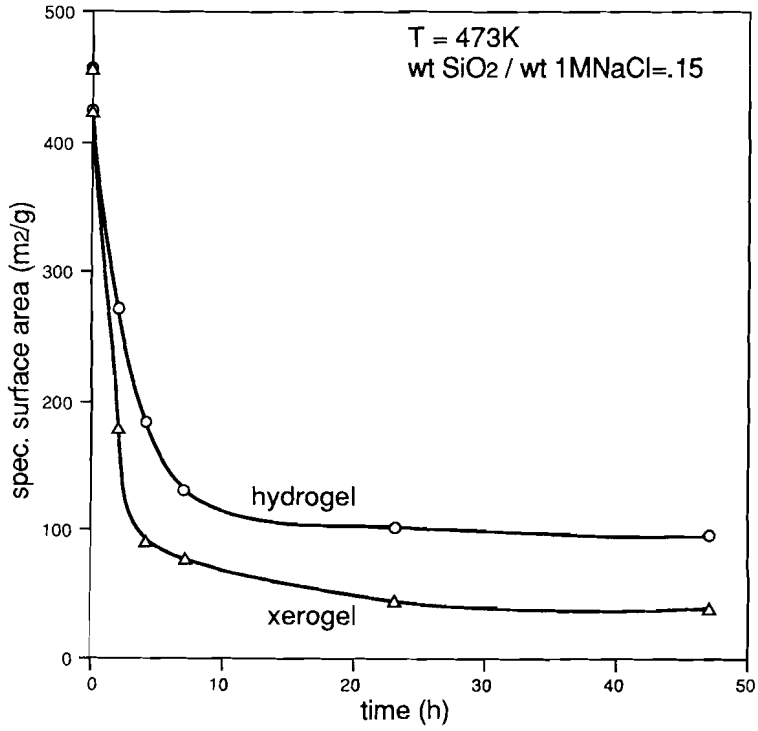

Figure 5 Development of the specific surface area of hydrogel and xerogel spheres with the period of time of hydrothermal treatment.

Effect of the drying temperature

Shrinkage during drying is affected by two factors, viz., i) the capillary stress in the liquid pressing the primary particles together, and ii) neck growth between the primary particles and strengthening of the gel structure, which counteracts the capillary stress. The shrinkage proceeds until the mechanical strength of the porous body can withstand the pressure exerted at the silica-liquid contact angle. Eqn. 9 expresses the capillary stress in the liquid, P, on the pore surface, as a function of pore radius, R_p (nm), water-vapor surface tension, γ (N/m), and θ the contact angle, derived from the relations $P*dV = \gamma*dA$, $dA/dV = 2/r$, and the radius of curvature $r = R_p/\cos\theta$:

$$P = 2\,\gamma * \cos\theta \,/\, R_p \qquad \text{(Pa)} \qquad (9)$$

The surface tension of water-vapor at drying temperatures of 293, 333, and 393 K is 0.073, 0.066, and 0.059 N/m by extrapolation, respectively (Handbook, 56th edition). The capillary force probably is less important at high drying temperatures, which is caused by

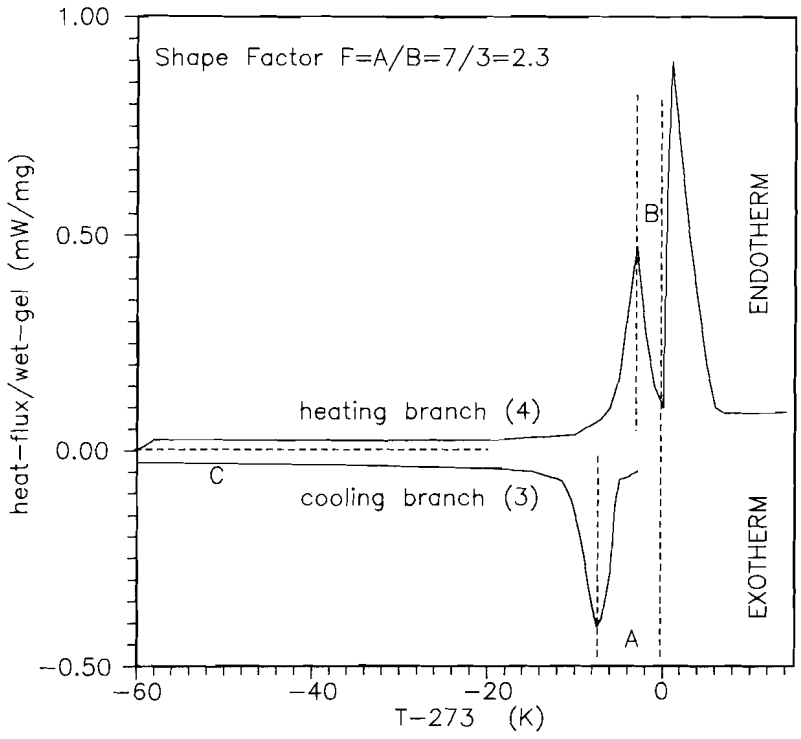

Figure 6 Thermogram of silica gel sample 7. 5.4 mg xerogel and 30 mg water, together 35.4 mg of the wet gel, is measured by thermoporometry. Exothermic peaks are plotted negatively, and endothermic peaks positively. The thermogram comprises a cooling branch (3) (rate -1 K/min) with an exotherm peak of water in the pores of the gel and a heating branch (4) (rate 1 K/min) with two endotherm peaks, one of water in the pores at -3° C and one of bulk water at 0° C. The shape factor F , dT(A)/dT(B), is 2.3. The heating branch (4) lies above and the cooling branch (3) lies below the dashed line of 0 mW/mg at point C. This is due to the C_p of ice. The C_p can be estimated: 0.03 heat-flux/wet-gel*35.4 mg wet-gel/ (30 mg water* 60 sec/K) = 2.1 J/g.

the reduced surface tension of water. The effect of the surface tension of the evaporating solvent on the final decreased pore volume of the xerogel is clearly demonstrated in work of Dashpande et al. [39]. Furthermore, the residence time of the meniscus in the pores decreases with drying at high temperatures. Therefore, the specific pore volume in the pores of the spheres increases when they are dried at higher temperatures.

Comparison between aged hydrogel and xerogel

From Fig. 3, a pore growth more rapid with the xerogel 2b than with the hydrogel 2a is evident. In the literature [7] similar results have been attributed to the effect of the initial pore and surface structure. The initial pore radius, R_p, of the xerogel 2b is smaller than the initial radius, R_n, of hydrogel 2a (Tab. 2). The xerogels probably contain more condensed silanol groups than the hydrogels. The fact that the surface silanol groups play an important role in the deposition of silica is confirmed by the literature [7,9,36,40].

The meso pore volume of xerogel being virtually constant with ageing, as indicated in Fig. 4, is also confirmed by low-field NMR spin-lattice relaxation [41]. Some decrease of the pore volume of the xerogel is probably due to condensation of OH groups present on different elementary silica particles, which leads to densification of the gel matrix. The process is called syneresis. The increasing pore volume of aged hydrogels agrees with the result of Pauthe et al. [42]. The authors found an increase of the meso pore volume ($1nm < R < 30nm$) with ageing of not dried alcogels.

The ice-water transformation enthalpy

Our expression (3) of the ice-water transformation enthalpy, H, differs from the expression introduced by Brun et al. [15]. The authors use the following relation for H :

$$H = 332 + 7.43*dT + 5.56*10^{-2}*dT^2 \qquad (J/g) \qquad (10)$$

Eqn. 10 assumes the presence of a layer of thickness t of water which cannot solidify due to interaction with the surface of the solid. With a cylindrical pore shape, the volume of the non-freezing water, which affects the value of H, the transformation enthalpy according to Eqn. 10, depends on dT, the drop in the solidification temperature. Because R_n is a function of dT, the volume of the non-freezing water is a function of dT. The following equation of H has been given in [18] :

$$H = 332 + 0.25*dT \quad (J/g) \quad (11)$$

The origin of the constant 0.25 J/g*K in Eqn. 11 has not been clarified. Recently, Cuperus et al. [20] reported a value of H, where it is not clearly described whether the apparent transition energy H is corrected for the non-freezing layer ;

$$H = 332 + 11.39*dT + 0.155*dT^2 \quad (J/g) \quad (12)$$

We prefer an expression of H applicable to water within pores of different shapes, because the pore volume can be corrected for the non-freezing layer afterwards (without assumption of a spherical shape). The enthalpy, H, should be corrected for the energy involved in the formation of a ice-water interface, that is :

$$dH_1 = dS°*dT = 1.2*dT \quad (J/g) \quad (13)$$

Besides, the heat of phase transformation must be corrected for the difference in heat capacity C_p of supercooled water and ice ($C_l°$, and $C_s°$) (zero order approximation) :

$$dH_2 = (C_l°-C_s°)*dT = (4.2-2.1)*dT = 2.1*dT \quad (J/g) \quad (14)$$

Both corrections ($dH_1 + dH_2$) are applied in our Eqn. 15 and earlier in Eqn. 3.

$$H = 332 + (dH_1 + dH_2) = 332 + 3.3*dT \quad (J/g) \quad (15)$$

The shape factor F in thermoporometric characterization

The theory of the shape factor [18] assumes exclusively spherical and cylindrical pores. Accordingly the value of the shape factor F should necessarily be confined to values between 1 (spherical pores) and 2 (cylindrical pores), since the pore shape can be neither pure cylindrical nor pure spherical [17,19] :

$$1 < F < 2 \quad (16)$$

However, open slit-shaped pores exhibit theoretically a shape factor of infinity, which is of course with real pore systems never observed. Our experimental data (Table 2) indicate for the hydrogel sample 2a a mean shape factor F of 2.7. With cooling rates of 2 and 30 K/h shape factors of 2.6 and 2.8, respectively, have been measured. The shape factor of the xerogel sample 7 is 2.3. Bearing in mind the fact that the sample 7 is a dried gel and that the shape factor F is diminished after drying, the shape factor of the not dried sample 7 was probably larger than 2.3.

The value m, which gives together with the radius, R_n, the surface-to-volume ratio of the pores according to Eqn. 17, is 2 for cylindrical and 3 for spherical pores. The factor m, which thus is used to calculate the surface area, A_n, from the ice crystal radius, R_n, and the pore volume, V_n, is related to the shape factor F by $m = 4\text{-}F$ [19].

$$A_n = m * V_n / R_n \qquad (m^2/g) \qquad (17)$$

According to ref. [19], F is limited to values < 4. Therefore, we prefer the empirical relation $m = 1 + 2/F$ above the empirical relation $m = 4\text{-}F$. The relation $m = 1 + 2/F$ is used in Eqn. 4.

CONCLUSIONS

1) A procedure to prepare spherical gel bodies of a uniform pore structure is described. The xerogel pore structure is mainly determined by the drying temperature and not by the silica concentration. Pore volumes between 0.2 and 0.8 ml/g can be obtained upon drying at temperatures between 293 and 363 K. Even values for the pore volume as high as 1.4 ml/g are attained after hydrothermal treatment of hydrogel spheres. The pore radius varies between 0.8 and 60 nm and, consequently, the surface area between 690 and 38 m^2/g with ageing times varying between 0 and 47 h.

2) When the hydrogel samples are treated hydrothermally, the elementary particles in the gel are compressed to a more dense xerogel. A change of the pore shape to a more spherical shape is detected by thermoporometry. The radius of the dried xerogel pores, as determined by thermoporometry, is larger than the radius measured by N_2 adsorption and desorption ($R_n > R_p$), because thermoporometry yields the internal radius of the pores instead of the pore neck radius. Moreover, the pore volume and the internal surface area of the xerogel spheres as obtained by thermoporometry are too low; $V_n < V_p$, which is caused by a non-freezing layer of a thickness of 0.9 nm.

3) The features observed during hydrothermal ageing of hydrogel and xerogel spheres are remarkably different. A more pronounced pore growth of the xerogel spheres is observed. An increase of pore volume, on the other hand, is found with hydrogel spheres, whereas the pore volume of xerogel spheres which were already submitted to a certain extent of shrinkage remains constant.

ACKNOWLEDGMENTS

This investigation is a result of participation in the Debye Institute. The authors wish to thank J.J. van Beek, dr. P.A. Buining, dr. J.T. Kloprogge, and dr. C.J.G. van der Grift for the critical review of the paper.

REFERENCES

1. J.W. Geus, Preparation of Catalysts III, Ed. G. Poncelet, P. Grange and P.A. Jacobs, Elsevier, Amsterdam, (1983) 1
2. J. Zarzycki, M. Prassas and J. Phalippou, *J. Mat. Sci.*, **17** (1982) 3371
3. A.J. Hurd and C.J. Brinker, *J. Phys. France*, **49** (1988) 1017
4. P.H. Berben, A. Scholten, M.K. Titulaer, N. Brahma, W.J.J. van der Wal and J.W. Geus, Stud. in Surf. Sci. and Catal. **34** : Catal. Deact. IV, Ed. B. Delmon and G. Froment, Elsevier, Amsterdam, (1987) 303
5. R.Yu. Sheinfain and I.E. Neimark, *Kinetika i Kataliz USSR*, **8** II (1967) 433, Engl. Transl. 370
6. G.A. Nicolaon and S.J. Teichner, *Bull. Soc. Chim. France*, **8** (1968) 3107, **5** (1968) 1906
7. V.M. Chertov and V.V. Tsyrina, *Coll. J. USSR*, **47** V (1985) 922
8. A.V. Kiselev, V.M. Luk'yanovich, Yu.S. Nikitin, E.B. Oganesyan and A.I.Sarakhov, *Coll. J. USSR*, **31** III (1969) 388
9. V.A. Fenelov, V.Yu. Gavrilov and L.G. Simonova, Preparation of Catalysts III, Ed. G. Poncelet, P. Grange and P.A. Jacobs, Elsevier, Amsterdam, (1983) 665
10. C.J.G. van der Grift, J.W. Geus, H. Barten, R.G.I. Leferink, J.C. van Miltenburg and A.T. den Ouden, Characterization of Porous Solids, Eds. K.K. Unger *et al.*, Elsevier, Amsterdam, (1988) 619
11. B.J.J. Zelinski and D.R. Uhlmann, *J. Phys. Chem. Solids*, **45** X 1069
12. C.J. Brinker, K.D. Keefer, D.W. Schaefer and C.S. Ashley, *J. Non-Cryst. Solids*, **48** (1982) 47
13. M. Prassas, J. Phalippou, J. Zarzycki, *J. de Physique*, **43** (1982) C9-257
14. I. Shapiro and I.M.Kolthoff, *J. Am. Chem. Soc.*, **72** I (1950) 776

15. M. Brun, A. Lallemand, J.F. Quinson and C. Eyraud, *Thermochimica Acta*, **21** (1977) 59
16. C. Jallut, J. Lenoir, C. Bardot and C. Eyraud, J. Membr. Sci., **68** (1992) 271
17. C. Eyraud, J.F. Quinson and M. Brun, Characterization of Porous Solids, Eds. K.K. Unger *et al.*, Elsevier Amsterdam, (1988) 295
18. J.F. Quinson and M. Brun, Characterization of Porous Solids, Eds K.K. Unger *et al.*, Elsevier Amsterdam, (1988) 307
19. J.F. Quinson, M. Astier and M. Brun, *Applied Catal.*, **30** (1987) 123
20. F.P. Cuperus, D. Bargeman and C.A. Smolders, J. Membr. Sci., **66** (1992) 45
21. C.J. Plank and L.C. Drake, *J. Coll. Sc.*, **2** (1947) 399
22. R.H. Busey and R.E. Mesmer, *Inorg. Chem.*, **16** X (1977) 2444
23. R.P. Abendroth, *J. Coll. Interf. Sci.*, **34** IV (1970) 591
24. P.W.J.M. Boumans, Inductively Coupled Plasma Emission Spectroscopy, 90 I, Wiley Interscience, (1987)
25. R.K. Iler, The Chemistry of Silica, Wiley N.Y., (1979) 94-101
26. J.D. Rimstidt and H.L. Barnes, *Geochim. et Cosmochim. Acta*, **44** (1980) 1683
27. A.C. Makrides, M. Turner and J. Slaughter, *J. Coll. Interf. Sci.*, **73** (1980) 345
28. C.B. Hurd, R.C. Pomatti and J.H. Spittle, *J. Am. Chem. Soc.*, **66** (1944) 388
29. N.V. Akshinskaya, T.A. Baigubekova, A.V. Kiselev and Yu.S. Nikitin, *Coll. J. USSR*, **28** II (1966) 164. Engl. Transl. 139
30. S. Lowell and J.E. Shields, Powder Surface Area and Porosity, 2nd. Ed., Chapman and Hall London, (1984) 1-135
31. G.B. Alexander, *J. Phys. Chem.*, **61** (1957) 1563
32. R.K. Iler, Soluble Silicates, Ed. J.S. Falcone Jr., ACS Symposium Series 194, Washington D.C. (1982) 96
33. J.A. Otterstedt, M. Ghuzel and J.P. Sterte, *J. Coll. Interf. Sci.*, **115** I (1987) 95
34. C. Okkerse and J.H. de Boer, *J. Chim. Phys.*, **57** (1960) 534
35. I.V. Yazynina, V.I. Kvlividze and A.V. Krasnushkin, *Coll. J. USSR*, **49** VI (1987) 1188
36. B.A. Fleming, *J. Coll. Interf. Sci.*, **110** I (1986) 40
37. K. Gärtner and R.Griessbach, *Kolloid-Zeitschrift*, **160** I (1958) 21
38. K.S.W. Sing and J.D. Madeley, *J. Appl. Chem.*, **3** (1953) 549
39. R, Deshpande, D.W. Hua, D.M. Smith and C.J. Brinker, J. Non-Cryst. Sol., **144** (1992) 32
40. E.G. Bohlman, R.E. Mesmer and P. Berlinsky, *Soc. Pet. Eng. J.*, **20** (1980) 239
41. P.J. Davis, C.J. Brinker and D.M. Smith, J. Non-Crystal. Sol., **144** (1992) 32
42. M. Pauthe, J.F. Quinson, H. Hdach, T. Woignier, J. Phalippou and G.W. Scherer, J. Non-Crystal. Sol., **130** (1991) 1
43. S.A. Greenberg, *J. Am. Chem. Soc.*, **80** (1958) 6508

Chapter 3

The differences in the elementary processes proceeding during ageing of hydrogels and of xerogels

M.K. Titulaer, P.E. Groenendijk[1], J.B.H. Jansen, and J.W. Geus[1]

Department of Geochemistry, Institute of Earth Sciences, University of Utrecht, Budapestlaan 4, P.O. Box 80.021, 3508 TA Utrecht, The Netherlands.
[1]Department of Inorganic Chemistry, University of Utrecht, Sorbonnelaan 16, P.O. Box 80.083, 3508 TB Utrecht, The Netherlands.

ABSTRACT

Spherical porous sol-gel silica bodies are prepared by addition of a sodium silicate solution to a dilute nitric acid solution. The thus prepared silica sol of 13 wt% silica in water is introduced dropwise into hot paraffin oil, which results in spherical hydrogel spheres. Some batches of the hydrogel spheres are dried at 393 K, forming xerogel spheres. The spheres of a few mm's size have been aged under different hydrothermal conditions. The pore structure of the spheres is modified by an autoclave treatment in water. Differences in the ageing mechanisms of hydrogel and xerogel spheres are monitored by the development of the pore radius, pore volume, and surface area. The differences can be ascribed to the different kinetics of silica polymerization of hydrogel and xerogel. Various ageing conditions are compared, viz., 1) temperatures between 298 and 523 K, 2) pH levels between 3.3 and 6.8, 3) ion strengths between 0 and 6 M, and 4) pressures between 1 and 2800 hecto Pa. The hydrothermal treatment is performed at a constant duration of 24 h. The pore structure of the spheres is mainly influenced by the temperature, the pH, and the silica over water ratio with ageing, whereas the ion strength and the pressure have little effect.

INTRODUCTION

Though a large body of literature has been published on the preparation of alcogels and the adaption of the pore structure, mainly dealing with utilization of the alcogels in the

production of glass at low temperature, only a few amount of papers are considering the differences in the elementary processes proceeding during ageing of the hydrogels, on the one, and xerogels, on the other hand. The gels studied in this work are prepared from sodium silicate solutions. We are mainly interested in the development of the pore structure of the gels, in view of the use of the aged gels as a model system of a catalyst support.

In the previous Chapter 2 we have described the preparation of porous silica bodies of a few mm's size with a pore structure controlled by varying the drying conditions and the duration of a subsequent hydrothermal treatment. The spheres are prepared by addition of 76 ml of a sodium silicate solution (3 M Si, 1.5 M Na) to 50 ml of a 2 M HNO_3 solution present in a plastic cup in an ice-water bath. The resulting silica sol containing 13 wt% SiO_2 in water is immediately after preparation introduced dropwise into a cylinder of paraffin oil kept at 363 K, forming spherical hydrogel bodies. After washing with demineralized water, some batches of hydrogel spheres are dried at 393 K, forming xerogel spheres.

The silica gel spheres consists of a network of primary sol particles of 5 nm size. Ostwald ripening of the primary particles in the gel is accelerated by hydrothermal treatment of the spheres. Reorganization of the silica results in the final pore structure. As a result of ageing, the specific surface area decreases, and the pore size is increases. The research dealt with in this chapter is focused upon the effects of different ageing conditions, such as, 1) temperature, 2) pH, 3) concentration of NaCl, 4) pressure, and 5) silica-to-water ratio. Ageing of hydrogels and xerogels is especially compared. The development of the pore structure is assessed with nitrogen sorption on untreated xerogel spheres, and with mercury penetration with gels treated at stepwise varied conditions after drying.

Silica solubility in the hydrothermal fluid

The ripening of silica gel proceeds rapidly at high temperature, because i) of the large silica solubility S(T), and thus expected large gradients of the silica solubility, and ii) a high rate of polymerization and depolymerization. Empirical functions for the solubility S(T) of silica are Eqn. 1 published by Fournier and Rowe [1] and Eqn. 2 by Fleming and Crerar [2] :

$$\log S(T) = -731/T + 4.52 \qquad (1)$$

$$\log S(T) = -840/T + 5.12 - 7.9\times10^{-4}*T \qquad (2)$$

where S(T) is the solubility (ppm = mg SiO_2/l), and T the temperature (K). By application of the equation $d\log S(T)/ d(1/T) = -H_s/2.303*R$ using Eqn. 1 with R = 8.314

$J*mole^{-1}*K^{-1}$, the heat of solution is calculated to be 14 kJ/mole. The solubility strongly depends on the structure of the silica-electrolyte interface. At 298 K a value of 115 ppm monosilicic acid (MSA) is generally accepted for amorphous silica, whereas the solubility of quartz is approximately ten times lower, viz., 11 ppm [3].

The effect of the silica sol particle size

The equilibrium solubility S(T,d) in ppm of a sol particle of a diameter d (nm) at a given temperature T (K) according to the Kelvin equation of ref. [4] is :

$$\log [S(T,d)/S(T)] = 4*\gamma*V_m/(2.303*R*T*d) = 257/(T*d) \quad (3)$$

S(T) is the solubility of a silica surface of a virtually infinite large radius of curvature, which is 115 ppm at 298 K, γ the surface tension of silica, which is 0.045 N/m, V_m the molar volume of $2.73*10^{-5}$ m^3/mole, and R the gas constant of 8.314 $J*mole^{-1}*K^{-1}$. The silica in the hydrothermal fluid is transported due to a concentration gradient caused by the equilibrium solubility of particles of different sizes (Ostwald ripening). The silica is transported from the small sol particles of a high equilibrium solubility to the large particles of a lower equilibrium solubility. The small particles thus dissolve, and attain an even higher equilibrium solubility by the reduced particle size. A combination of Eqn. 1 with Eqn. 3, yields the Eqn. 4 :

$$\log S(T,d) = 257/(T*d) - 731/T + 4.52 \quad (4)$$

, which can be rewritten by the relation $A_s = 2727/d$ with A_s is the specific surface area of the silica sol particles (in m^2/g) to :

$$\log S(T,A_s) = 0.094*A_s/T - 731/T + 4.52 \quad (5)$$

Effect of the pH

An apparently high silica solubility is established when the pH reaches the first MSA ionization constant of 9.8 at 298 K [5]. Fleming and Crerar have reviewed the literature

[2]. The authors arrived at Eqn. 11, which completely describes the relationship between the solubility of silica, the pH and the temperature.

$$MSA + OH^- \rightarrow MSA^- + H_2O \quad (6)$$

$$K_w(T) = [H^+] * [OH^-] \quad (7)$$

$$\log K_w(T) = 0.0265*T-22.03 \quad (8)$$

$$K_B(T) = [MSA^-]/([MSA]*[OH^-]) \quad (9)$$

$$\log K_B(T) = 1479/T-0.65 \quad (10)$$

$$S(pH,T) = S(T) * (1 + K_B(T) * K_w(T) * 10^{pH}) \quad (11)$$

with S(pH,T) the silica solubility (ppm) as a function of the temperature T (K), and the pH.

Effect of the concentration of NaCl

The values of K_w and of K_B at 298 K, the equilibrium constant defined in Eqn. 9, depend on the concentration NaCl, [NaCl] in ref. [6] by :

$$\log K_w(298K,NaCl) = \log K_w + 0.22[NaCl] + 1.022\sqrt{[NaCl]}/(1+\sqrt{[NaCl]}) \quad (12)$$

$$\log K_B(298K,NaCl) = \log K_B + 0.11[NaCl] + 1.022\sqrt{[NaCl]}/(1+\sqrt{[NaCl]}) \quad (13)$$

Furthermore, the addition of NaCl has several effects on the development of the pore structure during hydrothermal ageing. NaCl affects both the number of ionized surface silanol groups and the solubility of amorphous silica. Marshal [7] has made a detailed study on the effect of 0 to 6 M of a 1-1 electrolyte on the solubility of silica between 298 and 573 K. An important conclusion is that the solubility does not depend on the anion of the salt added but decreases in the order $Mg^{2+}, Ca^{2+} > Li^+ > Na^+ > K^+$. Smaller cations bind water more strongly. The cations remove 'free' water from the solvent and thus decrease the solubility of silica. Since the ionic radii Li^+, Na^+, and K^+ are 0.68, 0.98, and 1.33 Å, respectively, the effect of the above cations on the solubility of silica agrees with the removal of 'free' water. The solubility in 0 to 6 M NaCl, similar to that in $NaNO_3$, is given by Eqn. 14 :

$$\log [S(T)/S(NaCl,T)] = 0.008285 * [NaCl] * 10^{280/T} \quad (14)$$

where S(NaCl,T) is the silica solubility in NaCl (in ppm = mg SiO_2/l) at a given temperature T (in K), S(T) the salt free solubility as a function of the temperature, and [NaCl] the sodium chloride concentration (in mole/l). The solubility in 6 M NaCl at 298 K, which is 42 ppm is considerably lower than that in water, which is 115 ppm, a decrease of 63%. At the higher temperature of 573 K in 6 M NaCl, the decrease of solubility is less, viz., the solubility is only 30% lower than the level of 1700 ppm in pure water.

Effect of the pressure

Increasing the pressure from 1 to 1,000 hecto Pa, shifts the equilibrium of Eqn. 15 to the smallest molar volume ($V_m(SiO_2+2H_2O\text{-MSA}) > 0$ m^3/mole). Raising the pressure increases the density of water at 473 K from 0.86 to 0.92 g/ml and consequently, the solubility of silica from 900 to 1237 ppm (Eqs. 16-20, and experimentally derived Eqn. 21) [1,8,9].

$$SiO_2 + 2H_2O \text{ --> MSA} \quad (15)$$

$$dU = q + w_{ref} = T*dS - P*dV + \Sigma_i \mu_i*dn_i \quad (J) \quad (16)$$

where dU is the energy of the system, q is the thermal energy and w_{ref} the volume work of the system, which decreases the energy of the system and has a negative sign. The Gibbs free energy, dG, of the system for the reaction of Eqn. 15, thus free of the thermal energy change and the volume work is given by ;

$$dG = dU - d(TS) + d(PV) = -S*dT + V*dP + \Sigma_i \mu_i*dn_i = 0 \quad (J) \quad (17)$$

$$dG_T = V(MSA\text{-}SiO_2\text{-}2H_2O)*dP + \Sigma_i \mu_i*dn_i \quad (J) \quad (18)$$

$$\Sigma_i \mu(MSA\text{-}SiO_2\text{-}2H_2O) = 2.303*R*T \, d\log [[MSA]/([SiO_2]*[H_2O]^2)] \quad (19)$$

$$V_m(SiO_2+2H_2O\text{-}MSA) * dP \sim 2.303*R*T * d\log [MSA] \text{ (J/mole)} \quad (20)$$

and experimentally derived from Eqn. 20 :

$$\log [S(P,T)/S(P_o,T)] = 2.3 * (D(P,T)-D(P_o,T)) \quad (21)$$

where V_m is the change in molar volume with polymerization (m^3/mole), dP the increased pressure (N/m^2), R is 8.3 (J/mole*K), T the temperature (K), [MSA] the monosilicic acid concentration (mole/l), S(P,T) the silica solubility as a function of pressure and temperature (ppm), D(P,T)-D(P_o,T) the change in density of water with increased pressure (in g/ml).

Polymerization at the silica surface in the hydrothermal fluid

The kinetics of the polymerization of silica from supersaturated MSA solutions has been studied in three ways, viz., i) quenching a hot silica solution [10,11], ii) lowering the pH of a sodium silicate solution by addition of a strong acid [12], and iii) cation exchange over a resin column [13,14]. The dissolution kinetics is simply investigated by addition of silica to water, and measuring the MSA concentration as function of time [15]. The kinetics of the polymerization of silica can roughly be divided into two regimes : 1) nucleation and formation of LMS (Low Molecular Silica), and 2) growth of large colloidal particles in later stages of the polymerization. The dimerization of MSA follows in all probability an SN2 reaction path, exhibiting a second order in MSA and a first order in the hydroxyl concentration [16-19]. Only MSA, and not the dimers and LMS species, is probably responsible for the transport of silica in the hydrothermal fluid, because the diffusion coefficient decreases with the polymeric size, according to a Stokes-Einstein relationship [20]. In the literature, the rate of the drop in MSA has reported to be first order [21,22], third order [23-25], and even fourth order [10] with respect to the MSA concentration, depending on the various models used. As the polymerization proceeds, large colloidal particles appear, which take over the role as nucleophile instead of ionized MSA. Furthermore, the silica concentration reaches the equilibrium solubility. The growth of the sol particles is first order with respect to not ionized MSA and ionized surface silanols (Eqn. 22) [12,26,27]. The rate of dissolution is proportional to the number of ionized surface silanols, but zero order with respect to MSA (Eqn. 23).

$$d[MSA]/dt = -k_f(T) * [Si_sO^-] * ([MSA]-S_x(T)) \quad (22)$$

$$d[MSA]/dt = k_b(T) * [Si_sO^-] \quad (23)$$

$$k_b(T) = k_f(T) * S_x(T) \quad (24)$$

with [MSA] the concentration of MSA in solution (ppm), $S_x(T)$ the equilibrium solubility of MSA adsorbed at the silica-water interface, which is 200 ppm at 298 K (Eqn. 25), d[MSA]/dt (ppm*s^{-1}), $k_f(T)$, and $k_b(T)$ the forward and backward rate constant ($mole^{-1}$*l*s and s^{-1}), respectively, and [Si_sO^-] the concentration of ionized surface silanol groups (mole/l). The salt-free forward rate constant $k_f(T)$ for amorphous silica is 1.03 $mole^{-1}$*l*s^{-1} at 298 K [26].

$$\log S_x(T) = -575/T + 4.23 \quad (25)$$

where $S_x(T)$ is the solubility of adsorbed MSA (ppm), and T (in K). The pH and the ion strength are determining the number of ionized surface silanol groups. There is confusion about the number of surface silanols per unit surface area, probably due to the presence of adsorbed MSA during polymerization, and the effect of the calcining step before the measurement of the amount surface silanols. The density of silicon atoms on a fully condensed surface (9.2 nm^{-2}) is similar to the density of the a x b plane of hexagonal β-tridymite or of the (110) plane of cristobalite, which surface is covered with tertiary silanol groups. Fifty percent of the silanol groups point out of plane, which leads to a density of 4.6 nm^{-2} [28-30]. A value of 3.5 nm^{-2} silanol groups at the surface is reported in ref. [31]. The spectroscopic amount of silanol groups comprises 1,4 nm^{-2} of isolated, 3.2 nm^{-2} of vicinally paired (together with the isolated silanols 4.6 nm^{-2}), and 1.6 nm^{-2} of internal groups in bulk SiO_2 (together 5.8 nm^{-2}) after drying at 383 K [16,32-35]. The vicinally paired silanol groups seem to be hydrogen bonded to each other on the surface and are chemically much less reactive than the free silanol groups [28]. The maximum proton exchange capacity of 5.8 nm^{-2} of silica gel in 3 M $NaClO_3$ is determined by a coulometric titration, which shows that internal groups can participate in the exchange reaction [36]. The activation energy of polymerization is 61 kJ/mole and that of dissolution 50 kJ/mole. The difference is about the heat of solution H_s of 11-14 kJ/mole [1,19,26,37].

$S_x(T)$ is the equilibrium concentration of an intermediate reaction species at a silica surface covered by adsorbed MSA, which amounts to 200 ppm at 298 K. Holt and King [38,15] established the existence of the adsorbed layer exhibiting a high solubility. An instantaneous rapid dissolution of the adsorbed layer is observed, when silica powder or quartz is added to a NaOH solution [27], whereas rapid adsorption of the layer takes place when calcined (and, hence, MSA-free) silica powder is added to not saturated MSA solutions. The existence of adsorbed MSA on the silica surface is probably the main difference between a hydrogel and a calcined xerogel.

The presence of the adsorbed species during polymerization implies that the density of silanol groups is higher than 4.6 nm^{-2}. Weres et al. [39] found a value of 6.8 nm^{-2} during

the early stages of polymerization, with a maximum of 7.85 nm^{-2}.

The order of the particle growth rate in the hydroxyl concentration decreases from 1.3 to 0 when the pH is raised from 6 to 7.3, because at a high pH level the surface is saturated with Si_sO^- groups. Efforts to explain the surface ionization with physical absorption of OH^- have failed. In refs. [40-44], a site-binding model has been proposed in which both chemical and physical interactions are considered simultaneously. In this model the surface charge and the solution equilibria can be calculated in the presence of most electrolyte ions. The surface ionization and complexation with sodium is represented in Eqn. 26.

$$Si_sOH + Na_s^+ \text{ --> } Si_sO^-Na^+ + H_s^+ \qquad (26)$$

The subscript s means surface. The SiO^-Na^+ surface species have no particular bonding structure. Both Na_s^+ and H_s^+ show a Boltzmann distribution (Eqn. 27).

$$[H_s^+] / [Na_s^+] = \exp(4.3*f) * [H^+] / [Na^+] \qquad (27)$$

with $[H_s^+]$ the concentration at the silica surface, $[H^+]$ the concentration in the bulk of the solution, 4.3 factor varying with the reciprocal temperature, which is 4.3 at 298 K, and f the fraction ionized surface sites. If the fraction f is known, the concentration $[Si_sO^-]$ in solution can be calculated with Eqn. 28 and used in Eqs. 22 and 23.

$$[Si_sO^-] = W * A_s * f * 7.85*10^{18} / 6*10^{23} * V \qquad (28)$$

with W the weight of SiO_2 (in g), A_s the specific surface area (m^2/g), f the fraction ionized silanol groups, $7.85*10^{18}$ m^{-2} the quantity of surface silanol groups during the polymerization, $6*10^{23}$ Avogadro's number ($mole^{-1}$), and V the volume of the hydrothermal fluid (l). Eqn. 30 shows the relation between the fraction f of the ionized surface silanol groups, the pH, and the [NaCl], which is derived from the experimental Eqn. 29. It appears that the amount ionized surface silanol groups is increased with the pH and the [NaCl], explaining the decreased critical coagulation activity (cca) for NaCl of Ludox silica at higher pH levels with dlog(cca) / dpH = -0.326. Only small differences between NaCl, $NaNO_3$, $NaBrO_3$ are measured due to the mean activity coefficients introduced by the different anions [45,46]. According to the DLVO theory the cca is usually increased with increased pH.

$$K_i = \exp(4.3*f) * [H^+]*[Si_sO^-Na^+] / [Si_sOH]*[Na^+] \quad (29)$$

$$\log [f/(1-f)] + 1.87*f = pH - pK_i + \log [NaCl] \quad (30)$$

where K_i is the intrinsic acid constant, which is determined by a double extrapolation technique in [44]. The pK_i in the presence of NaCl is 6.4-6.9, while the 'salt free' pK_i used in Eqn. 30 is relatively high, viz., 8.2 [36,43,44]. However, a low spectroscopic salt-free value of the ionization constant pK_a of surface silanols is reported in ref. [47], viz., 7.1.

EXPERIMENTAL

Hydrogel spheres of a few mm's size are dried at 393 K for 24 h, and calcined at 723 K for 24 h, resulting in a xerogel. The results of treatments of xerogel spheres are compared with those of hydrogel spheres with an equal concentration of silica in water. In the hydrothermal experiments an amount of 3.15 g xerogel spheres is treated with 20.85 ml of a 1 M NaCl solution in rotating teflon cups in steel pressure vessels of 48 ml. An amount of 24 g of the hydrogel spheres is washed with 1 M NaCl and treated simultaneously in the pressure vessels. All hydrothermal experiments are performed at the vapor saturation pressure [8], except for the high-pressure experiments.

High-pressure experiments are carried out in Tuttle type autoclaves [48]. The sample is sealed in a ductile gold capsule with a graphite arc welder. The fluid filling grade is chosen so, as to not exceed the excess external argon pressure. The autoclaves are placed vertically and externally heated. Temperatures are measured by chromel alumel thermocouples at several spots in the autoclaves. A fillerrod holds the capsule at the hot spot of the furnace and minimizes the argon content of the vessel. The closure nut of the autoclave is cooled to prevent damage of the thread and the closure rings by the high temperature.

First, the effect of different ageing temperatures is investigated. The temperature is varied in five intervals between 373 and 523 K at a fixed duration of 24 h, a silica-to-water ratio of 0.15 g/g, a NaCl concentration of 1 M, and a pH of 6. The silica-to-water ratio of 0.15 g/g is equal to the 13 wt% silica content of the hydrogel spheres.

The pH values are varied from 3.2 to 8.6 with increments of two pH units, at a temperature of 473 K. Diluted hydrochloric acid and sodium hydroxide solution are used to establish the desired pH. The sodium chloride concentrations used are 0, 1, 2, 4, and 6 M, and the silica-to-water ratio 0.15, 0.4, 0.6, and 0.8 wt/wt. The variation of the silica-to-water ratio is only performed with xerogel spheres, because the ratio of the hydrogel spheres is fixed. High-pressure experiments are done at the vapor saturation pressure, 500, 1500, and 2800 hecto Pa.

After the hydrothermal treatment the xerogel and hydrogel spheres are washed, dried at 393 K for 24 h, and subsequently calcined at 723 K for 24 h. The pore radius, pore volume, and internal surface area are assessed by Hg penetration (Carlo Erba 2000). Only the intrusion is measured.

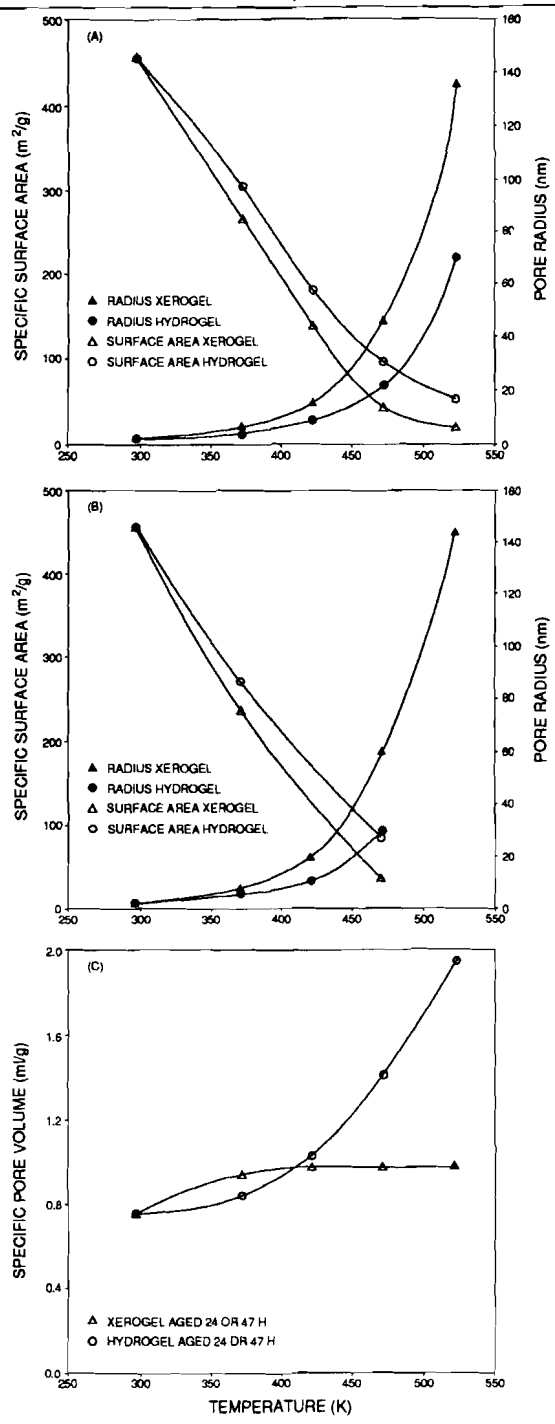
(A)
SPECIFIC SURFACE AREA (m^2/g)
PORE RADIUS (nm)
RADIUS XEROGEL
RADIUS HYDROGEL
SURFACE AREA XEROGEL
SURFACE AREA HYDROGEL
24 h
(B)
SPECIFIC SURFACE AREA (m^2/g)
PORE RADIUS (nm)
RADIUS XEROGEL
RADIUS HYDROGEL
SURFACE AREA XEROGEL
SURFACE AREA HYDROGEL
47 h
(C)
SPECIFIC PORE VOLUME (ml/g)
XEROGEL AGED 24 OR 47 H
HYDROGEL AGED 24 OR 47 H
TEMPERATURE (K)

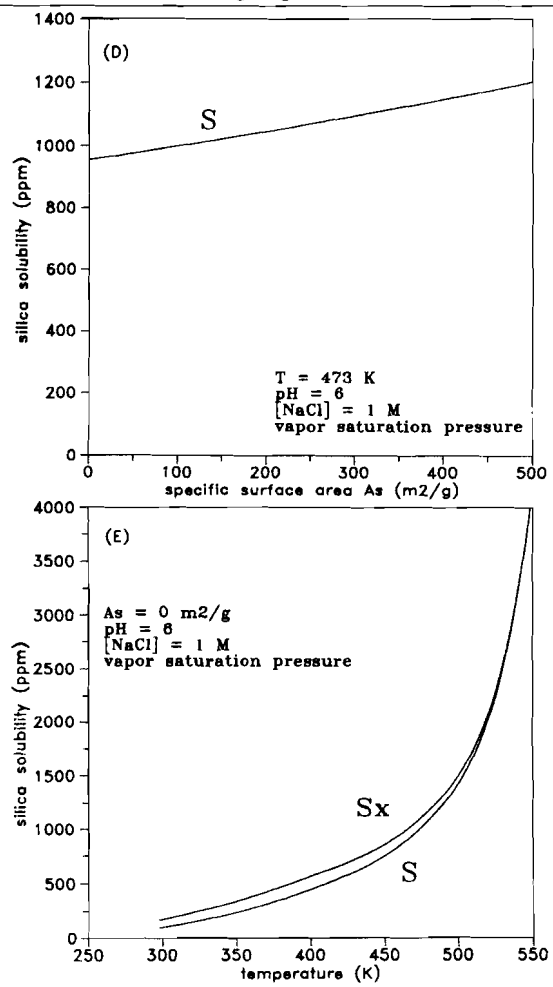

Figure 1

Ageing of hydrogel and xerogel spheres as a function of temperature at a duration of 24 h (a), and 47 h (b). The initial pore radius, surface area, and pore volume of the xerogel spheres is 2.3 nm, 455 m^2/g, and 0.76 ml. The spheres are treated in 1 M NaCl with a pH of 6 with a silica-to-water ratio of 0.15 g/g. (c) The progress of the pore volume. (d) Evolution of the equilibrium solubility of silica at 473 K as a function of the specific surface area of the silica sol particles, which is the engine of the Ostwald ripening. The values of the solubility in the plot are based on the relations of the introduction. Eqs. 12 and 13 are not considered here, but do not play an important role at a medium pH level of 6. (e) Evolution of the equilibrium solubility of silica under the experimental conditions as a function of the temperature. Both the solubility of silica, S, and the solubility of adsorbed MSA, S_x, are plotted as a function of the temperature. Again, Eqs. 12 and 13 are not considered in the calculation of the equilibrium solubility of the silica, because the extrapolations of Eqs. 12 and 13 to high temperature are unknown.

RESULTS

Effect of the ageing temperature

Figure 1a and 1b show the development of the specific surface area and the pore radius of the silica spheres at different ageing temperatures and at a fixed duration of 24 h and 47 h, respectively. The spheres are treated in 1 M NaCl, because in the absence of NaCl, the hydrogel spheres are destroyed, the spherical shape is lost, and a powder is obtained. The initial pore volume of the xerogel spheres is 0.76 ml/g, the pore radius 2.3 nm, and the specific surface area 455 m^2/g, measured by N_2 adsorption and desorption. A rapid decrease of the surface area of both xerogel and hydrogel samples is observed with increased temperature of thermal treatment, which is due to an increase of the primary particle size due to the treatment. The initial primary particle size before the treatment is 5 nm as determined with TEM. The particle size after treating for 24 h at 525 K according to Fig. 1a is estimated by the method in ref. [49] by application of $d = 6/(D * A_s)$ with D the particle density of $2.2 * 10^6$ g/m^3, and A_s the specific surface area in m^2/g. The resulting particle size $d = 52$ nm with the hydrogel (52 m^2/g), and $d = 130$ nm with the xerogel (21 m^2/g). The primary particle size is 72 nm of the xerogel after being treated for 47 h at 523 K according to Fig. 1b. Hence, the primary particle size is increased by a factor of $130/5 \approx 26$ after the thermal treatment. It appears that the decline in surface area is faster with the xerogel than with the hydrogel, whereas the pore radius of the xerogel grows more rapidly than that of the hydrogel (Fig. 1a). A difference in ageing between hydrogel and xerogel spheres is again apparent in Fig. 1c. A specific pore volume of the hydrogel spheres, rising from 0.76 to 1.9 ml/g with increased ageing temperature is displayed. The difference in pore volume after ageing for 24 and 47 h, and recorded as one set of data (Fig. 1c). The pore volume of the xerogel spheres in Fig. 1c is only slightly increased from 0.76 to 0.99 ml/g at 298 and 523 K, respectively.

Effect of the pH

Changes in surface area and pore volume with ageing as a function of pH are displayed in Fig. 2a. Especially the hydrogel spheres show a more profound development of the pore radius at higher pH levels, ranging from 7 to 46 nm at pH levels of 3.2 to 8.6, respectively. The surface area of the hydrogel rapidly drops from 190 to 40 m^2/g.

Xerogels show only a small development of the pore radius at higher pH levels, which is less pronounced than that of hydrogels (Fig. 2a). The pore radius of xerogels increases from 40 to 51 nm at pH levels of 3.2 to 8.6, respectively. The change in surface area of the xerogels is consequently very small, and the surface area remains more or less

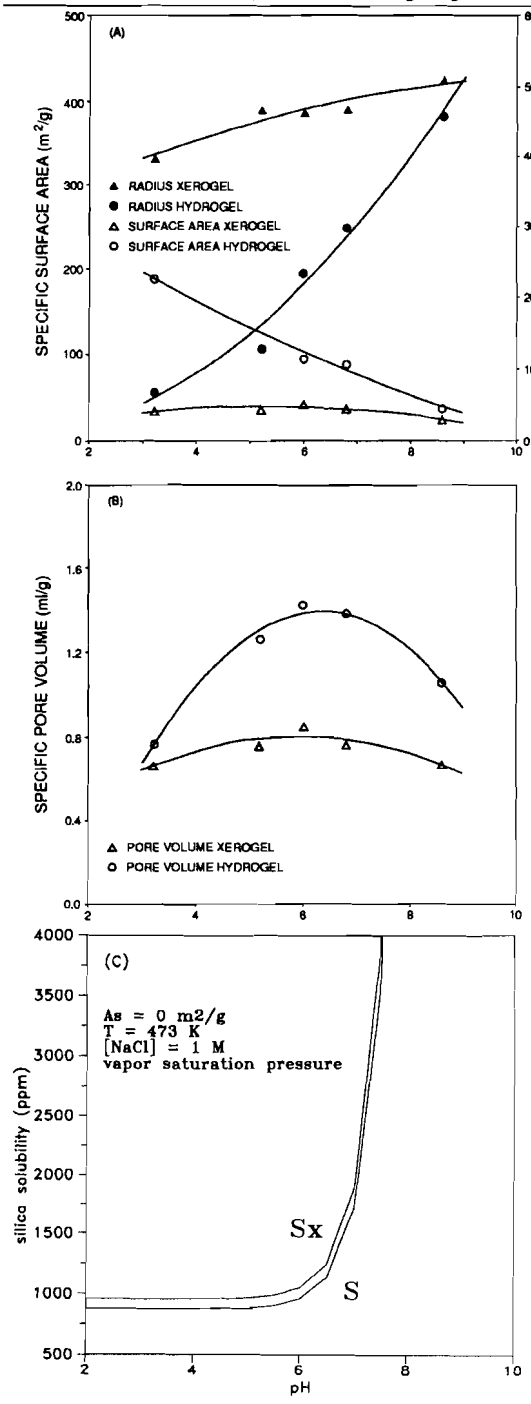

Figure 2

Effect of the pH on (a) the specific surface area and pore radius of aged hydrogel and xerogel spheres treated in 1 M NaCl with a silica-to-water ratio of 0.15 g/g, a duration of 24 h at a temperature of 473 K. The initial surface area is 455 m^2/g, and pore radius 2.3 nm.

(b) Progress of the pore volume. The initial pore volume is 0.76 ml/g.

(c) The solubility of silica (in ppm) as a function of the pH under the experimental conditions based on the equations of the introduction. Since the extrapolations of Eqs. 12 and 13 to high temperature are unknown, Eqs. 12 and 13 are not considered in the calculation of the equilibrium solubility of the silica.

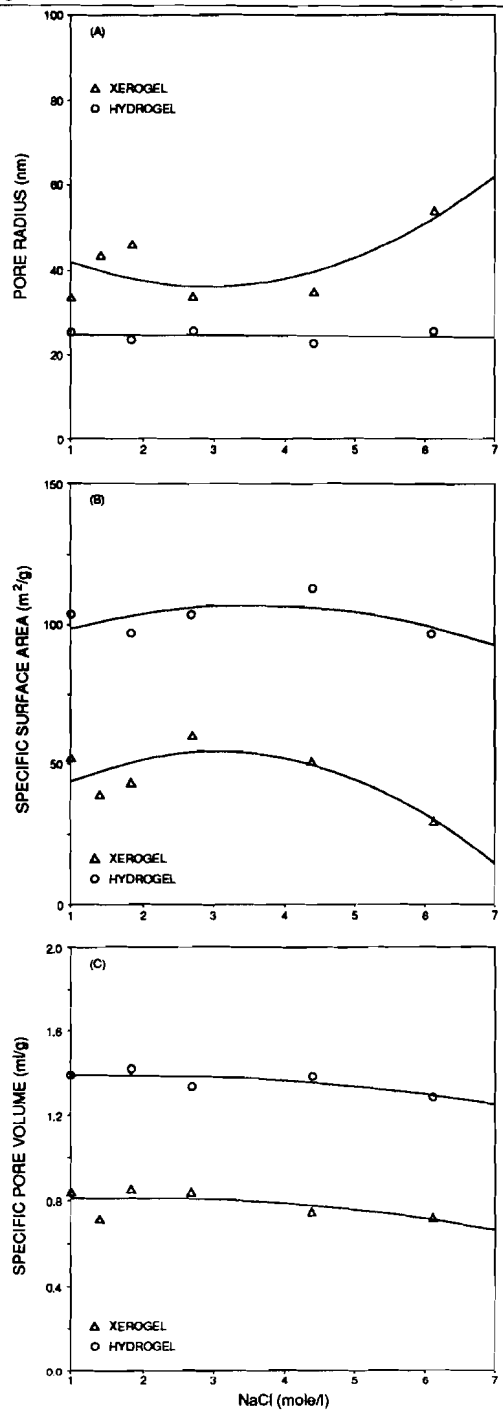

Figure 3

Effect of the concentration NaCl on
(a) the pore radius,
(b) the specific surface area, and
(c) the pore volume of aged hydrogel and xerogel spheres, treated at a constant duration of 24 h, temperature of 473 K, silica-to-water ratio of 0.15 g/g, and a pH of 6. The initial pore radius, surface area, and pore volume of the xerogel spheres is 2.3 nm, 455 m^2/g, and 0.76 ml/g.
(d) Development of the equilibrium solubility of silica under experimental conditions as a function of the concentration of NaCl calculated with the equations of the introduction. S and S_x denote the equilibrium solubility of amorphous silica and of the layer of adsorbed MSA present on the silica surface, respectively.

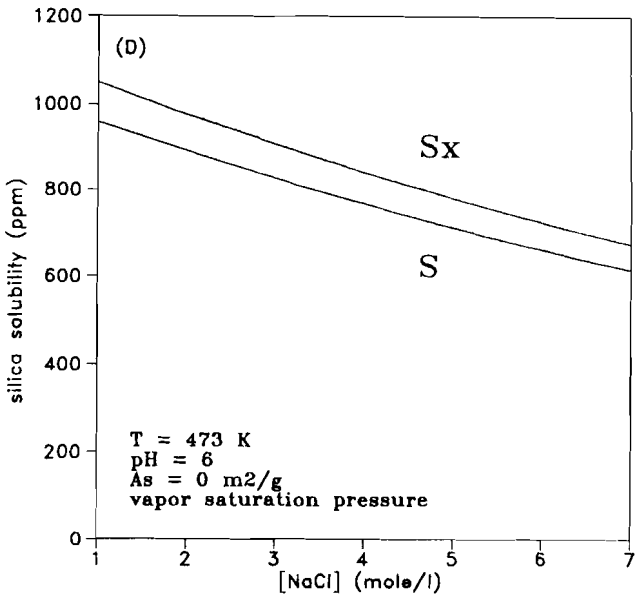

constant at a low level 38 m^2/g. At a pH of 8.6, the hydrogel and xerogel have almost identical pore radii and surface areas.

The dependence of the pore volume on the pH is illustrated in Fig. 2b. At pH levels from 3 to 6, initially fast increase of the pore volume is observed for both hydrogel and xerogel spheres. The increase continuous until the pore volume reaches a maximum at a pH of about 6, thereafter the pore volume declines. Ageing of hydrogels leads again to high pore volumes as compared to that of xerogels.

Effect of the concentration of NaCl

Ageing in fluids of 0 to 6 M NaCl merely affects the pore radius of hydro- and xerogel spheres as is apparent from Fig. 3a. Only the pore radius of the xerogel shows a slight minimum between a [NaCl] of 2 and 4 M. The specific surface area of the xerogel is relatively small at a high [NaCl] of 6 M as shown by Fig. 3b. The surface area of the hydrogels is hardly affected by the [NaCl]. In the whole range, the pore radius of the xerogel spheres is two times as large, and the surface is two times as small as that of the hydrogel spheres according to Fig. 3a and b. The specific pore volume of treated hydrogels and xerogels weakly declines with the [NaCl] in Fig. 3c. The specific pore volume of the hydrogel is again large with respect to that of the xerogel.

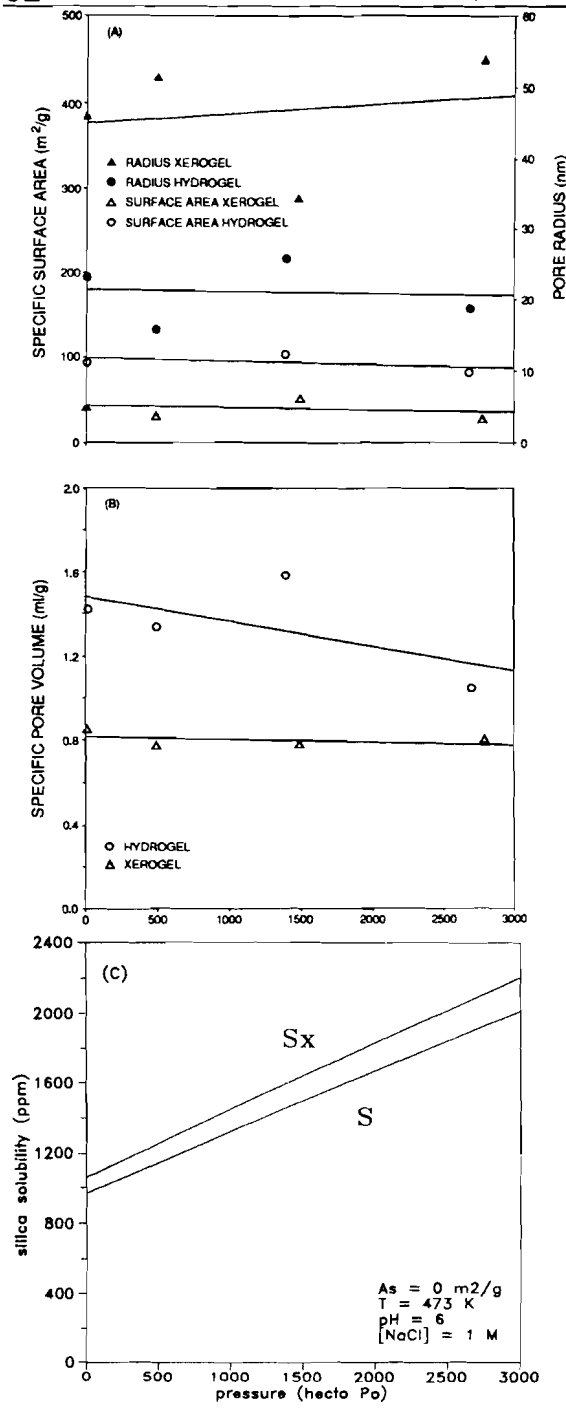

Figure 4

Effect of the pressure on the development of
(a) the pore radius and specific surface area, and
(b) the pore volume of hydrogel and xerogel spheres, treated in 1 M NaCl at a constant duration of 24 h, temperature of 473 K, silica-to-water ratio of 0.15 g/g, and pH of 6. The initial pore radius, surface area, and pore volume of the xerogel spheres is 2.3 nm, 455 m^2/g, and 0.76 ml/g.
(c) Development of the equilibrium solubility of silica under experimental conditions as a function of the pressure calculated with the equations of the introduction. S and S_x denote the equilibrium solubility of amorphous silica , and of the layer of adsorbed MSA present on the silica surface, respectively.

Effect of the pressure

The pore radius, surface area, and pore volume of silica gel spheres treated at 473 K is hardly affected by the pressure as can be seen in Fig. 4a and b. The pore size of xerogel spheres is twice as large as that of the hydrogel spheres, whereas the specific surface area is twice as small. The course of the pore volume shows the same pressure-independent pattern in Fig. 4b. The pore volume of aged hydrogels is again about twice as high as that of xerogel.

Effect of the silica-to-water ratio

A strange stepwise development of the pore radius and specific surface area with the silica-to-water ratio is exhibited in Fig. 5a to c. No experiments are performed with hydrogel spheres, because it is impossible to raise the silica weight ratio of 0.15 g/g without drying the hydrogel spheres before treatment. The pore radius of the xerogel spheres remains more or less constant until a ratio of 0.6 g/g (Fig. 5a), thereafter the pore radius steeply increases from 30 to 80 nm. A bimodal pore size distribution is seen with the xerogel sample of 0.6 g/g. Rapid ripening is evident when the excess of water is diminished. Because there is no change in the pore volume in Fig. 5b, the specific surface area of xerogel steeply drops from 55 to 30 m^2/g (Fig. 5c).

DISCUSSION

The kinetics of polymerization and depolymerization is at high temperatures is favored, because the $k_f(T)$ and $k_b(T)$, the forward and backward rate constant of polymerization increase exponentially with temperature, explaining the exponentially increase of pore radius, and the decrease of surface area in Fig. 1a and b, respectively. The high temperature, T, does not necessary increase the gradient of silica solubility between particles of different sizes, d, thus of different specific surface area, A_s (Fig. 1d), as explained by Eqs. 4 and 5, which contain a factor $1/T*d$ and A_s/T, respectively. The ripening of xerogel spheres proceeds more rapidly than that of hydrogel spheres, probably due to the surface structure of xerogel, which contains more tertiary silanol groups. The acidity of tertiary silanol groups is high with respect to that of secondary and primary silanol groups. The charge on the xerogel surface is negative, which favors the dissolution and deposition of silica. The increased pore volume of the hydrogel after ageing at high temperatures as shown in Fig. 1c and reported in ref. [50] is probably due to repelling forces between the primary particles, in agreement with SAXS measurements [51], where

less dense gel clusters are observed at high temperatures. No particular increase of the pore volume of xerogel proceeds in Fig. 1c, because with xerogel a dense structure has already formed with strong bonds between the sol particles, counteracting the repelling force with ageing.

The effect of the pH is twofold. First, the equilibrium silica solubility is increased (Fig. 2c), and an increased gradient between particles of different sizes is expected, and secondly, the silica gel surface has a more negative charge. The increase of the pore radius at high pH levels is more pronounced with hydrogel than with xerogel according to Fig. 2a. Obviously, the pH more strongly affects the surface charge and solubility, and thus the ripening of the hydrogel spheres. The surface of hydrogel spheres is covered with not fully condensed MSA of a high acidity constant. The surface of xerogels is already saturated with ionized groups. The pH therefore influences more strongly the surface charge of hydrogel spheres, which leads to differences in the ripening rate. An increased pore volume of hydrogels after an acid treatment is reported in work of Okkerse [6]. The explanation is sought in the fact that sol particles are rapidly fixed by dehydratation, which impedes the mutual approach, resulting in an open packing. We feel the packing density in the hydrogel to be mainly a function of the surface charge. The maximum in pore volume as a function of the pH in Fig. 2b can be explained as follows. First, the gel structure is less dense at higher pH levels by repelling electrostatic forces and a more rapid deposition of silica, thus strengthening the gel structure. Above a pH of 6 the solubility of silica is high and a large amount of primary particles dissolve. Consequently the gel network weakens, is more seriously affected by shrinkage, and the pore volume decreases. At high pH levels a large part of the silica remains in solution as soluble silica.

Fig. 3a to c show a small effect of NaCl on the development of the pore structure. The reduction of the solubility (Fig. 3d), thus a decreased gradient of the solubility between the particles of different sizes, is counteracted by the increase of surface ionization and, hence, the polymerization rate (see introduction). Net identical ripening rates are found. Only at high [NaCl], the radius of the xerogel increases, and the surface area and specific pore volume decrease.

Some decrease of the silica solubility by the increased pressure is expected (Fig. 4c), but minor changes of the pore structure are observed in Fig. 4a and b. The pressure is, therefore, less important than the treating temperature and the pH of the hydrothermal fluid.

An explanation for the sudden steep increase of the pore radius (Fig. 4a) and the decrease of the surface area (Fig. 5c) above a silica-to-water ratio of 0.6 g/g, cannot be readily developed. The spheres are homogeneously treated in a rocking system, with rotating steel vessels. Some reasons for the steep increases might be i) a more rapid transport by volatile MSA species ; ii) transport of silica along the silica surface, or iii) a more rapid rise of the pH in a smaller volume of the fluid.

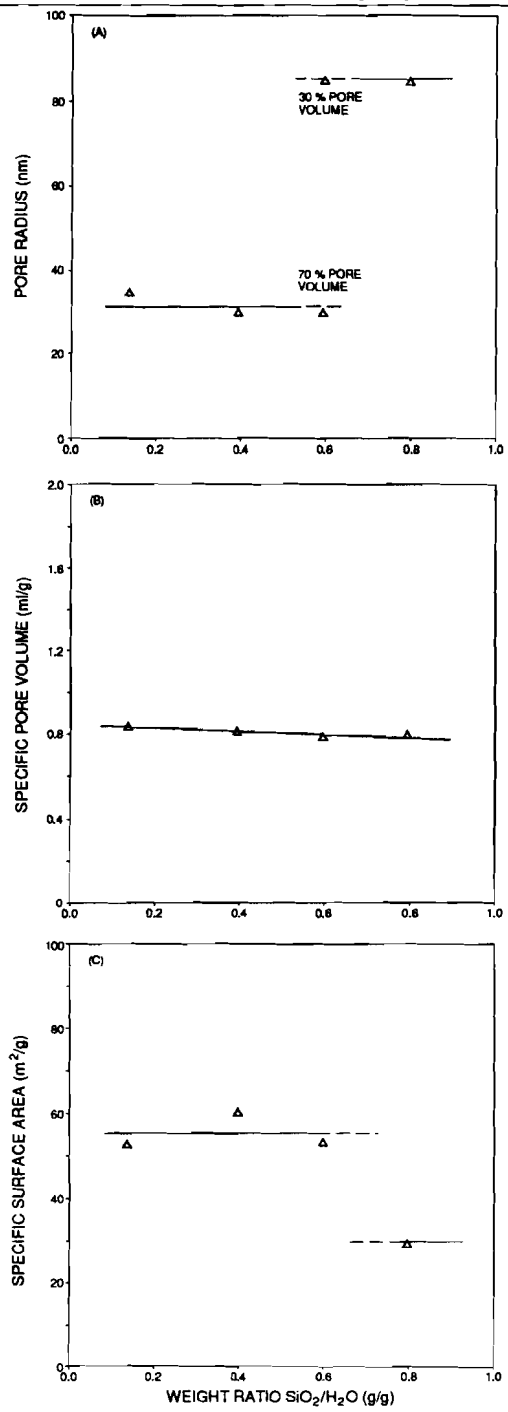

Figure 5

Effect of the silica-to-water ratio on
(a) the pore radius,
(b) the pore volume, and
(c) the specific surface area of aged xerogel spheres, at a constant duration of 24 h, temperature of 473 K, concentration NaCl of 1 M, and a pH of 6. The initial pore radius, surface area, and pore volume of the xerogel spheres is 2.3 nm, 455 m^2/g, and 0.76 ml/g.

CONCLUSIONS

1) With ageing temperatures from 298 to 523 K at a constant duration of 24 h the pore structure of xerogels is considerably affected, which results in pore radii ranging from 2.7 to 136 nm, surface areas decreasing from 455 to 21 m^2/g, whereas the pore volume remains constant at about 0.8 ml/g. Hydrothermal treatment of hydrogel spheres results in pore radii between 2.7 and 70 nm, surface areas decreasing from 455 to 53 m^2/g, and pore volumes between 0.8 and 1.9 ml/g.

2) Under all conditions the ripening of the xerogel silica bodies is faster than that of the hydrogel bodies, which is probably due to the more dense structure and the acidity of the xerogel silica surface, which contains ionized groups. However, the hydrogel spheres attain a high pore volume by repelling forces between the primary sol particles, whereas the pore volume of the xerogel, which has already been subjected to a certain extent of shrinkage remains constant. The silica is mainly reorganized within the pores.

3) The temperature, pH, and silica-to-water ratio are important parameters with the ageing of silica. The [NaCl] and pressure hardly affect the development of the pore structure. The increased polymerization and ageing rate with increased [NaCl] is counteracted by the decreased solubility of silica.

4) Ripening of the primary particles in the gel structure is fast at high temperatures and pH levels, because the silica solubility and the related transport of silica is increased at high temperatures and pH levels. The pH level influences more strongly the ageing of hydrogel spheres, because the acidity of the hydrogel surface covered with more primary and secondary silanol groups is low, and more affected by the pH.

5) Stepwise variation of the pH of xerogel spheres from 3.2 to 8.6 at 473 K leads to pore radii from 40 to 50 nm, surface areas from 37 to 27 m^2/g, at a constant pore volume of 0.8 ml/g. For hydrogel spheres the changes with the variation of the pH level with ageing are more profound, pore radii varying from 7 to 46 nm, surface areas from 190 to 40 m^2/g, and a maximum pore volume of 1.5 ml/g at a pH of 6.

6) The effect of hydrothermal ageing with different silica-to-water ratios on xerogel spheres at 473 K can be divided into two regions. Below a silica-to-water ratio of 0.6 g/g, the pore radius is constant at 30 nm, and the surface area at 53 m^2/g. Above this ratio the pore size steeply increases to 78 nm, and consequently the surface area decreases to 30 m^2/g. The pore volume, however, remains at 0.8 ml/g.

REFERENCES

1. R.O. Fournier and J.J. Rowe, *American Mineralogist*, **62** (1977) 1052
2. B.A. Fleming and D.A. Crerar, *Geothermics*, **11** (1982) 15
3. J.A. van Lier, P.L. de Bruyn and J.Th.G. Overbeek, *J. Phys. Chem.*, **64** (1960) 1675
4. G.B. Alexander, *J. Phys. Chem.*, **61** (1957) 1563
5. R.H. Busey and R.E. Mesmer, *Inorganic Chemistry*, **16** (1977) 2444
6. I.L. Svensson, S. Sjöberg, and L.O. Öhmann, *J. Chem. Soc., Faraday Trans.*, (1) **82** (1986) 3635
7. W.L. Marshall, *Geochimica et Cosmochimica Acta*, **44** (1980) 907
8. J.R. Fischer, *J. Research U.S. Geol. Surv.*, II **4** (1976) 189
9. R.O. Fournier, *Geochimica et Cosmochimica Acta*, **47** (1983) 579
10. H.P. Rothbaum and A.G. Rohde, *J. Coll. Interf. Sci.*, **71** (1979) 533
11. E.G. Bohlmann, R.E. Mesmer and P. Berlinsky, *Soc. Pet. Eng. J.*, **20** (1980)239,533
12. L. Righetto, A. Polissi, D. Comi, B. Marcandalli, I.R. Bellobono and G. Bidoglio, *Annali di Chimica*, 77 (1987) 437
13. G.B. Alexander, *J. Am. Chem. Soc.*, **76** (1954) 2094
14. M.F. Bechtold, *J. Phys. Chem.*, **59** (1955) 532
15. G.S. Wirth and J.M. Gieskes, *J. Coll. Interf. Sci.*, **68** (1979) 492
16. Physical and Chemical Aspects of Adsorbents and Catalysts, Ed. B.G. Linsen (1970), Academic Press, London, 213-264
17. S.A. Greenberg and D. Sinclair, *J. Phys. Chem.*, **59** (1955) 435
18. V.V. Strelko, *Coll. J. USSR*, **32** (1970) 430
19. A.D. Bischop Jr and J.J.Bear, *Thermochimica Acta*, **3** (1972) 399
20. K.R. Applin, *Geochimica et Cosmochimica Acta*, **51** (1987) 2147
21. H. Baumann, *Kolloid Zeitschrift*, **162** (1959) 28
22. A.C. Makrides, M. Turner and J. Slaughter, *J. Coll. Interf. Sci.*, **73** (1980) 345
23. C.B. Hurd, *Chem. Rev.*, **22** (1938) 403
24. K. Goto, *J. Phys. Chem.*, **60** (1956) 1007
25. S.P. Maulik, B.N. Gosh and S. Bandyopahyay, *J. Ind. Chem. Soc.*, **40** (8) (1963) 607
26. B.A. Fleming, *J. Coll. Interf. Sci.*, **110** (1986) 40
27. G. Bird, J. Boon and T. Stone, *Chemical Geology*, **54** (1986) 69
28. S. Kondo, M. Igarashi and K. Nakai, Colloids and Surfaces, **63** (1992) 33
29. L.T. Zhuravlev, *Langmuir*, **3** (1987) 316
30. W.A. Deer, R.A. Howie and J. Zussman, An Introduction to the Rock-forming Minerals, Longman Group Limited, England (1966), 340-344
31. W.M. Heston, Jr., R.K. Iler and G.W. Sears, Jr., *J. Phys. Chem.*, **64** (1960) 147
32. J. Erkelens, B.G. Linsen, *J. Coll. Interf. Sci.*, **29** (1969) 464
33. C.G. Armistead, A.J. Tyler. et.al , *J. Phys. Chem.*, **73** (1969) 3947
34. C.H. Lochmüller, M.T. Kersey, *Langmuir*, **4** (1988) 572

35. R.Sh. Mikhail, A.M. Khalil, and S. Nashed, *Thermochimica Acta*, **24** (1978) 383
36. P. Schindler and H.R. Kamber, *Helvetica Chimica Acta*, **51** (1968) 1781
37. J.D. Rimstidt and H.L. Barnes, *Geochimica et Cosmochimica Acta*, **44** (1980) 1683
38. P.F. Holt and D.T. King, *J. Chem. Soc.*, **24** (1955) 773
39. O. Weres, A. Yee and L. Tsao, *J. Coll. Interf. Sci.*, **84** (1981) 379
40. L.H. Allen and E. Matyevic, *J. Coll. Interf. Sci.*, **33** (1970) 420
41. L.H. Allen, E. Matyevic, L. Meites, *J. Inorg. Nucl. Chem.*, **33** (1971) 1293
42. D.E. Yates, S. Levine, T.W. Healy, *J. Chem. Soc. Faraday Trans.*, **70** (1974) 1807
43. J.A. Davis, R.O. James and J.O.Leckie, *J. Coll. Interf. Sci.*, **63** (1978) 480
44. S.K. Milonjic, *Colloids and Surfaces*, **23** (1987) 301
45. L.H. Allen and E. Matijevic, *J. Coll. Interf. Sci.*, **31** (1969) 287
46. S.K. Milonjic, M.M. Kopecni and Z.E. Ilic, *Bulletin de la Société Chimique Beograd*, **48** (1983) 351
47. M.L. Hair and W. Hertl, *J. Phys. Chem.*, **74** (1970) 91
48. A.D. Edgar, Experimental Petrology, Oxford University Press, London (1973), 94-118
49. R. Snel, *Applied Catalysis*, **12** (1984) 189
50. V.I. Malkiman, V.L. Struzhko, V.M. Shamrikov, V.M. Chertov, and E.I. Kosenko, *Coll. J. USSR*, **51** (1989) 691, Engl. Transl. (1990) 596
51. P. Tang, D.E. Colflesh and B. Chu, *J. Coll. Interf. Sci.*, **126** (1988) 304

Chapter 4

The rise in pH during ageing of porous sol-gel silica spheres

M.K. Titulaer, W.K. Kegel[1], J.B.H. Jansen, and J.W. Geus[1]

Department of Geochemistry, Institute for Earth Sciences. University of Utrecht, Budapestlaan 4, P.O. Box 80.021, 3508 TA Utrecht, The Netherlands.
[1]Department of Inorganic Chemistry, University of Utrecht, Sorbonnelaan 16, P.O. Box 80.083, 3508 TB Utrecht, The Netherlands.

ABSTRACT

The increase in pH observed after hydrothermal ageing of porous silica gel spheres of 1-3 mm in size in 1 M NaCl is studied. The rise in pH influences the solubility of silica in the hydrothermal fluid. A model explaining the increase in the pH comprises condensation of silanol groups and the release of ionized monosilicic acid in the fluid. The amount of surface silanol groups is investigated by DRIFTS and surface titration. The decrease of the number of surface silanol groups with ageing of the porous spheres is established with DRIFTS. The presence of a layer of adsorbed sodium on the silica surface is demonstrated by surface titration.

INTRODUCTION

Silica-rich sol-gel spheres are used to manufacture catalysts and catalyst supports. The silica gel spheres dealt with in this chapter are porous bodies of a diameter 1 to 3 mm, containing a three-dimensional network of submicron primary sol particles. The preparing conditions of the spheres have been described in Chapter 2 and ref. [1]. The silica gel spheres were prepared by a sol-gel procedure, which can also be used in the preparation of ceramic separation membranes [2]. Variations in the conditions during preparation and in the hydrothermal treatment of the spheres enable one to control the pore structure so as to establish the desired pore structure of the catalyst support or the separation membrane.

The use of hydrothermally treated silica spheres have several advantages over the commonly use of dry powders. For example, powders have to be processed to shaped bodies by pressing to pellets or extrusion with a suitable binder. With a silica sol, furthermore, the catalyst precursor, for example, a transition metal oxide or a clay mineral, can be mixed with the silica before gelling. An excellent dispersion of the precursor within the gel is thus obtained. The pore dimensions of the gel can be controlled subsequently by hydrothermally ageing.

The cause of the rise of the pH level and the silica solubility in the hydrothermal fluid is the topic of the present work. To explain the observed changes in the pH the surface structure of the silica spheres is investigated by diffuse reflected infrared Fourier transformed spectroscopy (DRIFTS) and surface titration.

MATERIALS AND PROCEDURES

Preparation and hydrothermally treatment of silica gel

The sol-gel method of producing porous silica comprises the following steps. A supersaturated silica sol solution can be prepared from a Na silicate solution according to three procedures, viz., (i) adding a sodium silicate solution to a concentrated aqueous acid solution [1], (ii) exchange of Na^+ for protons by an appropriate exchange resin column [3], and (iii) removal of the Na^+ by electro-dialysis [4]. The primary silica sol particles in solution coagulate in a reticular gel network. Particle growth and ripening under hydrothermal conditions above 298 K results in a gel of an increased pore size [5]. The temperature, the duration and the initial pH level are important control variables of the hydrothermal treatment [6]. An increase of the pH affect the solubility of silica and the ionization of surface silanol groups, and thus the ripening process of silica under hydrothermal conditions [6].

Spherical silica sol gel bodies are prepared according to the first of the above procedures [1]. The hydrogel spheres are dried at 393 K, resulting in xerogel spheres. An amount of 3.15 g of the xerogel spheres is hydrothermally aged in 20.85 ml of a 0, 1, 2, 4, and 6 M NaCl solution. The periods of time of ageing are varied from 2 to 47 h, and the temperature from 298 to 523 K. Some batches of the hydrogel spheres were not dried before hydrothermal ageing. The thus obtained batches are designated as hydrothermally aged hydrogels. After hydrothermal treatment, the spheres are separated from the hydrothermal fluid by filtration, and dried at 393 K. The pH of the filtered fluid is measured.

The solubility of silica in the hydrothermal fluid

The silica solubility in the hydrothermal fluid after ageing of silica spheres in 1,2,4 and 6 M NaCl is measured. Since the filtered solid does not contain solids, the silica solubility can be assessed by measuring the silica concentration in the solution. Two different solubilities can be distinguished, viz., (i) the MSA (monosilicic acid) solubility, and (ii) the 'true' solubility, comprising both MSA and colloidal forms of silica. The MSA solubility is usually determined by using the reaction of the silicate ion with an acidified ammonium heptamolybdate solution, followed by colorimetric determination of the resulting yellow silicomolybdate complex [7,8]. The α- and β-silicomolybdate complexes are stable at the pH range of 3.8 to 4.8 and 1.0 to 1.8, respectively. A minor depolymerization of silica proceeds at the low pH range [9]. The α-complex is the most stable, but asks for a relatively long period of time, viz., 12 to 30 minutes, to form, whereas the β-complex, which has a large absorption coefficient in the UV spectrum, is easily produced in 2 to 7 minutes. The β-silicomolybdate procedure is followed in this work.

Reagents (A) is prepared having an acidity of 1.5 M. Reagents (B) of pH = 7 contains 0.56 M MoO_4^{2-}, 1.16 M NH_4^+, and $6.7*10^{-3}$ M NH_3. The unstable reagents (C) is prepared by adding of 200 ml of reagents (A) and 100 ml of reagents (B) to 500 ml distilled water [10]. An aliquot of 50 ml of solution (C) is added to 1 ml of the filtered hydrothermal fluid (D). After two minutes, the absorption of the yellow silicomolybdate complex at 410 nm is measured in a 1 cm quartz-glass cuvette on a Perkin Elmer Lambda 1 UV/VIS spectrophotometer.

The 'true' silica the solubility in solution is established by inductively coupled plasma atomic emission spectrophotometry (ICP-AES) on a 30 channel simultaneous instrument type 34000 (Applied Research Laboratories, Valencia, USA). The colloidal forms of silica in solution are estimated by subtracting the β-silicomolybdate solubility from the 'true' solubility. The hydrothermal fluids of the various samples are diluted ten times to reduce the expected interference of Na on the silicon determination by ICP-AES.

DRIFTS of powdered silica spheres

Hydrothermally aged xerogel and hydrogel spheres, representing a series of descending surface areas, are measured with DRIFTS. After powdering the hydrogel spheres are dried for the first, and the xerogel spheres for a second time for a period of 17 h at 393 K, shortly before the DRIFT spectra are recorded. One xerogel sample is stored for a longer period at room temperature, before the DRIFT spectrum is recorded. The infrared spectra are recorded in the range 4000-2500 cm^{-1} on a Perkin Elmer FT-1720 device, with a Spectra-Tech Diffuse Reflectance Accessory 'Collector'. The specific absorption bands of the surface silanols are [10-12] :

1.	3748 cm^{-1}	sharp band of isolated silanol groups at the surface
2.	3670 cm^{-1}	inner silanol groups (perturbed OH in the bulk SiO_2)
3.	3600 cm^{-1}	broad band of interparticle hydrogen bonded silanol groups (and vicinal paired silanols)
4.	3000-3500 cm^{-1}	band of absorbed water

The band of vicinal paired hydroxyls is in some cases not clearly separated from the band of absorbed water.

Percolation of OH- in the porous spheres

The adsorption of OH^- on the silica surface is measured as a function of time. After equilibrium, the adsorption of hydroxyls on the silica surface is complete. The period of time to reach equilibrium is determined for different samples. A few drops of 2 wt% NH_3 are added to 50 ml distilled water, until a pH of 9 is obtained. The solution is kept under a constant N_2 flow and is separated from the atmosphere by a 30 cm long tube of a diameter of 1 cm. In each experiment 1 g of the spheres is added via the tube to the solution. The spheres have pore volumes of 1 ml/g and pore radii ranging from 2.5 to 9 nm. The rate of adsorption of hydroxyl ions on the silica surface is compared with that of 1 g pore-free fumed silica (Aerosil 380, Degussa BRD). The specific surface area of the fumed silica sample is 300 m^2/g.

The decrease in pH is recorded as a function of time with an antimony (Sb) electrode and silver-silver chloride (Ag/AgCl/KCl) reference electrode [13,14]. The period of time is determined where the pH has exactly covered 50% of the range between the initial pH_o and the equilibrium pH_∞. The accuracy is within 1 mV or 0.02 pH unit.

Spheres added to solutions of different pH

After the equilibrium period of time of the different samples has been determined, which is less than 20 h, the maximal adsorption of hydroxyl ions is measured after 20 h as a function of the pH. An amount of 1 g of xerogel spheres, having a pore radius 8 nm and a surface area of 156 m^2/g, is added to 50 ml of either (i) distilled water, or (ii) 1 M NaCl , or (iii) 3 M NaCl. Different pH values, ranging from 1 to 12, are established by adding a few drops of diluted 27 wt% ammonia or of 37 wt% HCl. The exchanged [Na] after addition of the spheres is measured by AES.

RESULTS

Rise in pH with hydrothermally ageing

Fig. 1 shows the pH of the hydrothermal fluid as a function of the internal surface area of the xerogel spheres after hydrothermal treatment. The initial starting pH of the 1 M NaCl solution, in which the spheres have been suspended, is 6. The specific surface area of the untreated spheres is 455 m^2/g. The final pH of the hydrothermal fluid rises as the surface area of the spheres has decreased by the treatment. This process continues until the surface area has decreased to about 50 m^2/g, and the pH of the fluid has reached a level between 10 and 11.

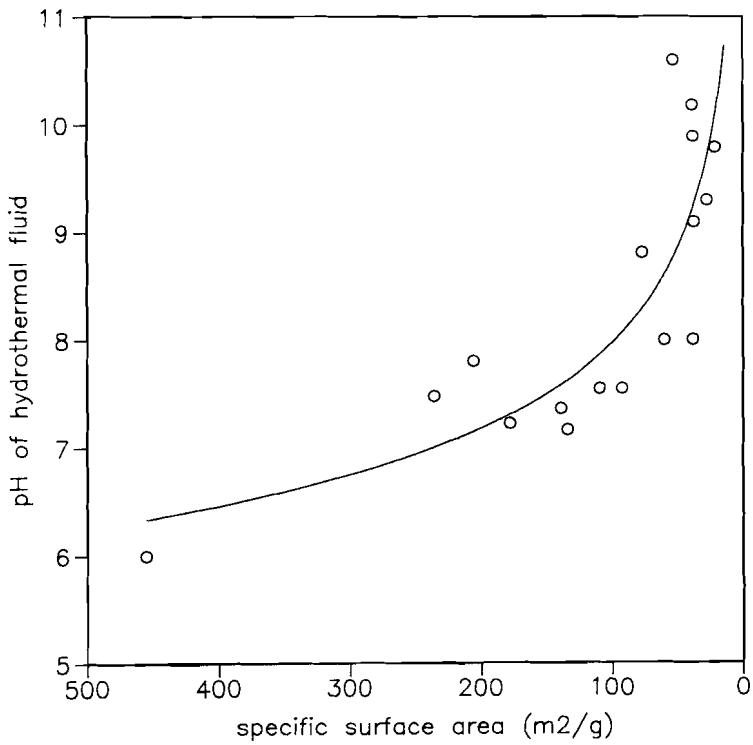

Figure 1 Increase of the pH after hydrothermal ageing of the xerogel spheres. The solid line represent the best fit.

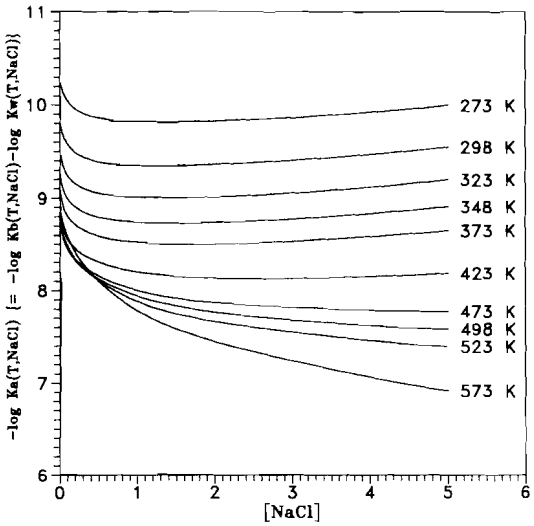

Figure 2

The first ionization constant of MSA as a function of the temperature and the [NaCl] as reported by Busey and Mesmer [15].

Increased silica solubility at high pH levels

The increased silica solubility at high final pH levels of the hydrothermal fluid is represented in Fig. 3. The pattern of Fig. 3 is common for amorphous silica [16,17]. Both the 'true' and MSA solubility rapidly increase when the pH reaches the first ionization constant of MSA, which is 9.35 in 1 M NaCl at 298 K reported by Busey and Mesmer [15] and displayed in Fig. 2. The reported first ionization constant is significantly higher than the value of 8.47 calculated with the Eqs. 8, 10, 12, and 13 of the previous Chapter 3 and the relation : -log K_A(T,NaCl) = -log K_B(T,NaCl) -log K_w(T,NaCl)

The solubility of silica as measured from the yellow silicomolybdate complex is slightly below the 'true' solubility of silica, because a small quantity of silica is present as polymers. The amount of silica present as polymers is about 36 and 120 ppm at a pH of 7 and 10, respectively (ppm = mg SiO_2/l) (Fig. 3). The solubility calculated from the silicomolybdate concentration suggests a faint minimum between a pH of 7 and 8, which agrees with the data from the literature [16,17].

Solubility of silica after ageing in 1,2,4 and 6 M NaCl

The solubility of silica after ageing as a function of the concentration of NaCl is shown in Fig. 4. The pH of the fluid is 6 to 7. The solubility decreases at rising sodium chloride

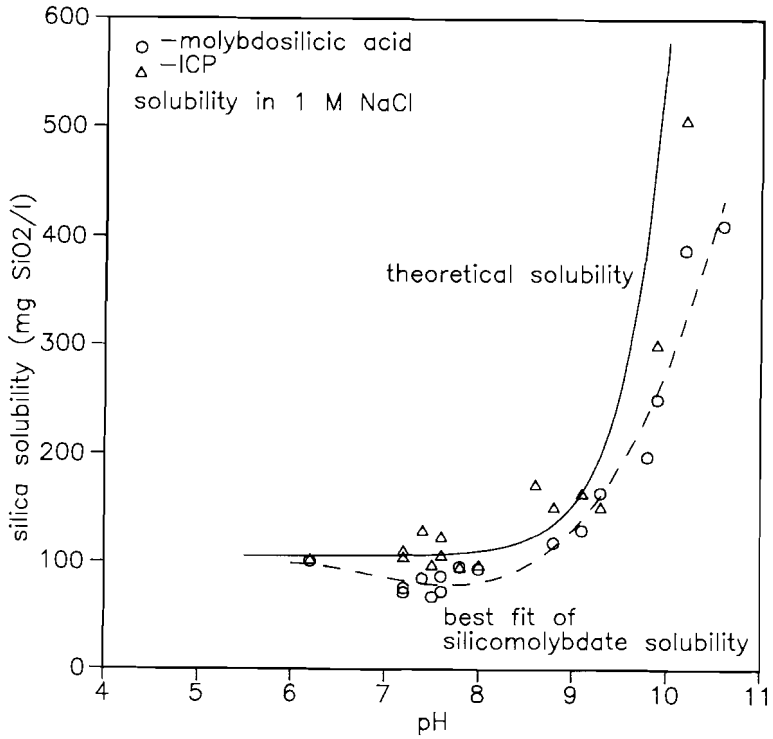

Figure 3 The solubility of silica in the hydrothermal fluid as a function of the pH measured after hydrothermal treatment. The dashed line is the best fit. The solid line is the pure theoretical solubility based on the relation :
$S(298\ K, 1M\ NaCl, pH) = 106*(1+10^{pH-9.35})$.

concentrations. The experimental 'true' solubility as assessed by ICP-AES is slightly above that measured by the silicomolybdate procedure. Both solubilities are situated at levels below the curve representing the literature data of Marshall [18,19].

The amount of surface silanol groups as measured by DRIFTS

The infrared spectra of hydrothermally aged xerogel and hydrogel spheres are represented in Fig. 5a and b, respectively. The absorption of isolated surface silanols at 3738 cm^{-1} decreases lineary with the drop of the surface area measured after ageing. The band due to adsorbed water at 3500-3000 cm^{-1} exhibits a lower intensity, and the band

due to internal silanol groups at 3670-3663 cm^{-1} a higher intensity at lower surface areas. The position of the bands is different from the positions reported by Kondo and coworkers [12]. The peak due to free silanol groups at 3738 cm^{-1} is at a lower frequency than the value of 3748 cm^{-1} reported in the literature [12] as well as the band due to inner silanol groups, which peaks at 3663 cm^{-1}, while the literature mentions a peak at 3670 cm^{-1}, and the band of due to vicinally hydrogen bonded silanol groups, the peak of which is at 3588 cm^{-1} below the value of 3600 cm^{-1} mentioned in the literature. The effect of drying just before recording a DRIFT spectrum is illustrated in Fig. 5c. Drying just before recording the spectrum increases the absorption of isolated silanols at 3738 cm^{-1}, and diminishes the adsorption of water at 3500-3000 cm^{-1}.

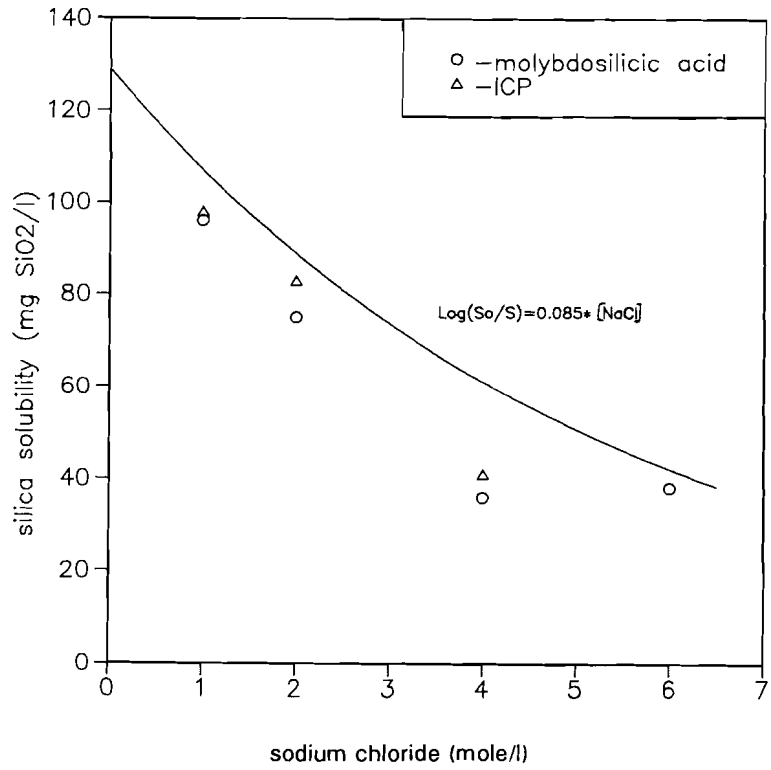

Figure 4 The silica solubility as a function of the concentration of NaCl in the hydrothermal fluid at 293 K. The solid line represents the literature data of Marshall : $\log(S/S_o) = 0.085*[NaCl]$, with S_o the salt-free solubility of 115 to 130 ppm.

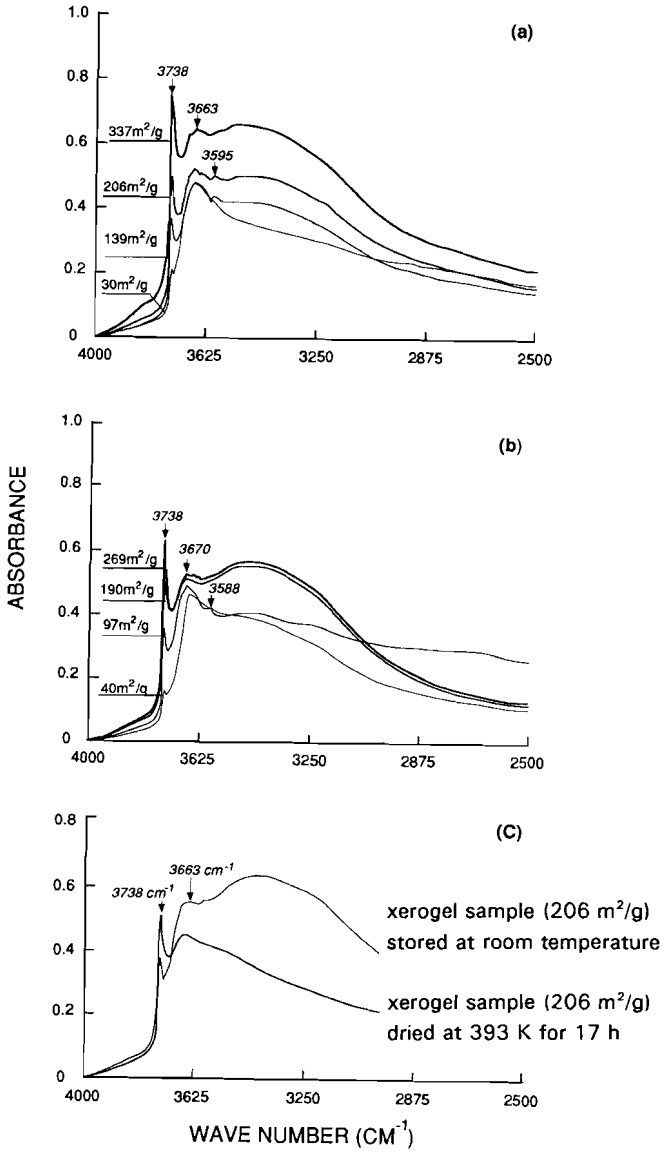

Figure 5 DRIFT spectra of hydrothermally aged xerogel and hydrogel spheres : (a) aged xerogel spheres, dried and calcined at 393 K of a surface area decreasing from 337 to 30 m^2/g; (b) aged hydrogel spheres, dried at 393 K of a surface area decreasing from 269 to 40 m^2/g; (c) influence of the calcining temperature of aged xerogel spheres before measuring the infrared spectra.

Rate of OH- adsorption as a function of the pore radius

Addition of an amount of 1 g fumed silica to 50 ml solution of a pH of 10.5 results in an instantaneous decrease of the pH (Fig. 6a), whereas addition of 1 g of silica sol-gel spheres results in a gradual decline of the pH (Fig. 6b). The maximal adsorption of OH^- at a pH of 9 and the period of time to reach 50% of the decrease in pH are recorded as a function of the pore size of the xerogel spheres and mentioned in Tab. 1. It appears from Tab. 1 that the period of time to reach 50% of the pH drop increases with smaller pore radii, and that the maximum adsorption capacity drops with decreasing pore radii. The small adsorption capacity of small pore radii is probably caused by the repulsive pore potential in smaller pores [20]. The charge density cannot achieve its maximum value, because there is an overlap of the negative surface potentials. The rate of OH- absorption can be fitted with the empirical relation :

$$\text{Ln}\,[(pH-pH_\infty)/(pH_o-pH_\infty)] = -5*10^{-6} * R_p^{2.43} * (t-t_o) \qquad (1)$$

where the pH changes with time t (in s), pH_∞ is the pH after equilibration, pH_o the initial pH of 9 at t_o, which is the starting time (in s), $-5*10^{-6}$ a constant (in $nm^{-2.43}*s^{-1}$), and R_p the pore radius (in nm).

Table 1 The halftime t ½ (s) of the percolation process of OH^-, where $pH = (pH_o + pH_\infty)/2$. An amount of 1 g of the spheres is added to 50 ml of a solution of a pH of 9. The maximal adsorption is measured as a function of the pore radius R_p.

	R_p	t ½ (s)	Log(OH^-_{ads}*m^2/mole)
Aerosil 380	0	0	-7.38
silica spheres	9.0	465	-8.39
	8.7	828	-8.69
	8.0	1080	-8.93
	7.0	1266	-9.01
	2.5	14520	-8.99

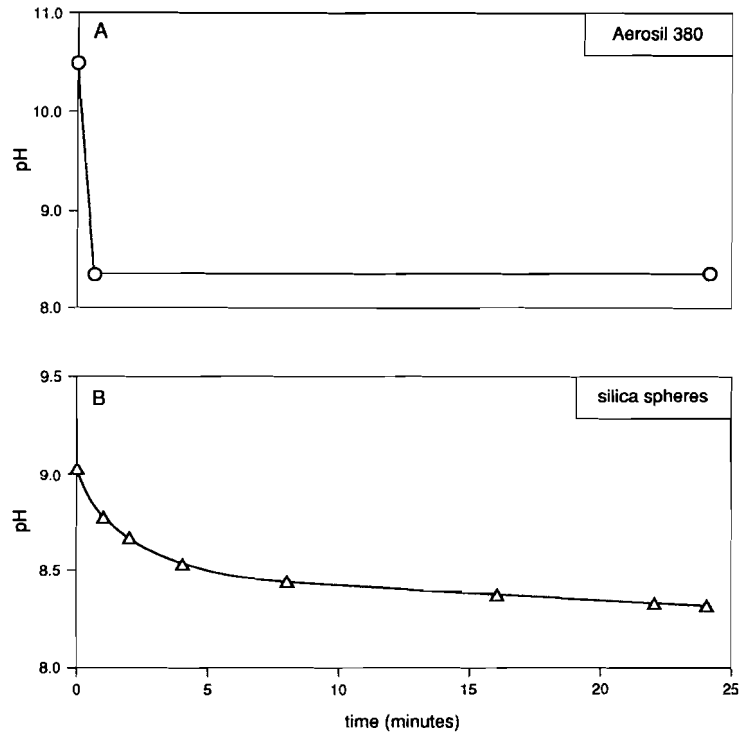

Figure 6 Course of the pH during adsorption of hydroxyls by (a) non-porous Degussa Aerosil 380, and (b) porous silica sol gel spheres.

Adsorption of OH- or H^+ as a function of the pH

In distilled water, above a pH of 7.7, adsorption of OH^- and below this pH, adsorption of H^+ is obvious (Fig. 7). Below the pH of 5 in distilled water, the amount of desorbed Na^+ is measured by AES (diamonds). The amount of desorbed Na^+ is equal to the amount of adsorbed H^+. The slope of 0.85 of the solid line below the pH of 5, indicates that Na^+ and H^+ are exchanged. In 1 and 3 M NaCl OH^- is adsorbed above a pH of 6.2 and below this pH, H^+ is adsorbed (triangles). The results of the experiments in 1 and 3 M NaCl are not significantly different.

Acid treatment of the spheres

The silica sol-gel spheres are treated with 50 wt% sulphuric acid, washed with distilled water until neutral pH, and dried. The acid-treated spheres are added to the solutions of a different pH. Above a pH of 3 only OH^- is adsorbed (Fig. 7). The slope of the dashed line is exactly unity intersecting the x-axis at a pH of 3. Sodium-free fumed silica (Aerosil 380,Degussa, BRD) is also added to the solutions of different pH. The experiment is not represented in Fig. 7. Above a pH of 3 only OH^- is adsorbed. The pattern resembles the experiment of the acid-treated spheres in Fig. 7.

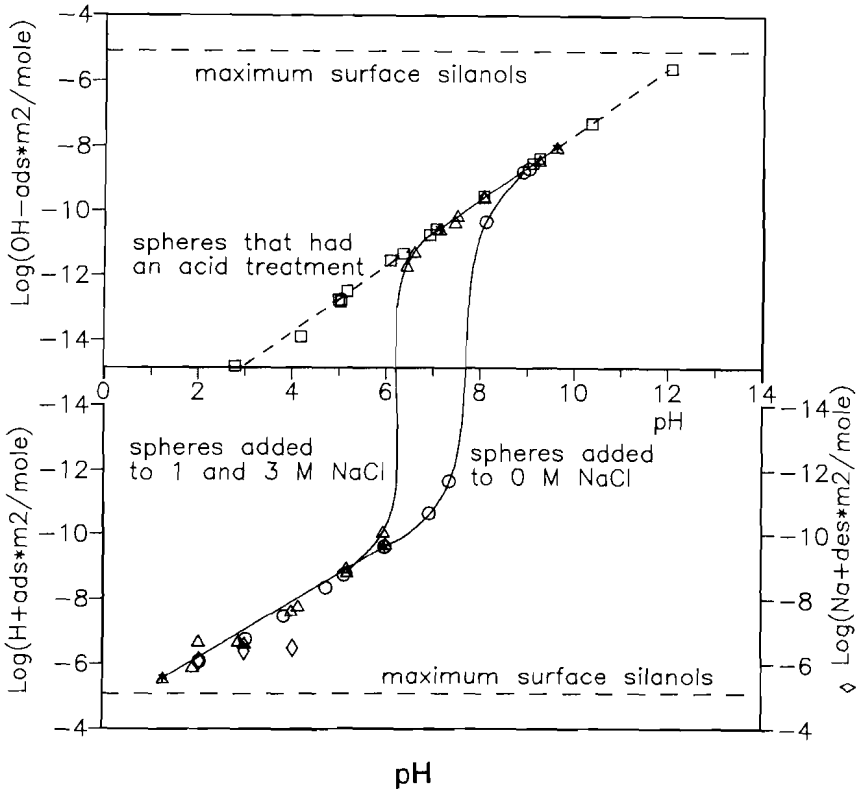

Figure 7 Exchange of Na^+ at the surface of an aged silica xerogel sample of a specific surface area of 156 m^2/g as a function of the pH. Addition of spheres to 50 ml distilled water (circles) and 1 and 3 M NaCl (triangles). The exchanged Na^+ in solution is measured with AES (diamonds). The squares and dashed line represents the same sample, which had an acid treatment before the Na exchange experiments.

DISCUSSION

Solubility of silica in the hydrothermal fluid of different pH levels

Changes in the pH affect the silica solubility, and, thus the ripening process and porous structure of the silica gel [21,22]. The ripening process involves condensation of (surface) silanol groups. Techniques, providing evidence of the condensation of silanol groups and release of Na^+ (Eqn. 2) are DRIFTS and surface titration. The depolymerization of silica is catalyzed by hydroxyl ions and by the increased negative charge of the silica surface at high pH levels [23] (Eqn. 3).

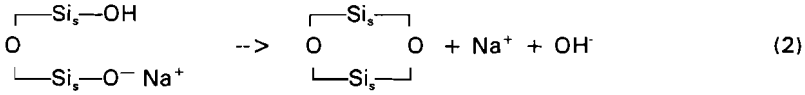

(2)

$$(SiO_2)_nSi_sOH + H_2O + OH^- \rightarrow (SiO_2)_{n-1}Si_sOH + (OH)_3SiO^- \quad (3)$$

The subscript s means surface. More ionized MSA in solution increases the pH, because MSA is a weak acid (pK_a = 9.8) with respect to that of the ionized surface silanol groups (pK_a is 7.2). The acid constant pK_a of the MSA is 9.35 in 1 M NaCl [23]. According to Eqn. 3 the solubility of silica is increased after the hydrothermal treatment. With the pK_a of 9.35 and Eqn. 3, the solubility, S, at any pH can be estimated from the relation $S = S_o * (1+10^{pH-9.35})$ [21] with the neutral pH solubility S_o of about 106 ppm in 1 M NaCl. The theoretical solubility with the relation based on Eqn. 3, is shown by the solid line in Fig. 3.

Decreased silica solubility with increased sodium chloride concentration

The decrease of the silica solubility after ageing at higher sodium chloride concentrations is known as the 'salting out' effect. Therefore, the silica solubility obtained by the β-silicomolybdate method of about 101 ppm at a neutral pH, represented in Fig. 3, is below the salt-free value of 115 to 130 ppm [17]. At temperatures up to 573 K, the salting-out effect is counteracted by complexes of MSA with the anions in solution [18,19]. In the neutral pH region, at low temperatures, the solubility of silica depends on the electrolyte concentration, obeying the relation (Eqn. 4) :

$$\text{Log}(S_o/S) = \Sigma_i D_i * [M_i] \quad (4)$$

where S_o is the salt-free solubility (in ppm), S the actual silica solubility (in ppm), Σ_i the sum of the various electrolytes present, D_i the proportionality constant of the electrolyte, which is 0.085 (l/mole) for NaCl [18], and $[M_i]$ is the electrolyte concentration (in mole/l).

Amount of surface silanol groups

The DRIFTS absorption due to isolated silanols at 3738 cm^{-1} decreases at lower surface area, whereas the absorption due to perturbed inner silanols at 3663 cm^{-1} increases, in accordance with results of Kondo et al. [12]. The existence of the 3663 cm^{-1} band is attributed to the enclosed intra-globular hydroxyls present between the necks, which increases during growth of the sol particles [24]. The IR absorption bands of free, inner, and hydrogen-bonded silanol groups at 3738, 3663, and 3588 cm^{-1}, respectively, being at lower wavenumbers than the literature values of 3748, 3670, and 3600 cm^{-1}, respectively, in ref. [12] may be due to the presence of sodium near the silanol groups. The relationship between the amount of surface silanol groups and the specific surface area agrees with the results by Sears [25] and by Mefford and Langenfeld [26]. These authors performed titration of surface silanol groups of colloidal silica particles from a pH of 4 to 9 in 0.1 M NaCl. A linear relationship between the surface area and the consumption of NaOH was established. Hence, the number of OH^- adsorption sites (silanol groups) on the silica surface is constant. This implies that a decrease of OH^- adsorption sites after ageing is mainly caused by a decrease of surface area. Calcining a xerogel sample just before recording the DRIFT spectrum increases the absorption by isolated silanol groups at 3738 cm^{-1}, and decreases the absorption due to adsorbed water at 3500-3000 cm^{-1} in Fig. 5c [27]. The favorable arrangement of six-membered silicon rings at the surface might be the explanation. Three silanol groups, number 1, 3, and 5, respectively, point out of the plane of the ring at mutual distances of 5.5 Å. At the centre of the triangle water is adsorbed with three hydrogen bonds of 2.7 Å each [28]. The OH band is shifted to a wave number between 3500 and 3000 cm^{-1}, and no longer separated from the band of adsorbed water.

Two approaches are followed in the literature to explain the adsorption of hydroxyl ions on glasses and porous gels [29]. The first approach considers the silica surface to be a porous gel [30]. Various cations can penetrate the gel, in which most of the cations are present in the double layer. More successful is the second approach, the 'site-binding' model, which involves a combination of electrostatic effects and complexation of counter ions on localized sites of the surface. The difference between the two approaches is the affinity of alkali metal adsorption. According to the first approach the extent of adsorption decreases with larger ionic radii of the adsorbing ions. Since the ionic radii increase in the order $Li^+ < Na^+ < K^+$, the extent of adsorption should drop in the order $Li^+ > Na^+ > K^+$. The

second approach, the site binding model, predicts the affinity to rise in the reverse order $Li^+ < Na^+ < K^+$ [31,32]. The appropriate explanation therefore depends on the nature of the silica. The 'site-binding' model is the most suitable with our gels. The surface complexation is described by the purely theoretical Eqn. 5, the equilibrium constant is given by Eqn. 6, and the surface potential by a Nernst type Eqn. 7.

$$Si_sOH + M^{z+} <-> SiOM^{(z-1)+} + H^+ \quad (5)$$

$$K_i = \exp((z-1)F\Phi/RT)) * [H^+] * [Si_sOM^{(z-1)+}]/[M^{z+}] * [Si_sOH] \quad (6)$$

$$\Phi = (-2.303 * R * T/F) * (pH - PZC) \quad (7)$$

z+ is the charge (in C) of M, the metal ion, F is the Faraday constant of $9.6 * 10^4$ C/mole, Φ the surface potential (in V), R the gas constant of 8.314 $J * mole^{-1} * K^{-1}$, T the temperature (in K), and PZC the point of zero charge. The maximum silanol group coverage of the silica surface is about 5.8 nm^{-2} after calcination at 383 K, often written as 92.6 $\mu C * cm^{-2}$ or 9.60 $\mu mole * m^{-2}$ [33]. The iso electric point (IEP) and the PZC of amorphous silica are both located between a pH of 2 and 3 [34], while the first ionization constant pK_a of the silanol group is 7.2. Normally, the difference between the IEP and the pK_a of other oxides is less than 2 [29]. The surface ionization is increased at a high sodium chloride concentration [34,35].

The existence of a layer of adsorbed Na^+

The intrinsic acid constant pK_i for complexation with Na^+ is 6.2. No adsorption of H^+ or OH^- should proceed, when the Na complexed spheres are added to a 1 and a 3 M NaCl solution of this pH, as is illustrated in Fig. 7. Addition of the Na^+ containing spheres to Na-free solutions, results in more H^+ being exchanged against Na^+ in order to establish the corresponding Na^+ concentration in the solution. Consequently, the curve intersects the pH-axis at a pH higher than 6.2 approaching the pK_a of silanols, viz., 7.7 in a sodium-free experiment. The layer of adsorbed Na^+ is completely removed by treating the spheres with 50 wt% sulphuric acid. After all the Na^+ has been removed from the silica surface, the IEP is 3.

CONCLUSIONS

1) The condensation of Na^+ complexed silanol groups and the rise in the concentration of ionized MSA increase the pH in the hydrothermal fluid after ageing of porous silica spheres. The silica solubility plays an important role in the ageing process of the spheres.

2) The condensation of surface silanol groups after the hydrothermal ageing can be monitored by measuring the intensity of the 3738 cm^{-1} band by DRIFTS. Attention should be paid to the fact that drying silica at 393 K before recording the DRIFT spectrum influences the intensity of the 3738 cm^{-1} band.

3) The IR-bands of free, inner, and hydrogen-bonded silanol groups at 3738, 3663, and 3588 cm^{-1}, respectively, are at wavenumbers smaller than 3748, 3670, and 3600 cm^{-1} mentioned in the literature, possibly due to the presence of sodium ions near the surface silanol groups.

4) The existence of a layer of adsorbed Na on the spheres has been satisfactory demonstrated, because H^+ and Na^+ are exchanged below a pH of 6.2. Addition of spheres to basic solutions results in the adsorption of OH^- on these specific sites of the silica surface. The percolation process of OH^- into the pores of the porous spheres can be described as diffusion controlled.

5) Silica samples, containing Na, behave differently from samples, free of Na. When a pseudo-IEP of 6.2 is observed, the sample contains Na, because 6.2 is the intrinsic constant of a Na^+ and H^+ exchange equilibrium. Observation of an IEP of 3 implies that the silica surface is free of Na.

ACKNOWLEDGMENTS

This investigation is a result of participation in the Debye Institute. The authors thank J.J. van Beek, dr.P.A. Buining and dr.J.T. Kloprogge for the critical review of the paper.

REFERENCES

1. C.J.G. van der Grift, J.W. Geus, H. Barten, R.G.I. Leferink, J.C. van Miltenburg and A.T. den Ouden, Characterization of Porous Solids, Ed. K.K. Unger et al., Elsevier, Amsterdam, (1988) 619
2. D. Gallagher and L.C. Klein, *J. Coll. Interf. Sci.*, **109** (1986) 40
3. D.D. Lasic, *Colloids and Surfaces*, **20** (1986) 265
4. U.S. Patent 3668088, R.K.Iler, Method of Producing Colloidal Silica by Electrodialysis of a Silicate (1972)
5. N.V. Akshinskaya, V.E. Beznogovan, A.V. Kiselev and Yu.S. Nikitin, *J. Phys. Chem. USSR*, **36** (1962) 1233
6. V.V. Popov, E.N. Lebedev, L.M. Antonova, A.P. Tomilov, A.S. Pushkin, V.F. Golikov, and T.A. Gerasina, *Coll. J. USSR*, **51** (1989) 610-615, Engl. Trans. 535-539
7. J.D.H. Strickland, *J. Am. Chem. Soc.*, **74** (1952) 868
8. V.W. Treusdale and C.J. Smith, *Analyst* **100** (1975) 203, *Analyst* **100** (1975) 797, *Analyst* **101** (1976) 19
9. G.B. Alexander, *J. Am. Chem. Soc.*, **75** (1953) 5655
10. R.K. Iler, The Chemistry of Silica, Wiley N.Y. (1979)
11. S. Kondo, H. Fujiwara, T. Jchii, and I. Tsuboi, *J. Chem. Soc. Faraday Trans.*, (I) **75** (1979) 646
12. S. Kondo, M. Igarashi and K. Nakai, *Colloids and Surfaces*, **63** (1992) 33
13. R.G. Bates, Determination of pH, 2nd ed., Wiley N.Y. (1973)
14. C.C. Westcott, pH measurements, 1st ed., Ac. Press. N.Y. (1978)
15. R.H. Busey and R.E. Mesmer, *Inorg. Chem.*, **16** (1977) 2445
16. G.B. Alexander, W.M. Heston and R.K. Iler, *J. Phys. Chem.*, **58** (1954) 453
17. A.G. Volosov, I.L. Khodakovskiy , B.N. Ryzhenko and V.I. Vernadskiy, Geochemistry International, **9** (1972) 362 Trans. from *Gheokhimiya*, **5** (1972) 575
18. W.L. Marshall, *Geochimica et Cosmochimica Acta*, **46** (1982) 289
19. W.L. Marshall, *Geochimica et Cosmochimica Acta*, **44** (1980) 907
20. R.P. Abendroth, *J. Phys. Chem.*, **76** (1972) 2547
21. R. Snel, *Applied Catalysis*, **12** (1984) 189
22. M. Yamane, in: Sol-Gel technology for thin films, fiber, preforms, electronics and specialty shapes, Ed. L.C. Klein, Noyes Publications, New Jersey (1988), 200-225
23. G. Okamoto, T. Okura and K. Goto, *Geochimica et Cosmochimica Acta*, **12** (1957) 123
24. A.V. Kiselev, V.I. Lygin, Infrared Spectra of Surface Compounds, Wiley N.Y. (1975), 75-103
25. G.W. Sears Jr., *Anal. Chem.*, **28** (1956) 1981
26. A. Meffert and A. Langenfeld, *Z. Anal. Chem.*, **249** (1970) 231

27. J. Erkelens and B.G. Linsen, *J. Coll. Interf. Sci.*, **29** (1969) 464
28. G. Foti and E.sz. Kovats, *Langmuir* 1989, **5**, 232
29. D.E. Yates and T.W. Healy, *J. Coll. Interf. Sci.*, **55** (1976) 9
30. Th.F. Tadros and J. Lyklema, *J. Electroanalytical Chem.*, **22** (1969) 9
31. P.W.Schindler, B. Fürst, R. Dick and P.U. Wolf, *J. Coll. Interf. Sci.*, **55** (1976) 469
32. Yu.G. Frolov, V.A. Kasaikin and S.B. Tarasov, *Coll. J. USSR*, **47** (1986) 856, Trans. from *Kolloidnyi Zhurnal*, **47** (1985) 989
33. R.Sh. Mikhail, A.M. Khalil, and S. Nashed, *Thermochimica Acta*, **24** (1978) 383
34. G.H. Bolt, *J. Phys. Chem.*, **61** (1957) 1166
35. Th.F. Tadros and J. Lyklema, *J. Electroanalytical Chem.*, **17** (1968) 267

Chapter 5

The shrinkage of hydrothermally aged porous silica spheres measured by thermoporometry

M.K. Titulaer, J.C. van Miltenburg[1], J.B.H. Jansen, and J.W. Geus[2]

Department of Geochemistry, Institute for Earth Sciences, University of Utrecht, Budapestlaan 4, P.O. Box 80.021, 3508 TA Utrecht, The Netherlands
[1]Chemical Thermodynamics Group, University of Utrecht, Transitorium 3, Padualaan 8, 3584 CH Utrecht, The Netherlands.
[2]Department of Inorganic Chemistry, University of Utrecht, Sorbonnelaan 16, P.O. Box 80.083, 3508 TB Utrecht, The Netherlands.

ABSTRACT

Spherical sol-gel silica hydrogel bodies of a size of few mm's are aged in 1 M NaCl solutions under hydrothermal conditions. The hydrogel bodies have a spherical shape and are prepared by the sol-gel technique. The aged spheres suspended in water are characterized by thermoporometry. With this technique the depression of the freezing point of water in the micro-porous body is measured, which provides information about the pore size, pore volume, and the pore shape. Hydrothermal treatment at high temperatures increases both the pore volume and pore size of the hydrogel spheres. By thermoporometry the pore size and pore volume is determined before and after drying. It appears that the pore volume and pore size of the dried gel (xerogel) is a function of the pore volume and pore size of the hydrogel after ageing. The pore size and pore volume decrease upon drying. The measured ice crystal radius by thermoporometry, R_n, is indicative for the pore radius, R_p, and the ice pore volume, V_n, indicative for the pore volume, V_p. With increased intensity of hydrothermal treatment, resulting in increased values of R_n in hydrogels of 8.6 to 27 nm, the absolute drop of R_n by drying is 5.1 and 7 nm, but relatively 59 and 26 %. The absolute drop of the ice pore volume, V_n, is 0.4 and 0.6 ml/g, and relative 44 and 43 %. With drying the ice surface area A_n is slightly increased with 42 and 30 m^2/g at a R_n of 10.9 and 25 nm, respectively. Clearly the decrease of the pore radius is due to the densification of the gel structure, but no pores are enclosed because the surface area is hardly affected by the drying step.

INTRODUCTION

Amorphous silica is used as a thermostable support for catalytically active solids. An important example is the nickel-on-silica catalyst employed in the hydrogenation of fatty oils. Another example is the chrome-on-silica catalyst of the Phillips process for the polymerization of ethylene. The porous structure of catalyst supports is often of decisive importance for the performance of the catalyst obtained after application of the active component.

Together with the size of the support bodies, the porous structure of the support determines the rate of transport of reactants and reaction products through the solid catalyst. With many industrial catalysts the permissible pressure drop over a fixed catalyst bed asks for catalyst bodies thus large that the physical transport within the catalyst bodies is controlling the overall rate of the catalytic reaction. The effect of transport limitations on the selectivity of catalytic reactions is often more serious than merely decreasing the reaction rate. A low rate of transport can favor the proceeding of undesired sequential reactions. An instance is the oxidation to carbon (di)oxide and water with the selective catalytic oxidation of organic compounds, as with the production of ethylene oxide and maleic anhydride.

As said above, the size of the catalyst bodies is often prescribed by the pressure drop over a fixed catalyst bed. With catalysts being used suspended in a liquid, the requirement to separate the catalyst readily from the liquid also calls for a minimum size of the catalyst bodies. When the size of the catalyst bodies cannot be decreased, control of the porous structure of the catalyst, and thus of the support, can only remedy transport limitations. The most generally used supports, viz., alumina and silica, are mainly produced by chemical reactions in an aqueous liquid. After separation from the liquid, the supports are dried and, if desired, calcined at more elevated temperatures. The high surface energy of water brings about that the elementary particles of the support are compressed when during the drying process the meniscus of the liquid travels through the pores of the solid.

The importance of the porous structure of the catalyst renders a thorough investigation of the effects of the drying step on the porous structure of the support very worthwhile. The catalyst support studied in this work has been prepared by a sol-gel process. The drying step, which is critical in the preparation of the silica support [1-3], is the main subject of this study. Also the effect of (hydrothermal) ageing of silica before drying on the porous structure will be investigated. To study the porous structure of solids suspended in water, thermoporometry is very suitable. This study therefore also deals with the theoretical background of thermoporometry and evaluates the experimental results of thermoporometry by comparison with mercury penetration and nitrogen sorption.

Porous spherical hydrogel bodies are prepared by the sol-gel procedure and are aged at room temperature in water or under hydrothermal conditions without being dried. The hydrothermal conditions are varied in this study. The aim of the study is to establish whether hydrothermal ageing strengthens the gel structure by transport and deposition of silica. If the gel structure is reinforced, it can withstand the capillary forces during subse-

quent drying. Thermoporometry, which yields information about the pore size, the pore volume, and the pore shape of porous materials can characterize the wet silica spheres before drying. Thermoporometry is based on the depressing of the solidification point of a fluid, such as, water, benzene, dicyclohexane ($C_{10}H_{18}$) [4-6]. In the case of water, thermodynamics predicts the formation of ice within narrow pores at temperatures lower than the freezing point of bulk water, viz., 273.15 K. Provided the concentration of soluble salts within the pores of the solid is negligible, the freezing point depression, dT, which is $T\text{-}T_o < 0$, is a function of the pore radius.

The amount of water freezing or melting within the porous system can be detected separately from bulk water by differential scanning calorimetry (DSC). The heat-flow during freezing of water and fusion of ice within the porous material is recorded. Thermoporometry enables one to measure ice crystal radii, R_n, between 1 and 150 nm [7]. The minimum value of 1 nm of the radius which can be measured is due to (i) the minimum temperature of 210 K that can be established within the DSC apparatus used in this work with gaseous nitrogen as a cooling agent, and (ii) the fact that water present in pores of radii, R_p, smaller than 1 nm is strongly bonded to the silica surface and does not freeze. Interference with the peaks of 'bulk water' and 'pore water' in the thermogram leads to the upper limit of 150 nm.

After dealing with the theoretical background of thermoporometry, experimental results on silica samples before and after drying are presented. The dried silica samples are also characterized by mercury intrusion and nitrogen sorption. First the results obtained by the different techniques on the same samples will be compared to evaluate the thermoporometric results. Subsequently the effects of drying of differently pretreated silica spheres will be considered.

Thermoporometry

Since many catalyst supports are produced by reactions in aqueous solutions and drying strongly affects the porous structure of gels, it is important to assess the porous structure of solids dispersed in the liquid in which they have been prepared. Thermoporometry is a technique that enables one to establish the porous structure of solids dispersed in water.

Thermoporometry is based upon the fact that the temperature at which a liquid freezes or melts depends on the curvature of the interface between the liquid and the solid. During penetration of the interface into the pores of a solid, the interface has to assume a semi-spherical shape of a radius that is equal to the radius of the pore. Alternatively nucleation of the solid can proceed within the pores of the solid provided the radius of the smallest stable nucleus fits in the pore.

To derive the required thermodynamic relations, we will consider a solid the pores of which have been completely filled with the liquid. The porous solid is present within the solidified bulk liquid. The penetration of the solid-liquid interface into the pores or the generation of stable nuclei of the solid within the pores now will be dealt with. A reversible

transfer of dn moles from the liquid to the solid phase involves a change in energy, dU, given by :

$$dU = T*dS - P*dV + \gamma_{ls}*dA_{ls} + \mu_s dn_s + \mu_l dn_l \quad (J) \quad (1)$$

where TdS and PdV have the usual meaning, γ_{ls} is the interfacial energy, dA_{ls} the change in the interfacial area, μ_s and μ_l the molar Gibbs free energy of the solid and the liquid, respectively,and dn_s and dn_l the number of moles added to the liquid and solid phase, respectively. The change in Gibbs free energy, dG, accordingly is :

$$dG = -S*dT + V*dP + \gamma_{ls}*dA_{ls} + \mu_s dn_s + \mu_l dn_l \quad (J) \quad (2)$$

The condition for equilibrium is :

$$dG_{P,T} = 0 \quad (J) \quad (3)$$

, or :

$$\gamma_{ls}*dA_{ls} + \mu_s dn_s + \mu_l dn_l = 0 \quad (J) \quad (4)$$

With the transfer of dn_l moles from the solid to the liquid the relation between the number of moles is :

$$dn_s = -dn_l \quad (mole) \quad (5)$$

, and the condition for equilibrium becomes :

$$\gamma_{ls}*dA_{ls} + (\mu_l-\mu_s)*dn_l = 0 \quad (J) \quad (6)$$

When the interfacial area does not change during the transfer of the material, the usual equilibrium condition results, viz.,

$$(\mu_l-\mu_s)*dn_l = 0 \quad (J) \quad (7)$$

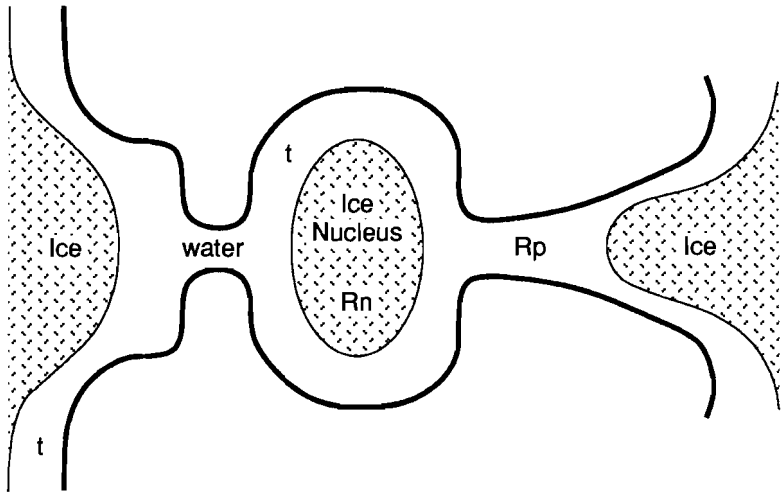

Figure 1 Formation of a critical ice-nucleus with radius R_n, and the penetration of the ice-meniscus in the wet gel.

and :

$$\mu_l = \mu_s \qquad \text{(J/mole)} \qquad (8)$$

The equilibrium is established at a temperature T_o, where the enthalpy difference, $h_l^\circ - h_s^\circ$, is compensated by the entropy difference according to :

$$h_l^\circ - T_o S_l = h_s^\circ - T_o S_s \qquad \text{(J/mole)} \qquad (9)$$

$$T_o = (h_l^\circ - h_s^\circ)/(S_l - S_s) \qquad \text{(K)} \qquad (10)$$

When the interfacial area changes during the transfer of material as displayed in Fig. 1, the equilibrium condition is :

$$\mu_l - \mu_s = -\gamma_{ls} * (dA_{ls}/dn_l) \qquad \text{(J/mole)} \qquad (11)$$

, or :

$$\mu_s = \mu_l + \gamma_{ls} * (dA_{ls}/dn_l) \quad \text{(J/mole)} \quad (12)$$

With the semi-spherical interface at the entrance of the pores and the spherical interface of the nuclei within the pores (Fig.1) :

$$dA_{ls}/dn_l < 0 \quad \text{(m}^2\text{/mole)} \quad (13)$$

With V_L being the molar volume of the liquid and dv_l the change in the volume of the liquid phase, the following relation holds,

$$dn = dv_l / V_L \quad \text{(mole)} \quad (14)$$

, and (dA_{ls}/dn_l) can be rewritten to :

$$V_L * (dA_{ls}/dv_l) \quad \text{(m}^2\text{/mole)} \quad (15)$$

The surface A_{ls} can be expressed in the coordinates x*y, the change in surface area dA_{ls} in $(x*dy)+(y*dx)$, and the change in the volume, dv_l, in the coordinates $-x*y*dz$. With the radii of curvature, R_1 and R_2, of the meniscus the following relations can be derived :

$$dx/x = dz/R_1 \quad \text{and} \quad dy/y = dz/R_2 \quad (16)$$

With aid of Eqn. 16 can be deduced :

$$dA_{ls}/dv_l = -1/R_1 - 1/R_2 \quad \text{(m}^{-1}\text{)} \quad (17)$$

With a semi-spherical interface, where R_1 and R_2 are equal to R_n, the relation between the change in the volume of the liquid phase and the interfacial area is :

$$dA_{ls}/dn_l = -V_L * 2/R_n \quad \text{(m}^2\text{/mole)} \quad (18)$$

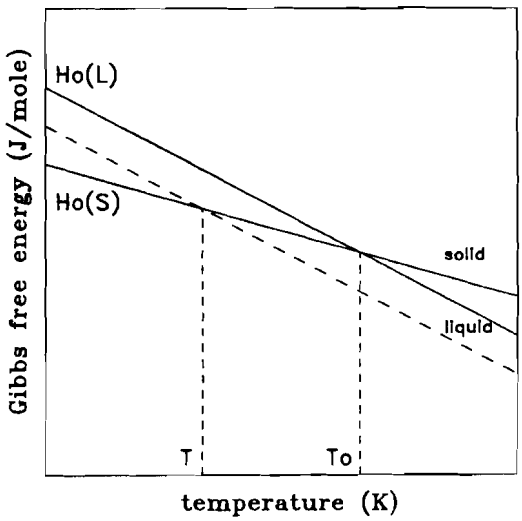

Figure 2

Gibbs free energy (μ_s, μ_l) as a function of the temperature.

The minus sign accounts for the combination of the increase in the interfacial area from a plane to a curved surface just when the penetration starts (dA_{ls} = +) (Fig. 1), when dn_l moles are transferred from the liquid to the solid with freezing (dn_l = -). The following condition for equilibrium results,

$$\mu_s = \mu_l - \gamma_{ls} * V_L * 2/R_n \qquad \text{(J/mole)} \qquad (19)$$

Now the molar Gibbs free energy of the solid must be equal to that of the liquid minus the energy involved with the change in the interfacial area to achieve equilibrium. The drop of μ_l by the change in interfacial energy results in the equilibrium to be established at a temperature, T, which is lower than the equilibrium temperatures with a flat interface, T_o.

The relation between the temperature and the molar free energies is schematically indicated in Fig.2. Neglecting the temperature and pressure dependence of the enthalpy and entropy, the molar Gibbs free energy of the solid and the liquid can be represented by straight lines intersecting at the temperature T_o. At T_o the solid and liquid are in equilibrium across a flat interface. When the solid phase is at atmospheric pressure and the liquid phase is present within the pores of the solid having a radius R_n, the equilibrium temperature is at the intersection of the straight line representing the free energy of the solid and the dashed line drawn at a vertical distance from the line representing the free energy of the liquid of :

$$\gamma_{ls} * V_L * 2/R_n \qquad \text{(J/mole)} \qquad (20)$$

At the intersection of the dashed line holds :

$$H_s(T)-T*S_s(T) = H_l(T)-T*S_l(T) \quad -\gamma_{ls}*V_L*2/R_n \qquad \text{(J/mole)} \qquad (21)$$

$H_s(T)$ and $S_s(T)$ are terms, which describe the enthalpy and entropy as function of the temperature. The temperature dependence of the enthalpy is :

$$H_s(T) = H_s^\circ + \int Cp_s(T) * dT \qquad \text{(J/mole)} \qquad (22)$$

, and that of the entropy :

$$S_s(T) = S_s^\circ + \int Cp_s(T)/T * dT \qquad \text{(J/mole*K)} \qquad (23)$$

Thus :

$$H_s^\circ - T*S_s^\circ = H_l^\circ - T*S_l^\circ \quad -\gamma_{ls}*V_L*2/R_n \qquad \text{(J/mole)} \qquad (24)$$

$$T * (S_l^\circ-S_s^\circ) = H_l^\circ-H_s^\circ \quad -\gamma_{ls}*V_L*2/R_n \qquad \text{(J/mole)} \qquad (25)$$

$$T = (H_l^\circ-H_s^\circ)/(S_l^\circ-S_s^\circ) \quad -2\gamma_{ls}*V_L / (S_l^\circ-S_s^\circ)*R_n \qquad \text{(K)} \qquad (26)$$

Hence :

$$T = T_o \quad - 2\gamma_{ls}*V_L / dS_f^\circ*R_n \qquad \text{(K)} \qquad (27)$$

where dS_f° is the entropy of fusion. The value reported by Brun et al. [8] is 1.2227 $J*g^{-1}*K^{-1}$, while a value of 1.215 $J*g^{-1}*K^{-1}$ is calculated with the fusion enthalpy of water mentioned in the literature [9], which amounts to 332 J/g.

$$R_n = -2*\gamma_{ls}*V_L / dS_f^\circ*(T-T_o) \qquad \text{(m)} \qquad (28)$$

Brun et al. [8] have determined the value of the interfacial energy of the liquid water-ice interface that led to the best agreement with porous dimensions determined by mercury penetration and nitrogen sorption. The interfacial energy γ_{ls} is :

$$\gamma_{ls} = (40.9+0.39*dT) * 10^{-3} \quad \text{(N/m)} \quad (29)$$

where dT is the decrease in the freezing point, $(T-T_o)$. For the fusion enthalpy at 273 K we use the same value as used by Brun et al., viz.,

$$dS_f^\circ = 1.2227 \quad \text{(J/g*K)} \quad (30)$$

, and with $V_L = (1.004-9.11*10^{-5}*dT)*10^{-6}$ m^3/g :

$$R_n = 10^9*-2*(40.9+0.39*dT)*10^{-3}*(1.004-9.11*10^{-5}*dT)10^{-6}/1.2227*dT$$

$$= -67.17/dT - 0.64 \quad \text{(nm)} \quad (31)$$

However, the dependence of R_n on dT mentioned by Brun et al. [8] is :

$$R_n = -64.67/dT - 0.23 \quad \text{(nm)} \quad (32)$$

The volume of water, V_n, undergoing the phase transformation, is smaller than the real pore volume, V_p, because a non-freezing layer of a thickness, t, of about 0.9 nm does show up at the silica-ice interface [3,8,10,11] (Fig. 1). The value of 0.9 nm is the average of the values of 0.8 and 1.0 nm mentioned in the literature. The non-freezing layer consisting of three monolayers of water [12] has been satisfactorily demonstrated by proton NMR spectroscopy [11], DSC [13,14], and viscosity measurements [15], though a low thickness of 0.3 ± 0.1 nm has been obtained by low-field proton NMR spin relaxation measurements [16]. Brun et al. [8] applies a value of t of 0.8 nm, and therefore :

$$R_p = -64.67/dT + 0.57 \quad \text{(nm)} \quad (33)$$

The relation of Eqn. 33 is used to determine the interfacial energy, γ_{ls}, as a function of the temperature.

It is possible to correct for the temperature dependence of the entropy by using the specific heats of the solid and the liquid according to :

$$dS_f = dS_f^\circ + {}_{T_o}\int^{T} (Cp_l-Cp_s)/T * dT \quad \text{(J/mole*K)} \quad (34)$$

The entropy of Eqn. 34 is merely a property of the bulk of the water, schematized by the solid lines in Fig. 2. The dS_f° and Cp_l-Cp_s term are quoted as the A and B term on page 66 in ref. [8], the normal entropy, and the entropy variation due to the lowering of the transformation temperature.

As said earlier in Eqn. 21, at the intersection of the dashed line holds :

$$H_s(T)-T*S_s(T) = H_l(T)-T*S_l(T) - \gamma_{ls}*V_L*2/R_n \quad \text{(J/mole)} \quad (35)$$

$$S_l(T)-S_s(T) = (H_l(T)-H_s(T))/T - \gamma_{ls}*V_L*2/(T*R_n) \quad \text{(J/mole*K)} \quad (36)$$

, and with Eqn. 28 :

$$S_l(T)-S_s(T) = (H_l(T)-H_s(T))/T + dS_f^\circ*(T-T_o)/T \quad \text{(J/mole*K)} \quad (37)$$

$$S_l(T)-S_s(T) = (H_l^\circ-H_s^\circ)/T + (Cp_l-Cp_s/T)*dT + (dS_f^\circ/T)*dT \quad \text{(J/mole*K)} \quad (38)$$

$$dS_f = dS_f^\circ + {}_{To}\int^{T} (Cp_l-Cp_s/T)*dT + {}_{To}\int^{T} (dS_f^\circ/T)*dT \quad \text{(J/mole*K)} \quad (39)$$

Eqn. 39 contains a third correcting term C mentioned by Brun et. al. [8] due to the liquid-solid interface curvature. It can clearly be seen from Eqn. 39 that the ice-water enthalpy H can be expressed by :

$$H = T*dS_f = T_o*dS_f^\circ + (Cp_l-Cp_s)*dT + dS_f^\circ*dT \quad \text{(J/mole)} \quad (40)$$

The ice-water enthalpy H is corrected for the energy dH involved in the preparation of the meniscus, which is 1.2*dT, and for the difference in heat capacity between water and ice, $(Cp_l-Cp_s)*dT$, respectively [6]. According to Angell et al. [17], the heat capacity of water, Cp_l, is $4.1 - 2.8*10^{-3}*dT + 9.5*10^{-4}*dT^2$ (J/g*K). The heat capacity of ice, Cp_s, is $2.11 + 7.9*10^{-3}*dT$ (J/g*K) [9]. Both corrections are applied to the enthalpy :

$$H = 332 + 3.2*dT - 10.7*10^{-3}*dT^2 + 9.5*10^{-4}*dT^3 \quad \text{(J/g)} \quad (41)$$

Another correction involves the entropy of the interface. Brun et al. [8] assume the

presence of cylindrical pores to develop an expression for the correction. The surface area, A, of a cylindrical pore is :

$$A = 2\pi * R_n * L \qquad (m^2) \qquad (42)$$

where L is the pore length.

$$A = 2\pi * (R_n)^2 * L/R_n = 2 * v_l/R_n \qquad (m^2) \qquad (43)$$

The surface free energy, G^s, is equal to the interfacial energy $\gamma * A$ (J) :

$$G^s = \gamma * A = (H^s - T * S^s) \qquad (J) \qquad (44)$$

, whence :

$$dG^s = d\gamma * A = (dH^s - T * dS^s - dT * S^s) \qquad (J) \qquad (45)$$

The entropy contribution of the interface accordingly is :

$$(dS_f)_{sup} = S^s/n_l = -(d\gamma/dT) * A/n_l = -(d\gamma/dT) * 2 * V_L/R_n \qquad (J/mole*K) \qquad (46)$$

The total energy, W'_{th}, released during the transition of the liquid to the solid raising the interfacial area by an amount A hence is :

$$W'_{th} = T * (dS_f + (dS_f)_{sup}) \qquad (J/mole) \qquad (47)$$

$$W'_{th} = T * dS_f * (1 - (d\gamma/dT) * 2 * V_L/(dS_f * R_n)) \qquad (J/mole) \qquad (48)$$

, and thus with aid of Eqn. 28 :

$$W'_{th} = T * dS_f * (1 + (d\gamma/dT) * ((T-T_o)/\gamma_{ls}) * (dS_f^o/dS_f)) \qquad (J/mole) \qquad (49)$$

where $d\gamma/dT = 0.39 * 10^{-3}$ N/m*K. We do not include the correction for the interfacial entropy and in view of small correction also not derivation of the correction for the pressure dependence of the fusion entropy, for which we refer to [8,18]. The value of the ice-water surface tension, γ_{is}, of $(40.9 + 0.39 * dT) * 10^{-3}$ N/m is close to the silica-water surface tension of $45 * 10^{-3}$ N/m [19,20].

The pore volume of wet gel determined in four ways

The pore volume of the silica sample can be determined directly by integrating the heat-flux with time in two ways : 1) in the cooling step of the measurement sequence (freezing water), and 2) in the heating step (melting ice). The pore volume, V_n, is calculated by :

$$V_n = \Sigma_i P_i * (t_{i+1} - t_i) / H * W * D \qquad \text{(ml/g)} \qquad (50)$$

in which P_i is the heat-flux (in W), $t_{i+1} - t_i$ the measuring interval of 20 s, H is the ice-water enthalpy of Eqn. 41 (in J/g), and W is the amount of silica (in g). Two alternative ways of measuring the pore volume are the use of 3) the crystal size distribution, and 4) the amount of bulk water.

The pore volume V_n by using the ice crystal size distribution

The ice crystal size distribution in a cooling experiment, dV_n/dR against R_n, can be derived from Eqn. 32 [4,21]. The contribution to the total ice volume of measurement point i is :

$$dV_n/dR_i = (P_i/HD) * (1/cr) * (dT_i^2/64.67) \qquad \text{(ml/nm)} \qquad (51)$$

in which P_i is the heat-flux (in J/s), H is the ice-water enthalpy of Eqn. 41 (J/g), D the density of ice (g/ml), cr is the cooling rate (K/s), dT_i is the freezing-point depression (K), and 64.67 a constant (nm*K). The determination of the pore volume is integration of the product dV/dR_i with dR_i (Eqn. 52), with dR_i the change in the value of the radius at measurement point i (Eqn. 53) :

$$V_n = \Sigma_i dV_n/dR_i * dR_i * 1/W \qquad \text{(ml/g)} \qquad (52)$$

$$dR_i = R_{i+k} + R_{i-k} / k \qquad \text{(nm)} \qquad (53)$$

in which V_n is the pore volume of the wet gel (in ml/g), and k an integer, representing the interval before and after measurement point i, varying from 1 to 20. Applying a cooling rate of 30 K/h, a value k of 1 is sufficient to measure an accurate dR_i and pore volume V_n. However, for small cooling rates, 1 K/h, a relative high value of k must be chosen, k = 20, because the fault in dT_i is relative large on the Setaram DSC 111.

Measurement of V_n by using the amount of bulk water

Finally, the pore volume can be measured in a less laborious manner : by subtraction of the amount of bulk water in the thermogram, melting at 273 K, from weight of water, expressed by Eqn. 54.

$$V_n = (W(H_2O)_T - W(H_2O)_B) / (W(SiO_2) * D) \qquad \text{(ml/g)} \qquad (54)$$

V_n is the pore volume of the wet gel, $W(H_2O)_T$ the total amount of water obtained with a balance, $W(H_2O)_B$ the amount water melting at 273 K obtained by DSC, and $W(SiO_2)$ the weight of dry silica (in g), and D the density of water (g/ml). The total amount of water in the sample cup is determined by measuring the weight loss after drying of the wet xero- or hydrogel.

The role of the pore shape factor F and the non-freezing layer t

Ice crystals in pores of solid materials melt at temperatures below the bulk freezing temperatures. The quotient of the freezing point depression with solidification, dT_s, and with fusion, dT_f, is the shape factor F.

$$F = dT_s / dT_f \qquad (55)$$

The magnitude of the shape factor F provides information about the shape of the pores. The shape factor F has a value of 1 for pure spherical pockets, and a value of 2 for cylindrical pores [7]. Usually, a value of F between 1 and 2 is experimentally found. If the

temperature of the solidification and fusion curves overlap, the contribution of the spherical and cylindrical pores can be separated using the procedure of Jallut et al. [4]. Quinson et al. [22] derive a factor m from the shape factor F, viz., m = (4-F). However, we prefer m = (1 + 2/F).

The value V_n can be corrected for the non-freezing layer t by :

$$V_n^* = V_n * ((R_n + t) / R_n)^m \qquad \text{(ml/g)} \qquad (56)$$

in which V_n^* is the corrected pore volume (in ml/g), R_n is the crystal size (nm), and t is the non-freezing layer (in nm). Jackson and McKenna [5], studying the solidification of dicyclodecane do not correct for the 'non-freezing' layer. As a result the apparent solidification enthalpy measured within pores of a radius of 5 nm is 30 % lower than the enthalpy in pores of a radius 25 nm or more.

The surface area of the ice crystal A_n (m^2/g SiO_2) can be derived from the pore volume V_n according to Eqn. 57.

$$A_n = m * V_n / R_n \qquad (m^2/g) \qquad (57)$$

The value of A_n can also be corrected for the non-freezing layer t in Eqn. 58.

$$A_n^* = m*V_n^* / (R_n+t) = A_n*((R_n+t)/R_n)^{m-1} \qquad (m^2/g) \qquad (58)$$

The corrected specific surface area A_n^* can be compared with the BET surface area of the dried silica spheres.

EXPERIMENTAL

Preparation and hydrothermally ageing of the spheres

The preparation of porous silica gel by means of the sol-gel procedure has been known for more than 50 years [23]. Recently, the preparation of spherical silica gel bodies has been developed [24]. The pore structure of the resulting silica can be modified by adapting one or more of the steps in the sol-gel preparation of the spheres.

The steps are :

A. preparing a hydrosol by acidifying a sodium silicate solution,
B. gelling of the spherical sol droplets in hot paraffin oil, forming hydrogel spheres. The density of the sol aggregates is influenced by the gelling temperature, and the pH [25],
C. ageing of the hydrogel, which causes an increase of the pore radius, and of the pore volume, and a decrease of the silica surface area [26],
D. removal of the excess of the electrolyte by washing, or by adding sodium exchange media,
E. drying of the hydrogel, forming a xerogel,
F. addition of an electrolyte, and ageing of the xerogel,
G. drying of the aged xerogel,
H. calcining the dried gel.

It is not necessary to apply either step C, or steps F-G. Ageing at high pH levels leads to an enhanced pore volume due to the repulsion amongst negatively charged particles. The effect will be even more pronounced when (i) the silica concentration is high at high pH, or (ii) pore regulating agents (PRA's) are used, because an increased charge density raises the repulsion [27,28]. While we have to use thermoporometry to characterize the wet gels, we used additional techniques to investigate the dried silica spheres, viz., N_2 sorption, and Hg penetration.

Sample codes

Six fractions of hydrogel spheres are prepared, consisting of 5 nm primary particles, and having a concentration of 13 wt% silica in water, viz., two standard hydrogel fractions, H1 and H2, which are stored in water (Steps A, B and D). Fraction H1 is gelled at room temperature, while fraction H2 is gelled in hot paraffin oil of 363 K. Four hydrogel fractions, H3 to H6, are washed with 1 M NaCl, and are aged (Steps A to D), viz., 2 h at 473 K at a pH of 6 (H3), 23 h at 423 K and a pH of 6 (H4), 24 h at 473 K and a pH of 5.2 (H5), and 7 h at 473 K and a pH of 6 (H6).

One standard xerogel fraction (X7) is prepared by drying H2 at 393 K (Steps A, B, D and E). Two xerogel fractions are aged in 1 M NaCl of pH = 6 (Steps A, B, D to H) for 7 h at 473 K (X8), and for 23 h at 373 K (X9). The weight ratio of silica/water with ageing is 0.15.

The aged hydrogels H1 to H6, before and after drying, and the xerogels X7 to X9 only after drying are characterized by thermoporometry. The drying temperature is 393 K. Before thermoporometry is applied to the dried samples, the pores are completely filled with water. Amounts of 0.24 to 0.30 g not dried hydrogel, containing 0.02 g dry silica are measured. Xerogel spheres, containing 0.09 g silica, are added to an excess of water and

are measured. The weight of the aluminum sample cup is 0.22 g. Thermograms are recorded at low cooling and heating rates, viz., -1 and +1 K/h, respectively. With samples containing narrow pores, the measurements have to be extended to low temperatures with slightly higher cooling and heating rates, larger than 1 K/h. For example, samples H2 and X7 are measured at cooling rates of -2 and -5 K/h.

All the samples are measured on the Setaram DSC 111, except for one hydrogel, viz., H1, which is measured on a Netzsch 43 DSC in combination with a model 200 data station (Selb, Germany).

RESULTS AND DISCUSSION

Evaluation of thermoporometric results

The thermogram of the hydrogel H2 is represented in Fig. 3. Formation of ice crystallites during cooling is evident from the exothermic peak at 265.8 K. The branch measured during heating exhibits an endothermic fusion peak at a higher temperature, viz., 270.3 K. The melting of bulk water shows up at 273.15 K during heating. An appreciable hysteresis between the freezing and the fusion temperature, dT_s and dT_f, respectively, thus is apparent. The shape factor corresponding to the hysteresis, dT_s/dT_f, is high, viz., 2.6.

Table 1 Thermoporometry applied on sample (a) X8 with $R_p = 30$ nm, $V_p = 1.0$ ml/g, and (b) X9 with $R_p = 8$ nm, $V_p = 0.8$ ml/g, and BET surface area 156 m^2/g on a Setaram DSC 111, and (c) H1 on a Netzsch DSC 43.

	rate (K/h)	R_n (nm)	V_n (ml/g)		F	A_n (m^2/g)	
(a) X8	-30	15					
7h	-7	20	0.8[1]		1.5	62	
473K	-1	30					
(b) X9	1		0.7[2]	1.0[3]			first time heating
23h	-1	8.3	0.8[1]		2.1	172	second time cooling
373K	1		0.6[2]				fourth time heating
(c)	-60	5.0	0.4[1]	0.4[2]	1.6	180	after 4 days
H1	-60	5.1	0.3[1]	0.3[2]	1.6	132	after 27 days
	-60	5.5	0.3[1]	0.3[2]	1.6	123	after 180 days

V_n obtained by 1) cooling, 2) heating, and 3) the bulk peak

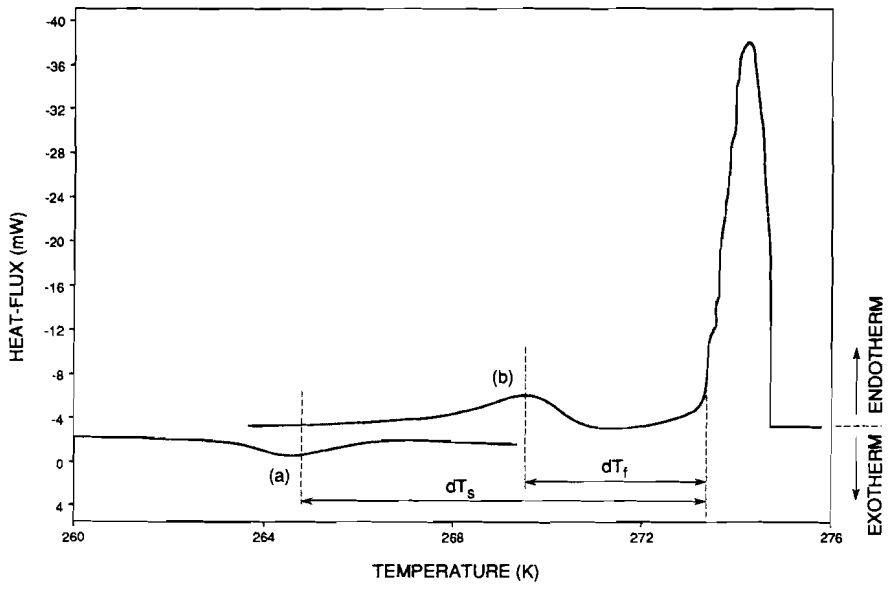

Figure 3 Thermogram represents standard hydrogel H2 with a concentration silica of 13 wt% SiO_2 in water. The amount solid silica is 0.02 g. The cooling and heating rate is -2 and +2 K/h, respectively. The measuring interval is 20 s, and the sensitivity of the Setaram DSC 111 is 250 μW. The cooling step is (a), and the heating step (b).

The effect of the cooling rate on the pore radius calculated from the experimental thermogram has been investigated on sample X8, the xerogel dried at 393 K and hydrothermally treated for 7 h at 473 K. For the xerogel X8 mercury porosimetry provided a mean pore radius of 30 nm and a pore volume of 1.0 ml/g. As can be seen in Tab. 1, cooling rates of 30 and of 7 K/h led to pore radii of 15 and 20 nm, respectively, while only the low cooling rate of 1 K/h resulted in the pore radius of 30 nm, which was observed with mercury porosimetry.

In Tab. 1 and 2 the pore volumes determined according to the four procedures indicated above are mentioned. It can be seen that the value of V_n determined from the surface area of the peak in the cooling step is mostly slightly smaller than the V_n value calculated from the fusion peak. The hydrogel H2 showed a value for V_n that is considerably higher than pore volume calculated from the peak measured during the heating step. It is remarkable that the hydrogel H2 also exhibited an exceptionally high value of F, the pore shape factor, viz., 2.6. The hydrogel H5 also has a pore volume calculated from the fusion peak that is significantly higher than that calculated from the freezing peak, viz., 1.9 and 1.6 ml/g,

Table 2 Pore structure of aged hydrogels (a) before drying, and (b) after drying, compared with (c) Hg penetration, and (d) N_2 adsorption and desorption, both applied on dried spheres.

	sample	H2 gelling 363 K	H3 2 h pH = 6 473 K	H4 23 h pH = 6 423 K	H5 24h pH = 5 473 K	H6 7 h pH = 6 473 K
(a)	R_n (nm)	8.6	10.9	19	25	27
	V_n (ml/g)	0.9[1] 1.5[2]	1.0[1] 1.1[2] 1.0[3] 1.9[4]	0.9[1]	1.6[1] 1.9[2] 2.1[3]	1.4[1]
	F	2.6	1.6		2.3	
	A_n (m^2/g)	240	204		115	
(b)	R_n (nm)	3.5	7.1	11.1	15	20
	V_n (ml/g)	0.5[1]	0.7[1] 0.6[2] 0.7[3] 1.0[4]	0.6[1]	1.0[1] 1.1[2] 1.0[3] 1.1[4]	0.8[1] 0.9[3]
	V_n^* (ml/g)	0.8[1]	0.9[1]	0.7[1]	1.1[1]	0.9[1]
	F		1.4		1.8	
	A_n (m^2/g)	286[5]	246		145	
	A_n^* (m^2/g)	360[5]	285		150	
(a-b)	$-dR_n$ (nm)	5.1	3.8	7.9	10	7
	$-dR_n$ (%)	59	35	42	40	26
	$-dV_n$ (ml/g)	0.4	0.3	0.3	0.6	0.6
	$-dV_n$ (%)	44	30	33	38	43
	dA_n (m^2/g)	46[5]	42		30	
(c)	R_p (nm)		5.2	9.4	13	16
	V_p (ml/g)		0.8	1.0	1.3	1.1
(d)	R_p (nm)	2.3	6.6		15	
	V_p (ml/g)	0.76	1.0		1.4	
	A_s (m^2/g)	455	218		123	

V_n obtained by 1) the cooling step, 2) the heating step, 3) the pore size distribution, 4) measuring the amount bulk water. The surface area A_n obtained by 5) assumption of a cylindrical pore shape.

respectively. The shape factor is also relatively high, viz., 2.3. The V_n value calculated according to the above procedure (iii) from the cumulative ice crystal size distribution does not differ significantly from that calculated from the cooling step. However, the pore volume calculated from the cumulative ice crystallite size distribution is even larger with the hydrogel H5, viz., 2.1 ml/g. The pore volume calculated from the peak due to bulk water is larger than the pore volumes calculated according to the other procedures. Since this procedure also measures the non-freezing layer, t, it should be the most reliable. Unfortunately, however, the procedure has experimentally the lowest accuracy, due to weighing errors and leakage of water from the aluminum sample cup. Additionally some water may be present in pores within the gel structure of radii R_n smaller than 1 nm, which will lead to a greater pore volume. However, the amount of water present in micropockets within the gel structure is assumed to be negligible in base catalyzed silica gels [29].

A number of reasons other than merely an experimental error can be raised to explain that the pore volume V_n calculated from the freezing peak is smaller than that calculated from the thawing peak. First of all, water may be freezing initially to an amorphous solid, which subsequently more slowly recrystallizes to ice, and which melts as crystalline ice during the heating cycle. A delayed crystallization to ice may lead to a freezing peak which is relatively low and which is exhibited at an appreciably lower temperature than with direct crystallization to ice. The low temperature of the freezing peak should lead to a high pore shape factor and the low peak to a relatively low pore volume, V_n. Also the temperature correction of the enthalpy, Cp_l, has been debated. If the value of Cp_l is not entirely correct, the value of the pore volume can also be affected. Etzler [30] has established that the heat capacity of liquid water, Cp_l, strongly depends on the pore radius of the silica. It is strange, however, that the heat capacity passes through a maximum at decreasing pore sizes. The maximum, 5.52 J/K*g, is exhibited at a pore radius of 7 nm.

Everett [31] has extensively dealt with the effects of solidification of a liquid present within a porous material on the structure of the material. Often solidification of the liquid results in disintegration of the porous solid. Everett emphasizes that the disintegration is not due to expansion of the impregnated liquid during freezing. Also with liquids that take up a lower volume with the transition to the solid can bring about disintegration due to transport of the liquid to pores of larger dimensions. Since the density of ice at 273.15 K is significantly lower than that of liquid water at 277 K, a volume expansion, which may be as high as 8 to 20 % depending on the temperature and the pressure [32], will proceed during the freezing of water. The freezing of water present within a porous material therefore may severely affect the structure of the material. Jallut et al. [4] have mentioned that the effect of the solidification of an impregnated liquid on the structure of a porous material caused thermoporometry to be a destructive analysis procedure.

To assess an effect of the freezing of water on the structure of porous silica, we measured several times consecutively the thermogram of the xerogel X9, which was dried at 393 K and subsequently treated for 23 h at 373 K. From the data of Tab. 1 it appears that freezing and thawing of water present within the pores of xerogel X9 does not significantly affect the pore volume. The first measurement led to a pore volume of 0.7 ml/g, while the fourth time heating measurement (after three times solidification of

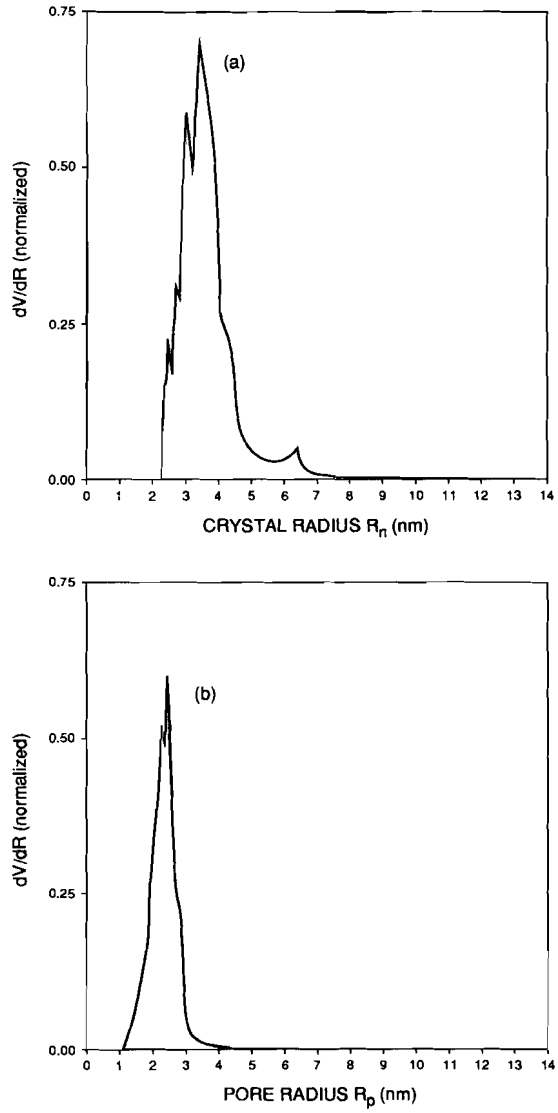

Figure 4 Crystal size distribution of standard xerogel X7 by thermoporometry (a), and the pore size distribution by N_2 adsorption, and desorption (b). The integral under curve (a) and (b), (Σ_i dV_n/dR_i * dR_i /V_n) is normalized on 1.

water) resulted in a pore volume of 0.6 ml/g. Apparently the structure of the xerogel of silica is sufficiently strong to withstand the mechanical pressure differences caused by the transport of freezing water. Cracking of the narrow pores present in the silica xerogel is unlikely. Investigating water present in polymer in an ultrafiltration membrane Cuperus et al., on the other hand, observed an increase in pore radius due to freezing and thawing. Cracking of pores seems to proceed within wide pores that are in contact with narrow pores. Ice extruded from the narrow pores into the wide pores that are cracked.

Comparison with mercury porosimetry and nitrogen sorption

The research described in this chapter is aimed at the effect of drying and thermal treatment on the porous structure of silica. Nevertheless it is interesting to compare the pore radii and pore volumes as determined by thermoporometry with the values resulting from mercury porosimetry and nitrogen desorption.

Using Eqn. 32 the ice crystal size distribution of sample X7, the xerogel which is obtained by drying H2 at 393 K, has been calculated from a thermogram measured on the sample. The resulting ice crystal size distribution, R_n, is represented in Fig. 4a. The pore size distribution, R_p, has also been determined from the desorption of nitrogen. The distribution is shown in Fig. 4b. The shape of both distributions is remarkably similar. However, the mean pore radius as determined from the thermogram, viz., 3.5 nm, is slightly larger than the mean pore radius calculated from the desorption of nitrogen, viz., 2.3 nm. The mean value of the thermoporometric pore radius is thus higher than the mean value calculated from nitrogen desorption in spite of the presence of the non-freezing layer of water. The smaller value of the nitrogen pore radius is attributed to the presence of spherical pores, which is indicated by the pore shape factor of 1.5. The nitrogen desorption is determined by the neck radius of the pores, which is smaller than the dimension measured by thermoporometry.

In Fig. 5 the other mean pore radii as resulting from mercury porosimetry and nitrogen desorption have been plotted as a function of the pore radius resulting from thermoporometry. It can be seen that now the agreement is remarkably good. The pore radii determined by mercury intrusion are about 2 nm smaller than the radii calculated by thermoporometry.

The values determined thermoporometrically being equal or even larger than those measured by mercury penetration and nitrogen desorption is unexpected, as mentioned above. The presence of a layer of non-freezing water suggests the pore radii determined by thermoporometry to be smaller than those measured by nitrogen desorption or mercury intrusion. With ink bottles pores, however, desorption of nitrogen and penetration of mercury is dominated by the relatively small entrance of the pores. With thermoporometry the diameter of the spherical pore itself and not that of the entrance is measured (Fig. 1). We therefore attribute the results of Fig. 5 to the presence of spherical pores in the hydrogels.

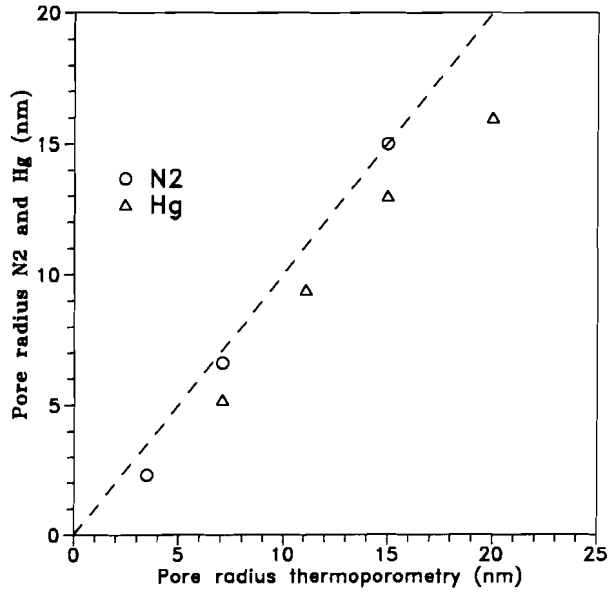

Figure 5

Pore radii, R_p, of nitrogen sorption and mercury penetration plotted against the radii, R_n, obtained by thermoporometry.

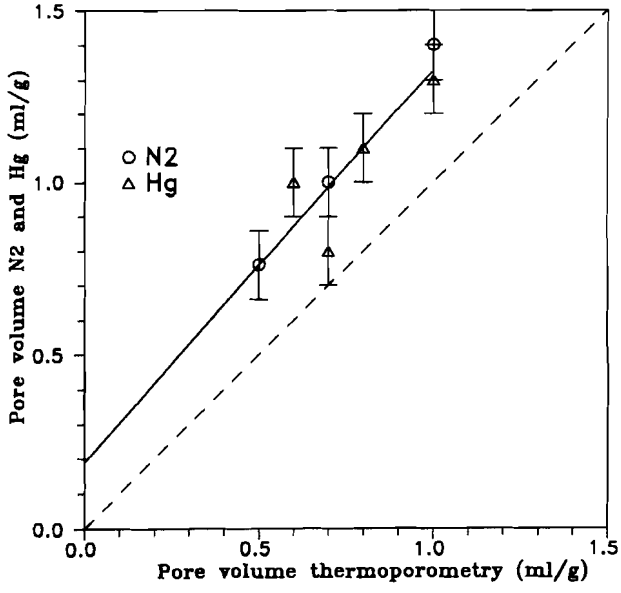

Figure 6

The pore volume, V_p, of nitrogen sorption and mercury penetration plotted against the ice-pore volume, V_n, obtained by thermoporometry.

The values for the pore volume are plotted in Fig. 6. The pore volume determined by thermoporometry, V_n, appears to be consistently about 0.2-0.3 ml/g lower than the volumes measured by mercury penetration and nitrogen sorption. It is obvious to attribute the lower value measured by thermoporometry to the non-freezing layer of water. The surface area calculated from the surface of the ice crystallites, A_n, is (22 ± 6) m^2/g higher than the BET surface area (Tab. 3). The presence of micropores in the hydrogel H2 is evident from the fact that the BET surface area is much larger than the surface area calculated from the thermoporometrically determined pore radius and pore volume. The mean pore radius calculated from the BET surface area and the pore volume determined by nitrogen sorption is 3.3 nm. The difference with the experimentally determined pore radius of 2.3 nm again indicates the presence of narrow pores in the hydrogel H2.

Table 3 BET surface areas compared with surface areas determined thermoporometrically.

Sample	X9	H2	H3	H5
BET surface area (m^2/g)	156	455	218	123
Therm. surface area A_n (m^2/g)	172	286*	246	145

*) assumption of a cylindrical pore shape

A pore radius which is equal with thermoporometry, mercury penetration, and nitrogen desorption, and a pore volume, which is smaller with thermoporometry, suggests the surface area calculated from thermoporometric data to be smaller. However, the thermoporometric surface areas are consistently larger than the BET surface areas.

Effect of thermally ageing and subsequent drying and on the porous structure of hydrogels

The effect of ageing hydrogels at room temperatures and hydrothermally at higher temperatures can be studied readily by thermoporometry. As indicated by the data of Tab. 1, the value of R_n which is indicative for the pore radius, R_p, of the hydrogel increased and the value of V_n, indicative for the pore volume, V_p, slightly decreased during ageing in the solution at room temperature. The surface area consequently dropped by 32 %. Gelling at 383 K led to a higher ice-pore radius, viz., 8.6 nm, a higher ice-pore volume, viz., 0.9 ml/g, and a higher ice-surface area, viz., 240 m^2/g, than observed for the gel aged

in water at room temperature. Thermally treating for 2 hours at 473 K does not strongly decreased the pore volume, but raised the pore radius to 19 nm. Finally treating the hydrogel for 7 or 24 hours at 473 K led to a pore radius of 27 nm, and a surface area of 115 m^2/g.

Drying the aged silica gel severely affected the pore radius and the pore volume. The pore volume dropped by 30 to 44 % in accordance with values reported in the literature [3]. The decrease of the pore volume does not depend on the thermal pretreatment. The decrease of the pore radius of the gel treated at 393 K is no less than 59 %. The gel thermally treated at higher temperatures showed a drop in pore radius of 26 to 40 %. The compressing action of the meniscus travelling through the gel causes the pore volume and the mean pore radius to drop considerably, without bringing about a loss in surface area. The surface area even rises during drying. Fig. 7 shows the effect of drying on the mean pore radius. The experimental points representing the mean pore radii after drying are situated appreciably below the dashed straight line which corresponds to no shrinkage at all.

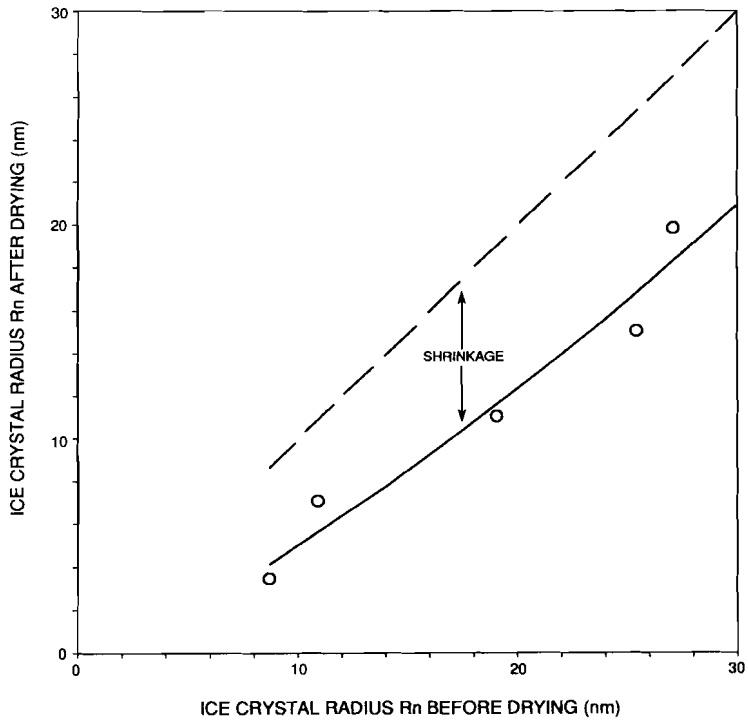

Figure 7 Shrinkage of hydrothermally aged hydrogels with drying measured by thermoporometry. The dashed line represents no shrinkage. The solid line represents the crystal radius before drying, R_n, is drawn against the R_n of dried, and with water impregnated spheres.

The increase in surface area A_n during drying (Tab. 2a-b) is in sharp contrast to the behaviour of two-step acid-base alcogels during drying. It has been reported [33] that the alcogel loose about 50 % of the surface area on drying.

An increase of the ice-pore volume, V_n, of the hydrogels with ageing, resulting in larger ice-pore radii, R_n, is visible in Tab. 2a. The ice-pore volume increases from 0.9 to 1.4 ml/g, while the ice-pore radius increases from 8.6 to 27 nm. An increase of the pore volume with ageing before drying should be visible as an increase of the pore volume of the hydrogels after drying. In Fig. 8, the pore volume V_p of aged and dried hydrogel spheres is drawn against the pore radius R_p by Hg penetration. The samples with different ageing conditions are those of Chapter 3. The pore radius R_p increases with intensity of treatment. It appears that the value of V_p of the hydrogel spheres increases with R_p. The increase of the pore volume of the dried gels is not only due to the reinforcement of the gel structure by ageing [3], but also due to repelling forces amongst the silica sol particle with ageing.

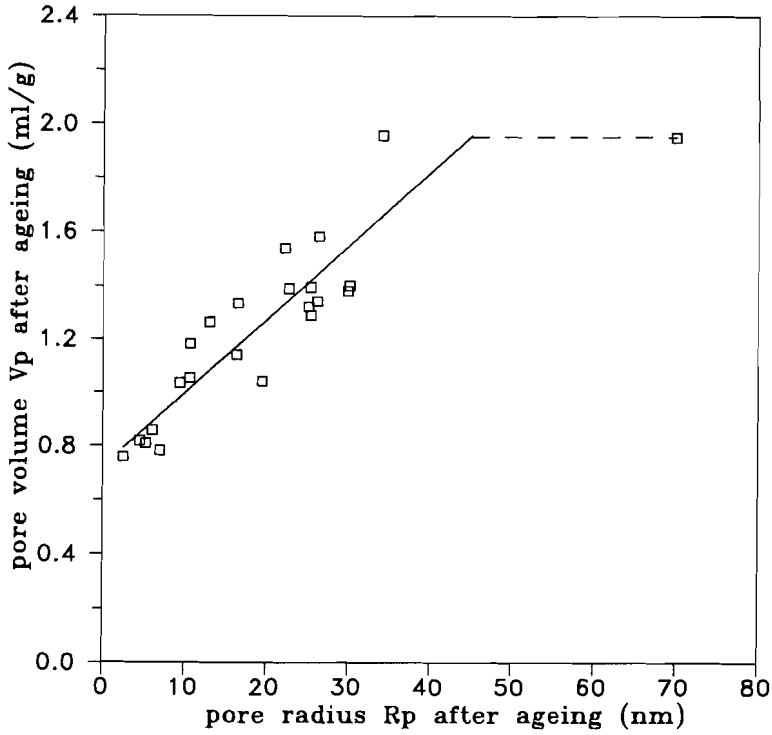

Figure 8 Pore volume V_p of hydrothermally aged hydrogel spheres against the pore radius R_p after drying with Hg penetration.

The fractal nature of silica hydrogels

The silica particles of the hydrogel is believed to have a fractal structure. A fractal structure of the silica sol particles could be demonstrated by a fractal pore size distribution. Recently, the fractal nature of carbon blacks, dispersed in water is investigated by Ehrburger-Dolle and coworkers [34]. The mass fractal of a silica gel is obtained by measuring the mass included by an exponential increasing volume block with the dimension $(l^3)^n = l^{3n}$, where l is the ruler (m), and n an integer 1,2,..,∞. The mass M (in g) is a function of l by ; $M \sim l^{nd}$. In the increasing volume l^{3n} a repetition of the structure is seen. If the volume contains a rod ($M \sim l$), plate ($M \sim l^2$), or body ($M \sim l^3$) with uniform density D, the dimensions d are 1,2, and 3, respectively, and not fractal. The fractal dimension of a gel with not uniform density varies as a real between 1 and 3. The density D is expressed by :

$$D = M/V \sim l^{nd}/l^{n3} \sim l^{n(d-3)} \quad \text{(g/ml)} \qquad (59)$$

, and the pore volume V_p ($R_p = l^n$) :

$$V_p \sim 1/D \sim l^{n(3-d)} \sim R_p^{(3-d)} \quad \text{(ml/g)} \qquad (60)$$

, and :

$$-dV_n/dR_i \sim R_{n,i}^{2-d} \quad \text{(ml/g*nm)} \qquad (61)$$

where dV_n/dR_i is obtained from Eqn. 51 and $R_{n,i}$ from Eqn. 32. From the right side of the distribution curve, the fractal dimension can be obtained by the slope of the $-\log(dV_n/dR_n)$ against the $\log R_n$ plot, which is 2-d (Eqn. 61) at least if $d > 2$, which is not the case of linear aggregates of carbon blacks in work of Ehrburger-Dolle et al. [34]. The fractal dimension ($d < 2$) is obtained in a more laborious manner from the left side of the distribution curve using Eqn. 60 :

$$(V_n^i - V_{n,min}^i)/(V_{n,max}^i - V_n^i) \sim [(R_n - R_{min})/(R_{max} - R_n)]^{3-d} \qquad (62)$$

R_{min} denotes the left onset radius of the distribution curve, and R_{max} the radius at the

maximum of the crystal size distribution curve ; $dV_n/dR_i = max$, and V_n^i is integration of the ice volume from the minimum radius R_{min} ;

$$(V_n^i - V_{n,min}^i) = {}_{Rmin}\int^{R} dV_n/dR * dR_n \qquad (63)$$

However, in ref. [34], the pore volume V_n is integrated from the maximum of the crystal size distribution ;

$$(V_n - V_{n,min}) = {}_{R}\int^{Rmax} dV_n/dR * dR_n \qquad (64)$$

where $(V_n - V_{n,min}) = 0$ at $R_n = R_{max}$, and ;

$$(V_{n,max} - V_n) = {}_{Rmin}\int^{R} dV_n/dR * dR_n \qquad (65)$$

,thus ;

$$(V_n^i - V_{n,min}^i)/(V_{n,max}^i - V_n^i) = (V_{n,max} - V_n)/(V_n - V_{n,min}) \qquad (66)$$

, and Eqn. 62 can be rewritten to ;

$$(V_n - V_{n,min})/(V_{n,max} - V_n) \sim [(R_n - R_{min})/(R_{max} - R_n)]^{d-3} \qquad (67)$$

The slope of the $\log(V_n - V_{n,min})/(V_{n,max} - V_n)$ against the $\log(R_n - R_{min})/(R_{max} - R_n)$ plot should deliver the fractal dimension d by (d-3). Since $R_p = l^n$, very broad pore size distributions are expected with fractal structures. The pore size distribution curves of our gels are very small and uniform. The fractal nature of our silica hydrogels does at least not show up in a fractal pore size distribution.

CONCLUSIONS

1) Thermoporometry offers the possibility to investigate the shrinkage processes with drying of wet hydrothermally aged silica spheres.

2) When the technique is performed on a Setaram DSC 111, the cooling and heating rates should have the smallest practical values of +1 and -1 K/h, at least on a Setaram DSC 111. However, when thermoporometry is applied on a Netszch 43 DSC and model 200 data station, it is possible to work at much higher cooling and heating rates, 60 K/h. Obviously, the Netszch DSC, which is far less sensitive, has no heat transport problems.

3) Serious cracking of the pores by applying thermoporometry is not evidenced. Probably, the non-freezing layer t receives the expansion of ice by extrudation.

4) Silica hydrogel, prepared by the sol-gel technique, and stored at room temperatures, is only slightly affected by ageing. In contrast, ageing at high temperatures, causes an increase of the pore volume and pore radius of the hydrogel. With thermoporometry it appears that the increase already proceed before drying.

ACKNOWLEDGMENTS

The authors thank J.J. van Beek for his critical review of the article.

REFERENCES

1. A.E. Afanasèev, and A.N. Boltushkin, *Coll. J. USSR*, **49** (1987) 1043
2. T. Kawaguchi, J. Iura, N. Taneda, H. Hishikura, and Y. Kokubu, *J. Non Cryst. Sol.*, **82** (1986) 50
3. L.L. Hench, and J.K. West, *Chem. Rev.*, **1990** (90) 33
4. C. Jallut, J. Lenoir, C.Bardot, and C. Eyraud, J. Membran. Sci, **68** (1992) 271
5. C.J. Jackson, and G.B. McKenna, ASC Polymer Preprints, **32** (1992) 439
6. I. Higuti, and Y. Iwagami, *J. Phys. Chem.*, **56** (1952) 921
7. J.F. Quinson, M. Astier, and M. Brun, *Applied Catalysis*, **30** (1987) 123
8. M. Brun, A. Lallemand, J.F. Quinson, and C. Eyraud, *Thermochimica Acta*, **21** (1978) 59
9. Handbook of Chemistry and Physics, 56th ed., Ed. R.C. Weast, CRC Press,

Cleveland (1975)
10. S. Takagi, *J. of Coll. Interf. Sci.*, **137** (1990) 446
11. F. Ehrburger, V. Querin, J. Lahaye, *Colloids and Surfaces*, **14** (1985) 31
12. I.V. Yazyna, V.I. Kvlividze, and A.V. Krasnushkin, *Coll. J. USSR*, **49** (1987) 1188
13. T. Sakamoto, H. Nakamura, H. Uedaira, and A. Wada, *J. Phys. Chem.*, **93** (1989) 357
14. M. Tasaka, S. Suzuki, Y. Ogawa, and M. Kamaya, *J. of Membr. Sci.*, **38** (1988) 175
15. I.V. Dedyulya, and N.V. Churaev, *Coll. J. USSR*, **50** (1988) 204
16. P.J. Davis, C.J. Brinker, and D.M. Smith, J. Non-Cryst. Sol., **142** (1992) 189
17. C.A. Angell, M. Oguni, and W.J. Slichina, *J. Phys. Chem.*, **86** (1982) 998
18. M. Brun, A. Lallemand, J.F. Quinson, and C. Eyraud, *J. Chim. Phys. (France)*, **70** (1973) 973-978, 979-989, 990-996
19. G.B. Alexander, *J. Phys. Chem.*, **61** (1957) 1563
20. A.C. Makrides, M. Turner, and J. Slaughter, *J. Coll. Interf. Sci.*, **73** (1980) 345
21. L.G. Homshaw, *J. Coll. Interf. Sci.*, **84** (1981) 127, 141
22. J.F. Quinson, J. Dumas, J. Serughetti, *J. Non. Cryst. Sol.*, **79** (1986) 397
23. S.S. Kistler, *J. Phys. Chem.*, **36** (1932) 475
24. C.J.G. van der Grift, H. Barten, J.C. van Miltenburg et al., in 'Characterization of Porous Solids', Ed. K.K. Unger et al., Elsevier, Amsterdam (1988), 619
25. P. Tang, D.E. Colflesh, B. Chu, *J. Coll. Interf. Sci.*, **126** (1988) 304
26. R. Snel, *Applied Catalysis*, **11** (1984) 271
27. R. Snel, *Applied Catalysis*, **12** (1984) 189
28. R. Snel, *Applied Catalysis*, **12** (1984) 347
29. M. Pauthe, J.F. Quinson, H. Hdach, T. Wignier, J. Phalippou, and G.W. Scherer, J. Non-Crystal. Sol., **130** (1991) 1
30. F.M. Etzler, *Langmuir*, **4** (1988) 878
31. D.H. Everett, *J. Chem. Soc., Faraday Trans.*, **57** (1961) 1541
32. F.P. Cuperus, D. Bargeman, and C.A. Smolders, J. Membran. Sci., **66** (1992) 45
33. P.J. Davis, C.J. Brinker, D.M. Smith, and R.A. Assink, J. Non-Crystal. Sol., **142** (1992) 197
34. F. Ehrburger-Dolle, S. Misono, and J. Lahaye, J. Coll. Interf. Sci, **135** (1990) 468

Chapter 6

Control of the porous structure of silica gel by the preparation pH and drying*

M.K. Titulaer, M.J. den Exter[1], H. Talsma[2], J.B.H. Jansen, and J.W. Geus[1]

Department of Geochemistry, Institute for Earth Sciences, University of Utrecht, Budapestlaan 4, P.O. Box 80.021, 3508 TA Utrecht, The Netherlands
[1]Department of Inorganic Chemistry, University of Utrecht, Sorbonnelaan 16, P.O. Box 80.082, 3508 TB Utrecht, The Netherlands
[2]Department of Pharmaceutics, University of Utrecht, Sorbonnelaan 16, P.O. Box 80.083, 3508 TB Utrecht, The Netherlands

*This paper is a contribution of the Debye Institute, University of Utrecht, The Netherlands.

ABSTRACT

The decrease of pore dimensions with drying of silica gels as a function of the preparation pH is investigated. The gels of 8.2 wt% SiO_2 in water are precipitated between a pH of 1 and 10 in a computerized static pH equipment. The shrinkage is exclusively monitored by thermoporometry, which is applied to the wet as well to the dried gels. The dried gels are characterized with four traditional techniques : transmission electron microscopy, nitrogen sorption at 77 K, mercury penetration, and a Sears titration. The fixed pH influences the polymerization rate of silicate anions, and therefore the size and branching of the sol particles in the gel. At a low static pH of 1 to 2, very small but highly branched sol particles of 2 to 3 nm diameter are developed in the gel with an extreme microporosity. It is established that each sol particle is surrounded by approximately eleven others. With thermoporometry it is determined that particle aggregation behaves as hydrogel. Shrinkage proceeds with drying, and no pores can be measured by thermoporometry. The pore radius R_p decreases from 3.1 nm to a value below 3.1 nm, and the specific pore volume from 0.4 ml/g to about 0.13 ml/g. At a high static preparation pH above 4, less branched and platy sol particles are formed with sizes up to 26 nm at a pH of 10. Before drying, the aggregates are highly porous and the pores to large to be determined by thermoporometry. At a pH of 4 and 5, excessive shrinkage

proceeds, and the pore radii R_p decrease to 2.8 and 6.8 nm, and the pore volumes to 0.8 and 0.9 ml/g, respectively. The mercury pore volume of the dried gels with a maximum of 2.8 ml/g is essentially larger than both the thermoporometry and nitrogen pore volume, which is explained by macro-pores, not being measured with latter techniques. The gels measured with thermoporometry, mercury penetration and nitrogen adsorption exhibit a maximum in pore volume between a pH of 4 and 8. The silica sol particles in the gel grow larger and repel each other at high pH. Finally, at very high pH above 8, the gel weakens and suffers more from the capillary forces with drying, due to the decreasing amount interparticle bonds.

INTRODUCTION

Silica gel is widely applied as a filler, a paint thickener, a filter, a catalyst carrier, or as a clay- or zeolite precursor. Because reactions proceed at the silica surface in water, the amount of surface area is very important. Besides, the pore size and pore volume of the gel influence the processes of diffusion of the reactant to the silica surface. Undesired shrinkage by the decrease in pore size and pore volume has to be minimized with drying. Usually, silica gels prepared by the addition of sodium silicate to a strong acid (nitric acid). A sodium silicate solution (water glass) is prepared from heated quartz and soda, and subsequently dissolved in water. Subsequent drying of the wet gel (hydrogel) consisting of silica sol particles leads to a dried gel (xerogel). Disadvantage is the fact that the size of the silica sol particles, the branching of the sol, and pore volume of the silica gel, can not be desirably varied, because the point of gelling is always attained by quickly raising the pH from a very low value. The knowledge of the effects of sol particle size and branching as controlled by the preparation pH on the amount shrinkage of the gel is therefore limited [1].

A method to evaluate these effects is developed by the preparation of gels at a static pH. A new pH-static method of gel preparation is introduced in this paper. The preparation is deviating from the method in ref. [1], where different amounts of acid and sodium silicate of high pH are rapidly mixed to obtain the desired pH. Firstly, the composition of the starting silica sodium silicate solution is investigated with ^{29}Si-NMR. The pore size, pore volume, specific surface area, and pore shape of the desired hydrogels is explored by thermoporometry. The shrinkage with drying of the hydrogels is monitored. Thermoporometry is applied on the hydrogels as well as on the xerogels. The xerogels are examined with five techniques, thermoporometry, transmission electron microscopy (TEM), Hg penetration, N_2 sorption at 77 K, and a Sears titration.

MATERIALS AND METHODS

^{29}Si NMR spectroscopy

The chemical surroundings of the ^{29}Si isotopes in the various polymers of the starting sodium silicate solution are investigated by ^{29}Si Nuclear Magnetic Resonance (NMR). A high silicium concentration of 0.5 to 1.5 M is required [2] even at the low temperature of -13°C [3,4], and mostly a long measuring time of 2 to 4 h must be used in order to obtain an accurate signal, even with an enriched ^{29}Si solution of 95 mole% [2]. In Tab. 1 the specific chemical shifts in ppm of the NMR resonance peaks are listed relative to the peak of tetra methyl silane (TMS). The listed values of the literature [5,6] are used as a reference for the experimental determined values of our solution.

An amount of 400 ml Merck sodium silicate solution (Art. 5621, 6.85 M Si, 3.91 M Na) is diluted with 1600 ml demineralized water to a concentration of 1.37 M Si, 0.98 M Na and a pH of 11.3. The chemical shifts of the polysilicate anions expressed in ppm are measured relative to the resonance frequency of TMS on a Bruker WP 200 WB equipment, with the following specifications : a magnetfield of 4.69 Tesla: a radio frequency of 39.76 MHz: and a frequency band of 5 kHz, which is about 125 ppm. The pulse angle with the magnetfield is 45° and the duration of the pulse is 0.82 μs. The scan delay is 16 s. The spectrum is recorded with 512 scans and takes about nine quarters of an hour.

Manufacture of pH-static silica gels

The molar ratio of SiO_2/Na_2O of the starting sodium silicate solution is 3.5/1. The [Si] is 6.85 M and the [Na] is 3.91 M. The solution contains various silicium polymers and mono silicic acid (MSA). The sodium silicate solution is slowly injected into a dilute nitric acid solution, which is kept at a constant pH level by simultaneously injection of nitric acid. To investigate the effect of the pH of the solution, the pH is kept at 1,2,4,5,8,9, and 10.

Fig. 1 shows schematically the equipment for the synthesis of the various pH-statically prepared silica gels. A double walled and water cooled vessel of 3.5 l contains an initial amount of 1925 ml demineralized water of 293 K. A concentrated sodium silicate solution (Merck 5621, 6.85 M Si and 3.91 M Na) is injected into the water at a rate of 0.5 ml/min by a peristaltic pump (Gilson Minipuls 3, U.S.A.) over a period of 21 to 23 h.

The rate of the second peristaltic pump, which adds 3.2 M (18.5 wt%) nitric acid to the solution, is controlled by a microcomputer (Apple 2 Europlus, U.S.A.). The pH difference between the given set point, pH_{sp}, and the actual measured pH_i regulates the rate of addition. The measured pH_i is initially slightly higher than the set-point pH_{sp}.

Table 1 Chemical shift of ^{29}Si in polymeric species relative to TMS, according to ref. [5,6].

chemical shift (ppm)		literature MR 3/1[1]	literature pH 11.4	our solution	ratio Si(%)
monomer	Q_1^0	-71.1	-73.2	-73.9	0.3
dimer	Q_2^1	-79.3	-81.3	-82.15	3.2
linear trimer	$Q_2^1Q_1^2$				
cyclic trimer	Q_{3c}^2	-	-83.5	-	-
cyclic polymers and chain middle groups	Q_n^2	-87.6	-89.9	-90.45	27.2
prismatic tricyclic hexamer	Q_6^3	-	-92.3	-	-
branched polymers and cubic octamer	Q_n^3	-96.3	-99.2	-99.16	42.8
tridimensional linked groups	Q_n^4	-	-109.8	-107.97	26.3

1) MR = Molar ratio of SiO_2/Na_2O.

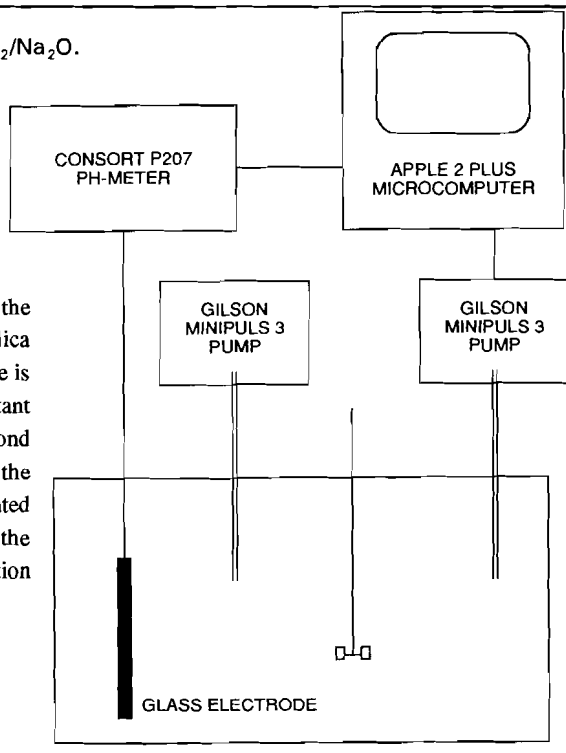

Figure 1

The equipment used for the preparation of pH-static silica gels. An amount sodium silicate is added by pump 1 with a constant rate of 0.5 ml/min. A second pump 2 is controlled by the computer and adds concentrated nitric acid in such a way, that the pH is constant during the addition of sodium silicate.

Eqn. 1 gives the rotation rate of the acid pump (RPM_i) as a function of the pH difference, pH_i-pH_{sp}, relating a proportional constant P (min^{-1}) and an integral constant I (min^{-1}). Both P and I are previously stored in the computer (Tab. 2). The measuring interval of pH_i in the program is 3 s.

$$RPM_i = P * (pH_i\text{-}pH_{sp}) + I * \Sigma_1^i (pH_i\text{-}pH_{sp}) \qquad (min^{-1}) \qquad (1)$$

with $0 < RPM_i < 47.9\ min^{-1}$, where RPM_i is expressed in min^{-1}, and Σ_1^i is the sum from measuring point 1 to i. The rate of addition, v_i, of the 3.2 M HNO_3 solution is a function of RPM_i by :

$$v_i = 0.16 * RPM_i + 0.05 \qquad (ml/min) \qquad (2)$$

with $0 < v_i < 7.7$ ml/min. At every measuring point i the rate of the acid addition is adjusted. The control system keeps the pH within 0.01 pH unity of the set-point. The set-point pH_{sp}, the total amount of sodium silicate added, and the nitric acid solution are listed in Tab. 2. The final silica concentration in the gel suspensions is about 1.37 M Si (7.9 wt% SiO_2).

The pH_i is measured with a microcomputer pH-meter (Consort P207, Belgium). The configuration of the RS-232 interface between the computer and the pH-meter is shown in Fig. 2a. Fig. 2b shows schematically the configuration of the RS-232 interface between the computer and the nitric acid pump. The pH-measuring and pump control program is written in Applesoft BASIC, and a small part, reading in the pH_i, in Big Mac Assembler language.

Thermoporometry of hydrogels

The pores of the gels are measured with thermoporometry, which is based on the freezing point depression of water. The depression of the freezing point and thermal energy released or absorbed is measured as a heat-flux with a differential scanning calorimeter (DSC) [7]. The ice-crystal radius R_n (nm) in a pore is inversely proportional to the freezing point depression dT_s (K) (Eqn. 3) [7]. The freezing point depression dT_s is the freezing temperature T_s subtracted from the normal freezing temperature T_o at 273.15 K, (T_s-T_o), which has a negative sign.

$$R_n = -64.67/dT_s\text{-}0.23 \qquad (nm) \qquad (3)$$

Table 2 Preparation conditions of the silica gels in the static pH equipment, with the set point pH_{sp}, the final amounts of the sodium silicate and nitric acid in 1925 ml HNO_3, and the proportional and integral constants to keep the pH at the desired level, pH_{sp}.

pH_{sp}	P[1] (min^{-1})	I[2] (min^{-1})	6.85 M Si[3] (ml)	3.2 M HNO_3[4] (ml)
1	20	0.2	680	835
2	20	0.2	635	710
4	5	0.05	635	675
5	5	0.05	635	705
6	20	0.2	661	737
8	20	0.2	625	630
9	20	0.2	690	645
10	20	0.2	655	562

sp = set point, 1) P = proportional constant, 2) I = integral constant, 3) ml added sodium silicate solution, 4) ml HNO_3 solution injected into initially 1925 ml H_2O

The specific pore volume V_n is expressed as the volume of water frozen within the pores per unit weight of dry silica. The specific pore volume V_n is calculated according to Eqn. 4, where W is the weight of the dry silica.

$$V_n = \Sigma_i P_i * (T_{i+1}-T_i) / (D_i*H_i*W*sr) \quad \text{(ml/g)} \quad (4)$$

where $\Sigma_i P_i$ is the integral of the heat-flux during freezing of the water of every sample point i (J/s), $T_{i+1}-T_i$ the temperature interval (K), D_i the density of water (about 1 g/ml), H_i the solidification enthalpy of 332 J/g, W the weight of silica (g), and sr the scan rate (K/s). Eqn. 4 accounts for the effect of the temperature on the solidification enthalpy.

The pore shape factor F provides information about the shape of the pore, and varies between 1 for spherical and 2 for cylindrical pores. The value of F is the ratio of dT_s, T_s-273.15, of the freezing plot, and dT_f , T_f-273.15, of the melting plot according to Eqn. 5 :

$$F = dT_s/dT_f \quad (5)$$

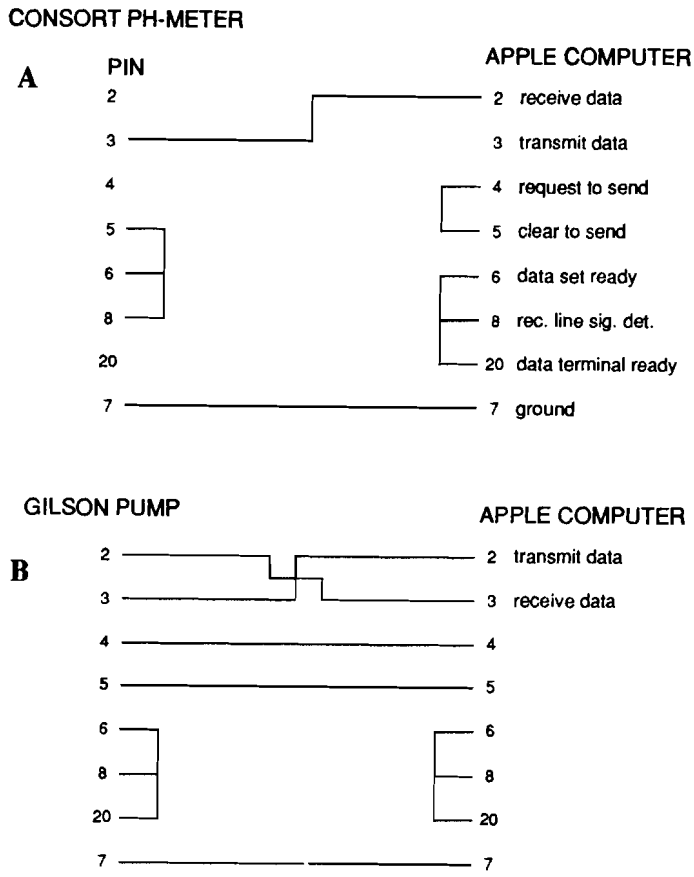

Figure 2 Configuration of the RS-232 interfaces, (a) between the computer and the pH-meter. The display of the pH-meter, represented as XX.XX pH is send one X after another to the Apple 2 Europlus computer in ASCII-codes by the RS-232 interface in slot 2 of the computer. The clock rate of the RS-232 card is 16 times the baud rate. The data are send a-synchronous, in a 8 bit format, no parity and 2 stop bits with a baud rate of 2400 s^{-1}. (b) between the pH-meter and the nitric acid pump 2. The communication between the microcomputer and the Gilson pump is provided by the RS-232 interface in slot 3 of the computer. The clock rate of the RS-232 card is 16 times the baud rate. A model 605 RS-232 adapter provides the interface between the RS-232 computer output and the Gilson Serial Input/Output Channel (GSIOC). In remote control the display of the Gilson pump, represented as XX.XX RPM respectively, is send one X after another by the computer in ASCII codes, asynchronous in a 8 bit format, even parity, 1 stop bit, with a baud rate of 9600 s^{-1}.

Finally, the surface area A_n (in m^2/g) of the ice-crystal in the gel is calculated according to Eqn. 6 :

$$A_n = 10^3 * (1+(2/F)) * V_n / R_n \qquad (m^2/g) \qquad (6)$$

A non-freezing layer of 0.9 nm thickness at the silica-water interface requires a correction of R_n, V_n, and A_n to calculate the real pore radius R_p, pore volume V_n^*, and surface area A_n^*, respectively [7].

The hydrogels (32 mg), which contain 28 mg water and 4 mg SiO_2, are brought in an aluminum sample cup. Subsequently, the heat-flux of freezing of water and, subsequently, of fusion of ice is measured as a function of the temperature with a Netzsch DSC model 43 measuring cell attached to 200 data station. The following measuring sequence is applied : (1) a cooling step from 293 to 213 K at a rate of -2 K/min, (2) a heating step from 213 to 268 K at a rate of 1 K/min, measuring the fusion peak of pore ice , (3) a cooling step from 268 to 213 K at a rate of -1 K/min, measuring the solidification peak of pore water, and, finally, (4) a heating step from 213 to 293 K at a rate of 1 K/min, measuring both pore and bulk ice.

Xerogels characterized with thermoporometry, TEM, Hg-penetration, and BET surface area

An amount of 14 mg of the xerogel is added to 37 mg water and examined with thermoporometry. For TEM investigation, the gels prepared at a pH_{sp} of 4 to 10 are filtrated on a Büchner funnel, washed twice with demineralized water, and dried at 393 K. The gels prepared at a pH_{sp} of 1 and 2 are washed, filtrated and dried after two days of gelling. A suspension of the dried gels in ethanol is prepared by ultrasonic treatment. A droplet of the suspension is brought upon a holey carbon film applied on a copper specimen grid and examined within a Philips EM 420 transmission electron microscope (TEM), operated at 100 kV.

Hg penetration is measured on 0.1 to 1.0 g of the samples in a Porosimeter 2000 (Carlo Erba) with a dilatometer volume of 16 ml. Hg (density 13.5 g/ml) is intruded into the sample with a maximum pressure of 2000 hPa.

N_2 is sorbed by about 0.25 g of the dried samples at 77 K within a Sorptomatic 1800 equipment (Carlo Erba). The sample is outgassed for 6 h at 473 K in vacuum before measuring the BET surface area and the pore volume from the sorption isotherm [8].

Sears titration of the xerogels

The specific surface area of the xerogels is measured by titration of the surface silanols with a concentrated sodium hydroxide solution [9]. The number of surface silanols per unit surface area is assumed to be a function of the drying and calcination temperature, and not of the particle diameter in the gel. A constant ion strength during the titration is achieved by addition of extra NaCl. The silica solubility at high pH is decreased by the addition of NaCl. The titration is therefore suitable up to high pH levels of about 12 [10]. The titration is performed under N_2 atmosphere to avoid interference of carbondioxide.

An amount of 1.5 g of the dried silica gels is introduced into 150 ml 3 M NaCl. The well stirred suspension is brought at a pH of 2 with a few drops of 2 M HCl. An amount of 0.5 ml 0.112 M NaOH solution is stepwise added until a pH of 4 is reached. Subsequently, the suspension is titrated from the pH of 4 to the pH of 9. The amount of NaOH needed for titration of fumed silica (Aerosil 380, 376 m^2/g: Aerosil 200, 186 m^2/g: Aerosil OX50, 43 m^2/g) is given by Eqn. 7.

$$A_s = 31.1 * V - 41.9 \qquad (m^2/g) \qquad (7)$$

where A_s is the specific surface area (m^2/g), V the volume of added 0.112 M NaOH solution (ml). With Eqn. 7, the specific surface areas of the group gels prepared under pH-static conditions is determined. From the slope of Eqn. 7 it follows that 1.44 silanol groups per unit area (nm^2) are ionized at a pH of 9 (Eqn. 8), which represents 41% of the 3.5 nm^{-2} silanol groups ionized at a pH of 12 [10,11].

$$N_{OH} = (10^{-3}*0.112*6*10^{23})/(1.5*31.1*10^{18}) = 1.44 \quad (nm^{-2}) \qquad (8)$$

where N_{OH} the number ionized surface silanols at a pH of 9 (nm^{-2}).

RESULTS AND DISCUSSION

The initial sodium silicate solution

-Composition

The ^{29}Si NMR spectrum of the 1.37 M Si, 0.98 M Na solution of pH 11.3 is recorded in Fig. 3. The ^{29}Si-NMR spectrum demonstrates the chemical shift of the monomer Q^0 at -73.9 ppm, the dimer Q_2^1, and the linear trimer ($Q_2^1Q_1^2$) at -82.15 ppm, the chain middle group Q_n^2 at -90.45 ppm, the branched polymer Q_n^3 at -99.16 ppm, and the tetrahedrally coordinated Si Q^4 at -107.97 ppm (Tab. 1). The ratio of the signal surface integrals Q^0 : Q^1 : Q^2 : Q^3 : Q^4 is 0.3 : 3.2 : 27.4 : 42.8 : 26.3. Only a small amount of silica appears to be present as monomer Q_1^0, which is $4.1*10^{-3}$ M or 247 mg SiO_2/l.

Particles of a size of 2 nm are present in the initial sodium silicate solution [11] : the particles may control the sol particle size in the gels formed at low pH_{sp} of 1 and 2. The ^{29}Si signal at -107.97 ppm is partly attributed to the particles of 2 nm. The equilibrium silica solubility of the 2 nm particles is calculated with Eqn. 9 [12] :

$$\text{Log } (S/S_o) = 4\gamma * V_m/(2.303*R*T*d) = 0.86/d \qquad (9)$$

where S is the silica solubility of the particle (mg/l), S_o the silica solubility at a plane surface area of an infinitely large particle, which amounts to 115 mg SiO_2/l [13,14], γ the interfacial energy of 0.045 N/m, V_m the molar volume of $2.73*10^{-5}$ m^3/mole, R the gasconstant, 8.3 $J*mole^{-1}*K^{-1}$, T the temperature of 298 K, and d the diameter (in nm).

According to Eqn. 9, the equilibrium solubility of the 2 nm particles is only 310 mg SiO_2/l, which is close to the amount of monomer calculated from the Q_1^0 peak, which is 247 mg SiO_2/l. It will appear that the size of the silica particles present in the gels formed at low pH levels of 1 and 2 are of the same order of magnitude as that of the nuclei in the sodium silicate solution [15], viz., 2 to 3 nm.

Small oligomers of a size less than the diameter 2 nm of the silica sol particles are also present in the initial sodium silicate solution. Svensson et al. [6] and Hoebel et al. [16,17] have shown that cage-like polysilicate species dominate in sodium silicate solutions at molar ratios $SiO_2/Na_2O \geq 3.3$, and in tetra methyl ammonium silicate solutions (TMA_nSi) at high Si/TMA ratios. The distribution of Si over the different polysilicate species has been calculated in ref. [6] with the known ionization constants $\beta_{q,n}$, where the Q^1 peak is assigned to the dimer (n = 2), representing a mole fraction Si of $\alpha = 0.05$ of the polysilicate species, Q^2 assigned to the (cyclic) tetramer [18] (n = 4, $\alpha = 0.24$), Q^3 to the (cyclic) octamer (n = 8, $\alpha = 0.39$), and Q^4 partly to structured oligomers (n = 32, $\alpha = 0.19$) and partly to the amorphous sol particles of 2 to 3 nm ($\alpha = 0.13$).

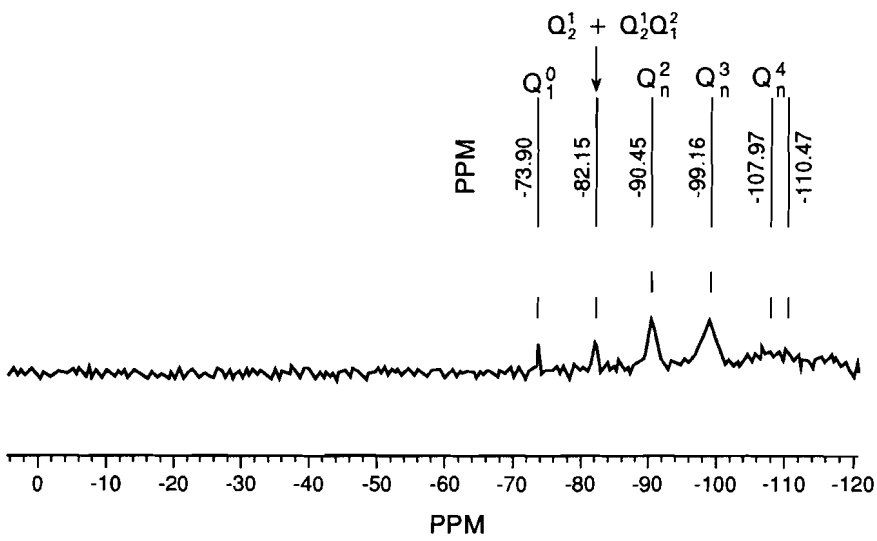

Figure 3 A ^{29}Si-NMR spectrum of the sodium silicate solution with a molar ratio SiO_2/Na_2O of 3.5/1 and a pH of 11.3. The concentration Si is equal to that of the prepared gels, which is 1.37 M Si.

-Charge on the polysilicate species

The average negative charge per Si on the monomer and oligomers, q(total), in the sodium silicate solution used is calculated from the relation :

$$[Na^+] - [OH^-] + q(total) * [Si^q] = 0 \qquad (10)$$

Eqn. 10 leads with the dissociation constant of water $k_w = -13.7$ to a q(total) of -0.7 in a 0.98 M Na solution [6]. The average negative charge per Si on the monomer q(mono) is calculated from the relation of Eqn. 11 and from the known ionization constants of MSA, $\beta_{1,1} = 3.5*10^{-10}$ mole/dm^3 and $\beta_{2,1} = 8.9*10^{-23}$ mole^2/dm^6, in the 0.98 M Na^+ solution [6,19].

$$q(mono) = \frac{-[Si(OH)_3O^-] - 2*[Si(OH)_2O^{2-}]}{[Si(OH)_4] + [Si(OH)_3O^-] + [Si(OH)_2O^{2-}]} =$$

$$\frac{-(\beta_{1,1}*[H^+]^{-1} + 2\beta_{2,1}*[H^+]^{-2})}{(1+\beta_{1,1}*[H^+]^{-1}+\beta_{2,1}*[H^+]^{-2})} = -1.03 \qquad (11)$$

A small fraction of the monomer is thus doubly ionized. Finally, the average charge per Si on the polymeric particles, q(poly), is calculated with Eqn. 12 :

$$q(poly)*([Si]-[Q_1^\circ]) + [Q_1^\circ]*q(mono) = [Si]*q(total) \qquad (12)$$

The q(poly) in our sodium silicate solution obtained from Eqn. 12 is -0.7, and hence equal to the q(total) calculated with Eqn. 10, due to the small amount of monomer present in the sodium silicate solution.

-Polymerization from monomers to silica sol particles.

The first step in silicic acid polymerization is the formation of a dimer Q_2^1, which is confirmed with ^{29}Si NMR [2] :

$$Q_1^\circ + OH^- \text{ --> } (Q_1^\circ)^- + H_2O \qquad (13)$$

$$(Q_1^\circ)^- + Q_1^\circ \text{ --> } (Q_2^1)^- + H_2O \qquad (14)$$

$$(Q_2^1)^- + H_2O \text{ --> } Q_2^1 + OH^- \qquad (15)$$

$$+$$

$$Q_1^\circ + Q_1^\circ \text{ --> } Q_2^1 + H_2O \qquad (16)$$

where Q_1° is the monomer, and $(Q_1^\circ)^-$ the ionized monomer. The ionization constant of the weak monosilicic acid Q°_1 is 9.8 [20]. Monosilicic acid is ionized for 50 % at a pH of 9.8. The polymerization rate is large when the concentration of $(Q_1^\circ)^-$ and Q_1° are reasonably high in the pH range 8 to 9 [20]. The equilibrium constant of reaction of Eqn. 16 : Q_2^1 / $(Q_1^\circ)^2$ is 10 $mole^{-1}dm^3$ [2]. The formation of a linear trimer ($Q_2^1Q_1^2$) is simultaneously with that of the dimer Q_2^1 [5] :

$$Q_2^1 + Q_1^\circ \text{ --> } (Q_2^1Q_1^2) \text{ --> } Q_{3c}^2 \text{ --> } Q_{nc}^2 \text{ --> } Q_n^3 \qquad (17)$$

The concentrations of the dimer and of the linear trimer decrease both with formation of the cyclic trimer Q_{3c}^2, the formation of which is immediately followed by that of the

multisilicate ring structures Q^2_{nc} and the branched structures Q^3_n with the double square ring silicate $Si_8O_{20}^{8-}$ [5,16]. The polymerization is described by the general Eqn. 18 :

$$nSi(OH)_4 \dashrightarrow (Si_nO_{3n+1-c}H_{2n+2-2c-q})^q + (n-1+c)*H_2O - qH^+ \qquad (18)$$

where n is the number of Si nuclei, c the number of ring closures, and q the negative charge on the polysilicate anion. The ionization constant $\beta_{-q,n}$ of the polymeric species is expressed by :

$$\beta_{-q,n} = [(Si_nO_{3n+1-c}H_{2n+2-2c-q})^q]*[H^+]^{-q}/[Si(OH)_4]^n \qquad (19)$$

The activation energy of polymerization is 61.1 kJ/mole [21]. At the low pH level of 2 the polymerization rate is second order in the monomer concentration (Eqn. 16) and first order in $[OH^-]$ (Eqn. 13). At the high pH level of 7.2 the rate is first order in the monomer, because the monomer is deposited on the surface of fast growing sol particles [21].

Large clusters of silica are formed in the final stages of the polymerization of silica. The final stages comprise the particle growth and the gelling the sol. An increase of the particle or cluster size is measured by an increase of the turbidity [14,20-24]. We have determined the size of the silica sol primaries and clusters after drying with transmission electron microscopy (TEM).

Transmission electron microscopy (TEM)

Representative electronmicrographs of the xerogels obtained after drying of hydrogels prepared at different pH levels are represented in Fig. 4a to 4g. The micrographs of the xerogels show that the primary sol particle size strongly depends on the pH_{sp} It can be seen in Fig. 4a that the diameter of the sol particles produced at a low pH_{sp} of 1 or 2 is only 2 to 3 nm. Apparently the solubility of silica at pH levels of 1 to 2 is small, which results in stable silica particles of a very small size. Above a pH level of 2 the size of the elementary silica particles increases ; sol particles of a size of 5 to 8 nm result on preparation of the hydrogel at a pH_{sp} of 4 and 5. Xerogels obtained from hydrogels prepared at a pH_{sp} level of 9 contain large particles, exhibiting a plate-like shape and less branched than the particles present in xerogels from hydrogels prepared at lower pH_{sp} levels. The size of the elementary particles is no less than 21 to 26 nm.

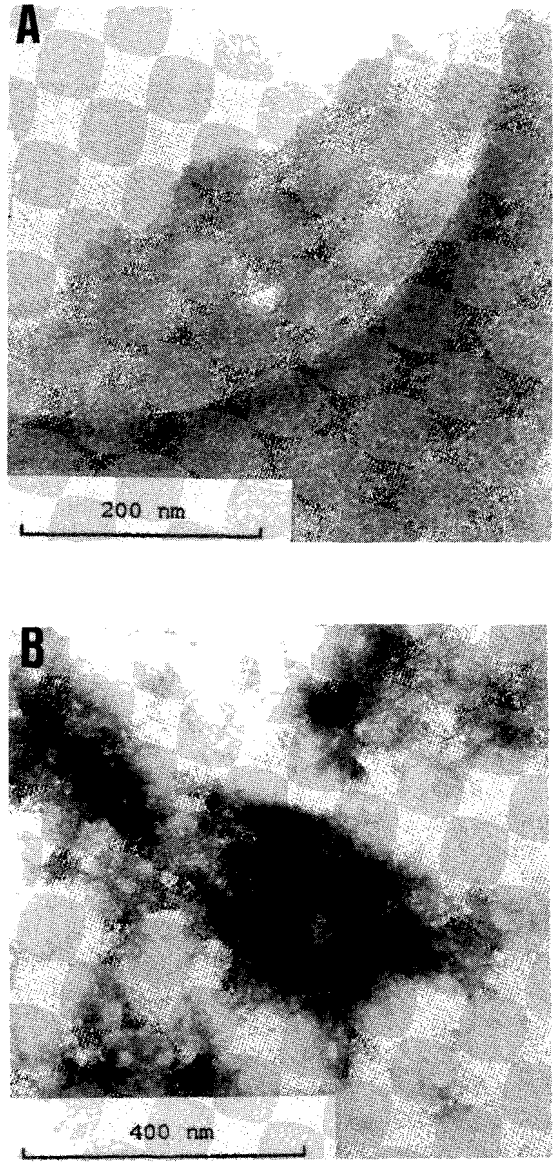

Figure 4 TEM images of silica gels, prepared at different static pH levels, (a) pH=1, magnification to the film 54000 times, (b) pH=2, 32000 times.

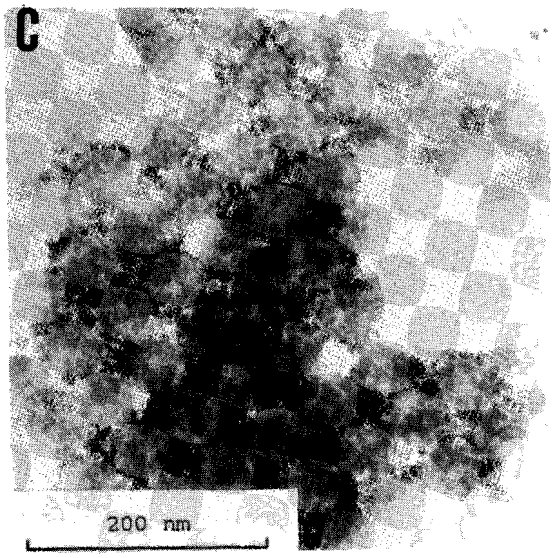

pH = 4

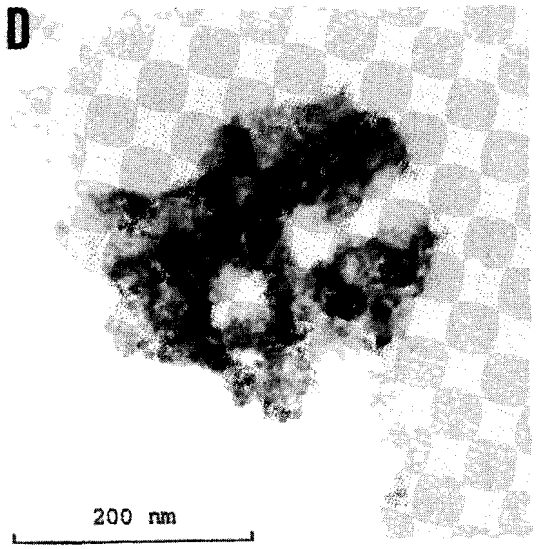

pH = 5

Figure 4 (continued) (c) pH=4, 54000 times to the film, (d) pH=5, 54000 times.

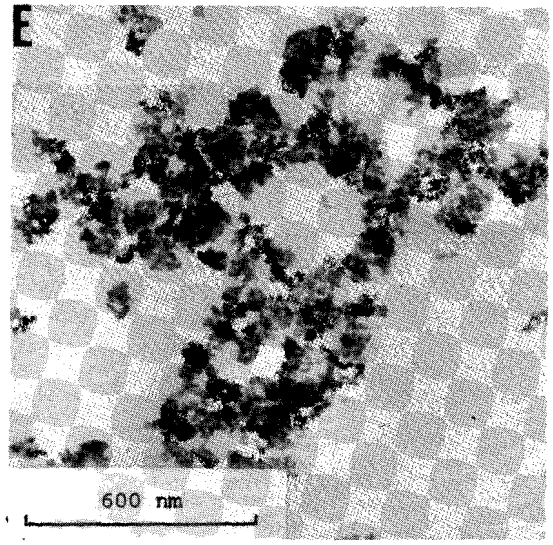

pH = 8

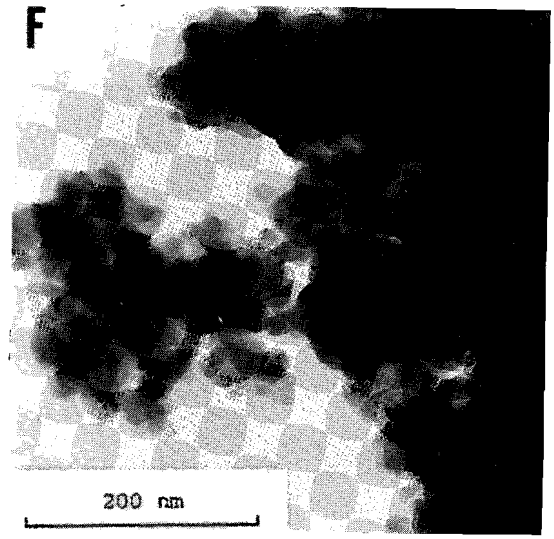

pH = 9

Figure 4 (continued) (e) pH=8, 18000 times to the film, (f) pH=9, 54000 times.

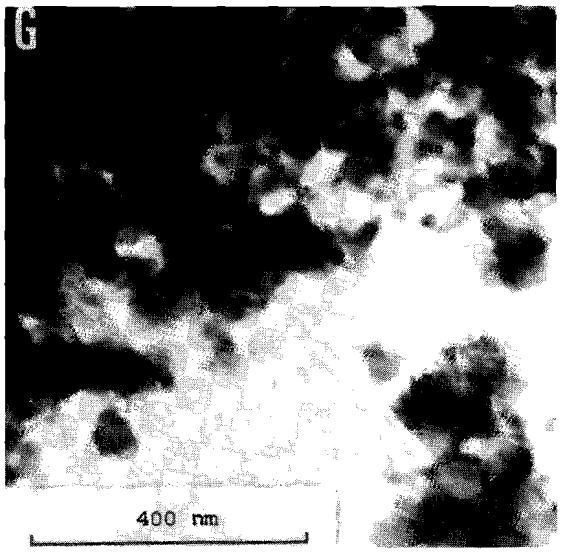

pH = 10

Figure 4 (continued) (g) pH = 10, 32000 times to the film.

The electronmicrographs thus show that at pH levels around the IEP the size of the elementary silica particles strongly changes; at higher pH levels much larger silica particles result. At still higher pH levels, where the solubility of the silica is much higher, the size, the shape and the aggregation of the elementary particles is much different from that at lower pH levels. It is interesting to investigate the effects of the size and aggregation of the elementary particles on the pore radii, pore volumes, and surface areas of hydrogels and xerogels.

Thermoporometry of hydrogels and xerogels

The thermoporometric data measured for the hydrogels and the xerogels are summarized in Tab. 3. The ice crystal radius, Rn, the ice volume, V_n, the shape factor, F, and the ice surface area, A_n, are indicated, as well as the characteristic properties corrected for the non-freezing layer of water of 0.9 nm, viz., the pore radius, R_p, the pore volume, V_n^*, and the surface area, A_n^*.

In the hydrogel samples prepared at a pH_{sp} of 1 and 2, small ice nuclei of a radius of 2.2 nm are formed, which points to pore radii of 3.1 nm (2.2 + 0.9 nm) after correction for

the non-freezing layer. The size of the pores in the hydrogels, viz., about 6 nm, is hence considerably larger than that of the particles, viz., 2 to 3 nm. When the hydrogels prepared at a pH_{sp} of 1 and 2 are dried, the resulting xerogels exhibit very narrow pores. The pores within the xerogels are too small to allow the formation of ice crystallites to proceed. Apparently the structure of the hydrogel containing silica particles of 2 to 3 nm is highly liable to a strong compression upon drying, which points to a limited number of chemical bonds between the silica particles. The compression of the elementary silica particles during drying to the xerogel is evident from the fairly small pore volume of 0.2 ml/g before correction. The surface areas of the hydrogels are relatively small, viz., about 280 m^2/g.

Table 3 Thermoporometric characterization of pH-static prepared silica hydrogel (28 mg water and 4 mg SiO_2) and xerogel (37 mg water and 14 mg SiO_2), where R_n is the ice crystal radius in nm, V_n the pore volume in ml/gSiO_2, A_n the ice crystal surface area in $m^2/gSiO_2$, and V_n^* and A_n^* the corrected pore volumes and the calculated surface areas of the gels, respectively.

pH_{sp}	R_n (nm)	R_p (nm)	V_n (ml/g)	V_n^* (ml/g)	F	A_n (m^2/g)	A_n^* (m^2/g)
hydrogel							
1	2.2	3.1	0.2	0.4	1.8	192	272
2	2.2	3.1	0.2	0.4	1.7	198	281
4-10 [1]							
xerogel							
1-2 [2]							
4	1.9	2.8	0.3	0.8	1.4	383	694
5	5.9	6.8	0.7	0.9	2.1	232	258
8-10 [1]							

1) shoulder on bulk water peak at 273 K, 2) no pore water detected

The hydrogels prepared at a pH_{sp} of 4 to 10 have large pores, which causes the peak due to freezing of water present within the pores to appear in the thermogram as shoulders of the peak due to bulk water at 273 K, because the dT_s and dT_f are very small (Eqn.3). Apparently the larger particles of diameters of 5 to 26 nm present in the hydrogels enclose much larger pores, which indicates a much more open gel structure. The xerogel resulting from drying of the hydrogel prepared at a pH_{sp} of 4, which contains elementary silica particles of 5 to 8 nm, exhibits a pore radius of 2.8 nm, which corresponds to pores of a dimension of about 6 nm. Hence drying of the hydrogel leads to a close packing of the elementary silica particles. The xerogel obtained by drying the hydrogel prepared at a pH_{sp}

of 5, however, displays a pore radius, which is substantially larger, viz., 6.8 nm. The larger pore radius indicates that at a pH_{sp} of 5 a much more stiff gel structure results, which shrinks much less on drying. Apparently at a pH of 5 reaction of hydroxyl groups on neighbouring silica particles proceeds more extensively leading to a more stiff structure. The different structures of the xerogels obtained from hydrogels prepared at pH_{sp} of 4 and 5 is also evident from the shape factors, which are 1.4 and 2.1, respectively. A higher pH_{sp} apparently leads to more cylindrical pores.

The change in structure of the xerogel when the pH_{sp} at which the hydrogel is prepared is raised from 4 to 5, is also evident from the pore volume. Before correction of the non-freezing layer the pore volume of the xerogel obtained on drying the hydrogel prepared at a pH_{sp} of 4 is 0.3 ml/g, while for the xerogel from the hydrogel prepared at a pH_{sp} of 5 the pore volume before correction is 0.7. Since the correction for the non-freezing layer of 0.9 nm is relatively large with the small pore radius of 1.9 nm measured for the xerogel obtained from the hydrogel prepared at a pH_{sp} of 4, the corrected pore volume and the surface area are fairly large, viz., 0.8 ml/g and 694 m^2/g, respectively. The xerogel from the hydrogel prepared at pH_{sp} of 5 exhibiting a significantly higher pore volume of 0.7 ml/g again points to a more stiff gel structure. The surface area before correction of the non-freezing layer is lower with the xerogel from the hydrogel prepared at pH_{sp} of 5 than of that from the hydrogel prepared at pH_{sp} of 4, viz., 232 and 383 m^2/g, respectively. Nevertheless the surface areas of the gels resulting from drying hydrogels prepared at pH_{sp} level of 4 and 5 are higher than the surface areas of the hydrogels prepared at pH_{sp} of 1 and 2. The surface areas therefore again indicate a higher extent of reaction between the elementary silica particles at higher pH levels.

With the hydrogels prepared at pH_{sp} levels of 8 to 10, the linking of the larger silica particles is that strong that also after drying fairly large pores remain. As a result freezing of the water within the large pores is evident only as a shoulder on the peak of bulk water situated at 273.15 K. From the thermograms therefore no pore radii and pore volumes can be derived.

Surface area measurements

The specific surface areas of the gels as obtained by different experimental techniques will be compared in this section. In Tab. 4 the surface area from the transmission electronmicrographs (TEM) is calculated from the particle size observed in the micrographs according to the relation :

$$A_s = 6/(D*d) = 2727/d \qquad (m^2/g) \qquad (20)$$

where A_s is the specific surface area (in m^2/g), D the density of silica, which is

$2.2*10^6$ g/m^3, and d the diameter of the elementary particles (nm). The surface area from the adsorption of N_2 is calculated according to the BET equation, and that from the Hg penetration from the pore radius and pore volume distribution. The calculation of the results of the Sears titration has been dealt with above.

Table 4 Particle size of sol particles or small sol aggregates in the silica gels measured with TEM and the reconstructed surface area if the particles where isolated in the solution.

pH_{sp}	sol diameter d(nm)	surface area[1] A_s(m^2/g)
1	2-3	1364-909
2	2-3	1364-909
4	5-8	545-341
5	5-8	545-341
8	16-21	170-130
9	21-26	130-105
10	21-26	130-105

1) $A_s = 6/(D*d) = 2727/d$, with the density D of SiO_2 = $2.2*10^6$ g/m^3

The surface areas obtained by the different techniques show the largest differences for the gels prepared at pH_{sp} levels of 1 and 2 in Fig. 5. The particle size observed in the electronmicroscope suggests a surface area of no less than 1100 m^2/g. Hg penetration results in surface areas of only 10 m^2/g, and the Sears titration to 62 and 21 m^2/g for xerogels obtained from hydrogels prepared at pH_{sp} levels of 1 and 2, respectively. It is interesting that thermoporometry on the hydrogels and N_2 adsorption on the xerogels lead to about an equal surface area. Thermoporometry shows surface areas of about 280 m^2/g, and N_2 adsorption of about 250 and 200 m^2/g. It is evident that the small elementary silica particles enclose very narrow pores into which Hg can hardly penetrate. Also the hydroxyl ions used in the Sears titration cannot enter readily all the narrow pores of the xerogel. Iler [13] showed that the BET surface area of the linked particles, A_s(BET), can be related to the surface area of isolated particles calculated from the dimensions determined with TEM, A_s(TEM), by Eqn. 21.

$$A_s(BET) = A_s(TEM) * (1 - n*0.177*(d+0.177)/d^2) \quad (m^2/g) \quad (21)$$

where n is the coordination number of the sol particles, and 0.177 nm the radius of the of the N_2 molecule. According to the relation of Eqn. 21 with $A_s(BET) \approx 225$ m^2/g, and

A_s(TEM) ≈ 1100 m^2/g, a coordination number n of 10 to 11 is derived for the particles with a diameter d of 2 to 3 nm prepared at a low pH_{sp} of 1 and 2. A hexagonal close packing would yield the vale n of 12.

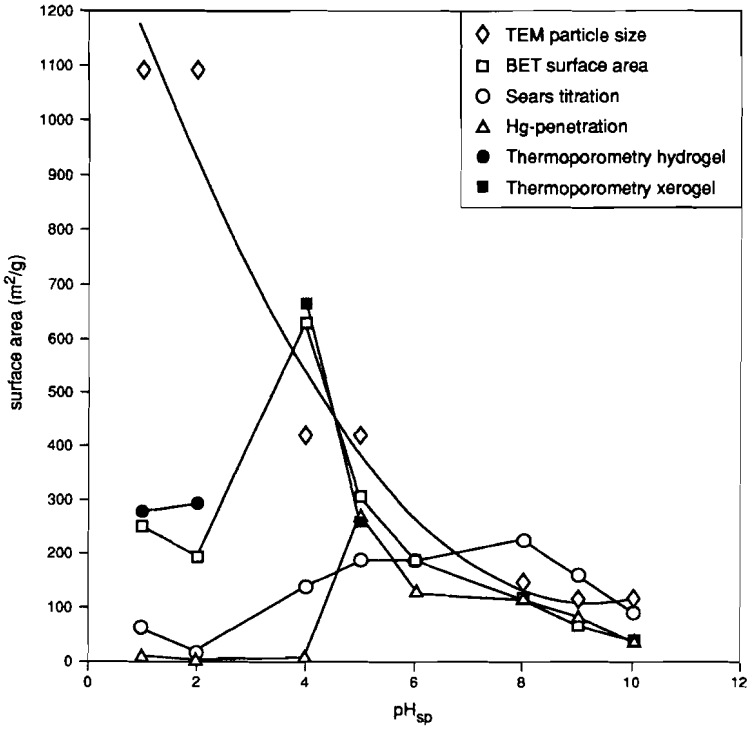

Figure 5 The surface area of the silica gels as function of the static preparation pH, obtained from TEM images (diamonds), thermoporometry of hydrogel (black spheres), thermoporometry of xerogel (black squares), N_2 adsorption at 77 K (open squares), Sears titration (open spheres), and Hg penetration (triangles).

When the pH_{sp} at which the hydrogel is prepared is increased from 4 to 5, thermoporometry of xerogel indicates a sharp increase in the pore radius and pore volume (Tab. 3). With N_2 adsorption and Hg intrusion the same sharp change is apparent. The BET surface area drops from about 630 m^2/g to about 300 m^2/g, whereas the surface area calculated from the intrusion of Hg rises from about 10 to about 250 m^2/g. It is remarkable that the surface area calculated from the Hg intrusion is about equal to that measured by thermoporometry, viz., about 258 m^2/g. The surface area measured according to the Sears titration, viz., about 200 m^2/g, is not much different from the values resulting from the

other techniques. In view of the accuracy of the assessment of the particle size in the electronmicroscope, the agreement with the surface area calculated from the particle size is very satisfactory.

The xerogels having fairly wide pores obtained on drying hydrogels prepared at pH_{sp} levels above 5 show surface areas from N_2 adsorption, Hg penetration, and electronmicroscopy that agree very well. The Sears titration exhibits a surface area that is consistently a factor of two higher than the surface area determined by the other techniques, except for the xerogel resulting from drying the hydrogel prepared at pH_{sp} of 6. The last xerogel displays a surface area by the BET procedure, the Sears titration, and the Hg penetration of 191, 187, and 131 m^2/g, respectively.

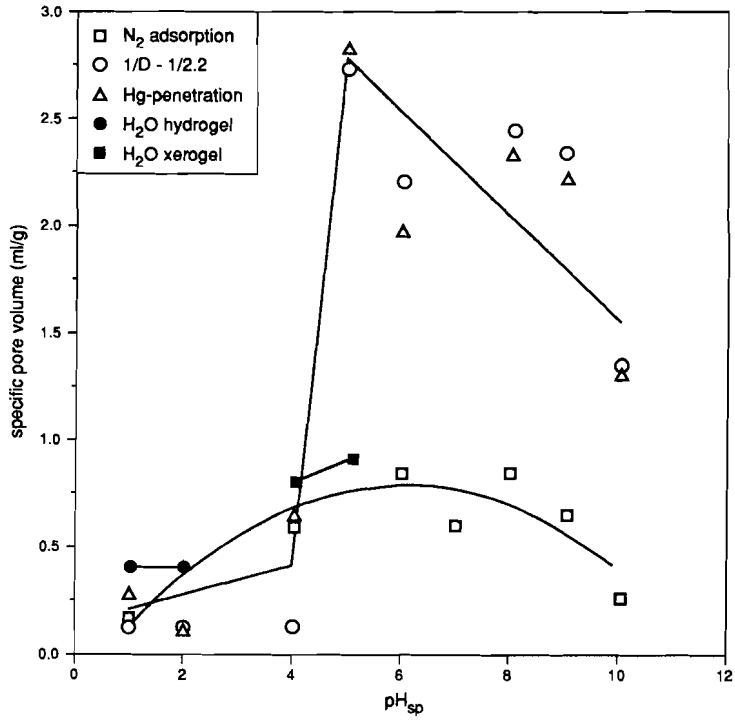

Figure 6 The specific pore volume of the silica gels as function of the static preparation pH, obtained from thermoporometry of hydrogel (black spheres), thermoporometry of xerogel (black squares), N_2 adsorption at 77 K (open squares), and Hg penetration, by measuring (i) the amount penetrated Hg at high pressure (open spheres), and (ii) the bulk density of the samples at atmospheric pressure (open triangles).

Pore volume measurements

The pore volumes are calculated from measurement of the Hg penetration, N_2 sorption at 77 K, and thermoporometry. The pore volume is calculated in two different ways, viz., from (i) the amount of Hg penetrated, and (ii) the bulk density of the sample with Hg in the measuring cell. The reciprocal true density of silica, 2.2 g/ml, is subtracted from the reciprocal bulk density D_b of the xerogel according to Eqn. 22.

$$V_p = 1/D_b - 1/2.2 \quad \text{(ml/g)} \qquad (22)$$

where V_p is the pore volume in ml/g.

The results are represented in Fig. 6. The plot of the pore volume exhibits a discontinuity with xerogels from hydrogels prepared at a pH_{sp} level above 4. The pore volumes of hydrogels and xerogels prepared at pHsp levels below 4 are lower than 0.4 ml/g, in accordance with results in ref. [19]. The very low pore volumes are at the same order of magnitude of a hexagonal close packing of sol particles, $(3\sqrt{2}-\pi)/2.2\pi = 0.16$ ml/g, or cubic close packing, $(1-\pi/6)/2.2 = 0.22$ ml/g. With preparation at pH_{sp} levels above 4 the pore volume steeply rises to a level of about 0.8 ml/g and slowly drops at pH_{sp} levels above about 8.

The pore volume of the hydrogel prepared at pH_{sp} 1 and 2 determined by thermoporometry is higher than that measured by N_2 adsorption and Hg penetration. In spite of the limited penetration of Hg into xerogels from hydrogels prepared at pH_{sp} levels of 1 and 2, the pore volume is about equal to the to that calculated from the sorption of N_2.

When the pH_{sp} during preparation is increased to 4, the pore volume of the xerogels measured by thermoporometry becomes 0.8 to 0.9 ml/g, and the pore volume measured by Hg intrusion and N_2 sorption to about 0.7 ml/g. At still higher levels of pH_{sp} during the preparation, the pore volume as measured by Hg penetration increases sharply to about 2.3 ml/g, whereas the N_2 pore volume passes through a faint maximum at a pH_{sp} of about 8. The maximum is at a pore volume of about 0.8 ml/g. The pore volumes of N_2 sorption and thermoporometry at high pH_{sp} of 5 to 10 are far below the pore volumes determined by Hg penetration (Fig. 6).

The shape of the pore volume against pH_{sp} plot determined by Hg penetration experiments is the same of that in ref. [1]. Though the shape is equal, the maximal pore volume in our plot of 2.8 ml/g is a factor 3.5 higher that the maximal pore volume in ref. [1], viz., 0.8 ml/g. The difference might be explained by the differences in the preparation conditions. Our hydrogels are prepared slowly over a period of 21 to 23 h, whereas the gels in ref. [1] are prepared by rapidly mixing of sodium silicate and acid. The slow preparation shows a larger effect of the pH on the resulting pore structure.

It is interesting that the differences in the surface area and the pore volume of the

xerogels obtained by drying hydrogels can be attributed to the particle growth and gelling kinetics, as controlled by the pH. Low rates of silica polymerization are observed at low pH levels below the IEP of silica [21]. The activation energy of particle growth at the IEP of 3 attains the relatively high value of 77.4 kJ/mole, as compared to a minimum of 65.3 kJ/mole at a pH of 4.3 in ref. [25], while 63.2 kJ/mole is measured at a pH of 4 in ref. [21]. Relatively low values of the activation energy, ranging from 57.6 kJ/mole at pH 3.5 to 30 kJ/mole at pH 4.5, are calculated from viscosity measurements in ref. [26]. Turbidity experiments have shown that the increase in molecular weight of the sol particles or clusters can be described by Eqn. 23 of Coudurier et al. [21] at medium pH levels of 4 to 5, and by Eqn. 24 of Greenberg and Sinclair [20] at high pH levels of 8 to 10.5 :

$$\text{Ln } Mw(t)/Mw(t_o) = k_1 * (t-t_o) \qquad (23)$$

$$Mw(t)-Mw(t_o) = k_2 * (t^2-t_o^2) \qquad (24)$$

where the molecular weight at time t, Mw(t), is a function of the turbidity, $\tau(t)$, by :

$$\tau(t) = {}_0\int^{\pi} [M] * I(\theta,t)/I^\circ * 2\pi R^2 * \sin\theta d\theta = A * Mw(t) \quad (m^{-1}) \qquad (25)$$

$$\text{with } A = 32\pi^3 n_o^2 (dn/dc)^2 c / 3\lambda^4 N_{av} \quad (\text{mole} * m^{-1} g^{-1})$$

where [M] is the concentration of sol particles (in m^{-3}), $I(\theta,t)/I^\circ$ the ratio of the intensity of the scattered light of a single particle at the angle θ and the time, t, n_o the refractive index of water of 1.336, dn/dc (in m^3/g) the increment of the refractive index with increasing weight concentration silica, c, λ the monochromatic wavelength (in nm), N_{av} Avogadro's number (in $mole^{-1}$). The turbidity with especially large sol particles or clusters is corrected for the dissymmetry with a Zimm-equation [20,22,27].

The agglomeration rate of the sol particles to large clusters clearly decreases from a fast exponential rate at the medium pH level of 4 to 5 (Eqn. 23) to a less rapid power rate function at high pH levels of 8 to 10.5 (Eqn. 24). It has been demonstrated that the rate of agglomeration of sol particles into large clusters increases until a pH of 6. Subsequently, above a pH of 6, the rate decreases, while the deposition of MSA on the sol particles still proceeds [21]. It is probably the reason why the pore volume measured by Hg penetration and N_2 sorption weakly declines above the pH level of 6. The large sol particles at high pH are less branched at high pH levels and suffer more from the capillary forces with drying.

CONCLUSIONS

1) Shrinkage during drying of hydrogels to xerogels can readily be monitored by thermoporometry. If thermoporometry is applied on the pH-statically prepared hydrogels, only those prepared at a low pH_{sp} of 1 and 2 lead to $R_p = 3.1$ nm, $V_n^* = 0.4$ ml/g, and $A_n^* = 272\text{-}281$ m^2/g. The hydrogels prepared above a pH_{sp} of 4 cannot be measured, because their macroporosity is too high. As a consequence of shrinkage, thermoporometry cannot be applied to the xerogels prepared at pH_{sp} of 1 and 2. During drying, the pores become too small to allow the formation of ice-nuclei. Thermoporometry can be applied to xerogels from hydrogels prepared at a pH_{sp} of 4 and 5, because of their decreased pore size and high pore volume. Thermoporometry is again not appropriate for xerogels from hydrogels prepared above a pH_{sp} of 5. The increased pore size and pore volume causes the formation of ice-nuclei just below 273 K, even after drying.

2) An elementary particle size increasing from 2-3 nm of silica gels prepared at a static pH_{sp} of 1 and 2, through 5-8 nm at pH_{sp} 5, to 21-26 nm at a pH_{sp} of 10 is very well illustrated by TEM. Consequently, the corresponding surface areas decrease from 1364-909 m^2/g at a pH_{sp} of 1 and 2, through 545-341 m^2/g at a pH_{sp} 5, to 130-105 m^2/g at a pH_{sp} of 10.

3) Pore volumes between 0.13 and 0.6 m^2/g obtained by Hg penetration show that very microporous xerogels are produced at a low static pH_{sp} below 4. Due to the fine microporosity, Hg and hydroxyl ions can hardly reach the surface area of the primary sol particles, and consequently too low surface areas are measured as compared to thermoporometry and N_2 sorption.

4) Surface areas of about 200 m^2/g measured by thermoporometry on hydrogels and by N_2 adsorption on xerogels are higher than those measured by Hg penetration and Sears titration on xerogels and obviously smaller than the TEM data of 1364 to 909 m^2/g. The discrepancy between thermoporometry and N_2 adsorption, on the one, and TEM, on the other hand, are presumably caused by the very close packing and the branching of the particles and the annular crevices at necks, where ice and N_2 cannot penetrate.

REFERENCES

1. Physical and Chemical Aspects of Adsorbents and Catalysts, Ed. B.G. Linsen, Academic Press, London (1970), 213-262
2. R.H. Meinhold, H.P. Rothbaum, R.H. Newman, *J. Coll. Interf. Sci.*, **108** (1985) 234-236
3. G. Engelhardt, H. Jancke, D. Hoebbel, W. Wieker, *Z. Chem.*, **14** (1974) 109-110
4. G. Engelhardt, D. Zeigan, H. Jancke, D. Hoebbel, W. Wieker, *Z. Anorg. Allg. Chem.*, **418** (1975) 17-28
5. P.W.J.G. Wijnen, T.P.M. Beelen, J.W. de Haan, C.P.J. Rummens, L.J.M. van de Ven, R.A van Santen, *J. Non-Cryst. Sol.*, **109** (1989) 85-94
6. J.L. Svensson, S. Sjöberg, and L-O Öhman, *J. Chem. Soc., Faraday Trans.*, **(1)** (1986) 3635-3646
7. J.F. Quinson, M. Astier, M. Brun, *Applied Catalysis*, **30** (1987) 123-130
8. S. Lowell, and J. E. Shields, Powder Surface Area and Porosity 2nd Ed., Chapman and Hall, London (1984), 1-135
9. G.W. Sears, *Anal. Chem.*, **28** (1956) 1981-1983
10 W.M. Heston, R.K. Iler, G.W. Sears, *J. Phys. Chem.*, **64** (1960) 147-150
11. J-E.A. Otterstedt, M. Ghuzel, J.P. Sterte, *J. Coll. Interf. Sci.*, **115** (1987) 95
12. G.B. Alexander, *J. Phys. Chem.*, **61** (1957) 1563-1564
13. R.K. Iler, The Chemistry of Silica, John Wiley and Sons N.Y. (1979)
14. E.D. Shchunkin, V.V. Yaminsky, *Colloids and Surfaces*, **32** (1988) 19-32
15. H. Ballacioglu, and D. Balköse, *Colloid Polym. Sci.*, **267** (1989) 460-464
16. D. Hoebbel, P. Starke, A. Vargha, *Z. Anorg. Allg. Chem.*, **530** (1985) 135-143
17. D. Hoebbel, R. Ebert, W. Wieker, E. Assmann, and H. Mende, *Z. Anorg. Allg. Chem.*, **558** (1988) 171-188
18. L.S. Dent Glasser, and C.K. Lee, *J. Appl. Chem. Biotechnol.*, **21** (1971) 127-133
19. N. Ingri, *Acta Chemica Scandinavica*, **13** (1959) 758-775
20. S.A. Greenberg, D. Sinclair, *J. Phys. Chem.*, **59** (1955) 435-440
21. M. Coudurier, B. Baudru, J-B. Donnet, *Bull. Soc. Chim. de France*, **9** (1971) 3147-3165
22. A. Audsley, and J. Aveston, *J. Chem. Soc.*, **6** (1962) 2320-2329
23. S.P. Moulik, B.N. Gosh, and S. Bandyopadhyay, *J. Indian. Chem. Soc.*, **40** (1963) 607-614
24. T.M. Karnaukhova, N.K. Ivanov, M.S. Zaharov, *Coll. J. USSR*, **48** (1986), Russ. 686-691, Engl. Transl. 580-584
25. H. Stade, and W. Wieker, *Z. Anorg. Allg. Chem.*, **384** (1971) 53-66
26. W. Vogelsberger, J. Opfermann, U. Wank, H. Schulze, and G. Rudakoff, *J. Non-Crystal. Sol.*, **145** (1992) 20-24

Chapter 7

The effect of drying on the pore dimensions of electrodialysed silica sol gels*

M.K. Titulaer, M.J. den Exter[1], H. Talsma[2], J.B.H. Jansen, and J.W. Geus[1]

Department of Geochemistry, Institute for Earth Sciences, University of Utrecht, Budapestlaan 4, P.O. Box 80.021, 3508 TA Utrecht, The Netherlands.
[1]Department of Inorganic Chemistry, University of Utrecht, Sorbonnelaan 16, P.O. Box 80.082, 3508 TB Utrecht, The Netherlands.
[2]Department of Pharmaceutics, University of Utrecht, Sorbonnelaan 16, P.O. Box 80.083, 3508 TB Utrecht, The Netherlands.

*This paper is a contribution of the Debye Institute, University of Utrecht, The Netherlands.

ABSTRACT

Electrodialysed silica sol-gels are prepared of a silica concentration of 1.37 M in water. The shrinkage of the gels with drying is investigated. The silica sol solutions are prepared by removal of sodium ions from a sodium silicate solution through a Nafion membrane. A uniform sol solution results containing sol particles of 5 nm diameter as measured by transmission electron microscopy, and 7.3 nm as measured with dynamic light scattering. The presence of a layer of structural water of about 1 nm on the silica surface is assumed. The dialysed silica sol particles of a few nm in size are gelled at several pH levels, ranging from 2.7 to 7.8. The sols display a minimum gelling time of 279 minutes at a pH of 5.9 established by measuring the shear viscosity with time. The gelling time increases below the pH level of 5.9 due to the low amount of ionized surface silanol groups, and above the pH level of 5.9 due to electrostatic repulsion between the sol particles.

The hydrogels, which are prepared from the silica sol solutions, have a size of the sol particles not depending on the gelling pH. The porous structure between the sol particles of the hydrogels is studied by thermoporometry in water.

Subsequently the gels are dried at 333 and 393 K, and again investigated in water. Air drying does not lead to shrinkage. The pore structure only depends on the gelling pH. The ice crystal radius, R_n, measured by thermoporometry, increases from 1.5 to 3.3 nm raising

the pH of gelling from 2.8 to 6.5, while the low ice pore volume increases from 0.15 to 0.4 ml/g SiO_2. The ice pore volume being increased, but the total pore volume (ice plus a non-freezing layer) being equal of differently prepared gels point to the formation of short pores with large radii at high pH levels.

INTRODUCTION

The former chapters are dealing with silica gels prepared by addition of waterglass to an acid or precipitation by simultaneous addition of an acid and waterglass to a solution at a constant pH. The resulting silica gels are present in solutions of a high ion strength. The high ion strength brings about that the clustering of the silica particles proceeds readily. Especially at low pH levels the silica particles agglomerate without chemical bonds between the particles being established. Without chemical bonds the agglomerated silica particles are liable to shrinkage upon drying.

Investigation of silica gels prepared at low ion strength is interesting to study the formation of chemical bonds between silica particles. Especially the extent of shrinking during drying may be considerably lower with silica gels produced at low ion strengths.

To prepare clear sodium-free silica sols electrodialysis is a very good procedure. The preparation of sodium-free colloidal silica solutions has been known from 1930, when Treadwell and Wieland published a procedure in which a platinum and a dripping mercury electrode mounted in a waterglass solution were utilized [1]. Hydrogen ions are generated at the platinum anode, while the mercury cathode absorbs the metallic sodium resulting from the reduction of dissolved sodium ions. Due to the replacement of sodium ions by hydrogen ions, the pH of the waterglass solution drops, which leads to polymerization of the silicate anions. In 1972 Iler improved the procedure separating the Pt anode and the mercury cathode by a cation exchange (NAFION) membrane [2]. The Nafion membrane (DuPont, F.R.G.) is composed of carbon fluoride chains with sulfonic (SO_3H) or carboxylic acid (COOH) side chains. The sulfonic or carboxylic acid groups are ionized and introduce a negative charge on the membrane. The negative charge causes the membrane to be impermeable for silicate anions. The membrane is stable within a broad range of pH levels and temperatures [3]. Using a Pt cathode together with a Nafion membrane we arrived at a mercury-free procedure for the electrodialysis of silicate solutions.

The silicate solution is present within the anode compartment. Due to the transport of sodium ions out of the anode compartment, a clear non-gelling silica sol is produced within the anode compartment and NaOH ends up in the cathode compartment. The electrodialysis process is monitored by measuring the current as a function of time, the sodium concentration and the pH in the anode and cathode anode compartment. Since the transport of the hydrogen ions generated at the Pt anode into the anode compartment proceeds very rapidly, a very homogeneous solution during the decrease of the pH results. The electrodialysis therefore can be performed extremely reproducibly.

The amount of the silicate anions present in the solution during the decrease in the pH

due to the electrolysis, can be established by measuring the reaction with heptamolybdate to the intensively yellow coloured silicomolybdate complex. The rate of the reaction to the silicomolybdate complex depends on the size of the silicate anions; larger silicate anions react more slowly than monosilicic acid (MSA). The size of the silicate anions therefore can be assessed by measuring the rate of the reaction to the silicomolybdate complex.

The size of the elementary silica particles present in the final sol of a low pH can be measured by dynamic light scattering (DLS). Also the effect of ageing of the colloidal silica solution on the size of the elementary silica particles can be assessed using DLS. The influence of the period of time of ageing and the temperature of the liquid during ageing on the size of the silica particles can also be studied.

Gelation due to the formation of chemical bonds between the elementary particles is induced by raising the pH by addition of hydroxyl ions. Ionization of the surface hydroxyl groups of the silica promotes the formation of chemical bonds between the silica particles due to condensation of water and formation of siloxane bridges. Ionization of the surface hydroxyl groups, on the other hand, leads to electrostatic repulsion between the negatively charged elementary silica particles.

The porous structure of the silica gels can be investigated excellently by thermoporometry. Since thermoporometry can be used with the hydrogels, the effect of drying on the porous structure can be reliably investigated by performing thermoporometry before and after drying. With a low ion strength a stiff gel structure and, hence, a small effect of drying on pore dimensions and pore volume can be expected.

To assess the relevance of dynamic light scattering and thermoporometry, it is important to corroborate the results of the above techniques with those of other well established techniques. The BET surface area and the pore volume calculated from the extent of nitrogen sorption at 77 K provides information that can be compared with the thermoporometric results. Assuming a small contact area a mean size of the elementary silica particles can be calculated from the BET surface area. The size of the elementary silica particles in the dried gels can also be determined from electronmicroscopy. Finally the surface area of the dried gels will be estimated by measuring the diffuse reflection Fourier transform infrared absorption due to the surface hydroxyl groups of the silica.

EXPERIMENTAL TECHNIQUES

Electrodialysis

Fig. 1 shows schematically the experimental set up of the electrodialysis. The platinum anode and cathode are separated by a Nafion type N-324 membrane. Boiling the membrane in water for 30 min swells the membrane as required for the electrodialysis. The resistance at room temperature of the membrane is 4.5 ohm*cm^2 in 0.6 M KCl according

to the specifications of DuPont. A two liter Na silicate solution is brought into the anode compartment. The solution is prepared by dilution of 400 ml Merck art. 5621 Na silicate (6.85 M Si and 3.98 M Na) with 1600 ml of demineralized water. The initial concentration of Si and Na is 1.37 M and 0.78 M, respectively. The cathode compartment contains 2 l of 0.05 M $NaNO_3$ solution, which initially enhances the conductance of the cell. The solutions in the anode and cathode compartment are vigorously stirred.

A potential of 7 V is put over the cell. Due to the electric field of 82.35 V/m, Na^+ migrates through the membrane from the anode to the cathode compartment. The electrodialysis takes 88 h to be completed.

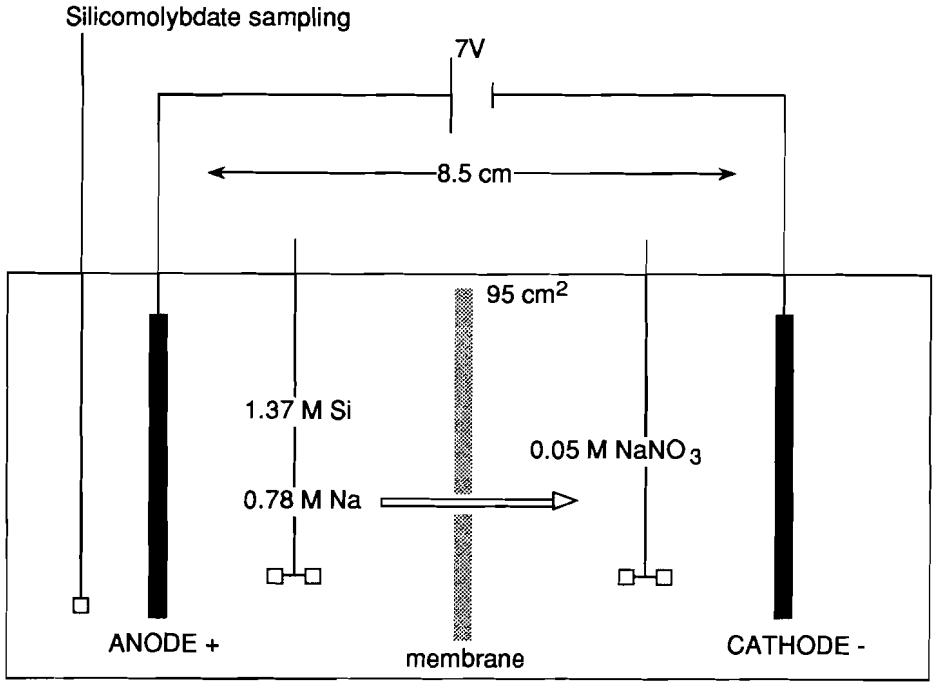

Figure 1 The electrodialysis cell. The anode and cathode compartment contain both 2 l liquid, and are separated by a Nafion N-324 cation exchange membrane. A voltage of 7 V is applied on the cell.

Determination of the solubility as silicomolybdate and sampling

The amount of small silicate anions, capable of reaction with heptamolybdate to intensively yellow silicomolybdate, present within the anode compartment is determined as a function of the period of time of electrodialysis. Six samples of 2 ml are drawn from the 1.37 M Si solution during the period of time of 88 h of the electrodialysis. The samples of 2 ml are diluted 50 times to a concentration of $2.74*10^{-2}$ M Si. Aliquots of 0.5 ml of the $2.74*10^{-2}$ M Si solutions are added to 25 ml acidified ammonium heptamolybdate solution, containing 0.07 M MoO_4^{2-}, 0.15 M NH_4^+, having a pH level of 1.2 [4]. A reaction of the silicate anions with ammonium heptamolybdate proceeds. The reaction to the yellow silicomolybdate complex in periods of time between 30 and 480 s is measured within a Perkin-Elmer Lambda1 UV-VIS spectrophotometer in a 1 cm cuvette at a wavelength of 410 nm.

Monomer standards of silica (Merck art. 9947), with concentrations of monomer (MSA) ranging between 0 and $1.14*10^{-2}$ M mono silicic acid (MSA), are measured after two minutes reaction with the ammonium heptamolybdate. Aliquots of 0.5 ml of the MSA solutions are added to 25 ml of the heptamolybdate solution.

Sol particles measured by DLS

The technique of dynamic light scattering is appropriate to measure the size of particles in sol solutions with sizes as small as 1.5 nm [5], which is of the order of magnitude of the size expected in our silica sol solutions. The sol particles of a silica solution having an concentration of silica equal as the prepared gels, viz., 1.37 M Si, would likely cluster within a short period of time to particles of a larger size. The rate of clustering of sol particles is expected to be smaller at low silica concentrations. Therefore, five time diluted silica sols, of final concentrations of 0.27 M Si are dialysed. The 0.27 Si sodium silicate solutions are prepared by addition of 80 ml of the sodium silicate solution (Merck Art 5621) to 1920 ml water.

Dust is removed from the dialysed sol by filtration over a Anatop 0.02 and 0.2 μm syringe filter (Anotec company, U.K.). The effect of the concentration and ageing of silica on the particle size as measured by DLS is studied. The dialysed sols are stored under different conditions, viz., (1) for a period of 10 weeks at 280 K, and for periods of (2) 4.5, (3) 5.5, and (4) 7.5 weeks at 298 K. Additionally, the silica sol solution (4) stored for a period of 7.5 weeks at 298 K is diluted by a factor 1.11 to 1.82 to concentrations of silica decreasing from 0.25 to 0.15 M Si.

The instrument used for almost all measurements is a Malvern 4700 C correlator with a GLC 5700 He-Ne gas laser (632.8 nm, slit 600, diaphragm 11, with a power output of 25 mW or more applied to silica sols kept at a temperature of 298 K. The fluctuation of

scattered intensity of light is measured at different angles, 35, 45 90, and 125 degree θ. Two measurements are performed with a Malvern Multibit K 7025 correlator with a Spectra Physics model 165, 400-600 mW, Ar-laser (488.0 nm) applied on silica sol solutions kept at a temperature of 293 K. The scattering angle of this instrument is 35 and 155 degree θ.

Formation of hydrogel monitored by measurement of the shear viscosity

The gelling time of the dialysed silica sol as a function of the pH is investigated. Aliquots of 0.11 to 0.33 ml of 1 M NaOH are added to 40 ml of a dialysed silica sol of a concentration of 1.37 M Si (Tab. 1). The effect of the different pH levels on the rate of the gelling process is compared. The rate of gelling is measured by the increase of the viscosity with time using a rheometer. The viscosity (Pa*s), expressed as the ratio of the shear stress (N/m^2) and the shear rate (s^{-1}), is measured on a Bohlin DG 24/27 rheometer with a torque element of 0.278 g*cm. No physical meaning can be derived from the measured viscosity of the silica sol solutions. The measurement can be used in a relative way, in the determination of the gelling time, the time where the viscosity has a infinitely large level.

The initial viscosity of the dialysed sol is measured as the shear stress at a shear rate between 46 and 92 s^{-1}. Addition of NaOH solution to the dialysed silica sol solutions causes the viscosity to increase. The increased viscosity with is measured at a constant shear rate of 463 s^{-1} as a function of time. With increased viscosity less sensitive torque elements must be used. The torque elements that are used are, 0.278 g*cm at gelling periods less than 100 minutes, 3.984 g*cm after 100 minutes for the sol with a pH level of 5.9, 6.3, and 5.3. Finally the torque element of 90.25 g*cm is used after 273 minutes for the silica sol of a pH level of 5.9, after 316 minutes for the silica sol of a pH level of 6.3, and after 432 minutes for the silica sol of a pH level of 5.3, respectively.

Table 1 Silica sols of different pH by addition of NaOH to 40 ml of the dialysed 1.37 M Si solution.

ml 1 M NaOH	pH	$[Na^+]*10^3$ (mole/l)	[Si] (mole/l)
0	2.7	5.87	1.37
0.109	4.2	8.03	1.37
0.218	5.3	10.18	1.36
0.264	5.9	11.09	1.36
0.330	6.3	12.39	1.36

The drying step of hydrogel to xerogel

The hydrogels formed after gelling of the silica sol solutions are subsequently dried. Usually, the pore radius and pore volume of the hydrogel decrease upon drying. The capillary force exerted by the water-vapor meniscus travelling through the pore is the main cause of the shrinkage. The effect of the drying step on the pore radius, pore volume, and surface area can be monitored by application of thermoporometry on the hydrogel before and the xerogel after drying.

The change in the pore structure of dialysed hydrogels gelled at various levels of pH are examined. Fresh hydrogels are gelled at pH levels of 2.8, 4.1, 5.0, and 6.5 (set A-D), and one hydrogel is gelled at a pH level of 2.7 and stored for a period of 7.5 month at room temperature (E). Xerogels are formed from hydrogels gelled at pH levels of 2.7 and 6.0 by drying at a temperature of 333 K (F,G). Xerogels are obtained by drying hydrogels gelled at the pH levels 2.7, 3.8, 4.0, and 6.0 at 393 K (H-K). And finally xerogels are prepared from hydrogels gelled at pH levels of 2.8, 3.8, 6.0, after 1 month ageing as hydrogel by drying at the temperature of 393 K (L-N).

Thermoporometry measures the heat-flux involved with freezing of water in the pores of the hydrogel or xerogel within a Netzsch 43 differential scanning calorimeter (DSC) connected to a type 200 data station. The ice crystal radius, R_n (nm), within the pores of the sample, the ice pore volume, $V_n(1)$ (ml/g SiO_2), and the ice surface area, A_n (m^2/g SiO_2), is obtained from the heat-flux against the time plot. A second ice pore volume, $V_n(2)$ (ml/g SiO_2), is obtained by subtraction of the amount bulk water freezing outside the pores from the total amount of water. The total amount of water is weighted in the sample holder.

A shape factor, F, is determined by thermoporometry, which is indicative for the pore shape, and varies between spherical, $F=1$, and cylindrical, $F=2$. From the value of R_n, $V_n(1)$, and the shape factor F, the ice surface area A_n is calculated. A non-freezing layer of 0.9 nm between the silica surface and ice, requires a correction of $V_n(1)$ and A_n to the real pore volume and surface area, V_n^* and A_n^*.

The following procedure is applied in thermoporometry : (1) the sample in water is cooled from a temperature of 293 to 213 K at a rate of -2 K/min measuring the super cooling peak of pore water within and bulk water outside the sample ; (2) the sample is heated from a temperature of 213 to 270.5 K at a rate of 1 K/min measuring exclusively the fusion peak of pore ice ; (3) the sample is cooling from a temperature of 270.5 to 213 K at a rate of -1 K/min measuring the solidification peak of pore ice, and finally ; (4) a heating step from a temperature of 213 to 293 K at a rate of 1 K/min measuring the fusion peak of pore and bulk ice separated.

The differential scanning calorimeter is well verified (1) for the relative calorimetric sensitivity, linear on Hg (234.35 K) and Ga (429.75 K), (2) for the time lag of 22.9 s, and (3) for the thermal heat resistance (THR) of 0.132 K/mW, which causes the freezing and thawing peaks to be exactly at the right temperatures.

Sol particles in the xerogels measured by TEM

After the gelling step the silica sol particle size in the xerogels is measured by TEM and compared with the size of the initial silica sol solutions as determined by DLS. Three hydrogels, gelled at pH 4.2, 6.3, and 7.8 (set O-Q) are finely dispersed in ethanol, and a droplet of the fluid is brought upon a holey carbon film and air dried forming a xerogel. TEM micrographs are recorded within a Philips EM 420 electron microscope with a magnification to the film of 54000 times for the samples O and P prepared at the pH levels of 4.2 and 6.3, and at 18000 times for the sample Q prepared at the pH level of 7.8. The primary particle size and branching of the silica sol particles in the gels as a function of pH is investigated.

Pore structure of xerogels

The internal surface area of the xerogels is measured by nitrogen sorption, which additionally assesses the silica sol particle size and the branching of the particles. The BET surface areas obtained from the adsorption isotherm [6] of the nitrogen adsorption measurements and determined of five xerogels obtained from hydrogels gelled at the pH levels of 2.8, 3.8, 5.1, 6.0 by drying at the temperature of 393 K (set R-U), and one sample gelled at the pH level of 5.0 and dried at the low temperature of 333 K (V). Nitrogen is adsorbed on the samples within a Sorptomatic 1800 instrument (Carlo Erba, Italy). The gels are previously evacuated in vacuum for a period of 6 h at a temperature of 473 K.

The specific surface area of the silica xerogels and the amount of adsorbed water on equal amounts of the samples is assessed by DRIFTS. The method is based the infrared absorption of the 3747 cm^{-1} band of free surface silanol groups relative to the absorption at 4000 cm^{-1}. The relative absorption at 3747 cm^{-1} is determined for samples with known surface areas.

The infrared absorption of xerogels are measured, prepared from electrodialysed hydrogels gelled at pH levels of 2.7, 4.0, 5.0, and 6.0 (set W-Z) by drying at a temperature of 393 K, are measured. The xerogels are powdered and measured by DRIFTS. The gels are dried for a second time at 393 K, shortly before measurement of the DRIFT spectrum. The DRIFT spectra are recorded in the range of 2500 to 4000 cm^{-1} on a Perkin Elmer FT-1720 equipment in combination with a Spectra-Tech Diffuse Reflectance Accessory Collector.

RESULTS

Electrodialysis

The solid curve in Fig. 2a represents the current through the cell measured during the electrodialysis. The sodium ion concentrations in the two compartments of the cell, the resistances of which are connected in series, are determining the overall resistance and, hence, the current. Initially the sodium ion concentration in the cathode compartment is only 0.05 M, and that in the anode compartment 0.78 M. During the electrodialysis sodium ions are transported through the membrane from the anode to the cathode compartment. Accordingly the current, which is initially 0.36 A, passes through a maximum of 0.9 A after 30 h of dialysis. The sodium ion concentrations measured in the anode and cathode compartment as a function of time of electrodialysis are shown in Fig. 2b. The dashed curve in Fig. 2b represents the sum of the sodium ion concentrations in the anode and cathode compartment. The consumption of water by reaction to gaseous H_2 and O_2 brings about the slight increase in the sum of the sodium concentrations. The dashed curve in Fig. 2a is the current calculated from the sodium ion concentration in the cathode and anode compartment according to

$$I=\frac{2K*Na_a*Na_c*A*V}{(Na_a+Na_c)*1000*l} \quad (A) \quad (1)$$

where I is the current (A), Na_a and Na_c the sodium concentration in the anode and cathode compartment (mole/l), K a chosen constant (39.1 $\Omega^{-1}cm^2mole^{-1}$), A the membrane area (95 cm^2), 1000 a constant dealing with the conversion of 1l to 1000 cm^3, l the distance between the electrodes (8.5 cm), and V the potential experienced over the cell. The value of K is slightly smaller than the value corresponding to the molar conductivity of Na, which is 50 $\Omega^{-1}cm^2mole^{-1}$ at infinite dilution [7]. The potential difference, V, over the liquid in the cell is calculated from

$$V=7-1.23+0.06*(pH_a-pH_c) \quad (V) \quad (2)$$

where pH_a and pH_c are the pH in the anode and cathode compartment.

The resistance of the Nafion N-324 membrane is small as compared to the resistance of the solution. The resistance of the Nafion N-324 membrane is 4.5 $\Omega*cm^2$ in 0.6 M KCl, which leads to a potential drop over the membrane at the maximum current density of

0.9/95 = 0.0095 A/cm^2, of about 0.0095*4.5 = 0.04 V, which is negligible as compared to the potential difference of 7 V applied over the cell.

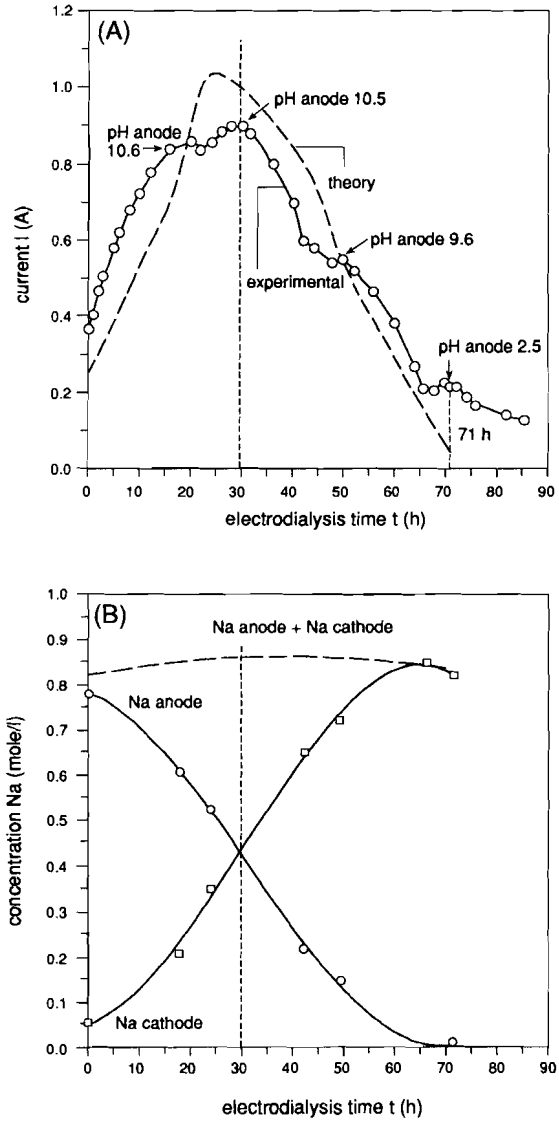

Figure 2 (a) the current as a function of electrodialysis time, which exhibits an initial current of 0.36 A, and a maximum current of 0.9 A after 30 h dialysis (solid line). The curve is averaged with the empirical function (dashed line).
(b) the concentration Na in the anode and cathode compartment with electrodialysis time. The dashed line represents the total amount of Na in the cell.

Fig. 3a shows the pH measured in the anode and cathode compartment during the electrodialysis. Whereas the pH of the anode department drops gradually from 11.3 to 2.8, the pH of the cathode department rapidly rises to about 11.6 and subsequently much more slowly to 13.2.

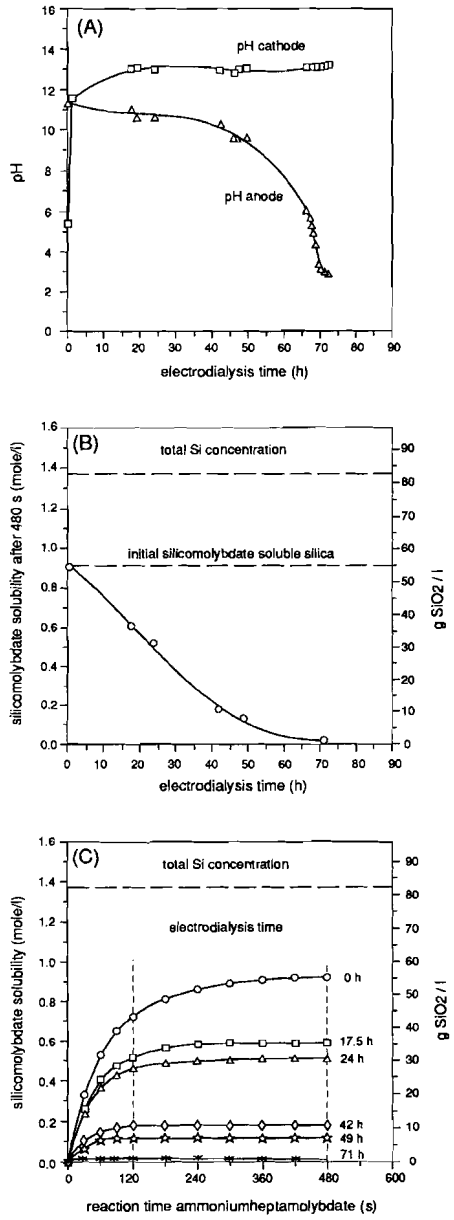

Figure 3

(a) the development of the pH in the anode and cathode compartment, decreasing at the anode from 11.3 to 2.8, and increasing at the cathode from 5.4 to 13.2 after 72 h dialysis.

(b) the development of silicomolybdate solubility as a function of electrodialysis time. The dashed line represents the total Si concentration as measured with ICP-AES.

(c) the reaction time needed for a complete reaction of silicomolybdate soluble silica with the acidified ammoniumheptamolybdate solution. The plateau of silicomolybdate solubility decreases with increasing electrodialysis time from 480 s at starting time to 120 s after 71 h dialysis.

The current-versus-time plot of Fig. 2a exhibits small discontinuities at pH levels of 10.6, 9.6, and 2.5 in the anode compartment. The ionization constant of MSA (monosilicic acid) corresponding to a pK_z value 9.6 can account readily for the discontinuity at a pH of 9.6, and that at pH 2.5 can be related to the IEP (iso-electric point) of silica. It is more difficult to explain the discontinuity at pH 10.6.

Reaction to Silicomolybdate

The amount of small silicate anions (oligomers) is determined from the extent of reaction within 480 s with an ammonium heptamolybdate solution to the yellow silicomolybdate. The time required for complete reaction of the small silicate anions with heptamolybdate to silicomolybdate is determined to be 480 s, as indicated in Fig. 3c. Fig. 3b shows the amount of silicate anions reacting to silicomolybdate within 480 s as a function of the time of the electrodialysis time. It can be seen that the concentration of silicate anions reacting to silicomolybdate decreases from 0.92 M Si (55 g Si/l), which is 67 mole% of the total amount of silicon, to 0.01 M Si (0.007 mole%) after electrodialysis for 71 h.

The initial amount of rapidly reacting small silicate anions of 0.92 M Si is of the same order of magnitude as the initial sodium concentration $[Na]_a$ of 0.8 M. The course of the drop in the Na concentration in the anode compartment (Fig. 2b) is analogous to that of the decrease in the concentration of silica capable of reaction to silicomolybdate (Fig. 3b).

The rate of reaction of silicate anions with heptamolybdate depends on the size of the silicate anions. Smaller silicate anions react much more rapidly. Fig. 3c represents the amount of silicate anions reacting to silicomolybdate as a function of the reaction time with heptamolybdate. Fig. 3c shows that initially a considerable fraction of larger silicate anions is present, which leads to a gradual increase in the amount of reacting silicate anions with time. Only after 480 s the amount of silicomolybdate does not increase further. After electrodialysis the final silicomolybdate concentration is lower, and is established much more rapidly. After electrodialysis for 42 h, e.g., the final concentration of silicomolybdate is reached already after 120 s. The disappearance of larger, more slowly reacting silicate anions is thus evident from Fig. 3c.

Mean size of sol particles measured by Dynamic Light Scattering

As dealt with in the experimental section, the size of the silica particles in the colloidal solutions is measured by DLS (dynamic light scattering). The silica sols are diluted and aged for either 10 weeks at 280 K or at least 4.5 weeks at 298 K. Before the measurements were carried out, dust was removed by filtration over a filter either having pores of either 200 nm or of 20 nm. ICP-AES is used to establish the fraction of silica

passing through the filter of a different pore size. The filter with pores of 0.2 μm retains 8.5 % of the silica and the filter with pores of 0.02 μm 17 % of the silica. Provided no interaction between the colloidal silica particles is present, which leads to larger clusters, the above data suggest that 83 % of the silica particles is smaller than 20 nm, 8.5 % is between 20 and 200 nm, and another 8.5 % is larger than 200 nm.

To assess the effect of the scattering angle of the light, measurements on the same sol aged for 5.5 weeks at 298 K are done at scattering angles of 35, 45, 90, and 125°. The results are summarized in Tab. 2a. At least three independent measurements provide the mean value and the scatter indicated in Tab. 2. The size of the silica particles varies from 8.8 to 11.8 nm without exhibiting a relation with the scattering angle. The experimental data thus suggest a reproducibility of 1 to 2 nm.

The effect of filtration through filters having pores of 0.2 and 0.02 μm has also been established. Tab. 2b summarizes the experimental data. The results also point to a reproducibility of 1 to 2 nm. In spite of the presence of 8.5 % of particles of a size between 20 and 200 nm the colloidal silica solution being passed through the filter of 0.2 μm shows a mean particle size as measured by dynamic light scattering not significantly larger than that of the sol passed through the 0.02 μm filter.

The above measurements are carried out within a Malvern 4700C at a wavelength of 632.8 nm equipped with a correlator. To roughly confirm the size of the silica particles, the same colloidal silica solution aged for 10 weeks at 280 K is also measured within a Malvern Multibit K 7025 apparatus operating at a wavelength of 488.0 nm. With the Malvern Multibit the reference time has to be determined by visual inspection of the experimental data. The measurements were done at scattering angles from 35 to 155°. Tab. 2c surveys the experimentally determined particle sizes. The particle size measured at a wavelength of 632.8 nm is about 7.4 nm and that at a wavelength of 488.0 nm about 5.1 nm, as indicated in Tab. 2c. Since we have not optimized the interval time τ with measurement of the size of 5 nm it is probably less accurate as the value of 7.4 nm. Both measurements are done at the same value of q of about $1 * 10^{-2}$ nm^{-1} at scattering angles of 35 and 45° (see appendix). The experimental data indicate that the sol is polydisperse, i.e., contains a particle size distribution. The polydispersity ($\sqrt{Q}$), as dealt with in the appendix, measured with both equipments is 0.3 and 0.5. We consider the measurements with the Malvern 4700C with a wavelength of 632.8 nm to be more accurate than the measurements with the Malvern Multibit with a wavelength of 488.0 nm, where the interval time has been established less accurately.

The effect of dilution on the mean size of the silica particles present in sols aged for 5.5 and for 7.5 weeks at 298 K is represented in Tab. 2d. The mean size of the silica particles consistently decreases with dilution of the sol from 9.2 nm at a concentration of 0.27 mole Si/l to 6.4 nm at 0.15 mole Si/l. Evidently dilution leads to selective dissolution of the larger silica particles, to dissociation of small clusters of silica particles, or to dissolution of a fraction of all silica particles.

The DLS measurements on sols aged for 5.5 weeks at 298 K or for 10 weeks at 280 K at scattering angles of 35, 45, 90, 125, and 135° represented in Tab. 2e point to a mean particle size d_h of 7.3 ± 0.6 nm after 10 weeks of aging at 280 K.

Table 2 Particle size in the silica sol measured with DLS as a function of the a) scattering angle, b) filtering, c) different equipments with variation in wavelength, d) silica concentration, e) ageing conditions.

	[Si] mole/l	θ	$q*10^2$ (nm^{-1})	filter (nm)	ageing (weeks)/ temperature (K)	particle size d_h (nm)*
a)			lambda = 632.8 nm			
	0.27	35	0.79	200	5.5 / 298	9.6 ± 0.1
	'	45	1.01	'	'	9.2 ± 0.1
	'	90	1.87	'	'	8.8 ± 0.4
	'	125	2.35	'	'	11.8 ± 0.6
b)			lambda = 632.8 nm			
	0.27	35	0.79	200	5.5 / 298	9.6 ± 0.1
	'	'	'	20	'	10.1 ± 0.1
	'	45	1.01	200	'	9.2 ± 0.1
	'	'	'	20	'	9.2 ± 0.8
	'	90	1.87	200	'	8.8 ± 0.4
	'	'	'	20	'	10.7 ± 1.0
	'	125	2.35	200	'	11.8 ± 0.6
	'	'	'	20	'	10.4 ± 1.2
c)	lambda (nm)					exp. fit/cum. fit
	632.8	45	1.01	200	10 / 280	7.4 ± 0.3
	488.0	35	1.03	'	'	5.1
	632.8	125	2.35	'	'	7.7 ± 0.7
	488.0	155	3.35	'	'	5.2
d)			lambda = 632.8 nm			
	0.27	45	1.01	200	5.5 / 298	9.2 ± 0.1
	0.25	'	'	'	7.5 / 298	9.1 ± 0.1
	0.22	'	'	'	'	8.0 ± 0.5
	0.19	'	'	'	'	7.7 ± 0.3
	0.19	'	'	'	5.5 / 298	7.0 ± 0.4
	0.16	'	'	'	7.5 / 298	6.9 ± 0.5
	0.15	'	'	'	'	6.4 ± 0.2
e)			lambda = 632.8 nm			
	0.27	35	0.79	200	5.5 / 298	9.6 ± 0.1
	'	'	'	'	10 / 280	7.5 ± 0.2
	'	45	1.01	'	5.5 / 298	9.2 ± 0.1
	'	'	'	'	10 / 280	7.4 ± 0.3
	'	90	1.87	'	5.5 / 298	8.8 ± 0.4
	'	'	'	'	10 / 280	6.4 ± 0.6
	'	125	2.35	'	5.5 / 298	11.8 ± 0.6
	'	'	'	'	10 / 280	7.7 ± 0.7
	0.27	125	2.35	20	5.5 / 298	10.4 ± 1.2
	'	'	'	'	4.5 / 298	6.7 ± 0.2
	'	'	'	none	4.5 / 298	6.4 ± 0.2

*) scatter of generally three measurements

Aging of the sol at a higher temperature of 298 K leads to a significantly larger d_h of 9.6 nm. As has to be expected an increase of the temperature, which strongly affects the solubility of silica, brings about a more rapid growth of the silica particles.

Gelling of the sol

The colloidal silica solution obtained by electrodialysis is subsequently gelled by addition of sodium hydroxide. Cluster formation of the sol particles raises the viscosity, which finally becomes infinitely large, when the cluster of silica particles link to a rigid gel. The increase of the viscosity with time is measured with sols brought by addition of NaOH at pH levels of 2.7, 5.3, 5.9, 6.3, and 7.8.

The initial viscosity of the sol is $1.06 \pm 0.05 * 10^{-3}$ Pa*s, in accordance with Einstein's law for a volume fraction of silica of 0.037. Fig. 4a shows the rise in the viscosity at 293 K as a function of the time elapsed after addition of NaOH to the dialysed sol. The gelling time, i.e., the period of time upon which the viscosity reaches infinity, is displayed in Fig. 4b as a function of the pH. The sol of pH 5.9 has the shortest gelling time, viz., 279 minutes. The gelling time exhibits a sharp minimum at a pH of 5.9. The viscosity of the sols having initial pH levels of 2.7 and 7.8 changes hardly with time. To form a rigid gel calls for a gelling time of no less than two weeks.

An exponential relationship can empirically describe the increase of the viscosity with time. The thick curves in Fig. 4a are representing exponential fits with the average equation

$$\eta = \eta_o * \exp\left(3.6 \frac{t}{t_{gel}}\right) \qquad (Pa*s) \qquad (3)$$

where η is the viscosity, η_o the initial viscosity of $(1.06 \pm 0.05) * 10^{-3}$ Pa*s, t the time, and t_{gel} the gelling time. The viscosity-versus-time plots are compared with those of the literature [8]. Whereas the above empirical relation Eqn. (3) describes well the curves measured with the sols of a pH of 2.7, 4.2, and 5.9, the viscosity of the sol of pH 6.3 increases more steeply. After about 300 min the viscosity of the sol of pH 5.3 abruptly rises to 0.35 Pa*s as indicated in Fig. 4a.

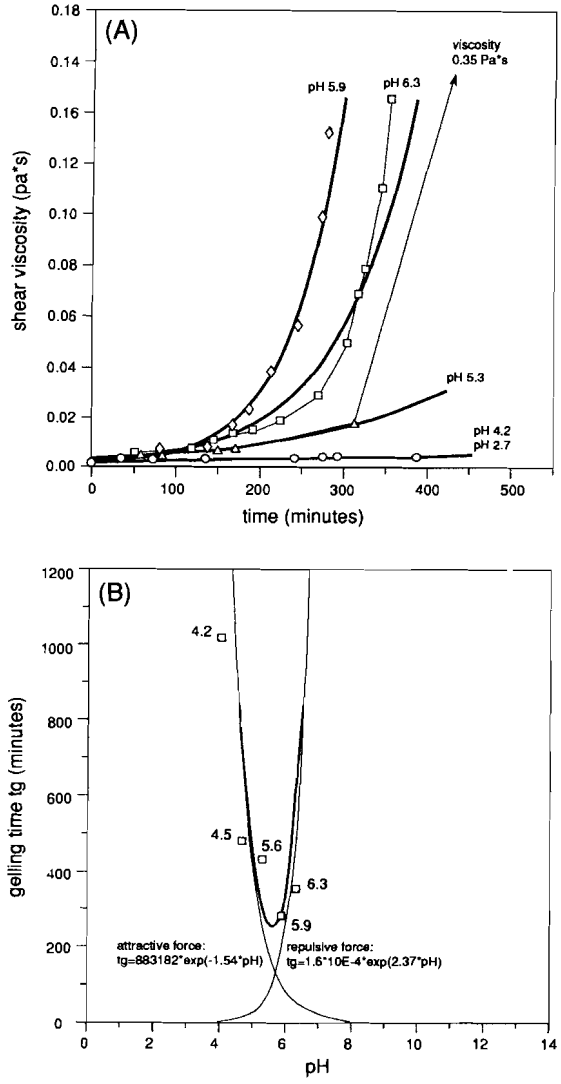

Figure 4 (a) the development of the shear viscosity in the 1.37 M Si sol with different pH, 5.9, 6.3, 5.3, 4.2, and 2.7, respectively. The solid lines represent exponential fits. (b) the gelling time, where the viscosity reaches a value of infinity as a function of the pH.

The experimental gelling time reflects the balance between the repulsive forces due to the electrostatic charge on the colloidal silica particles, which rises with the pH, and the attractive force, which increases at lower pH levels. The experimental gelling times, t_g, are in Fig. 4b described by two relations representing the attractive and the repulsive force between the colloidal silica particles. The attractive force is represented by

$$t_g = 8.83 * 10^5 \exp(-1.54 * pH) \qquad \text{(min)}$$

The repulsive force is represented by

$$t_g = 1.6 * 10^{-4} \exp(2.37 * pH) \qquad \text{(min)}$$

Shrinkage investigated by thermoporometry

Thermoporometry can provide reliable information about the effect of drying on the porous structure of the silica gels. Tab. 3 and Fig. 5a and 5b are representing the thermoporometric results measured on hydro- and xerogels. The ice-crystal radius, R_n, the pore volumes, $V_n(1)$ and $V_n(2)$, the surface area A_n, and the corrected values V_n^* and A_n^* of hydro- (H) and xerogels (X) are determined as a function of the pH during gelling. As dealt with above, the pore volume $V_n(1)$ is measured by the water freezing within the pores, and the pore volume $V_n(2)$ by subtracting the water freezing outside of the pores from the total amount of water.

Fig. 5a, which shows the ice crystal radii as a function of the gelling pH, indicates a steep increase of the pore radius from 1.9 to 3.3 nm when the gelling pH is raised from 5.0 to 6.5. Drying apparently does not significantly affect the pore dimensions; the pores within the xerogel are not narrower than that within the hydrogel. It must be concluded that gelling of the sols obtained by electrodialysis leads to a fairly stiff gel structure.

In Fig. 5b the pore volume calculated from the amount of water freezing and melting within the pores of the gels are represented as a function of the gelling pH. A more gradual rise of the pore volume than the increase of the pore radius with the pH during gelling is suggested by the measurements on gels prepared at pH levels of 2.8, 5.0, and 6.7. The pore volume measured after gelling at pH 4, however, does not exhibit the smoothly increasing pore volume.

The pore volume rather increases than decreases upon drying, which again points to a stiff gel structure. Neither the drying temperature nor aging for one month in the suspension significantly affect the porous structure of the silica gels. Aging at a low pH of 2.8 for 7.5 month in the liquid, however, raises both the pore radius and the pore

volume, but the increase of the pore volume is much higher.

Tab. 3 surveys the results more in detail. The effect of the pH during gelling on the porous structure of the hydrogel is evident from the data of Tab. 2a. The shape factor, F, indicates the presence of more cylindrical pores. The correction of the pore volume for the layer of non-freezing water is considerable. Due to the correction the pore volume has increased from 0.1 to 0.3 ml/g and from 0.3 to 0.5 ml/g. The effect of ageing in the liquid is apparent from the data of Tab. 3b. The data display a rise in a pore radius and the higher increase of the pore volume.

The effect of drying, which causes the conversion of a hydrogel to a xerogel is dealt with in Tab. 3c, 3d, and 3e. Neither the pore radius nor the pore volume significantly decrease by drying at 333 K, as shown by a comparison of the data of Tab. 3a and 3c. The steep rise of the pore radius with the gelling pH is evident from the fact that the pore radius of the silica gelled at pH 6.5 is 3.3 nm, and that of the silica gelled at pH 6.0 and dried at 333 K 2.3 nm. Drying at a higher temperature of 393 K neither decreases the pore radius and the pore volume as can be concluded from a comparison of the data of Tab. 3a and 3d. The pore radius and pore volume of the silica gelled at pH 6.0 and dried at 393 K are relatively high. The effect of previous ageing of the gel for one month is also limited as evident from Tab. 3e. The pore radius of the aged gel dried at 393 K is relatively large, viz., 3.1 nm.

The pore volume, $V_n(2)$, calculated from the amount of water outside of the pore system freezing at the temperature of bulk water is appreciably higher than that calculated from the water freezing within the pore system, which also points to the presence of a layer of non-freezing water at the pore walls. After correction for the layer of non-freezing water, some pore volumes calculated from the water freezing within the pores, $V_n(1)$, are even higher than that calculated from the water out of the pore system. With most of the samples the pore volume measured from the amount of water freezing outside of the pore system agrees reasonably well with that calculated from the water freezing within the pores after correction for the non-freezing layer of water. The mean pore volume calculated from the water freezing within the pores, $V_n(1)$, of hydro- and xerogels is 0.25 ± 0.11 ml/g and the mean pore volume calculated from the amount of water freezing at the temperature of bulk water, $V_n(2)$, 0.75 ± 0.25 ml/g. The mean pore volume $V_n(2)$ is close to the mean value of the corrected pore volume, V_n^*, of 0.6 ± 0.2 ml/g.

As mentioned in a previous chapter, the pore volume calculated from the amount of water freezing at the temperature of bulk water is liable to leakage of water into the capsule containing the sample. In Tab. 3d the pore volume of the gel obtained at a pH of 3.7 calculated from the amount of water freezing at the temperature of bulk water is considerably higher than that calculated from the water freezing within the pores, viz., 1.3 and 0.2 ml/g, respectively. Leakage of water into the sample holder thus is likely with this measurement.

The mean shape factor, F, of 1.75 ± 0.09 is between that of a spherical and cylindrical shape, but tending more to a cylindrical shape. The mean ice surface area, A_n, of 279 ± 61 m^2/g is far less than the corrected surface area, A_n^*, of 468 ± 110 m^2/g for the non-freezing layer. It is interesting to compare the surface area with the BET surface area

measured on the xerogels.

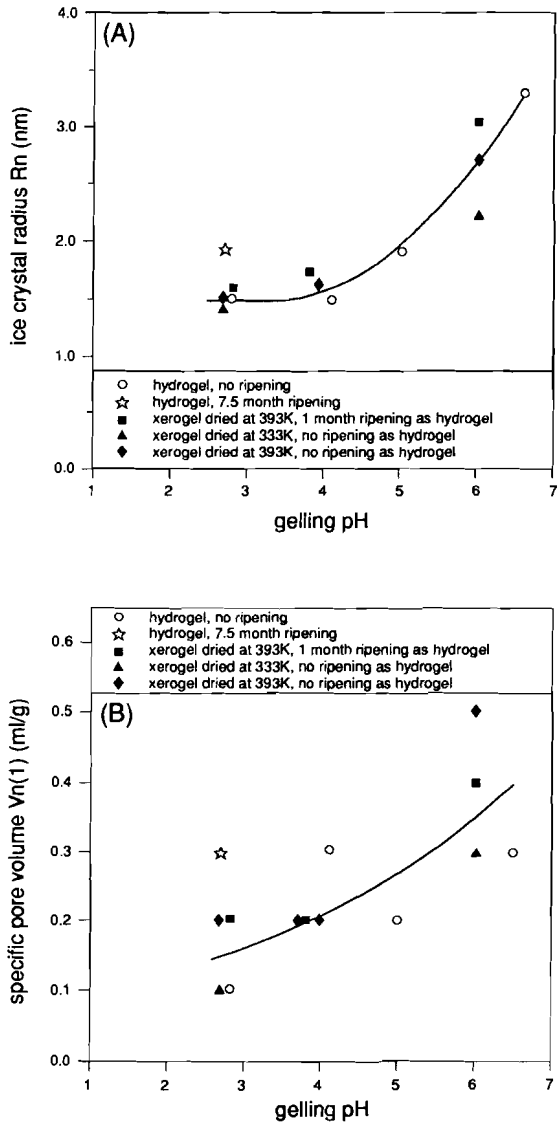

Figure 5 (a) the ice-crystal radius R_n in the pores of the gel, indicative for the pore radius R_p, as a function of the gelling pH. The solid line is a best fit increasing from 1.5 nm to 3.3 nm for a pH of 2.7 and 6.5, respectively. (b) the specific pore volume (ml.ice/g.SiO_2) as a function of the gelling pH, where the solid line is a best fit, increasing from 0.15 to 0.4 ml/g at a pH of 2.7 and 6.5, respectively.

Table 3 Thermoporometry applied on electrodialysed silica gels, both hydrogel (H) (2 $mgSiO_2$ + 32 mgH_2O) and xerogel (X) (13 $mgSiO_2$ + 21 mgH_2O) ; a) effect of the gelling pH on hydrogel, b) effect of ageing on hydrogel, c) xerogel dried at a medium temperature of 333 K, d) xerogel dried at a high temperature of 393 K, and e) effect of ageing as hydrogel on xerogel.

	pH	H/X	ripening (months)	drying T (K)	R_n (nm)	F	$V_n(1)$ (ml/g)	$V_n(2)$	V_n^*	A_n (m^2/g)	A_n^*
a)											
A	2.8	H	0	-	1.5	1.8	0.1	-	0.3	183	323
B	4.1	H	0	-	1.5	-	0.3	-	-	-	-
C	5.0	H	0	-	1.9	-	0.2	-	-	-	-
D	6.5	H	0	-	3.3	1.9	0.3	-	0.5	193	255
b)											
A	2.8	H	0	-	1.5	1.8	0.1	-	0.3	183	323
E	2.7	H	7.5	-	1.9	1.7	0.3	0.6	0.8	302	497
c)											
F	2.7	X	0	333	1.4	1.8	0.1	0.7	0.3	217	395
G	6.0	X	0	333	2.3	1.8	0.3	0.6	0.6	333	497
d)											
H	2.7	X	0	393	1.5	1.7	0.2	0.5	0.6	290	529
I	3.7	X	0	393	1.5	1.6	0.2	1.3	0.6	278	526
J	4.0	X	0	393	1.6	1.8	0.2	-	0.6	256	439
K	6.0	X	0	393	2.7	1.8	0.5	0.7	1.0	391	690
e)											
L	2.8	X	1	393	1.5	1.8	0.2	-	0.6	277	489
M	3.8	X	1	393	1.7	1.6	0.2	0.7	0.6	286	510
N	6.0	X	1	393	3.1	1.8	0.4	0.9	0.7	338	461

ripening always as hydrogel, $V_n(1)$ is the pore volume obtained from pore water, and $V_n(2)$ calculated from the amount of bulk water, V_n^* and A_n^* are the pore volume and surface area corrected for the non-freezing layer.

Sol particle size of xerogels from TEM, BET, and DRIFTS

A comparison of the sol particle size determined by dynamic light scattering (DLS) with that observed in the electron microscope and the size calculated from the BET surface area is highly relevant to assess the reliability of the dynamic light scattering. Transmission electron microscopy (TEM) indicates a sol particle size of the xerogels of 5 nm. The particle size is observed to be independent of the gelling pH (Fig. 6a to c, and Tab. 4a). The sol particles are homogeneously distributed after gelling at pH levels of 4.2 and lower, but oriented in chains after gelling at high pH levels of, e.g., 7.8. The effect of the electrostatic repulsion at higher pH levels is evident from the arrangement of the particles in chains, which keeps the electrostatic repulsion at a minimum.

From BET measurements a mean particle size of 5 nm is calculated (Tab. 4b). The particle size is calculated assuming a negligible contact area between the individual silica particles. An effect of the gelling pH on the particle size calculated from the BET surface area is not apparent. The surface area of the silica gelled at a pH level of 6.0 is relatively low, viz., 455 m^2 per g, which leads to relatively large particles, viz., of 6.0 nm. Nitrogen adsorption at 77 K (Tab. 4b) points to a mean pore volume of the xerogels of 0.55 ml/g, which again does not vary significantly with the pH of gelling.

The DRIFT spectra of xerogels gelled at pH 2.7, 4.0, 5.0, and 6.0 (set W-Z) show a sharp absorption band at 3747 cm^{-1} and a broad band at 3600-3000 cm^{-1} (Fig. 7). The absorption of the 3747 cm^{-1} band, showing an intensity which is 0.96 relative to the absorption at 4000 cm^{-1}, is independent of the gelling pH. The band at 3747 cm^{-1} is attributed to surface silanols (chemisorbed water) [9-13]. The absorption of the broad band at 3600-3000 cm^{-1} is lower at higher pH levels during gelling and ascribed to physisorbed water. From the relative absorption of 0.96 of the 3747 cm^{-1} band and the linear regression, surface area = relative absorption * 538.9 - 69.3, a surface area of 448 m^2/g is calculated, which leads to a sol particle size of 6.1 nm (Tab. 4c).

Table 4 The BET surface area, pore volume, and sol particle size of xerogels obtained from a) TEM, b) N_2 absorption (2727/BET), and c) DRIFTS

	sample	pH	drying T (K)	A_s (m^2/g)	pore volume (ml/g)	particle size (nm)
a)						
	O	4.2	293	-	-	5
	P	6.3	293	-	-	5
	Q	7.8	293	-	-	5
b)						
	R	2.8	393	612	0.54	4.5
	S	3.8	393	556	0.54	4.9
	T	5.1	393	553	-	4.9
	U	6.0	393	455	-	6.0
	V	5.0	333	573	0.58	4.8
c)						
	W	2.7	393	448	-	6.1
	X	4.0	393	448	-	6.1
	Y	5.0	393	448	-	6.1
	Z	6.0	393	448	-	6.1

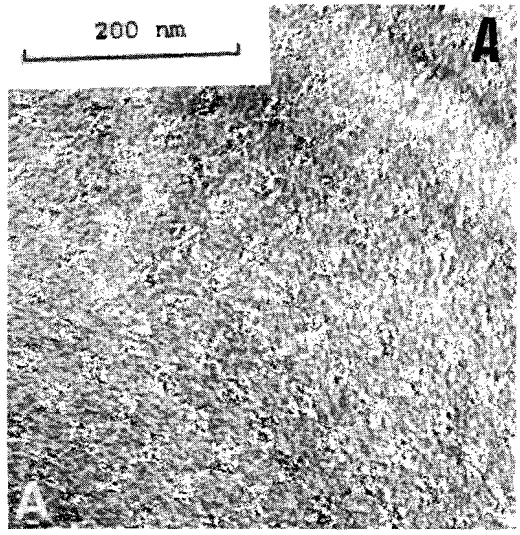

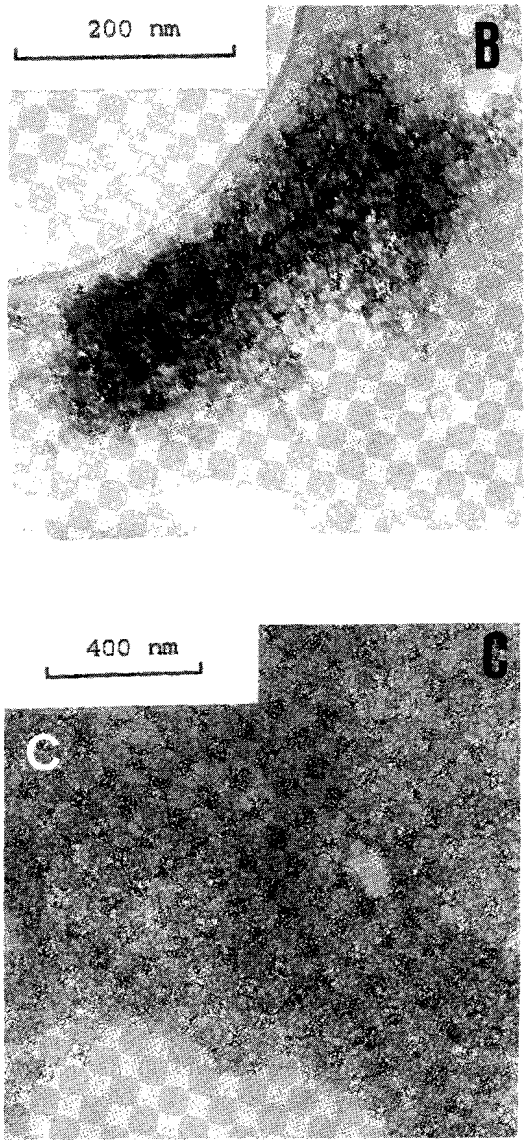

Figure 6 TEM images of silica gels, gelled at a pH of (a) 4.2, magnification to the film is 54000 times, (b) 6.3, magnification to the film 54000x, (c) 7.8, magnification to the film 18000x.

DISCUSSION

From the I-t curve (Fig. 2a) the amount of H^+ produced by the anode is calculated according to Eqn. 4

$$[H^+] = {}_0\int^T I(t)*dt/2F \qquad \text{(mole/l)} \qquad (4)$$

where $[H^+]$ is the concentration (mole/l) of the H^+ produced, F is the Faraday number ($9.6*10^4$ C/mole), and T the period of time of electrodialysis, which amounts to $88*3600 = 3.17*10^5$ s. The amount of H^+ produced, which is 0.875 mole/l, is higher than the amount of Na^+ transported, which is 0.78 mole/l. The yield of 0.78/0.875 * 100 = 89 % is equal to that of 90 % reported in [3,13]. The yield being lower than 100 % is due to the transport of minor amounts of OH^- and certainly of H^+ during the final stages of the electrodialysis, because the conductivity of H^+ is 7 times that for Na^+ [7].

The final pH of 13.2 within the cathode compartment reflects that of the produced 0.78 M NaOH solution. A large amount of silicate anions exists in the initial sodium silicate solution that react slowly with ammonium heptamolybdate. The period of time where the silicate anions have completely reacted with ammonium heptamolybdate is that where the silicomolybdate plot against the reaction time is flat (Fig. 3c). The period of time required for complete reaction drops at longer periods of time of electrodialysis. The period of time required for complete reaction is 480 s at the start of the electrodialysis, while it decreases to 120 s after 42 h of electrodialysis. The large silicate anions in the acidified anode compartment probably react first to amorphous silica, and finally the small silicate anions, because a period of time for complete reaction of 120 s reaction time is typical for MSA. The shape of the Na_a plot against dialysis time (Fig. 2b) being identical to the plot (Fig. 3b) of the silica able to react to soluble silicomolybdate, indicates that the concentration of silica soluble as silicomolybdate is equal to the sodium concentration, $[Na]_a$, present in the anode compartment.

As dialysis of the sodium silicate proceeds small silica sol particles are developed, and gelate at various values of pH according to the plot of Fig 4a. Vogelsberger et al. [8] have measured plots of the reduced viscosity between 0 and 250, thus the viscosity between $1*10^{-3}$ and 0.251 Pa*s. Our plots of Fig. 4a have the same the same shape of the initial of the curves of Vogelberger et al. [8]. The theory (see appendix) prescribes a viscosity against time plot obeying the relation :

$$\eta \approx \eta_o * \exp[A_o*([MSA]_{t=0}/S_o)*\ln[[MSA]_t/S_o] * \{(MSA_t-S_o)/S_o\} * t] \qquad (5)$$

From the relation of Eqn. 5 and our empirical relation of Eqn. 3 it can be derived that :

$$t_{gel} \sim 1/A_o \sim 1/[OH^-]^{0.7} \sim \exp[-2.3*0.7*pH] \sim \exp[-1.6*pH] \quad (6)$$

which happens to be the left hand slope of the gelling time against the gelling pH plot of Fig. 4b. The right hand slope of Fig. 4b is due to repulsion amongst negatively charged silica sol particles. The minimum in gelling time of the 1.37 M Si sol is 279 minutes at a pH of 5.9 (Fig. 4b), while the literature value is 50 minutes for 0.5 M Si sols at a pH of 5.8 [14]. Strangely the gelling time of Treadwell König [14] is short in spite of the fact that their concentration Si is low. We feel that the long periods of time for gelling exhibited in our experiments are due to the homogeneous decrease of the pH in the electrodialysis procedure, where a homogeneous solution can be easily achieved.

The negative logarithm of the ionization constant of the surface hydroxyl groups of silica in the absence of dissolved salts is 7. Using the above ionization constant it can be calculated that at a ph of 5.9, where the maximum rate of gelation is displayed, 10 % of the surface silanol groups are ionized. As dealt with in the literature, the rate of gelation is controlled by (i) the number of ionized surface silanol groups increasing with the pH, which catalyze the linking of silica spheres, which dominates below a pH level of 5.9, and (ii) the electrostatic repulsion, which dominates above a pH level of 5.9. The repulsion dominating at pH levels above about 5.5 causes a significant increase of the pore dimensions of hydro- and xerogels as measured by thermoporometry. The increased pore radius, R_n, and pore volume, $V_n(1)$, with gelation at higher pH levels exhibited in Fig. 5a and b, respectively, is due to the repulsive force between sol particles of an equal size, as confirmed on TEM micrographs (Fig. 6a-c). At high pH levels the particles are linked to particle chains enclosing relatively wide pores resulting in a larger pore volume. A pore radius, R_n, slowly increasing during ageing of the hydrogel is measured; however, the effect of ageing on the porous structure can be neglected if the gels are dried within a short period of time after gelling.

As evidenced by the R_n and $V_n(1)$ values of hydro- and xerogels of the electrodialyzed gels being equal (Fig. 5a and b), the silica gels prepared by electrodialysis display no shrinkage. The shrinking behavior of the electrodialyzed silica gels is thus completely different from the considerable shrinkage observed with gels prepared by addition of waterglass solutions to acids. The fact that silica gels prepared by electrodialysis do not shrink upon drying may be due to the absence of sodium. The electrostatic repulsive forces are larger without sodium ions being present in the solution.

The pore volumes $V_n(2)$ calculated from the amount of water freezing at the temperature of bulk water are larger than the pore volumes. $V_n(1)$, calculated from the amount of water freezing within the pores (Tab. 3). With the pore volume $V_n(2)$ clearly the non-freezing layer of a thickness 0.9 nm is involved. The mean pore volume measured by nitrogen sorption at 77 K of 0.55 ml/g is equal to the mean pore volume V_n^* measured by thermoporometry after correction for the non-freezing layer, which results in a mean value

of 0.6 ± 0.2 ml/g. The pore volume, $V_n(1)$, measured by thermoporometry may exhibit an increase at increasing pH levels during gelling. Fig. 5b suggests a pore volume rising when the gelling is performed at a pH level of 6 or higher. However, the pore volume measured by nitrogen sorption at 77 K shows a value of 0.55 ml/g that does not vary with the pH during gelling. The pore volume measured by thermoporometry and corrected for the layer of non-freezing water, which is 0.6 ml/g, neither varies with the pH during gelling. We therefore conclude that the rise in pore volume with the pH of gelling suggested by Fig. 5b is due to shorter pores with larger radii.

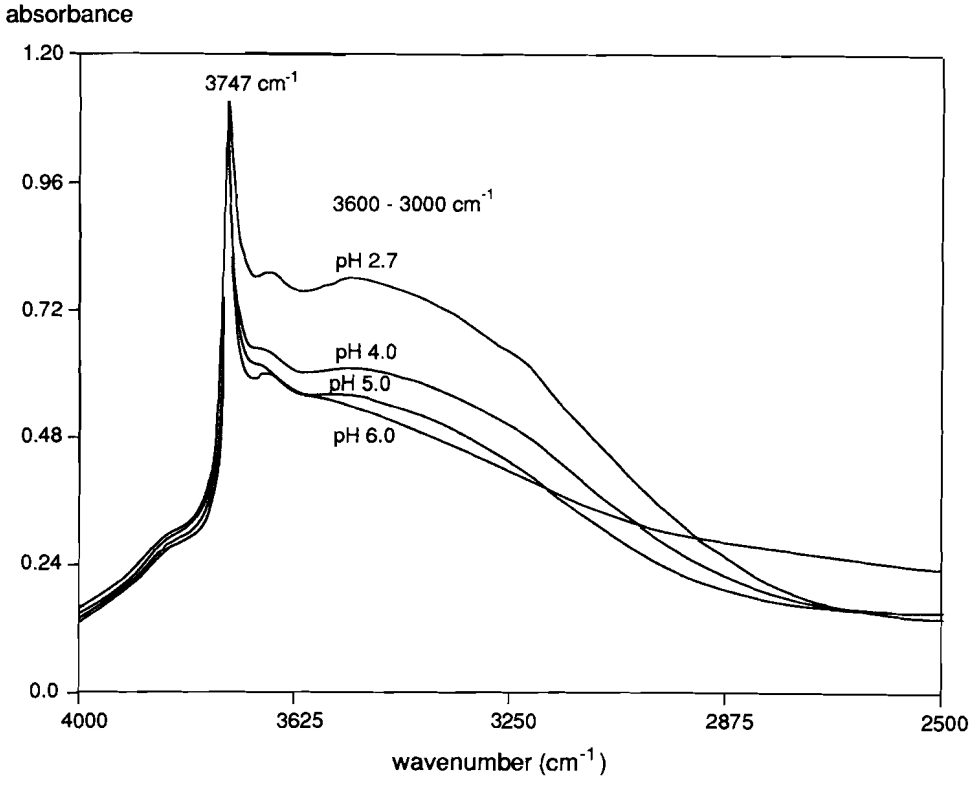

Figure 7 DRIFT spectra of silica gels, gelled at a pH of 2.7, 4.0, 5.0, 6.0, and dried at 393 K in air. Two peaks are visible, (i) a sharp peak ascribed to silanols, which intensity is independent of the gelling pH, and (ii) a broad absorption band between 3000 and 3600 cm^{-1} ascribed to physisorbed water, which decreases with increased gelling pH.

To establish the presence of a non-freezing water layer, it is highly interesting to compare the surface areas calculated from the thermoporometric data with the reliably measured BET surface areas. The xerogels obtained after drying the hydrogels at 393 K exhibit BET surface areas varying from 455 to 612 m^2 per g. The surface area does not seem to be related to the pH during gelling. Before correction for the non-freezing water layer, the surface area calculated from the thermoporometric data varies from 256 to 391 m^2 per g. The surface areas, A_n^*, resulting from correction of the thermoporometric surface areas, is between 439 and 690 m^2/g. Comparison of the surface areas of Tab. 3d and table 4b unambiguously indicates the relevance of the correction for the layer of non-freezing water.

The surface area of the xerogels obtained from transmission electronmicroscopy (TEM) assuming isolated particles is equal to the surface area measured using the BET procedure, which deals with coherent particles. The fact that the surface areas calculated from TEM and nitrogen sorption do not differ indicates that the extent of branching of the sol particles is low, and that neck-growth between the particles can be neglected. The low amount of dissolved electrolytes with the sols prepared by electrodialysis and the resulting strong electrostatic repulsion are causing the arrangement of silica particles in chains, which leads to a small contact surface area of the silica particles.

Another highly interesting comparison is that between the particle size observed in the transmission electron microscope and the size determined by dynamic light scattering (DLS). With TEM the volume being analyzed is usually very small and always the question about the relevance of the measurements has to be raised. The fact that the BET surface areas, which are measured on much larger sample volumes, agree with the size of the silica particles determined by TEM demonstrates that the TEM results are reliable. First of all it is interesting that the rough estimate of the particle size measured with the Malvern Multibit K 7025 at a wavelength of 488.0 nm agrees perfectly with the size resulting from electronmicroscopy and BET surface area determination. The particle size determined with the Malvern 4700 C at a wavelength of 632.8 nm is 7.3 nm, which is substantially larger. It is obvious to assume the layer of non-freezing water to be tightly attached to the silica particles and to diffuse together with the particle through the liquid. The difference in the particle size, which amounts to $(7.3\text{-}5)/2 \approx 1$ nm, which is remarkably equal to the thickness of the non-freezing layer. Shrinking of the silica particles during drying may also proceed. Finally clustering of the elementary silica particles in the liquid may be present, which raises the mean particle size measured by DLS.

The specific surface area calculated from DRIFTS is about 100 m^2/g smaller than the surface area calculated from TEM images and determined according to the BET procedure from the adsorption of nitrogen at 77 K. The surface area from DRIFTS is only about 20 m^2/g smaller than the surface area, A_n^*, measured by thermoporometry. Probably an amount of physisorbed water decreases the absorption at 3747 cm^{-1}. The infrared absorption of physisorbed water between 3600 and 3000 cm^{-1} clearly drops at a higher pH during gelling (Fig. 7). Because the larger pore size $R_n(1)$ and higher pore volume $V_n(1)$ at higher pH during gelling is established by thermoporometry, the amount of physisorbed water will be lower with larger pore radius and pore volume. Keeping the samples at a

temperature of 453 K instead of at 393 K may be required to remove the physically adsorbed water [12].

CONCLUSIONS

1) Silica gels are manufactured by electrodialysis, during which silicate anions polymerize to small sol particles, which link together in a gel. The polymerization proceeds by removal of Na and simultaneously lowering of the pH from 11.3 to 2.8. The course of the decrease in the amount of silica soluble as silicomolybdate is equal to that of the drop in the Na^+ concentration during electrodialysis.

2) The mean size of the silica particles within the sol formed in a dilute sodium silicate solution measured by DLS is 7.3 ± 0.6 nm. The thus measured size increases with ageing, and decreases by dissociation of aggregates or by dissolution during dilution from 0.27 to 0.15 M Si.

3) The viscosity of the dialysed sol, brought at the desired pH level with some NaOH solution, increases due to cluster formation. The most rapid rate of gelling and thus most rapidly increasing viscosity is measured at a pH of 5.9. Below a pH of 5.9 the rate of gelling drops due to the small fraction of ionized surface silanol groups. Above a pH of 5.9 the rate decreases due to the repulsion between the negatively charged sol particles.

4) No shrinkage takes place with air drying of the hydrogels to the xerogels, as is evident from the equal pore dimensions measured by thermoporometry.

5) The size of the sol particles within the xerogels measured with TEM is independently of the pH during gelling 5 nm, which is equal to the size calculated from the BET surface area. The size determined by TEM and N_2 adsorption is smaller than the size of 7.3 nm determined by dynamic light scattering (DLS), presumably due to a structural layer of water of a thickness of about 1 nm tightly bound to the silica.

6) An ice crystal radius, R_n, and pore volume, $V_n(1)$, in the pores of samples increasing with the pH level during gelling is established with thermoporometry. For example R_n increases from 1.5 to 3.3 nm, and $V_n(1)$ from 0.1 to 0.5 ml/g after gelling at a pH level of 2.8 and 6.0, respectively.

7) The pore volume, $V_n(1)$, obtained from thermoporometry, ranging from 0.1 to 0.5 ml/g, is smaller than the pore volume, $V_n(2)$, calculated from the amount of water exhibiting the freezing temperature of bulk water, which ranges from 0.6 to 1.3 ml/g. The procedure using the freezing of bulk water leading to a mean value of the pore volume of 0.75 ± 0.25 ml/g clearly measures also the non-freezing layer of about 0.9 nm. Correction of $V_n(1)$ for this layer yields a value, V_n^*, of 0.6 ± 0.2 ml/g, which agrees well with $V_n(2)$, and even better with the pore volume of 0.55 ml/g determined by nitrogen sorption at 77 K. The thickness of the non-freezing layer measured with thermoporometry is equal to the thickness of about 1 nm of the structural layer apparent from the dynamic light scattering (DLS) results.

8) The specific surface area obtained by measuring the absorption of the band at 3747 cm^{-1} by DRIFTS is lower than the BET surface area of 550 m^2/g. The difference is probably due to the amount of physisorbed water, affecting the intensity of absorption at 3747 cm^{-1}. The amount of physisorbed water, measured between 3000 and 3600 cm^{-1} in the DRIFT spectrum, decreases with pore size increasing after gelling at a high pH level.

ACKNOWLEDGMENTS

The authors thank Dr. J.K.G. Dhont for the review of the dynamic light scattering theory.

REFERENCES

1. W.D. Treatwell, and W. Wieland, *Helv. Chim. Acta*, **13** (1330) 842-864
2. R.K. Iler, U.S. Patent 3668088, Method of Producing Colloidal Silica by Electrodialysis of a Silicate (1972)
3. M. Seko, *Ind. Eng. Chem., Prod. Res. Dev.*, **15** (1976) 286
4. R.K. Iler, The Chemistry of Silica, Wiley Interscience, New York (1979), 94-101
5. A.H. Boonstra, T.P.M. Meeuwsen, J.M.E. Baken, G.V.A. Aben, *J. Non-Cryst. Solids*, **109** (1989) 153
6. J.S. Lowell, J.E. Shields, 'Powder surface area and porosity', 2nd ed., Chapman and Hall, London (1984), 1-135
7. P.W. Atkins, Physical Chemistry, 2nd. Ed., Oxford University Press (1982), 888-919
8. W. Vogelsberger, J. Opfermann, U. Wank, H. Schutze, G. Rudakoff, J. Non-Cryst. Sol., **145** (1992) 20-24
9. B.A. Moorow, J.D. Gay, *J. Phys. Chem.*, **92** (1988) 5569

10. Physical and Chemical Aspects of Adsorbents and Catalysts, Ed. B.G. Linsen, Academic Press, London (1970), 248-264
11. J.H. de Boer, M.E.A. Hermans, and J.M. Vleeskens, Proceedings of the Koninklijke Nederlandse Akademie van Wetenschappen, series B physical sciences, north-holland publishing company, **60** (1957) 45-59, 234-244
12. Y. Otsuboo, M. Horigome, K. Umeya, *J. Coll. Interf. Sci.*, **83** (1981) 240
13. S. Kondo, H. Fujiwara, T. Ischii, and J. Tsuboi, *J. Chem Soc. Faraday Transactions* (I), **75** (1979) 646
14. W.D. Treadwell, and W. König, *Helv. Chim. Acta*, **16** (1933) 468
15. V.R. Kaufman, S.C. Müller, K.H. Müller, D. Avnir, *Chem. Phys. Lett.*, **142** (1987) 551
16. W. Vogelsberger, *J. Coll. Interf. Sci.*, **103** (1985) 448
17. W. Vogelsberger, *J. Coll. Interf. Sci.*, **88** (1982) 17
18. W. Vogelsberger, *Z. Phys. Chem.*, Leipzig **258** (1977) 763
19. B.J. Berne, and R. Pecora, 'Dynamic Light Scattering with Applications to Chemistry, Biology, and Physics', John Wiley and Sons, New York (1976)
20. R. Pecora, 'Dynamic Light Scattering, Applications of Photon Correlation Spectroscopy', Plenum Press, New York (1985)

APPENDIX

A model for the increased viscosity with the sol-gel transformation

Vogelsberger et al. [8,16-18] have derived a model for the increased viscosity with gelling of the sol. The model is based on the nucleation and condensation of supersaturated vapor to microclusters of liquid in finite systems. The energy, $E_{k,f}$, involved with nucleation and condensation is expressed by :

$$E_{k,f} = \int V^* dP + w_{ref} \quad (J) \qquad (7)$$

which can be rewritten to :

$$E_{k,f} = {}_{Pa}\int^{Pe} V^* dP + \int \gamma^* dA \quad (J) \qquad (8)$$

and by a circular integral to :

$$E_{k,f} = {}_{Pa}\int^{Po} V*dP + dV*P_o + {}_{Po}\int^{Pe} (V-n_lV_L)*dP + \int \gamma*dA \quad (J) \qquad (9)$$

where P_a is the initial pressure (Pa), P_e the final pressure (Pa), P_o the normal saturation pressure, V the volume of the system (m^3), n_l the number of liquid molecules (mole), V_L the molar volume of the condensed liquid (m^3/mole), γ the surface tension of the liquid (N/m), and dA the increased surface area of the condensed liquid particles (m^2). The number of moles vapor, n_v, and liquid, n_l, is constant on N moles :

$$n_v + n_l = N \quad (mole) \qquad (10)$$

$$dV*P_o = (N-n_v)*V_V*P_o = n_l*RT \quad (J) \qquad (11)$$

The term $dV*P_o$ neglects the increased volume of the liquid as compared to that of the decreased volume of the vapor, where V_V is the molar volume of the vapor.

$$E_{k,f} = (n_l+n_v)*\ RTln[P_o/P_a] + n_l*RT + n_v*\ RTln[P_e/P_o] + \int \gamma*dA \qquad (12)$$

$$P_e/P_a = n_v / (n_v+n_l) = (1- n_l/N) \qquad (13)$$

The supersaturation, y, is expressed by :

$$y = P_a/P_o \qquad (14)$$

and therefore :

$$E_{k,f} = -N*\ RTln[y] + n_l*RT + (N-n_l)*\ RTln[(P_a/P_o)*(P_e/P_a)] + \int \gamma*dA \qquad (15)$$

$$E_{k,f} = -N*\ RTln[y] + n_l*RT + (N-n_l)*\ RTln[y*(1- n_l/N)] + \int \gamma*dA \qquad (16)$$

which can be rewritten to :

$$E_{k,f} = N*RT\{-\ln[y] + (n_l/N) + (1- n_l/N)* RT\ln[y*(1- n_l/N)] + \int \gamma*dA/N*RT\} \quad (J) \qquad (17)$$

The term comprising the surface tension, γ, can be expressed in the number of liquid particles, M, and the surface area of one particle, $4\pi r^2$, by :

$$\int \gamma*dA/N*RT = M*4\pi r^2*\gamma/N*RT \qquad (18)$$

where r is the radius of the particle. The fraction of molecules in the liquid phase is expressed by :

$$n_l/N = M*4\pi r^3/3N*V_L \qquad (19)$$

and the ratio of the number of particles, M, and number of molecules, N (mole), is expressed by :

$$Z = M/N \quad (mole^{-1}) \qquad (20)$$

The energy, $E_{k,f}$, involved with nucleation and condensation can be expressed in the particle radius r by :

$$E_{k,f}/N = RT\{-\ln[P_a/P_o] + Z*4\pi r^3/3V_L + (1-Z*4\pi r^3/3V_L)*RT\ln[P_a/P_o*(1-Z*4\pi r^3/3V_L)] + Z*4\pi r^2*\gamma/RT\} \quad (J/mole) \qquad (21)$$

$$E_{k,f}/N = RT\{-\ln[P_a/P_o] + Z*b*r^3 + (1-Z*b*r^3)*RT\ln[P_a/P_o*(1-Z*b*r^3)] + Z*a*r^2*\gamma\} \quad (J/mole) \qquad (22)$$

where two terms a and b, respectively, are introduced :

$$a = 4\pi/RT \ (mole/J), \ b = 4\pi/3V_L \ (mole/m^3) \qquad (23)$$

With the formation of a number of liquid particles M a path in the valley in the energy of $E_{k,f}/N$ is followed and expressed by :

$$d(E_{k,f}/N)/dr = 0 \qquad \text{(J/mole*m)} \qquad (24)$$

which leads to :

$$2V_L * \gamma/RT * r = \ln [(P_a/P_o) * (1 - Z * b * r^3)] = \ln[P_g/P_o] \qquad (25)$$

which we recognize as the Kelvin equation where P_g is the equilibrium pressure of a particle with radius r.

-kinetic of condensation.

The rate of increasing liquid molecules is given by :

$$dn_l/dt = M * 4\pi r^2 * (\alpha - ß) \qquad \text{(mole/s)} \qquad (26)$$

α is a term which describes the rate of condensing vapor molecules, n_v, on the surface per unit time (mole/m^2*s), and ß the evaporating liquid molecules, n_l, from the surface per unit time (mole/m^2*s). From the kinetic theory of gases can be derived :

$$\alpha = \sigma * n_v * \sqrt{(kT/2\pi m)}/V \qquad \text{(mole/m}^2\text{*s)} \qquad (27)$$

where σ is a condensation coefficient, and m the mass (kg)

$$ß = \sigma * (n_o * f(r)) * \sqrt{(kT/2\pi m)}/V \qquad \text{(mole/m}^2\text{*s)} \qquad (28)$$

where $n_o * RT = P_o * V$, and f(r) a function of the particle radius r [16-18].

$$dn_l/dt = M * 4\pi r^2 * \sigma * (n_v - n_o * f(r)) * \sqrt{(kT/2\pi m)}/V \qquad \text{(mole/s)} \qquad (29)$$

$$dn_l/dt = M*4\pi r^2*\sigma*(N-n_l-n_o*f(r))*\sqrt{(kT/2\pi m)}/V \quad \text{(mole/s)} \quad (30)$$

The condensation rate in a finite system is given by :

$$J_F = (1/V) * dn_l/dt \quad \text{(mole/m}^3\text{*s)} \quad (31)$$

thus :

$$J_F = M*4\pi r^2*\sigma*(N/V)^2*(1/N)*(1-n_l/N-(n_o/N)*f(r))*\sqrt{(kT/2\pi m)} \quad (32)$$

rewritten to :

$$J_F = \sigma*M*4\pi r^2*\sqrt{(kT/2\pi m)}*(N/V)^2*(1/N)*\{1-n_l/N-(1/y)*f(r)\} \quad (33)$$

$$J_F = \sigma*(3V_L/r)\sqrt{(kT/2\pi m)}*(N/V)^2*(M*4\pi r^3/3V_LN)*\{1-n_l/N-(1/y)*f(r)\} \quad (34)$$

$$J_F = \sigma*(3V_L/r)\sqrt{(kT/2\pi m)}*(N/V)^2*(n_l/N)*\{1-n_l/N-(1/y)*f(r)\} \quad (35)$$

with aid of :

$$2V_L*\gamma/RT*r = \ln [y*(1-Z*b*r^3)] \quad (36)$$

J_F can be rewritten to :

$$J_F = \sigma*(3N_{av}/2\gamma)\sqrt{((kT)^3/2\pi m)}*(N/V)^2*(n_l/N)*\ln[y*(1-n_l/N)]*\{1-n_l/N-(1/y)*f(r)\} \quad (37)$$

Hence, in the case of silica sol particles formed from supersaturated MSA solutions Vogelsberger et al. [8] arrive at :

$$1/V * dn_s/dt = A_1*y*n_s*\ln[y*(1-n_s/n_t)] * \{1-n_s/n_t-1/y\} \quad \text{(mole/m}^3\text{*s)} \quad (38)$$

n_s is the amount solid (mole), n_t the total amount Si (mole), A_1 is a constant, and f(r) is assumed 1. According to Vogelsberger et al [8] the increasing viscosity in the early stages of the sol-gel transformation can be well described by ;

$$d\eta_r/dt = A_o * y * \eta_r * \ln[y(1-(\eta_r/B_o y))] * \{1-(\eta_r/B_o y)-1/y\} \quad (s^{-1}) \quad (39)$$

A_o and B_o are given by ;

$$A_o = k_o * [OH^-]^{0.7} * \exp[-E_a/RT] \quad (s^{-1}) \quad (40)$$

and :

$$B_o = S_o * V_m * (\eta_r/\Phi) \quad (41)$$

where η_r denotes the reduced viscosity $(\eta/\eta_o)-1$, t the time (s), y the initial supersaturation $[MSA]_{t=0}/S_o$, k_o a pre-exponential frequency factor (s^{-1}), $[OH^-]$ the hydroxide concentration (mole/l), E_a the activation energy (kJ/mole), R = 8.3 J/mole*K, T the temperature (K), S_o the silica solubility, V_m the molar volume of the sol forming species (silica) (m^3/mole), Φ the volume fraction of silica, and η_r/Φ is a geometric factor, which is 5/2 for spheres.

(1) the term $\eta_r/B_o(t)y$ can be rewritten to $\Phi/(S_o * V_m(t) * y) \sim [SiO_2]/(S_o * y) \sim [SiO_2]/[MSA]_{t=0}$
(2) the complex term $y(1-(\eta_r/B_o(t)y)) \sim ([MSA]_{t=0}/S_o) * (1-[SiO_2]/[MSA]_{t=0}) \sim ([MSA]_{t=0}-[SiO_2])/S_o \sim [MSA]_t/S_o$, the supersaturation with time
(3) the complex term $\{1-(\eta_r/B_o(t)y)-1/y\} \sim ([MSA]_{t=0}-[SiO_2]-S_o)/[MSA]_{t=0} \sim ([MSA]_t-S_o)/[MSA]_{t=0}$

In our system with already formed sol particles, $[MSA]_t$ is assumed constant with time. With $\eta > \eta_o$ follows for the viscosity :

$$\eta \approx \eta_o * \exp[A_o * \ln[[MSA]_t/S_o] * \{([MSA]_t-S_o)/S_o\} * t] \quad (42)$$

Dynamic Light Scattering (Photon Correlation Spectroscopy)

The method of DLS is based on the observation that the fluctuation in the intensity of light scattered by the silica solution is a function of the Brownian motion of the sol particles [19,20]. The intensity shall fluctuate around the mean intensity $<I(q)>$, which results from the scattering of the individual particles. The motion of the particles causes the intensity of the scattered light to fluctuate at a rate depending on the particle size. Small particles move faster and cause a more rapid fluctuation of the scattered light. The fluctuations are analyzed with a digital autocorrelator.

We consider two particles at a distance $\underline{r}$ scattering light through the same angle θ. To deal with the phase difference of the light scattered by the two particles, a scattering vector $\underline{q}$ is defined. The vector $\underline{q}$ is the resultant of an incoming wave vector $\underline{k}_o$ of magnitude $n*2\pi/\lambda$, and a scattered vector $\underline{k}_f$ of magnitude $n*2\pi/\lambda$ at an angle θ.

$$|\underline{q}| = |\underline{k}_f - \underline{k}_o| = 2\,|\underline{k}_o|\sin(\theta/2) = n*4\pi/\lambda\,\sin(\theta/2)\ (nm^{-1}) \qquad (43)$$

where n is the refractive index of water (containing the silica sol), which is approximately 1.333, and λ the wavelength of the He-Ne laser of 632.8 nm or the Ar laser of 488.0 nm, and θ the angle of scattering. The difference in phase $\Delta\Phi$ of the light beam scattered by the two particles is $(\underline{k}_f - \underline{k}_o).\underline{r}$.

The autocorrelation function $g(q,p\tau)$ is defined as the mean product of the intensity $I(q,t_j)$ on time t_j with the intensity $I(q,t_j+p\tau)$ after a number p of a chosen time interval τ resulting in a period of time $p\tau$. The above mean product is the average over a large number N of intensities recorded at times t_j :

$$g(q,p\tau) = 1/N * \Sigma_{j=1}^{N} \{I(q,t_j+p\tau) * I(q,t_j)\} \qquad (W^2/m^4) \qquad (44)$$

$$= <I(q,t+p\tau)*I(q,t)>$$

Three properties of the correlation function are,

$$p\tau = 0\ ;\ g(q,0) = <I(q,t)^2> \qquad (45)$$

$$p\tau = \infty\ ;\ g(q,\infty) = <I(q,t+\infty)*I(q,t)> = <I(q,t+\infty)> * <I(q,t)> \qquad (46)$$

$$= <I(q,t)>^2$$

because $I(q,t+\infty)$ is statistically independent of $I(q,t)$, and

$$<I(q,t)^2> \; > \; g(q,p\tau) \; > \; <I(q,t)>^2 \qquad (47)$$

The correlation function $g(q,p\tau)$ is related to the particle size d_h of the silica. Two particles with index k have a distance $\underline{r}$ before- and a distance $\underline{r}+\Delta\underline{r}$ after a time interval $p\tau$, thus a difference $|\,\underline{r}(t+p\tau)-\underline{r}(t)\,|$. The change in phase difference $d\Delta\Phi$ is

$$d\Delta\Phi \; = \; \underline{q}.\{\underline{r}(t+p\tau)-\underline{r}(t)\} \; = \; |\,\underline{q}\,| \; * \; |\,\Delta\underline{r}\,| \; * \cos ß \qquad (48)$$

where $d\Delta\Phi$ the phase change, $\underline{q}$ the scattering vector, $\Delta\underline{r}$ the displacement vector of the particle after a time with magnitude $p\tau$, ß is the angle between the scattering vector $\underline{q}$, and the displacement vector $\Delta\underline{r}$. The particles move randomly over all angles ß. The product of the wave function of the electromagnetic radiation $E^*(q)$, scattered at time t_i and $E(q,\Delta\underline{r})$ at time $t_j+p\tau$ of all the particles M is expressed by :

$$\Sigma^M_{k=1}\,\Sigma^M_{l=1}\,E_k(q,t+p\tau)*E_l^*(q,t) \; = \; \Sigma^M_{k=1}\,\Sigma^M_{l=1}\,E_k(q,\Delta\underline{r})*E_l^*(q) \qquad (49)$$

$$\sim \; (B(q)/M)*\Sigma^M_{k=1}\exp\{i*d\Delta\Phi\} \; + \; \Sigma^M_{k\neq l=1}\{E_k(q,\Delta\underline{r})*E_l^*(q)\}$$

$$\approx \; B(q)/M \; * \; \Sigma^M_{k=1}\,\exp\{i*\underline{q}.\Delta\underline{r}_k\}$$

$$= \; B(q)/M \; * \; \Sigma^M_{k=1}\,\exp\{i* \; |\,\underline{q}\,| \; * \; |\,\Delta\underline{r}_k\,| \; *\cos\delta_k\}$$

where B(q) is an experimentally determined factor, and M the number of silica particles. By neglecting the interactions between the particles in the dilute silica solution, the second term $\Sigma^M_{k\neq l=1}\,E_k(q,\underline{r})*E_l^*(q)$ disappears, and Eqn. 49 is a function of the displacements, Δr_k, of the isolated particles. The factor B(q) is a function of the laser power output I_o (W/m^2), wavelength λ (nm), and scattering vector $\underline{q}$ given by

$$B(\underline{q}) \; \equiv \; [M]*<I(\theta,t)> \qquad (W/m^5) \qquad (50)$$

$$= \; I_o*2\pi^2*n_o^2(dn/dc)^2c*(1+\cos^2\theta)*Mw*P(\underline{q})*S(\underline{q}) \; / \; R^2*N_{av}*\lambda^4$$

where [M] is the concentration of particles (m^{-3}), $<I(\theta)>$ the mean scattered intensity of

one particle (W/m^2), n_o the refractive index of the dispersion, dn/dc the slope of the increase of the refractive index with rising silica concentration (m^3/g), c the silica concentration (g/m^3), R the distance to the detector (m), N_{av} Avogadro's number ($mole^{-1}$), P(q) and S(q) the intra- and interparticle scattering functions, and Mw the molar weight of the silica particles (g/mole), expressed in the diameter d (m) by :

$$Mw = (N_{av} * \pi * density/6) * d^3 \qquad (g/mole) \qquad (51)$$

where the density is that of silica (g/m^3). The intraparticle scattering function $P(q) \approx 1$ for $q*d \ll 6$, which is the case for the silica particles of a diameter of 5 nm with $q \approx 10^{-2}$ nm^{-1}. The interparticle scattering function $S(q) \approx 1$ in the dilute silica solution.

From Fick's second law applied in three dimensions follows [7];

$$1/M * \Sigma_{k=1}^{M} \Delta r_k^2 = 6Dp\tau \qquad (m^2) \qquad (52)$$

where D is the diffusion constant of the silica particles (m^2/s), p an integer, and τ the interval time. The correlation function is also a function of q, D, and $p\tau$. The correlation function $g(q,p\tau)$ is the average of $I(q,t_j+p\tau)*I(q,t_j)$ over a large amount number of instances, t_j, according to Eqn. 44 :

$$\begin{aligned} g(q,p\tau) = {} & <E(q,t+p\tau)E^*(q,t+p\tau)*E(q,t)E^*(q,t)> = \qquad (53) \\ & <E(q,t+p\tau)E^*(q,t+p\tau)> * <E(q,t)E^*(q,t)> + \\ & <E(q,t+p\tau)E^*(q,t)> * <E(q,t)E^*(q,t+p\tau)> + \\ & <E(q,t+p\tau)E(q,t)> * <E^*(q,t)E^*(q,t+p\tau)> \end{aligned}$$

or

$$g(q,p\tau) = <I(q,t)>^2 + |<E(q,t+p\tau)E^*(q,t)>|^2 + |<E(q,t+p\tau)E(q,t)>|^2 \qquad (54)$$

which can be expressed as

$$g(q,p\tau) = <I(q,t)>^2 + f^2(p\tau) + \delta^2(q) \qquad (55)$$

The third term of the right-hand side of Eqn. 54 and Eqn. 55 is the square of a Dirac δ function in q, which is 0 for $q \neq 0$. The function $f(p\tau)$ of Eqn. 55 can be rewritten using Eqn. 49 as :

$$f(p\tau) = (<I(q,t)>/M) * \mid \Sigma_{k=1}^{M} \exp\{i*\underline{q}.\Delta\underline{r}_k\} \mid \qquad (56)$$

$$= <I(q,t)> * \mid \int dr\, P(\underline{r}/p\tau)*\exp\{i*\underline{q}.\Delta\underline{r}_k\} \mid$$

where $P(\Delta\underline{r}/p\tau)$ is the probability function to find a particle at distance $\Delta\underline{r}$ after a time $p\tau$, and

$$_0\int^{\infty} d\Delta\underline{r}\, P(\Delta\underline{r}/p\tau) = 1 \qquad (57)$$

The integration of Eqn 56 can be converted to a time-dependent function, applying Fick's law :

$$d/dp\tau\, P(\Delta\underline{r}/p\tau) = D * \nabla^2 P(\Delta\underline{r}/p\tau) \qquad (58)$$

$\nabla = d/d\Delta\underline{r}$, and

$$d/dp\tau \mid \int d\Delta\underline{r}\, P(\Delta\underline{r}/p\tau)*\exp\{i*\underline{q}.\Delta\underline{r}\} \mid = D* \mid \int d\Delta\underline{r}\, \nabla^2 P(\Delta\underline{r}/p\tau)*\exp\{i*\underline{q}.\Delta\underline{r}\} \qquad (59)$$

$$= \mid D*[\nabla P(\Delta\underline{r}/p\tau)*\exp\{i*\underline{q}.\Delta\underline{r}\}]_0^{\infty}$$

$$- D*[i\underline{q}.\nabla\Delta\underline{r}\, P(\Delta\underline{r}/p\tau)*\exp\{i*\underline{q}.\Delta\underline{r}\}]_0^{\infty}$$

$$- Dq^2* \nabla\Delta\underline{r} * \int d\Delta\underline{r}\, P(\Delta\underline{r}/p\tau)*\exp\{i*\underline{q}.\Delta\underline{r}\} \mid$$

The probability to find the particle at exactly the same place, $P(0/p\tau)$, is 0, and the probability to find the particle at infinite distance, $P(\infty/p\tau)$, is 0, hence :

$$d/dp\tau \mid \int d\Delta\underline{r}\, P(\underline{r}/p\tau)*\exp\{i*\underline{q}.\Delta\underline{r}\} \mid = - Dq^2* \mid \int d\Delta\underline{r}\, P(\Delta\underline{r}/p\tau)*\exp\{i*\underline{q}.\Delta\underline{r}\} \mid \qquad (60)$$

The integration of Eqn. 60 results in

$$| \int d\Delta\underline{r}\ P(\Delta\underline{r}/p\tau)^{*}\exp\{i^{*}\underline{q}.\Delta\underline{r}\} | \ = \exp[-Dq^{2}p\tau] \qquad (61)$$

and the substitution of $f(p\tau) = <I(q,t)>\exp\{-Dq^{2}p\tau\}$ into Eqn. 55 yields ;

$$g(q,p\tau) \ = \{1+\exp[-2Dq^{2}p\tau]\} \ ^{*} \ <I(q,t)>^{2} \qquad (62)$$

Eqs. 45 and 46 lead for the correlation function $g(q,p\tau)$ to

$$g(q,0) \ = \ 2<I(q,t)>^{2} \approx \ <I(q,t)^{2}> \qquad (63)$$

$$g(q,\infty) \ = \ <I(q,t)>^{2} \qquad (64)$$

The experimentally determined function $g(q,p\tau)$ strongly depends on a correct selection of the interval time τ. Too high values of τ result in a flat $g(q,p\tau)$ curve, and no value of D can be determined. The value of τ is selected by the Malvern System 4700, and is of the order of few μs. The $g(p,p\tau)$ is determined as a function of p, where p counts from 1 to 128 for the 128 channel correlator. From the slope of the $g(p,p\tau)$ curve, $-2Dq^{2}p\tau$, the diffusion constant D can be calculated. The slope of the autocorrelation function is determined in two ways, viz., (i) by a least square fitting of $g(q,p\tau)$ by one exponential function (exp. fit), comprising the terms a and b of Eqn 65, or (ii) a cumulant fit (cum. fit), where $\ln [g(q,p\tau)-<I(q,t)>^{2}/<I(q,t)>^{2}]$ is recorded as a function of $p\tau$ and fitted with Eqn. 65 :

$$\ln [g(q,p\tau)-<I(q,t)>^{2}/<I(q,t)>^{2}] = a + b^{*}p\tau + c^{*}(p\tau)^{2} \qquad (65)$$

where the diffusion constant D is derived from b which is $-q^{2}{}^{*}2D$, and Q is c/b^{2}. Q is a constant which describes the deviation of ideal behavior. A constant Q above 0.02 to 0.03 indicates a poly-disperse sol solution. The relative polydispersity in size is equal to the square root of Q.

The diameter d_h of the sol particle follows from the Stokes-Einstein relation in ref. [7] :

$$d_h = k*T / 3\pi\eta D = 4.3*10^{-10}/D \text{ (nm) at 293 K} \qquad (66)$$

$$4.9*10^{-10}/D \text{ (nm) at 298 K}$$

where k is Boltzmann's constant of $1.38*10^{-23}$ J/K, T the temperature (K), η the viscosity of $1*10^{-3}$ Pa*s at 293 K or $0.89*10^{-3}$ Pa*s at 298 K, D the diffusion constant (m^2/s).

Chapter 8

Characterization of tubular chrysotile by thermoporometry nitrogen sorption, DRIFTS and TEM*

Mark K. Titulaer[1], J. Cees van Miltenburg[2], J. Ben H. Jansen[1], and John W. Geus[3]

[1]Department of Geochemistry, Institute for Earth Sciences, University of Utrecht, Budapestlaan 4, P.O. Box 80.021, 3508 TA Utrecht, The Netherlands; [2]Chemiaboutl Thermodynamics Group, University of Utrecht, Transitorium 3, Padualaan 8, 3584 CH Utrecht, The Netherlands;
[3]Department of Inorganic Chemistry, University of Utrecht, Sorbonnelaan 16, P.O. Box 80.083, 3508 TB Utrecht, The Netherlands.

*This paper is a contribution of the Debye Institute, University of Utrecht, the Netherlands.

ABSTRACT

The maximum crystal radius R_n of ice in hollow wet chrysotile tubes is established by thermoporometry to be between 2.8 and 3.2 nm, and the internal pore volume V_n of the tubes between 0.008 and 0.02 ml/g. The hollow tubes of chrysotile, and for comparative reasons small plates of talc, are hydrothermally synthesized at temperatures between 563 and 600 K, and pressures between 75 and 120 hPa. Mg/Si molar ratios in steps of 3/1.5, 3/2 (chrysotile), 3/3.6, and 3/4 (talc) are used to vary the size and shape of the pores. The tubular morphology of the aggregates dried at 393 K is investigated by 1) transmission electron microscopy (TEM), 2) nitrogen adsorption and desorption at 77 K, and 3) diffuse reflectance infrared fourier transformed spectroscopy (DRIFTS). The radius within the hollow tubes, R_i, is between 2.5 and 4.0 nm as measured by TEM, and between 2.8 and 3.2 nm as determined by nitrogen adsorption and desorption. The measured radii agree well with the value calculated from crystallographic data, which is smaller than 5.3 nm. Within the dried aggregates the tubes are clustered in regular patterns, in which each tube is surrounded by 6 other tubes. The external radius, R_o, between the clustered tubes is from 1.6 to 2.9 nm as observed by TEM, and from 1.8 to 2.3 nm by N_2 adsorption and desorption. The external radius is not measured by thermoporometry. Whereas thermoporometry only measures the average pore size and pore volume within the tubes,

TEM and N_2 adsorption and desorption additionally provide the corresponding values between the tubes. A third pore radius, 5 to 20 nm, between the clusters of chrysotile tubes is established with N_2 adsorption and desorption.

Key Words- Thermoporometry, Chrysotile Asbestos, X-ray diffraction, N_2 adsorption and desorption, Transmission electron microscopy, Infrared spectroscopy.

INTRODUCTION

Thermoporometry has been applied to characterize wet silica gels (Jallut *et al.*, 1992; Higuti and Iwagami, 1952) and, recently, polymers (Cuperus *et al.*, 1992; Sasthav *et al.*, 1992). Jallut *et al.* (1992) have published a critical state of the art review. The technique monitors the pore size, pore volume, and pore shape of porous solids. Thermoporometry is based upon the freezing point depression, dT_s, of water (or depression of the solidification point of benzene). The freezing point depression is determined within a differential scanning calorimeter (DSC), by measuring in a linear temperature program the heat-flux involved with freezing as a function of temperature. Water has the advantage over benzene, in the determination of the pore size, that the solid does not have to be dried first, which may cause a decrease of the pore volume. The freezing temperature is a function of the pore radius R_p within the solid, which is only valuable when the pores are completely filled with water.

Ice will form a continuous plastic mass in the pores and freezing proceeds by 1) migration of the ice-water interface into the porous material (Sasthav *et al.*, 1992) or 2) nucleation of isolated ice spheres at several spots. The value of the crystal radius R_n of the ice nuclei in the pores is inversely proportional to the freezing point depression as given by Equation (1) ;

$$R_n = -64.67/dT_s - 0.23 \quad \text{(nm)} \qquad (1)$$

where R_n is the radius of the ice crystal in nm, -64.67 a literature constant in nm*K (Quinson *et al.*, 1987), and dT_s the freezing point depression in K, which is expressed as a negative value. The thermoporometric measurement is appropriate for determination of ice crystal radii between 1 and 150 nm (Quinson *et al.*, 1987). The pore volume of the solid, V_n, expressed as the volume of ice in ml divided by the weight of the porous solid in g, is calculated by the summation of the heat-fluxes measured during freezing as a function of the temperature (Equation 2) ;

$$V_n = \Sigma_i P_i*(T_{i+1}-T_i)/(D*H*W*sr) \quad \text{(ml/g)} \qquad (2)$$

where P_i is the heat-flux in J/s measured at temperature T_i within the temperature interval $(T_{i+1}-T_i)$ of 0.04 K on the DSC, D is the density of ice, approximately 1 g/ml, H the solidification enthalpy of ice of about 332 J/g, W the weight of the porous material in g, and sr the scan rate of 0.5 K/min.

The radius R_n can also be measured in a heating experiment. The melting temperature of ice is shifted towards a temperature higher than the measured freezing temperature, and thus dT_f is smaller. Consequently the value $R_{heating}$, the size of the radius obtained in a heating experiment, is larger than the $R_{cooling}$ measured in a cooling experiment (Equation 1). The value of $R_{heating}/R_{cooling}$ is dependent on the pore shape. A pore shape determining factor F is introduced, which is expressed by Equation (3). The theoretical value of F varies between 1 and 2, with a spherical and a cylindrical pore shape, respectively (Quinson *et al.*, 1987).

$$F = R_{heating}/R_{cooling} = (64.67/dT_f-0.23)/(64.67/dT_s-0.23) \approx dT_s / dT_f \quad (3)$$

where dT_s is the freezing point depression in the cooling step of the measuring sequence, and dT_f the melting point depression of the ice occupying the pores in the heating step.

Chrysotile fibres, belonging to the serpentine mineral group, with the formula $Mg_3Si_2O_5(OH)_4$ display a perfectly cylindrical pore shape. The pore shape is of interest to check certain theoretical assumptions of the thermoporometric characterization, e.g., the pore shape factor F. Earlier, Scholten *et al.* (1975) used chrysotile tubes to check the validity of the Kelvin equation for capillary condensation of N_2 at 77 K, and the Washburn equation for penetration of mercury into the tubes. In this work thermoporometry is applied to fibrous chrysotile, and for comparative reasons also to talc platelets, of the formula $Mg_3Si_4O_{10}(OH)_2$.

Structure of chrysotile

The curvature of the tubes is due to the structure of the individual unit cells of clino-chrysotile present in the tube wall. Figure 1 shows the projection of the monoclinic unit cell of clino-chrysotile ($Mg_3Si_2O_5(OH)_4$) in the a x b plane. The space group of clino-chrysotile is C_m (Deer *et al.*, 1962). The oxygens of the SiO_4 tetrahedra not involved in the siloxane bonds point upwards and are connected to the brucite sheet. The brucite sheet contains Mg in octahedral positions with two oxygens and four hydroxyls groups.

Noll *et al.* (1951, 1958) previously studied the curvature in the b-direction of the layers. Without the curvature, a considerable misfit exists between the silica and brucite sheet as illustrated by the differences of the sheet parameters. A calculation in the b-direction is usually performed.

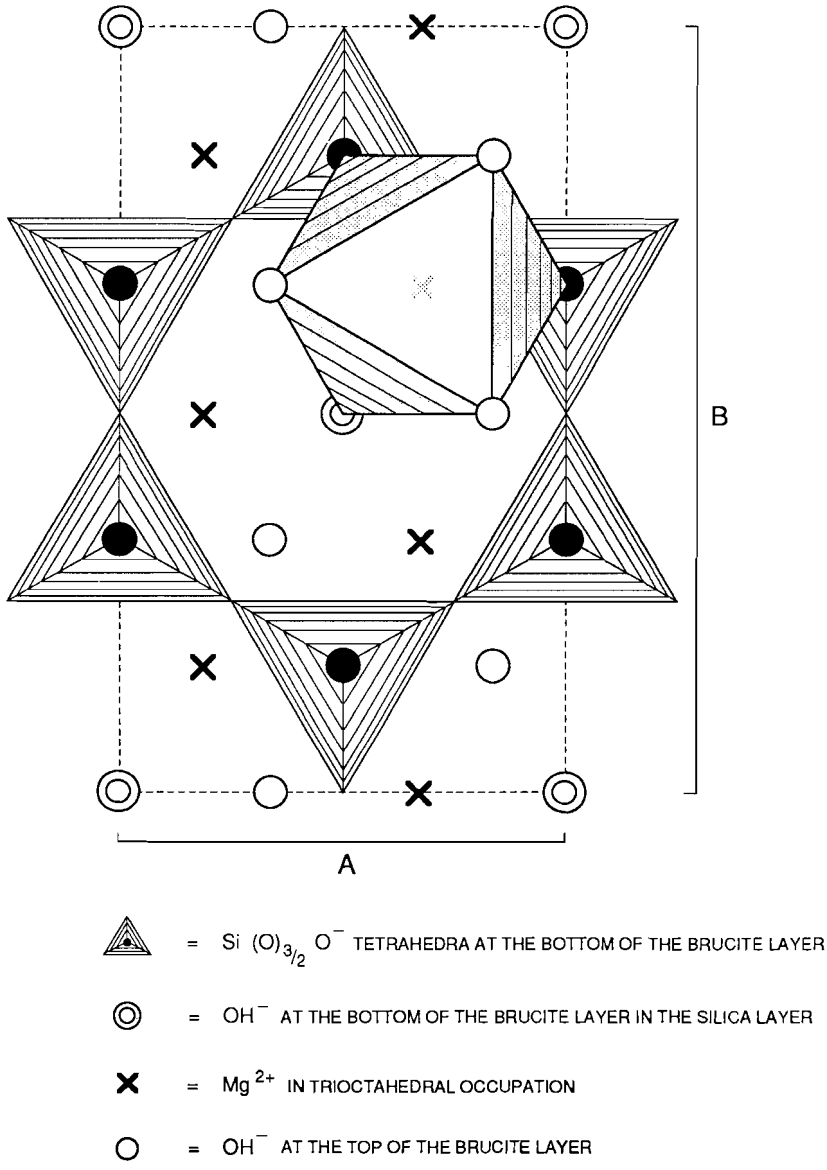

Figure 1 Projection of the monocline unit cell of clino-chrysotile in the a x b plane.

The brucite sheet exhibits lengths of a_b = 0.54 and b_b = 0.94 nm ($b_b = \sqrt{3}a_b$), and the silica sheet a_s = 0.50 and b_s = 0.87 nm (Noll *et al.*, 1951). A bending in the b-direction partly relieves the stress between the two sheets; the smaller silica sheet being at the internal side. The thickness of the tetrahedral Si sheet, measured from the weighted mean oxygen positions, is 0.226 nm, and that of the octahedral Mg sheet 0.208 nm, which corresponds to a combined layer of 0.434 nm (Wicks and O'Hanly, 1988). The combined thickness d of 0.434 nm is smaller than the sheet distance of 0.73 nm. The length of the c-axis, 1.464 nm, measures two basal Mg-Si sheet distances of 0.73 nm. The thickness of the layer of 0.73 nm has also been determined by electron microscopy on Ni-containing garnierite (Scholten *et al.*, 1975), which is structurally equivalent to chrysotile. The circle of connected unit cells of chrysotile in the b-direction is always an integer n of b_s and b_b (Equations 4 and 5).

$$2\pi R_i = n\, b_s \quad \text{(nm)} \qquad (4)$$

$$2\pi (R_i + d)) = n\, b_b \quad \text{(nm)} \qquad (5)$$

where R_i is the inner radius of curvature, d the effective thickness of the Si-Mg layer of 0.434 nm, and b_s and b_b are the cell parameters of the silica and brucite sheet. Equation (4) subtracted from Equation (5) yields Equation (6) :

$$2\pi d = n\,(b_b - b_s) \quad \text{(nm)} \qquad (6)$$

Finally, the division of Equation (4) by Equation (6) results in :

$$R_i = d\, b_s/(b_b - b_s) = 0.43*0.87/(0.94-0.87) = 5.3 \quad \text{(nm)} \qquad (7)$$

A similar calculation can be made for a bending in the a-direction with the result $R_i = 5.4$ nm. Calculation with bending in the a*b diagonal with length $\sqrt{(a^2+b^2)}$ gives the result $R_i = 5.4$ nm. The inner radius is smaller than the theoretical value of 5.3-5.4 nm, since the theoretical radius is situated within the tube wall. The molar ratio Mg/Si of talc being 3/4 is half that of chrysotile. In talc, the brucite sheet is bonded to two silica sheets, and talc will form plates. Thermoporometry should detect the absence of pores of talc platelets, and the validity of the method can be checked.

The aims of this paper are 1) the description of the hydrothermal synthesis of the serpentine minerals with molar Mg/Si ratios of 3/1.5, 3/2 (chrysotile), 3/3.6, and 3/4 (talc), using two different silica sources, viz., (i) sodium silicate , and (ii) fumed silica

powder (Aerosil, Degussa, BRD), 2) characterization of the reaction products with X-ray diffraction (XRD), 3) investigation of the pore structure of the dried samples with transmission electron microscopy (TEM), and nitrogen adsorption and desorption (N_2 ads. and des.). Additionally, 4) diffuse reflectance infrared fourier transformed spectroscopy (DRIFTS) offers the possibility to monitor the curvature of the tube wall, and measure the existence of adsorbed water on the clays. Adsorbed water may affect the size of the ice crystals formed in the tubes. Finally, the measured pore radii, volumes, and surface areas obtained by thermoporometry, TEM, and N_2 ads. and des. will be compared.

EXPERIMENTAL

Hydrothermal synthesis

- sodium silicate (S series)

A stock 2.5 M magnesium chloride solution is prepared. A 3.5 M SiO_2, 1.5 M Na^+ Si-containing solution is obtained by diluting Merck sodium silicate solution ART 5621 with water in a 1/1 volume ratio. Amounts of 200 ml of the Mg-solution with appropriate amounts of Si-solution are mixed, yielding Mg/Si molar ratios of 3/1.5, 3/2, 3/3.6, and 3/4 (Table 1). To provide a molar ratio Na-to-Cl of 1, additional NaOH (Merck, art. 6498) is added to the suspensions S1-S4.

-fumed silica (A series)

Appropriate amounts of Aerosil 380 powder (Degussa, BRD) for the above ratios are dissolved into 100 ml of a hot 2.5 M NaOH solution of 393 K. The Si-containing solutions thus prepared are cooled and added to 50 ml of the stock $MgCl_2$ solution, yielding suspensions with ratios identical to the series S (Table 1).

Aliquots of 110 g of the suspensions S1-S4 and A5-A8 are placed in 225 ml Teflon tubes of a diameter of 4 cm. The Teflon tubes are closed at both sides with Teflon stops and outer steel clamps. Two tubes are treated simultaneously in a two liter stainless steel vessel. An amount of 750 ml distilled water is added in the bomb outside the tubes to provide an equal water vapor pressure inside and outside the tubes. The bomb is externally heated for 24 h at temperatures ranging from 563 to 600 K, yielding hydrostatic pressures between 80 and 120 hPa. After a treatment the bomb is slowly cooled and the magnesium silicate suspensions are centrifuged for 10 minutes at 5000 rpm. The residues are resuspended in water, washed and centrifuged for 10 min at 5000 rpm to remove excess sodium. Any possible leaching occurring by washing with distilled water is not investigated. The last procedure is repeated twice. Finally, the synthetic clay is dried for 24 h at 393 K, and powdered.

Table 1 Composition of the starting Mg and Si containing solutions, and conditions of hydrothermal treatment.

sample	ml.A	ml.B	Addition of NaOH	pH	Ratio Mg/Si	T(K)	P (hPa)
sodium silicate							
S1	200	72	328 ml 2.8 M	11.1	3/1.5	568	80
S2	200	96	304 ml 3.0 M	11.1	3/2	600	120
S3	200	174	226 ml 3.7 M	10.6	3/3.6	563	75
S4	200	192	208 ml 3.8 M	10.6	3/4	573	85
	ml.A	silica in 2.5 M NaOH g SiO_2/100 ml		pH	Ratio Mg/Si	T(K)	P (hPa)
fumed silica (Aerosil)							
A5	50		3.8	10.4	3/1.5	568	80
A6	50		5.0	10.4	3/2	600	120
A7	50		9.1	9.6	3/3.6	563	75
A8	50		10.0	9.6	3/4	573	85

A: 510 g $MgCl_2.6H_2O$ in 1l H_2O ; 2.5 M Mg^{2+} and 5 M Cl^-
B: stock sodium silicate solution ; 3.5 M SiO_2 (0.21g SiO_2/ml) and 1.5 M Na^+

Analytical techniques

Powder XRD reflections are recorded on a Guinier-Johansson camera (CuK_{α_1} radiation 1.5406 Å). TEM micrographs and electron diffraction patterns are recorded with a Philips EM 420 transmission electron microscope. TEM samples are prepared by suspending the clay in ethanol by ultrasonical treatment. A droplet of the suspension is brought on a holey carbon film supported on a copper grid, and air dried. The diffraction maxima of TEM are measured as the radial distances, l, on the film in mm from the position of the incident electron beam on the film. The lattice plane distances d in Å are inversely proportional to the radial distances l in mm, with a constant of $11.9*10^{-13}$ m^2, unique to the camera. A gold film is used as reference. The diffraction points are indexed using Equation (8) of clino-chrysotile with the angle β of 93° (Brown, 1961; Zussman *et al.*, 1957).

$$1/d^2 = <1/d,1/d> = h^2/a^2\sin^2\beta + k^2/b^2 + l^2/c^2\sin^2\beta - 2hl\cos\beta/ac\sin^2\beta \quad (Å^{-2}) \quad (8)$$

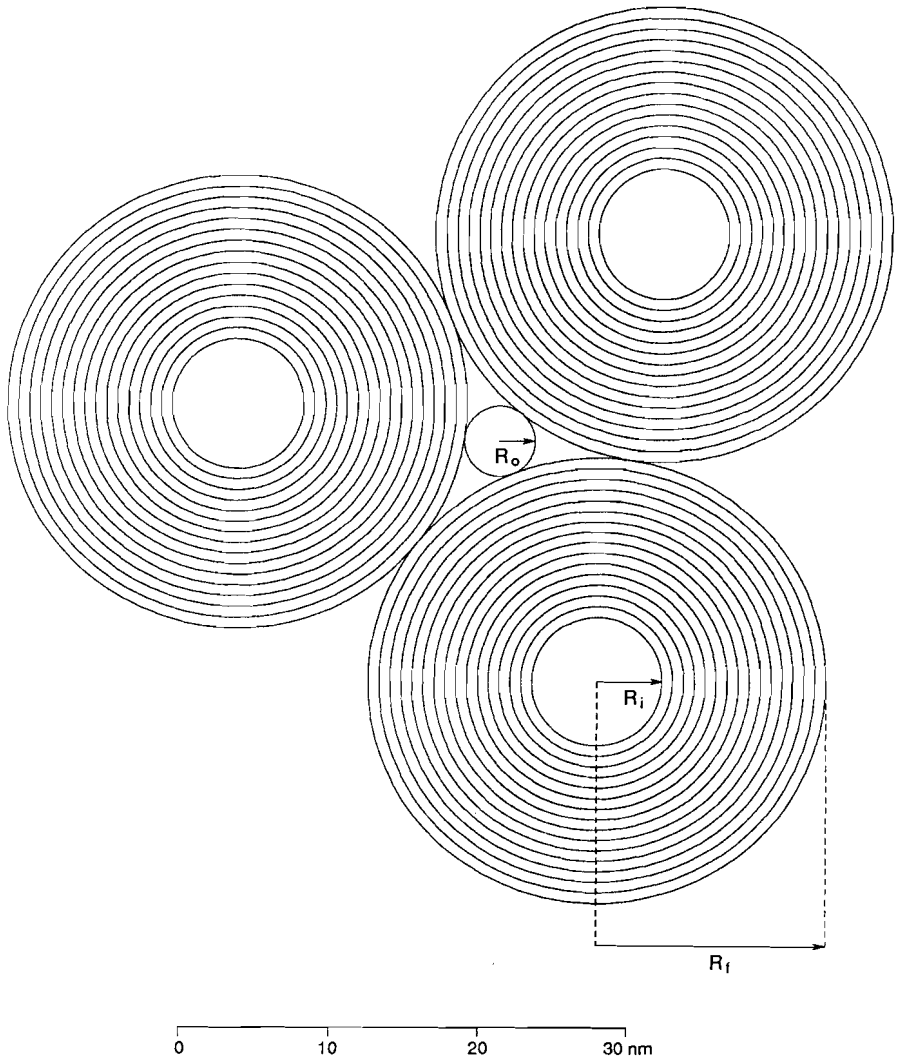

Figure 2 Projection of the hexagonal closed packing of chrysotile needles of S2 in the b x c plane, with R_f the radius of the fibres, R_i the internal radius, and R_o the external radius.

The projection of the clustered hollow needles of, e.g., sample S2 in the b and c plane is reconstructed in Figure 2, showing the fibre radius R_f, the intra radius R_i, and the derived inter particle radius R_o, assuming a surrounding of each needle by 6 others. This projection of serpentine is actually photographed in work of Wicks *et al.* (1988). The derived internal and external pore volume $V_{p,i}$ and $V_{p,o}$, and the internal and external surface area $A_{s,i}$ and $A_{s,o}$, are calculated with the formula 1) $R_o = ((2/\sqrt{3})-1)*R_f$, 2) $V_{p,i} = R_i^2$ /

$2.58*(R_f^2-R_i^2)$ (ml/g), 3) $V_{p,o}=(2\sqrt{3}-\pi)*R_f^2/(\pi*2.58*(R_f^2-R_i^2))$ (ml/g), 4) $A_{s,i}=2*10^3\ V_p/R_i$ (m^2/g), 5) $A_{s,o}=A_{s,i}*R_f/R_i$ (Table 3). With calculation of the pore characteristics from TEM images, a grain density of 2.58 g/ml of the chrysotile wall is used. The density is calculated with Equation (9) ;

$$D = 4 \times Mw(Mg_3(Si_2O_5)(OH)_4 / N_{av}*a*b*c*\sin\beta = 2.58 \text{ (g/ml)} \qquad (9)$$

where $Mw(Mg_3(Si_2O_5)(OH)_4$, the molar weight of chrysotile, is 277.1 g/mole, N_{av}, the Avogadro number ($6.02*10^{23}$ $mole^{-1}$), and $<[axc],b> = a*b*c*\sin\beta$, the volume of the unit cell, which is $7.13*10^{-24}$ ml.

Thermoporometry

A suspension of about 100 mg clay in 0.2 ml H_2O (in an aluminum cup) is cooled in a Setaram 111 differential scanning calorimeter (DSC) from 293 to 220 K at a cooling rate of 0.5 K/min. The heat flux during the solidification of water is recorded as a function of the temperature. Due to supercooling of bulk water present outside the pores of the solid, the heat of solidification is involved at about 264 K, as recorded in the thermogram (Charoenrein and Reid, 1989). In order to avoid the supercooling of bulk water, the sample is subsequently heated at a rate of 0.5 K/min from 220 to 265 K, just below the melting point of bulk water at 273 K. The heat-flux during melting of the ice in the pores is recorded. Finally, the sample is cooled a second time from 265 to 220 K, and the heat involved with solidification of water within the pores is exclusively measured.

N_2 adsorption and desorption and DRIFTS

The samples S1, S2, A5, and A6 are evacuated for 6 h at 473 K under vacuum before N_2 is adsorbed employing a Carlo Erba Omnisorp (TM) 100. The BET surface areas and pore volumes are calculated from the N_2 ads. isotherm, using a surface area of 16.2 $Å^2$ for a physically adsorbed N_2 molecule. The pore size distribution is calculated from the desorption isotherm according to the formula of Lowell and Shields (1984). The infrared absorption spectra in the range 4000-450 cm^{-1} of the finely powdered clays S1-S4, A5-A8 (25 wt% in KBr) are measured on a Perkin Elmer FT-1720 equipment, in combination with a spectra-tech diffuse reflectance accessory collector. DRIFTS show two types of vibrations, in the range of 4000 to 2000 cm^{-1} OH-stretching vibrations and in the range of 1225 to 450 cm^{-1} lattice vibrations.

RESULTS

XRD and TEM

The reaction products S1, S2, A5, and A6 are identified by XRD as a mixture of chrysotile and brucite ; A7 and A8 as talc ; and S3 and S4 as amorphous product (Table 2). Brucite in the samples S1, S2, A5, A6 is measured by XRD, which may introduce additional pores in the system. TEM micrographs and an electron diffraction pattern of S1 in Figure 3 clearly demonstrate the fibrous morphology of chrysotile. The electron diffraction pattern of S1 displays h00, 0k0, 00l, hk0, h0l reflections, but no hkl and 0kl reflections. The 0k0 and 00l reflections are located on a line, which illustrates the bending of the layers. No traces of brucite are seen, but brucite may be present as a few large crystals, probably with pores > 5 nm. Drying brings about a parallel orientation of the needles. Since the internal diameter is very unimodal as observed on different TEM micrographs, the average diameter is determined of some needles. The internal diameter D_i is 6 nm and the external diameter D_t is 37 nm for S1. The textural parameters obtained by TEM of S1, S2, A5, and A6 are given in Table 3. The needles of S1 have a length of 0.1-0.2 μm (Figure 3), which is about ten times shorter than that of S2 of 1-2 μm (Figure 4). Low Mg/Si molar ratios of 3/1.5, yield short chrysotile of a length of 0.1-0.2 μm, while the ratio corresponding to chrysotile of 3/2 yields long tubes of 1-2 μm. Amorphous sol particles, probably silica, are incorporated in the hollow tubes of S1, may be because the silica sheet is at the inner side of the chrysotile tubes. The sol particles seem to bear a surface charge and prefer a distance between them of about 22 nm.

In the TEM micrographs and the electron diffraction pattern of S2 (Figure 4), with the Mg/Si molar ratio corresponding to chrysotile, again parallel oriented needles are seen. The irregular spiral shape of some particles of S2 and of A6 (Figure 6) indicates a rotation axis in the direction of the fibre axis a-direction. This implies that the curvature model with bending only in the b-direction is oversimplified.

In Figure 5, the TEM micrographs of A5 with identical molar Mg/Si ratio as S1 illustrate that the length of the needles is also comparable to S1 (Table 3). Fortunately, one of the needles is oriented perpendicular on the copper grid, which causes the tubular shape to be clearly visible at the arrow. Small talc crystals of A7 display no tubular morphology (Figure 5). The talc crystals of A7 remain small due to the absence of reduction of the stress by bending. A ratio Mg/Si of 3/3.6 and 3/4 leads to platy talc crystals. Sample A6 with the same molar Mg/Si ratio as S2 exists of chrysotile needles of 1-2 μm length (Figure 6).

Table 2 X-ray powder diffraction data of hydrothermally prepared samples.

Chrysotile, monocline a = 5.32Å, b = 9.17Å, c = 14.64Å, β = 93° (JCPDS file No 25-645)

Sample	S1	I/I_1	S2	I/I_1	A5	I/I_1	A6	I/I_1	ref*	I/I_1	hkl
d(Å)	7.39	100	7.39	100	7.52	100	7.41	100	7.36	100	002
	4.56	55	4.56	50	4.48	35	4.56	30	4.56	50	020
	3.68	75	3.68	60	3.68	50	3.68	60	3.66	80	004
	2.66	25	2.66	10	-	-	2.66	20	2.66	30	200
	-	-	-	-	-	-	2.60	15	2.60	40	201
	-	-	2.54	20	2.57	-	-	-	2.53	-	20-2
	2.46	$>I_1$	2.49	$>I_1$	2.46	-	2.46	$>I_1$	2.50	50	202
	2.28	50	-	-	-	-	2.22	30	2.29	20	040
	2.07	40	2.10	20	2.03	-	2.10	20	1.97	20	205
	-	-	1.75	25	-	-	1.80	15	1.83	30	008
	1.54	95	1.54	80	1.53	65	1.54	70	1.53	65	060
	1.31	60	1.32	30	1.31	30	1.32	40	1.31	40	402

Talc, monocline a = 5.29Å, b = 9.17Å, c = 18.96Å, β = 99°61′ (JCPDS file No 19-770)

Sample	S3	I/I_1	S4	I/I_1	A7	I/I_1	A8	I/I_1	ref*	I/I_1	hkl
d(Å)	-	-	-	-	9.54	100	9.65	100	9.35	100	002
	-	-	-	-	4.58	$>I_1$	4.56	60	4.59	45	020
	-	-	-	-	2.60	$<I_1$	2.60	30	2.60	20	13-2
	-	-	-	-	2.49	$<I_1$	2.51	50	2.50	20	13-3
	-	-	-	-	1.53	$>I_1$	1.53	65	1.53	55	060

Brucite, hexagonal a = 3.147Å, c = 4.769Å (JCPDS file No 7-239)

Sample	S1	I/I_1	S2	I/I_1	A5	I/I_1	A6	I/I_1	ref*	I/I_1	hkl
d(Å)	4.76	50	4.77	35	4.77	40	4.79	30	4.77	90	001
	-	-	-	-	-	-	-	-	2.73	6	100
	2.37	100	2.37	100	2.37	100	2.37	100	2.37	100	101
	1.80	35	1.80	45	1.79	45	1.80	40	1.79	55	102
	1.58	30	1.58	30	1.57	30	1.58	30	1.57	35	110
	1.50	20	-	-	1.50	15	-	-	1.49	18	111
	1.38	10	-	-	-	-	-	-	1.37	16	103
	-	-	-	-	-	-	-	-	1.36	2	200
	1.31	15	-	-	-	-	-	-	1.31	12	201

*) JCPDS

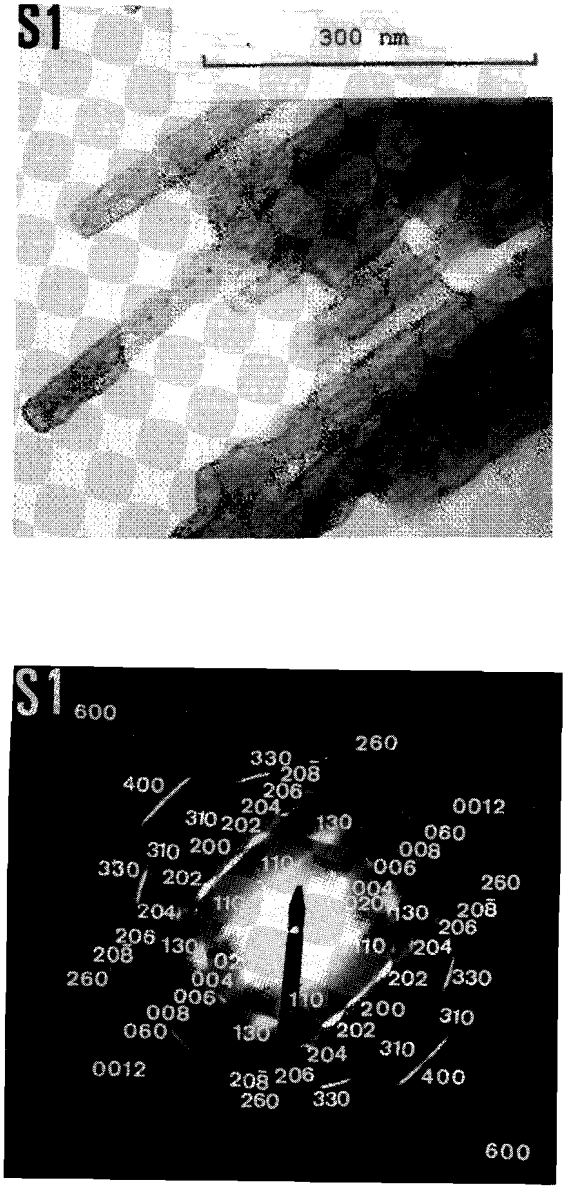

Figure 3 TEM micrographs and an electron diffraction pattern of S1 (chrysotile).

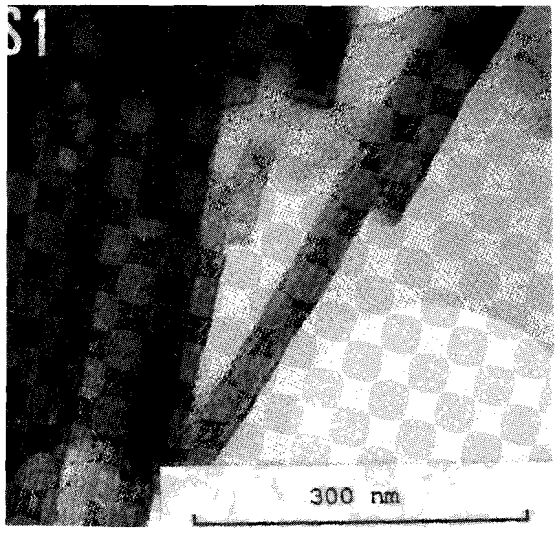

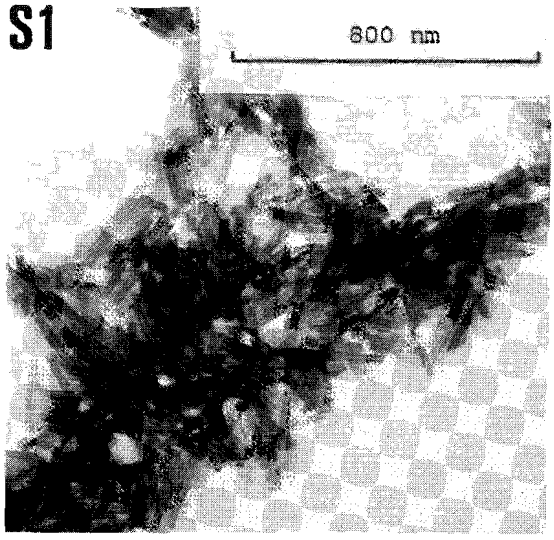

Figure 3 (continued)

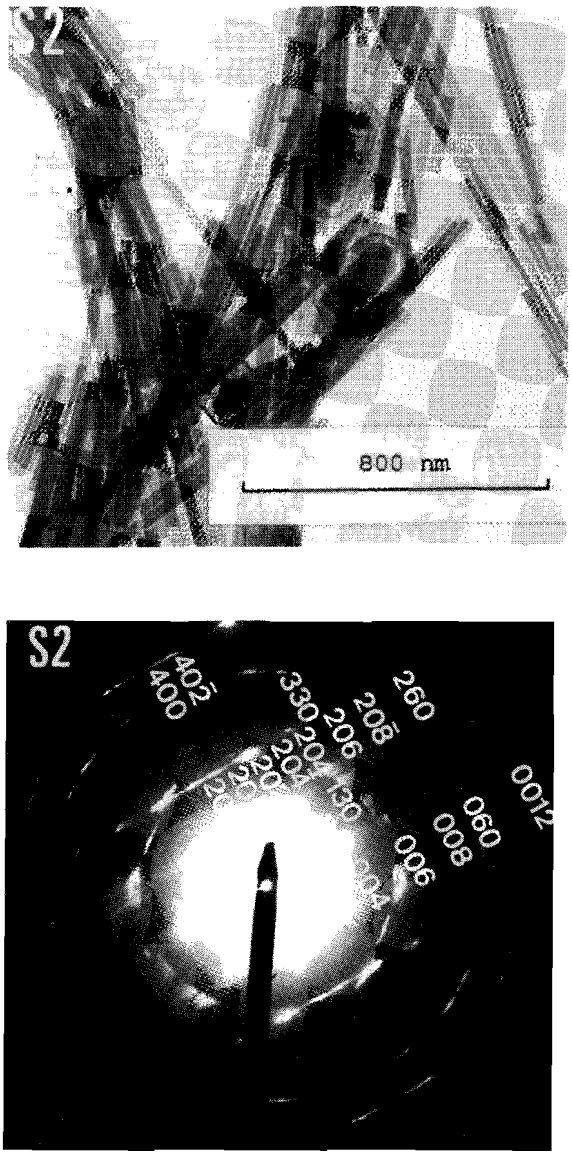

Figure 4 TEM micrographs and an electron diffraction pattern of S2 (chrysotile).

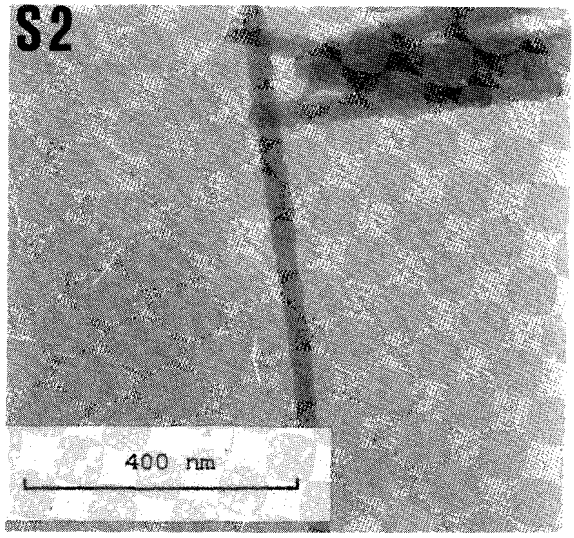

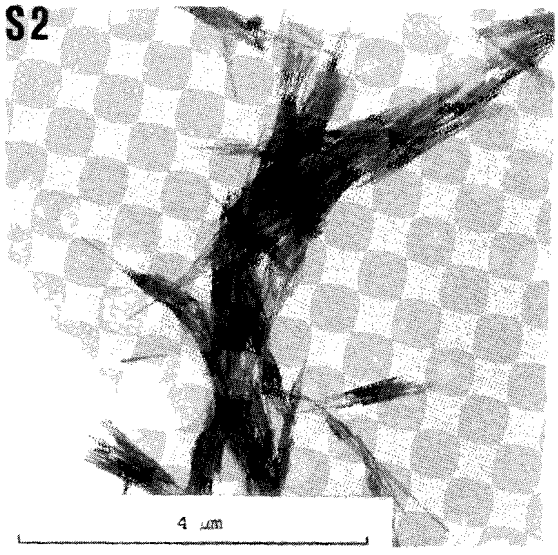

Figure 4 (continued)

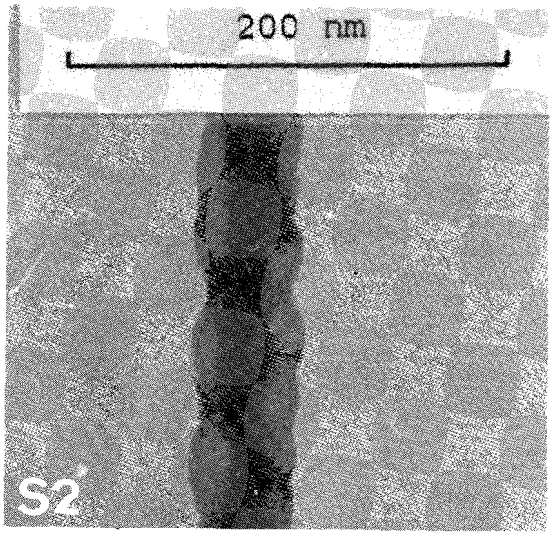

Figure 4 (continued)

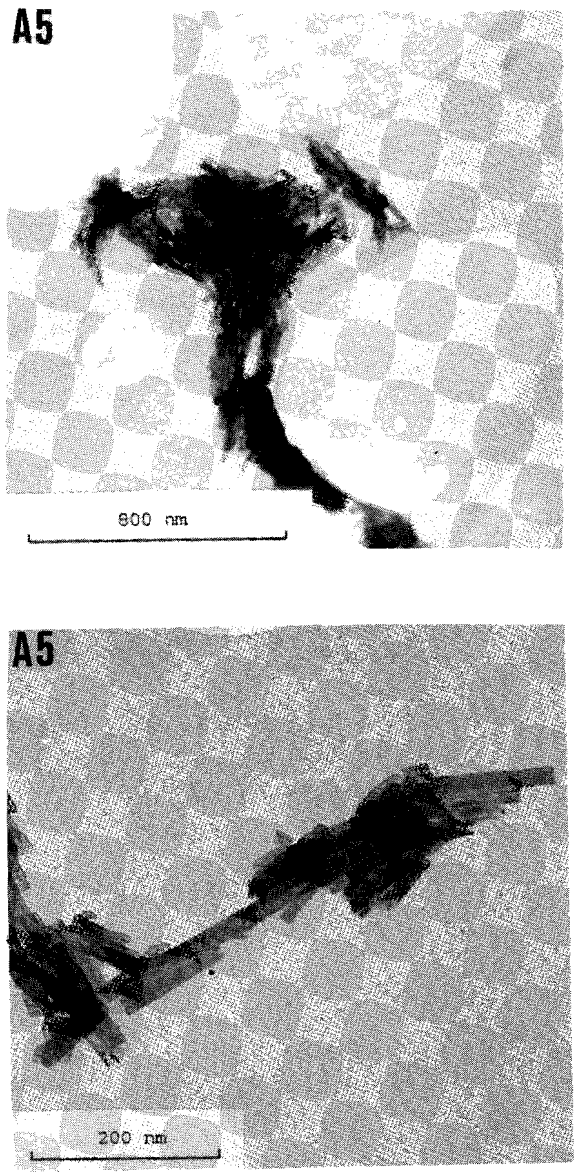

Figure 5 TEM micrographs of the A5 (chrysotile) and A7 (talc)

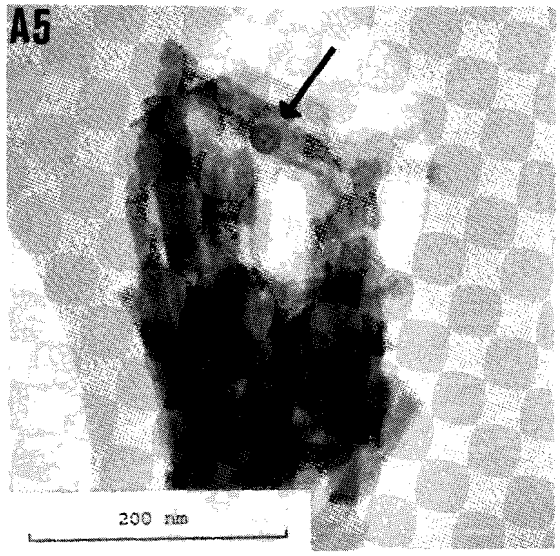

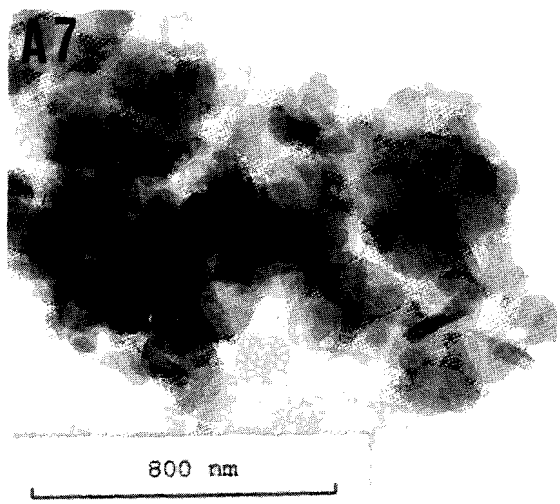

Figure 5 (continued)

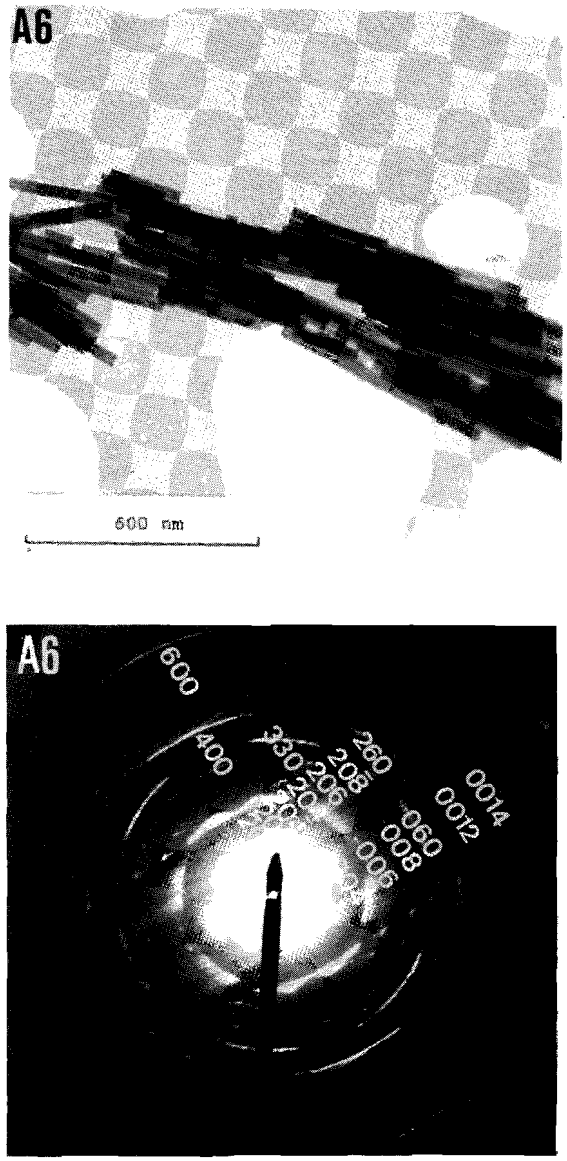

Figure 6 TEM micrographs and a electron diffraction pattern of A6 (chrysotile). The photograph, which is rather astigmatic, shows the spiral shape of the chrysotile tubes.

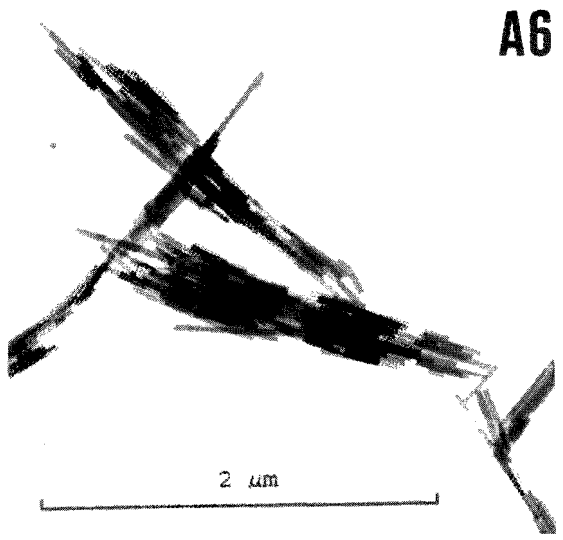

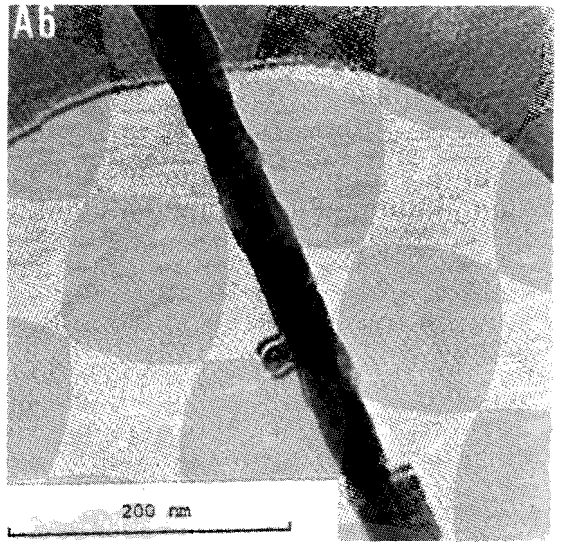

Figure 6 (continued)

Table 3 Porous structure of chrysotile by transmission electron microscopy (TEM).

sample	S1	S2	A5	A6
length of the tubes (μm)	0.1-0.2	1-2	0.1-0.2	1-2
diameter tubes $D_f(2*R_f)$ (nm)	37	31	21	36
inner tube radius R_i (nm)	3	4.5	2.5	4
inter tube radius R_o[1]	2.9	2.4	1.6	2.8
thickness of the wall δ (nm)	15	11	8	14
number of sheets in wall	21	15	11	19
internal porosity $V_{p,i}$ (ml/g)[2]	0.01	0.04	0.02	0.02
external porosity $V_{p,o}$ (ml/g)[3]	0.04	0.04	0.04	0.04
total porosity $V_{p,i+o}$ (ml/g)	0.05	0.08	0.06	0.06
internal area $A_{s,i}$ (m^2/g)[4]	7	16	19	10
external area $A_{s,o}$ (m^2/g)[5]	43	54	78	45
total surface area (m^2/g)	50	70	97	55

1) $R_o = ((2/\sqrt{3})-1)*R_f$ 2) $V_{p,i} = R_i^2/2.58*(R_f^2-R_i^2)$(ml/g)
3) $V_{p,o} = (2\sqrt{3}-\pi)*R_f^2/(\pi*2.58*(R_f^2-R_i^2))$ (ml/g) 4) $A_{s,i} = 2*10^3\ V_p/R_i$ (m^2/g)
5) $A_{s,o} = A_{s,i}*R_i/R_i$

Thermoporometry

An amount of water present within the pores can be deduced from the thermograms of pure chrysotile, e.g., S2 and A5 in Figure 7a and b (the position of the curves does not represent an absolute value of the heat-flux due to vertical displacement of the curves). In the first cooling step, S2 exhibits a large exothermic solidification peak at 265 K of supercooled bulk water (1), and a much smaller exothermic solidification peak at 255 K of pore water (2) (Figure 7a). The freezing point depression dT_s is 18.3 K. The melting peak of the ice present within the tubes is registered during the heating step at 256.6 K (3). The 'fusion point' depression, dT_f, of the melting of ice within the tubes is 16.6 K. The shape factor, F, is therefore 18.3/16.6 = 1.1, which is assumed to be characteristic for a spherical pore shape. During the second cooling cycle a solidification peak of pore water is observed at 255 K (4). The ice crystal radius R_n of S2 corresponding to the maximum of heat-flux is 3.3 nm (Equation 1).

The thermogram of chrysotile A5 in Figure 7b displays the solidification peak of pore water at 251.8 K (2) with dT_s = 21.5 K, and during the heating step an endothermic fusion peak at 257.9 K (3) with dT_f = 15.4 K. The shape factor F of A5, which is 21.5/15.4 = 1.4, is large as compared to the value of 1.1 of S2, which may imply that the ice crystals grow more cylindrically.

Macro pores appear as shoulders on the bulk peak at 273 K during the final heating step. Due to the overlap with the peak of bulk water at 273 K, no V_n of these peaks can be determined. The shoulder and bulk peak are not displayed in Figure 7, due to the dominant heat-flux involved with fusion of the bulk water. The peak of the macro pores of A5 has its maximum at 268 K, with a dT_f of -5.2 K, corresponding to a value for R_n of 6.1 nm.

The thermoporometric pore radii of the samples S1, S2, A5, A6 range from 2.8 to 3.3 nm, and the pore volumes V_n from 0.016 to 0.02 ml/g (Table 4).

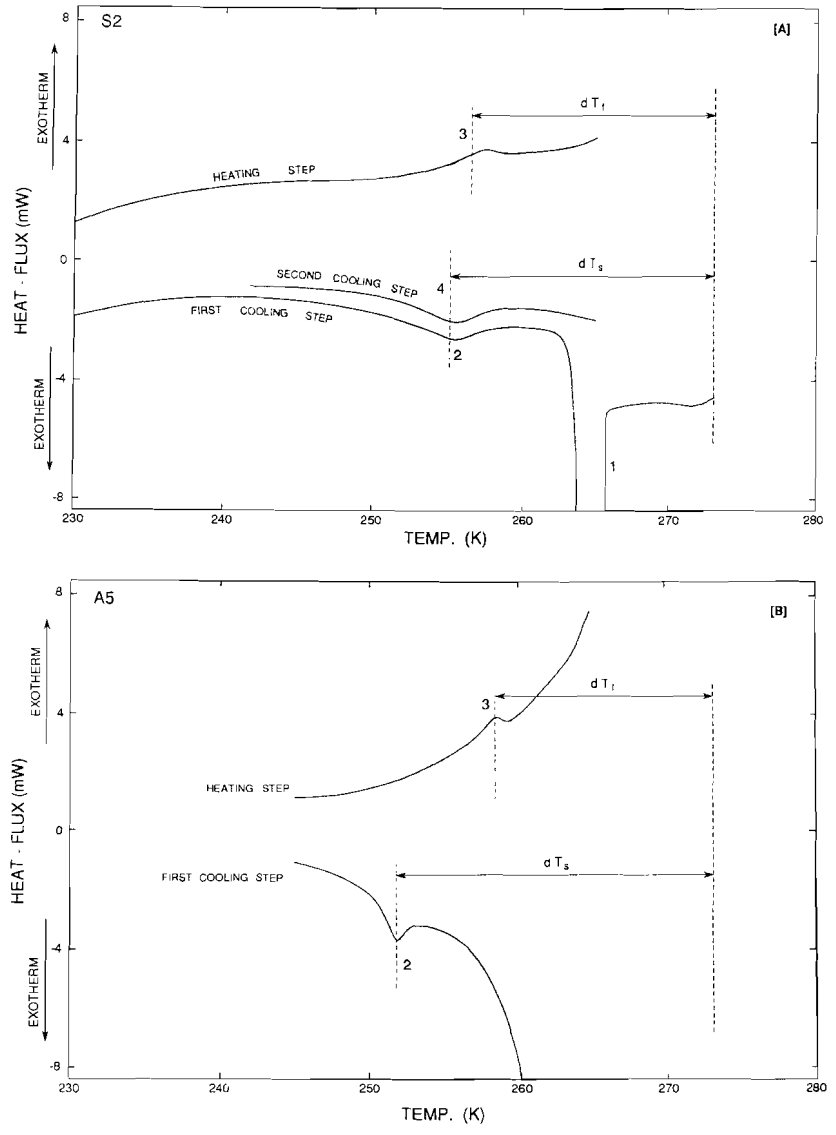

Figure 7 (a) Thermograms of S2, with 9 mg solid and 273 mg H_2O, illustrating the exothermic peak of supercooled bulk water at 265 K (1), the exothermic peak of pore water at 255 K (2), the melting peak of the pore ice at 256.6 K (3), and finally, the solidification peak of pore water at 255 K the second time (4). (b) A5 , with 142 mg solid and 161 mg H_2O, with the solidification peak of pore water at 251.8 K (2), and the endothermic fusion peak at 257.9 K (3) of pore water.

Table 4 Thermoporometry applied on wet chrysotile tubes. The amounts solid and water are : 125 mg S1 + 190 mg H_2O, 9 mg S2 and 273 mg H_2O, 142 mg A5 and 161 mg H_2O, and 113 mg A6 and 196 mg H_2O.

Sample	cooling rate (K/h)	R_n (nm)	V_n (ml/g)	F
S1	30	3.1	0.016[1] 0.008[2]	1.1
S2	30	3.3	-	1.1
A5	30	2.8	-	1.4
A6	30	3.3	0.02[1]	1.1

1) cooling step 2) heating step

Figure 8 displays the pore size distribution curves of S2 and A5, which are derived from the thermograms in Figure 7. The pore volume presented by the surface area under the curves is normalized on 1. Sample S2 displays a broad pore size distribution with a maximum at 3.3 nm. A small shoulder is observed at 2.8 nm. The curve of the sample A5 shows a sharp peak with a maximum at 2.8 nm.

Water present within pores is not detected with the 'talc samples' S3, S4, A7, and A8. The thermograms are, therefore, not displayed in this paper.

N_2 adsorption and desorption

The pore characteristics of S1, S2, A5, and A6 are summarized in Table 5. The pore size distribution of S2 in Figure 9a exhibit three main peaks ; a large peak at 3.2 nm (1), an additional peak at 2.3 nm (2), and a broad peak at 16 nm (3). The same type of pore size distribution exists in A5 (Figure 9b), but the peaks are shifted towards smaller dimensions, viz., 2.8 (1), 1.8 (2), and 5 nm (3). Due to the more compact character of the needle aggregates, the pore size distribution of the macro pores at 5 nm (3) (Figure 9b) is smaller than that of S2 (Figure 9a).

DRIFTS

The DRIFT spectra of the samples S1-S4 and A5-A8 are represented in Figure 10a and 10b, respectively. Samples S1, S2, A5, and A6 are identified as chrysotile, A7 and A8 as talc, S3 and S4 as amorphous silica. Broad absorption bands of adsorbed water are observed between 3000 and 3500 cm^{-1} and at 1635 cm^{-1} in all spectra.

The chrysotile samples S1, S2, A5, and A6 have two characteristic MgOH stretching vibrations at 3688 cm^{-1} and 3638 cm^{-1} (Figure 10a), attributed to the three external OH at the top of the brucite sheet, and one internal OH at the bottom of the brucite sheet (Jolicoeur and Duchesne, 1981). The intensity ratio of the peaks is predicted to be 3/1. The single, sharp peak at 3695 cm^{-1} of talc A7 and A8 in Figure 10b is due to the single

internal MgOH-stretching vibration. In talc all hydroxyls are equivalent. The internal OH-stretching vibration at 3695 cm^{-1} is located at about the same wavenumber as the external OH-stretching vibration of chrysotile.

The absorption bands at about 1081 cm^{-1}, 1010 cm^{-1}, and 947 cm^{-1} (Figure 10a) are typical for the Si-O-Si stretching vibrations of the silica network (Yariv and Heller-Kallai, 1975, Luys *et al.*, 1982). The 1081 cm^{-1} band is attributed to the out-of-plane symmetric stretching vibration of the silica sheet. The degeneracy of the single band at 1010 cm^{-1} in talc to two bands at 1010 cm^{-1} and 947 cm^{-1} in chrysotile is explained by the bending of the silica sheet. The 1010 cm^{-1} band is attributed to Si-O-Si stretching vibrations, mainly parallel to the *b*-axis in the direction of the curvature, while the 947 cm^{-1} is due to Si-O-Si stretching vibrations parallel to the a-axis. The relative intensity of both bands is affected by ultrasonic treatment of chrysotile (Yariv and Heller-Kallai, 1975).

The small peak at 1202 cm^{-1} for S1, S2, A5, and A6 represents small traces of amorphous silica. The absorption band of the Mg-O stretching vibration at 670 cm^{-1} of octahedrally coordinated Mg (A7 and A8) is shifted to a lower wavenumber of 655 cm^{-1} (A5 and A6). The Mg-O stretching vibration band at 660 cm^{-1} is the same for both the talc samples S3, S4, and the chrysotile samples S1, S2.

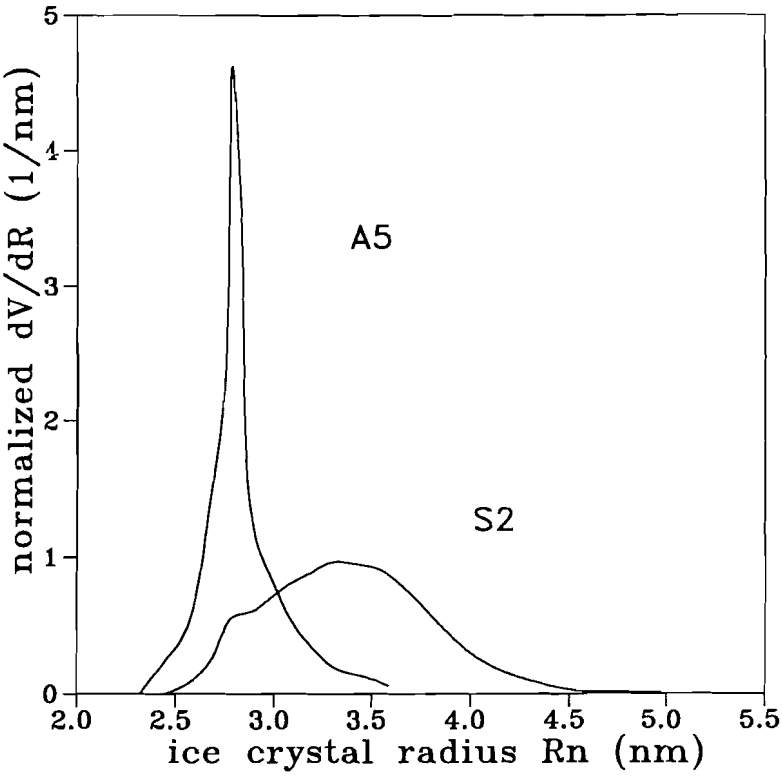

Figure 8 The heat flux curves of S2 and A5 transformed into not unimodal pore size distribution curves. The rather asymmetric distribution of the heat-flux curves, tailing to low temperatures has disappeared by the reciprocal dependency of the radius R_n on the temperature T_s by $R_n = -64.67/(T_s-273.15) -0.23$

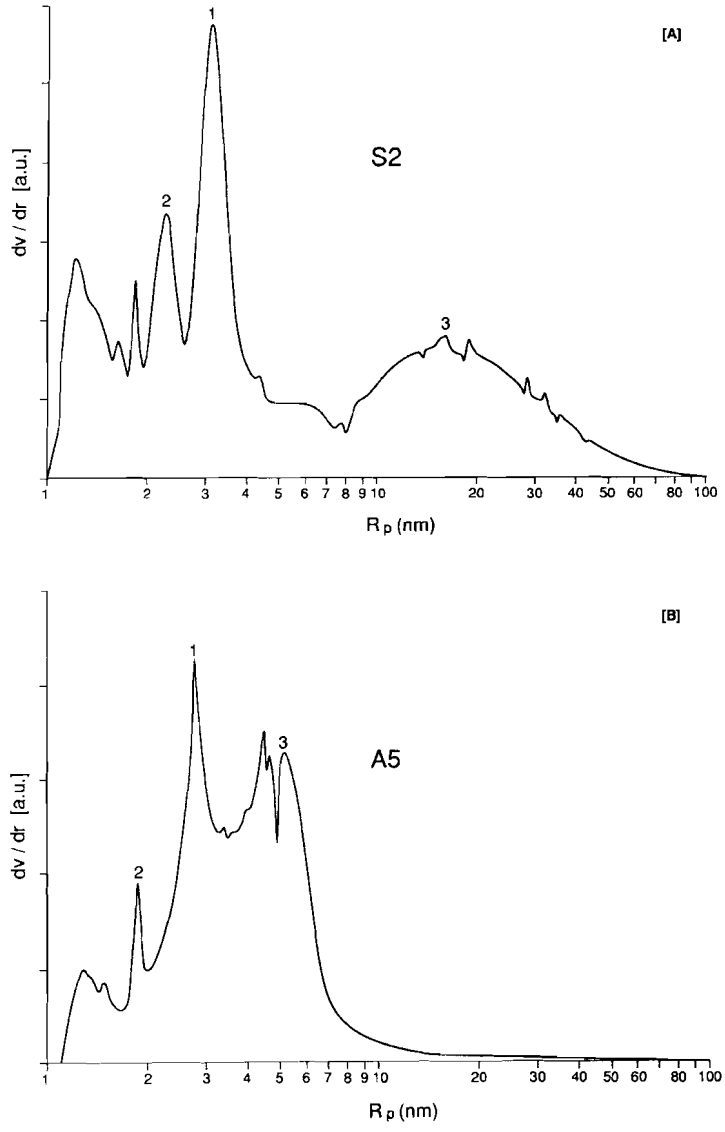

Figure 9 Pore size distribution of ; (a) S2 (chrysotile), with two major peaks, a main peak at 3.2 nm (1), a secondary peak at 2.3 nm (2), and furthermore, a broad peak with a maximum at about 16 nm (3), (b) A5 (chrysotile), but the three peaks are shifted towards low radii, 2.8 (1), 1.8 (2), and 5 nm (3).

DISCUSSION

The heat-flux measured by thermoporometry originates from water present within the hollow chrysotile tubes, which is supported by the absence of an analogous heat-flux in talc. A shape factor F of 2 in thermoporometric characterization of a cylindrical pore shape should be expected for the chrysotile samples. However, low shape factors between 1.1 and 1.4 are experimentally measured (Table 4). The shape factors are even smaller than the minimum value of 1.4 of Jallut *et al.* (1992) reported for a matrix of compacted alumina grains approximating spherical pores. The ice crystals remain spherical after solidification. Cylindrical shapes may be obstructed by the presence of amorphous sol particles in the tubes (Figure 3). A second possibility is that the ice crystals grow spherical to form a chain of crystals.

The DRIFTS absorption bands at 3000-3500 cm^{-1}, and at 1635 cm^{-1} are attributed to the stretching and bending vibration of water, and are especially strong for S3 and S4, which implies that water is bound to silica in the chrysotile structure (Suquet, 1989). The absorption bands are especially strong in 100 % leached samples and assigned to water adsorbed on Si-OH groups. Water adsorbed on silica may form a non-freezing layer of a thickness of 0.9 nm. The ice crystal radius R_n is expected to be 0.9 nm smaller than the pore radius R_p. The existence of such a layer in chrysotile can be verified by comparison of the thermoporometric results to the N_2 adsorption and desorption results.

The N_2 pore radius distribution curves of two chrysotile samples, S2 and A5, (Figure 9) can be explained using Figure 2. The peak (1) at about 3 nm is ascribed to the internal radius R_i of the tubes, the peak (2) at about 2 nm to the inter particle radius R_o between the tubes (the size of R_i is larger than R_o), and the peak (3) between 4 and 100 nm to macro pores between the chrysotile clusters, or to pores in amorphous silica or brucite. The comparison of the pore characteristics of the chrysotile tubes obtained by the three methods TEM, H_2O (thermoporometry), and N_2 can be split in 1) the pore size distribution, 2) the pore volume, and 3) the (internal) surface area.

-pore size distributions

The pore size distribution curves of S2 and A5 obtained by thermoporometry (Figure 8) can be compared directly to the N_2 ads. and des. curves (Figure 9). The maxima of the broad peak of S2 and the sharp peak of A5 at 3.3 and 2.8 nm, respectively, correspond to the main peak (1) of N_2 ads. and des. A very good agreement exists between the main peak radius R_p (1) as calculated from N_2 ads. and des., and the thermoporometric radius R_n (Table 6). The agreement indicates that the main peak in the desorption isotherm corresponds with the ice crystal radius R_n. Surprisingly, the pore radius R_p is not 0.9 nm larger than the ice crystal radius R_n, which is usually observed with amorphous silica (Jallut *et al.*, 1992). Probably all the silanol groups of the silica tetrahedra point to the brucite sheet and leave no hydrogen bonds to anchor the non-freezing layer. Due to the hydrophobic character of the inner chrysotile tubes the amount of adsorbed water measured by DRIFTS is situated elsewhere, maybe adsorbed to KBr. The secondary peak (2) of N_2 ads. and des., R_o, with a smaller radius than the main peak R_i (Table 5) is not measured by thermoporometry. Perhaps, the clustering of tubes disappears when resuspended in water, and the external radius R_o between the tubes becomes too large and the signal intensity too low to be measured with thermoporometry. The shoulder on the pore size distribution curve of S2 at 2.8 nm (Figure 9) may point to the existence of some clustering in water. The third N_2 peak (3) of A5 at 5 nm (Figure 9) is attributed to macropores corresponding to the large pore size R_n of 6.1 nm determined by thermoporometry, probably of ice formed between the chrysotile clusters.

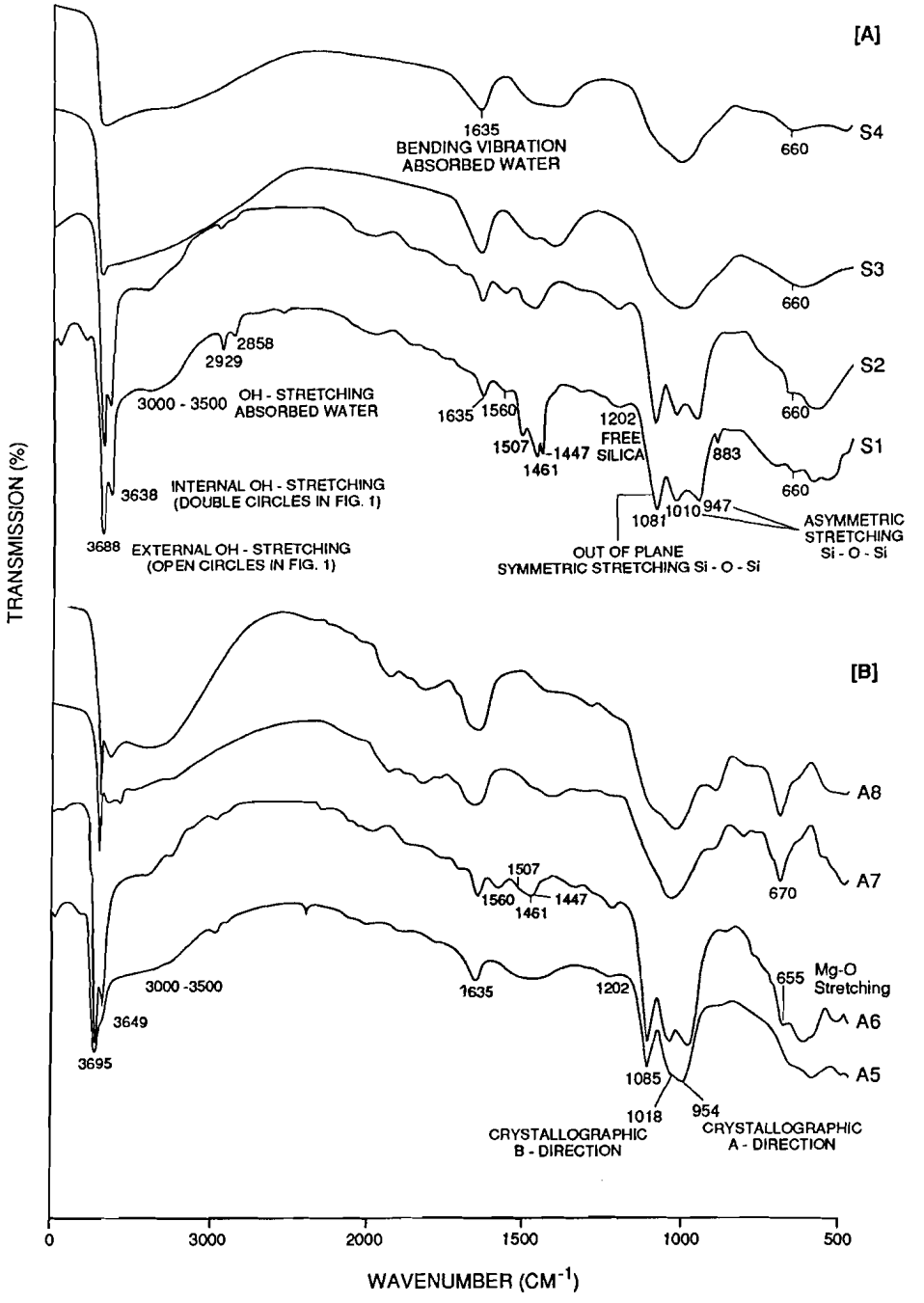

Figure 10 DRIFT spectra of (a) sodium silicate samples S1-S4, (b) fumed silica (Aerosil) samples A5-A8.

Table 5 N_2 ads. and des. applied on chrysotile after evacuation for a period of 6 h at 473 K.

Sample	R_p (nm)	V_p (ml/g) >1nm	$1\text{nm}<R_p<5\text{nm}$	surface area (m^2/g) BET	des. isotherm[3]
S1	3.2[1]	0.35	0.04	46	52
	2.2[2]				
S2	3.2[1]	0.39	0.06	54	70
	2.3[2]				
A5	2.8[1]	0.25	0.13	87	115
	1.8[2]				
A6	2.9[1]	0.54	0.05	63	74

1) main peak 2) secondary peak 3) $A_s = \Sigma_k\ 2V_{p,k}/R_{p,k}$ with $R_{p,k}$ between 1 and 30 nm

The crystal radii, R_n, obtained from thermoporometry agree well with the inner particle radii, R_i, determined from TEM micrographs (Table 6). Mostly the radii determined from TEM micrographs are slightly larger than those obtained by thermoporometry. The radii R_n (H_2O) and R_i (TEM) exhibit an identical trend with A5 < S1 < A6 < S2.

-pore volume measurements

The thermoporometric pore volumes V_n of S1 and A6 are smaller than the N_2 pore volumes $V_p(N_2)$ ($1\text{ nm}<R_p<5$ nm) (Table 6), because thermoporometry determines the pore volume within the tubes, $V_{p,i}$, and not in between the tubes, whereas N_2 ads. and des. measures both, $V_{p,i+o}$. The thermoporometric pore volumes, V_n, of the tubes agree well with the internal pore volumes, $V_{p,i}$, calculated from TEM data (Table 6). No problems are seen with the nucleation of ice by the fairly hydrophobic inner chrysotile walls, as expected from the results of Cuperus *et al.* (1992), resulting in too low pore volumes V_n. Maybe the hydrophillic silica sol particles in the cylinders initiate heterogeneous nucleation. The $V_{p,i+o}(N_2)$ ($1\text{ nm}<R_p<5$ nm) is slightly smaller than the TEM pore volume $V_{p,i+o}$, except with A5 (Table 6). The opposite is observed for $V_p(N_2)$ ($R_p>1$ nm) (Table 5), being larger than the total TEM pore volume ($V_{p,i+o}$) (Table 6). The high N_2 pore volume is probably due to the macro pore volume, which is present in pores larger than 5 nm between chrysotile clusters or in amorphous silica or brucite.

-surface area measurements

The BET surface areas by N_2 adsorption (Table 5) (except that of A6) are slightly smaller than the surface areas calculated from the TEM images (Table 3). For example, the BET surface area of S1 is 46 m^2/g, and the TEM surface area is 50 m^2/g. The BET surface areas exhibit a similar trend as the TEM data, which is S1 < (S2,A6) < A5. The surface areas calculated from the N_2 desorption isotherms based on the equation $\Sigma_k\ 2V_{p,k}/R_{p,k}$ are about 15 m^2/g larger than the BET surface areas (Table 5), and agree better with those of TEM. For example, the surface area of S1 is 52 m^2/g by N_2 desorption and 50 m^2/g by TEM. The difference between the BET and N_2 desorption surface area cannot readily be explained, but may be attributed to amorphous product in and between the needles measured with the BET method.

Table 6 Comparison between the values obtained for $R_{p,i}$, $V_{p,i}$, and $V_{p,i+o}$, given the different complex compositions of the samples by the three methods TEM, thermoporometry (H_2O), and N_2 ads. and des. The value δ% represents the maximal fault (in %) in the determination of R_i by the three techniques.

	Mg/Si	$R_{p,i}$ (TEM)	$R_{p,i}$ (H_2O)	$R_{p,i}$ (N_2)	δ% max	$V_{p,i}$ (TEM)	$V_{p,i}$ (Thermo)	$V_{p,i+o}$ (1nm<R<5nm) (TEM)	$V_{p,i+o}$ (1nm<R<5nm) (N_2)
S1	3/1.5	3.0	3.1	3.2	6	0.01	0.016	0.05	0.04
S2	3/2	4.5	3.3	3.2	41	0.04	-	0.08	0.06
A5	3/1.5	2.5	2.8	2.8	11	0.02	-	0.06	0.13
A6	3/2	4.0	3.3	2.9	38	0.02	0.02	0.06	0.05

CONCLUSIONS

1) The internal pore radius $R_{p,i}$ and pore volume $V_{p,i}$ of the tubes is established by thermoporometry. The pore radii agree well with that of TEM and N_2 adsorption and desorption.

2) Water attached to silica in chrysotile and talc as established by DRIFTS, does not form a layer of strongly bound water in the pores. The water within the pores completely participates in the water-ice phase transformation, because the internal pore radii obtained by thermoporometry and N_2 adsorption and desorption are identical.

3) The thermoporometric shape factor F of about 1 is smaller than the expected theoretical value of 2, because the ice crystals in the tubes develop to a chain of spheres. Some amorphous material incorporated in the hollow tubes may prevent the formation of one single ice cylinder.

4) The N_2 adsorption and desorption measurements point to a parallel orientation of clustered tubes. The value of the internal radius, R_i, and external radius, R_o, calculated from N_2 adsorption and desorption are equal to those from TEM micrographs. Furthermore, the N_2 pore volume V_p between a R_p of 1 and 5 nm is equal to that determined from TEM micrographs. The BET surface area obtained by N_2 adsorption is slightly smaller than that obtained from TEM, while the surface area obtained by N_2 desorption (Σ_k $2V_{p,k}/R_{p,k}$) agrees better.

5) Addition of water to the dried and clustered tubes probably results in the disappearance of the clustering. Thermoporometry only measures the internal radius R_i and pore volume $V_{p,i}$ within the tubes, while TEM and N_2 adsorption and desorption provide the radii and the pore volume within and between the tubes, $R_{p,i+o}$ and $V_{p,i+o}$, respectively.

6) Comparison of radii measured by thermoporometry and either TEM or nitrogen adsorption can indicate the hydrophobility of the surface of the porous solid.

ACKNOWLEDGMENTS

The authors thank P.A. Elberse for the N_2 ads. and des. measurements, M.J. Kappers for the DRIFTS measurements, and R.J. Bakker and J.T. Kloprogge for their critical review of the paper. Furthermore A.M.J. van der Eerden is thanked for the technical assistance with the hydrothermal synthesis experiments.

REFERENCES

Brown, G. (1961) (ed.) The X-ray identification and crystal structures of clay minerals : 25-33 and 88-101, Mineralogical Society, Jarrold and sons, London.

Charoenrein, S., and Reid, D.S. (1989) The use of DSC to study the kinetics of heterogeneous and homogeneous nucleation of ice in aqueous systems: *Thermochim. Act.* **156**, 373-381.

Cuperus, F.P., Bargeman, D., Smolders, C.A. (1992) Critical points in the analysis of membrane pore structures by thermoporometry : *J. Membr. Sci.* ***66, 45-53.***

Deer, W. A., Howie, R. A., Zussman, J. (1962) Rock forming minerals, Vol 3^2 Sheet silicates, Longmans, London, 170-190

Higuti, I. and Miyata, Y. (1952) Calorimetric evidence for the capillary condensation theory : *J. Phys. Chem.* **56**, 921-927.

Jallut, C., Lenoir, J., Bardot, C., Eyraud, C. (1992) Thermoporometry. Modelling and simulation of a mesoporous solid : *J. Membr. Sci.* **68**, 271-282.

Jolicoer, C., Duchesne, D. (1981) Infrared and thermogravimetric studies of the thermal degradation of chrysotile asbestos fibres, evidence for matrix effects : *Can. J.Chem*. **59**, 1521-1526.

Lowell, S., Shields, J.E. (1984) Powder surface area and porosity, 2nd ed., Chapman and Hall, London, 1-135.

Luys, M-J. *et al*. (1982) Characterization of asbestos minerals, structural aspects and infrared spectra : *J. Chem. Soc., Faraday Trans.* **78**, 3561-3571.

Noll, W., Kircher, H. (1951) Über die morphologie von asbesten und ihren zusammenhang mit der kristallstructur : Neues Jahrbuch für Mineralogie, Monatshefte, 219-240.

Noll, W., Kircher, H., and Sybertz, W. (1958) Adsorptionsvermögen und spezifische Oberfläche von Silikaten mit röhrenförmig gebauten Primärkristallen : *Kolloid Zeitschrift* **157**, 1-11.

Quinson, J.F., Astier, M., and Brun, M. (1987) Determination of surface areas by thermoporometry : *Appl. Catal.* **30**, 123-130.

Scholten, J.J.F., Beers, A.M., and Kiel, A.M. (1975) Studies on pore structure of adsorbents and Catalysts: *J. of Catal.* **36**, 23-29.

Sasthav, M., Raj, W.R.P., Cheung, H.M. (1992) Characterization of Microporous Polymeric Materials. Pore continuity and size distribution via thermal analysis : *J. Coll. Interf. Sci.* **152** (2), 376-385.

Suquet, H. (1989), Effects of dry grinding and leaching on the crystal structure of chrysotile: *Clays & Clay Minerals* **37**, 439-445.

Wicks, F.J, and O'Hanley, D.S. (1988) Serpentine Minerals, structure and petrology, in 'Reviews in Mineralogy vol. **19**, Hydrous Phyllosilicates (exclusive of micas)', Ed. Baily, S.W., BookCrafters, Chelsea, Michigan, 91-129.

Yariv, S., and Heller-Kallai (1975) The relationship between the I.R. spectra of serpentines and their structures: *Clays & Clay Minerals* **23**, 145-152.

Zussman, J., Brindley, G.W., and Comer, J.J. (1957) Electron diffraction studies of serpentine minerals: *Amer. Mineral.* **42**, 133-153.

Chapter 9

The shrinkage and swelling of differently pillared hydrotalcite investigated by thermoporometry*

M.K. Titulaer, H. Talsma[1], J.B.H. Jansen, and J.W. Geus[2]

Department of Geochemistry, Institute for Earth Sciences, University of Utrecht, Budapestlaan 4, P.O. Box 80.021, 3508 TA Utrecht, The Netherlands
[1]Department of Pharmaceutics, University of Utrecht, Sorbonnelaan 16, P.O. Box 80.082, 3508 TB Utrecht, The Netherlands
[2]Department of Inorganic Chemistry, University of Utrecht, Sorbonnelaan 16, P.O. Box 80.083, 3508 TB Utrecht, The Netherlands

*) This paper is a contribution of the Debye Institute, University of Utrecht, The Netherlands.

ABSTRACT

Pillared hydrotalcite minerals $Mg_6Al_2(OH)_{16}CO_3.4H_2O$ are prepared with different interlayer anions, viz., carbonate, oxalate, malonate, succinate, adipate, sebasate, and chloride. The chloride samples are prepared at pH values of 10, 9, 8, and 7. The substitution of the respective anions is assessed by X-ray diffraction, infrared spectroscopy, and transmission electron microscopy. The interlayer spacing of the hydrotalcite with specific anions increases from 7.82 Å (OH^-), to 7.89 Å (CO_3^{2-}), 8.06 Å (Cl^-) where the molar ratio Mg/Al is 3/1, 10.04 Å (oxalate), 10 Å (malonate), 12.4 Å (succinate), 13.15 Å (adipate), and 18.84 Å (sebasate) where the molar ratio Mg/Al is 2. Hydrotalcite interlayer spacings can be observed in the TEM photographs of succinate and adipate samples.

The chloride and bicarboxylic acid samples are almost free of carbonate as proved by the absence of the 3050 cm^{-1} carbonate-water bridging band in the IR spectra. Strong C-C bands at 1625-1572 cm^{-1} and C-H bands at 2865, 2940, and 2995 cm^{-1} are visible in the infra-red spectra of the hydrotalcites with bicarboxylic acids within the interlayer. Differential thermal analysis and thermogravimetric analysis indicate the contamination of the chloride samples at pH levels of 7 and 8 with hydroxyls.

The shrinkage and swelling of the interlayer is investigated by thermoporometry. First, the wet clays as prepared are examined by thermoporometry. Subsequently, the clays are dried i) at room temperature, and ii) at an elevated temperature of 120° C. After drying the clays are again suspended in water and re-examined with thermoporometry. Drying at room temperature and subsequent swelling in water leads to the same ice-crystal diameter of 4 nm as the fresh carbonate samples. Drying at an elevated temperature of 120° C and re-wetting leads to an interlayer distance reduced to 70%.

The radii of the ice-crystals measured in the wet clays with thermoporometry are plotted as a function of the ionic radii of the anions in the dry clays. The resulting plot points to a successful thermoporometric measurement of the interlayer spacing of the wet clays. The amount shrinkage can be calculated by a simple formula, viz., shrinkage = $2*R_n/(d(003)-4.8)$, where $2R_n$ (Å) is the diameter of the ice-crystal of the wet clay, and d(003)-4.8 (Å) the interlayer spacing of the dried clay. The amount of shrinkage of the clays with the anions carbonate, oxalate, and chloride as presented in the plot is assessed on 13, 11, and 9 times. The amount of shrinkage of the clays with the anions malonate, succinate, adipate, and sebasate is assessed on 11, 8, 7, and 4 times.

INTRODUCTION

Pillared hydrotalcite, which is an anionic clay, can be used as well for its catalytic activity as for its specific powder properties. Anionic clays have positively charged sheets with anions located at the interlayer. Examples of catalytic activity of hydrotalcite clays are 1) after calcination as catalyst for the aldol condensation in the vapor phase forming $CH_3CR=CH_2-C=O-R$ from 2 moles of $CH_3C=O-R$ (Reichle, 1985), where R are aliphatic carbon chains, 2) oxidation of alkenes (2-hexene, cyclohexene) to alcoxides by hydrotalcite intercalated with polyoxo-molybdate and tungstate. The thickness of the interlayer strongly affects the performance of the catalyst (Tatsumi et al., 1992), 3) use of hydrotalcite exchanged with mono- and bicarboxylic acids for the production of tetraalcoxisilanes at temperatures between 80 and 200° C by re-esterification of tetramethoxy- or tetraethoxysilane with alcohol and continuous removal of methanol or ethanol, 4) esterification of an alcoxide (R_i-$(O-CH_2-CR_jH)_n$-OH) with a polycarboxylic acid, for example, citric acid in the presence of a calcined hydrotalcite (Bunte et al., 1992).

Powder properties of hydrotalcite are, 1) halide exchanger forming R_i-Br and R_j-Cl from R_i-Cl and R_j-Br where R_i and R_j are aliphatic carbon chains (Suzuki et al., 1990), 2) addition of Zn-hydrotalcite to halogen containing polymers as filler, UV-radiation stabilizer, chloride scavenger, and thermic stabilizer (Endres et al.,1992, Iida et al., 1992; Izuka et al., 1992, Ogawa et al., 1992), 3) utilization as toner powder (Kumagai et al., 1992), 4) utilization as thixotropic agent in ceramic and glass compounds (Geismar et al., 1992), and 5) the use as photo-active cis-phenyl-carboxyl-ethene (cinnamate) hydrotalcite (Valim et al., 1992).

As said before, the performance of hydrotalcite as a catalyst is highly influenced by the

interlayer spacing. The determination of the interlayer spacing before and after drying is the main topic of this paper. A method to measure the interlayer spacing before drying in water is thermoporometry. The technique can also be applied to dried clays rewetted in water. Natural hydrotalcite minerals could have impurities and have no uniform structure. Therefore, synthetic hydrotalcite minerals are prepared with various interlayer spacings. The different interlayer spacings should be measured by the thermoporometric technique. The paper contains the following sections, viz., 1) preparation of synthetic hydrotalcite and incorporation into hydrotalcites of the anions carbonate, malonate, adipate, sebasate, and chloride, 2) characterization of the hydrotalcite clay minerals with pillars of a desired size by X-ray diffraction (XRD), transmission electron microscopy (TEM), infrared spectroscopy (IR), thermogravimetric analysis (TGA), differential thermal analysis (DTA), and inductively coupled plasma atomic emission spectroscopy (ICP-AES), 3) assessment of a possible relationship between the size of the pores of wet hydrotalcite before drying by thermoporometry and the interlayer spacing of hydrotalcite after drying by XRD, 4) the investigation of subsequent swelling after addition of hydrotalcite powder to water by thermoporometry, 5) determination the reversibility of the shrinkage and swelling processes. The various structures of hydrotalcite incorporated with different anions are discussed in the next section.

The structure of hydrotalcite, $Mg_6Al_2(OH)_{16}CO_3.4H_2O$, is based on the brucite structure, which consists of octahedra of hydroxyl ions sharing edges. The Mg^{2+} ions are present in octahedral sites. Replacement of one third of the Mg^{2+} ions by Al^{3+} ions causes the sheet to have a nett positive charge. The positive charge is neutralized by (hydrated) anions present in the interlayers between the sheets (Figure 1a). XRD demonstrates that Mg and Al form a mixed sheet, because superlattice effects due to cation ordering among the octahedral sites are observed by Serna et al. (1982) and Schutz and Biloen (1987). Feitknecht (1942) and Ross and Kodama (1967) incorrectly assumed that the Al ions occupied positions somewhere between the brucite sheets within the interlayer.

In natural hydrotalcite, the molar ratio Mg/Al is restricted to 3 and the molar fraction Al expressed as $x = Al/(Al+Mg)$ is 0.25, the interlayer anion is restricted to CO_3^{2-}, and the amount interlayer water 4 H_2O. A vacancy of one oxygen in the interlayer is calculated with the rule 8-3(carbonate)-4(water) = 1. The synthetic hydrotalcites of Miyata (1980), however, contain no oxygen vacancies because 5 H_2O is incorporated, which yields the result 8-3(carbonate)-5(water) = 0 vacancies.

Two rules have to be obeyed to prepare compounds having the structure of hydrotalcite (Miyata, 1973), viz., i) the ionic radii of M^{2+} and M^{3+} must not vary more than 30 % in size, e.g., 0.65 Å for Mg^{2+} and 0.45 Å for Al^{3+}, and ii) the solubility products S_1 and S_2 of $M^{2+}(OH)_2$ and $M^{2+}CO_3$ must satisfy $0 < pS_1\text{-}pS_2 < 10$, where pS_1 is the negative logarithm of the solubility product of $M^{2+}(OH)_2$, $1.8.10^{-11}$ $mole^3l^{-3}$ of $Mg(OH)_2$, and pS_2 the negative logarithm of the solubility product of $M^{2+}CO_3$, $1.58*10^{-6}$ $mole^2l^{-2}$ of $MgCO_3$, thus $10.74\text{-}5.80 \approx 5$.

A large variety of minerals exist with the general formula :

$$M^{2+}_{1-x}M^{3+}_{x}(OH)_2A^{n-}_{x/n}.(1-3/2x)H_2O \quad (1)$$

where M^{2+} = Mg^{2+}, Ni^{2+}, Zn^{2+}, Ca^{2+}, Sr^{2+}, Ba^{2+}, Cd^{2+}, Cu^{2+}, Mn^{2+}, and M^{3+} = Al^{3+}, Fe^{3+}, Cr^{3+}, OH the hydroxyls of the double hydroxide sheet. The variable x represents the molar fraction of M^{3+} expressed as $M^{3+}/(M^{2+}+M^{3+})$, where x can be varied between 0.2 (Mg/Al = 4) and 0.33 (Mg/Al = 2) for synthetic hydrotalcite (Miyata, 1980; Reichle, 1986; Misra and Perrotta, 1992). The anions, A, of which CO_3^{2-} is preferred, counterbalance the positive charge of the brucite-like sheets, where n is the charge on the anion, e.g., CO_3^{2-}, OH^-, SO_4^{2-}, F^-, Cl^-, Br^-, NO_2^-, NO_3^-, I^-, ClO_4^-, $V_{10}O_{28}^{6-}$, $Mo_7O_{24}^{6-}$, $Cr_2O_7^{2-}$, SiO_3^{2-}, HCO_2, $W_{12}O_{41}^{10-}$, cinnamate, benzenedicarboxylate (Miyata, 1975; Twu and Dutta, 1990; Schutz and Biloen, 1987), and, finally, H_2O interstitial water.

Some of the double hydroxide minerals are presented in Table 1.

Table 1 Some double hydroxide clay minerals of the pyroaurite-sjögrenite group.

	3R-polytype	2H-polytype
$Mg_6Fe_2(OH)_{16}CO_3.4H_2O$	pyroaurite	sjögrenite
$Mg_6Fe_2(OH)_{16}Cl_2.4H_2O$	iowaite	-
$Mg_6Fe_2(OH)_{16}(OH)_2.4H_2O$	igelströmite	-
$Mg_6Al_2(OH)_{16}CO_3.4H_2O$	hydrotalcite	manasseite
$Mg_6Al_2(OH)_{16}SO_4.4H_2O$	motukoreaite	-
$Mg_6Al_2(OH)_{16}(OH)_2.4H_2O$	meixnerite	-
$Mg_6Cr_2(OH)_{16}CO_3.4H_2O$	stichtite	barbertonite
$Ni_6Fe_2(OH)_{16}CO_3.4H_2O$	revesite	-
$Ni_6Fe_2(OH)_{16}SO_4.4H_2O$	honessite	-
$Ni_6Al_2(OH)_{16}CO_3.4H_2O$	takovite	-
$Ni_6Al_2(OH)_{16}SO_4.4H_2O$	carboydite	-
$Ca_6Al_3(OH)_{20.25}(CO_3)_{0.375}.7H_2O$	hydrocalumite	-
$Ca_6Al_2(OH)_{12}(SO_4)_3.26H_2O$	ettringite	-

Allmann (1968) has extensively investigated the crystal structure of the mineral group. Two poly-types or subgroups exist with different layer stackings, viz., the low-temperature rhombohedral 3R poly-type, and the high-temperature hexagonal 2H poly-type, with three and two basal layers in one unit cell, respectively. The length of the crystallographic a-axis measures 3.102 Å, and that of the c-axis 23.404 Å. A three fold screw-axis is parallel to the c-axis. The stacking of the centers of mass of the oxygens of the brucite-like sheet is

-AB-BC-CA- (Figure 1a), and the hydroxyls of two adjacent brucite-like sheets, B-B, are situated directly above each other. The oxygens of adjacent brucite sheets are separated by 2.72 Å, which is 0.2 Å less than the ionic diameter of O^{2-} in vacuum, which is 2.92 Å. In Figure 1b, the relative position of the oxygen of carbonate or water in the interlayer is displayed.

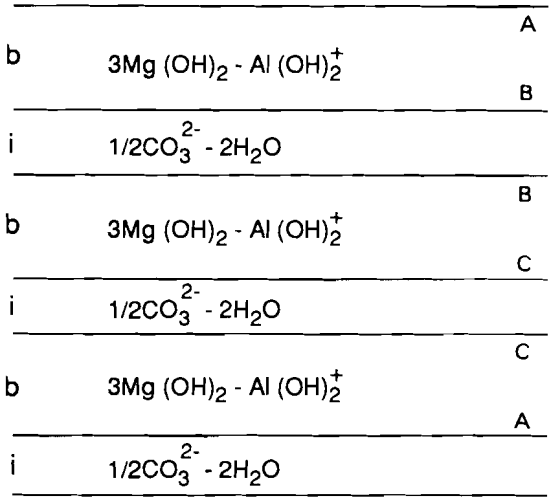

Figure 1 (a) schematic reproduction of the hydrotalcite clay minerals showing the positively charged brucite sheet, containing Mg and Al, alternated by the interlayer of carbonate and water molecules.

The oxygens of the double hydroxide sheet are plotted as solid spheres, and the oxygen of carbonate or water as a dashed sphere. The centers of mass of the oxygens of interlayer carbonate or water occupy a site distributed 0.58 Å from the bonding axis of hydroxyls of adjacent brucite sheets (Taylor, 1973). The angle between bonding axis of the brucite sheet and the line connecting the oxygen of the brucite sheet and that of interlayer carbonate (or water) is 22°. The distance between the oxygens of the brucite sheet and of carbonate (or water) is 1.47 Å.

The thickness of the brucite sheet can be calculated by $2*(1+\sqrt{(2/3)})$ * the crystal ionic radius of oxygen of 1.32 Å, yielding the result 4.8 Å. The value 4.8 Å together with the hydroxyl distance of 2.72 Å provides the minimum basal d(003) layer thickness of 7.52 Å. The basal thickness increases from 7.6 to 7.9 Å with a molar ratio Mg/Al rising from 2/1 to 5/1 (Taylor, 1973), and from 7.6 to 8.0 Å with a molar ratio Ni/Al rising from 2/1 to 5.6 /1 (Kruissink et al., 1981).

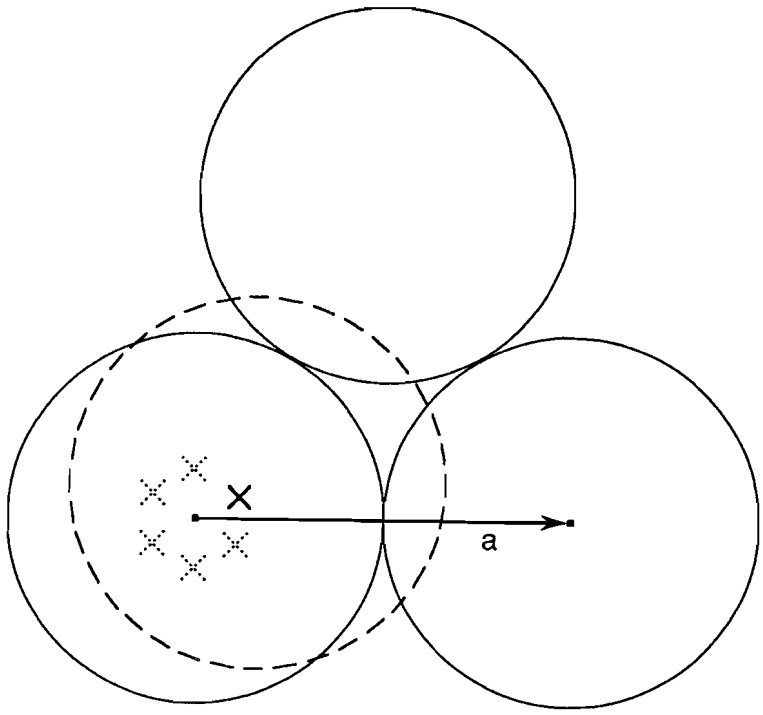

Figure 1 (continued) (b) oxygens of the brucite sheet and oxygens of the interlayer, containing CO_3^{2-} and H_2O. The centres of mass of the oxygens of CO_3^{2-} and H_2O occupy one of the six sites distributed 0.58 Å from the axis connecting the oxygens B-B of adjacent brucite sheets (parallel to the three fold axis).

The affinity of hydrotalcite for specific anions is a function of i) the negative charge of the anion, and ii) the size of the anion. The affinity decreases in the sequence $CO_3^{2-} > OH^- > SO_4^{2-} > F^- > Cl^- > Br^- > NO_3^- > I^-$ (Miyata, 1983). Especially CO_3^{2-} is incorporated in hydrotalcite, because the molecule lies flat with each oxygen exactly on one of the six sites distributed 0.56 Å from the hydroxyl bonding axis (Figure 1b). A different sequence of affinity has been published by Bish (1980), where the affinity decreases $CO_3^{2-} > NO_3^- > OH^- \approx Cl^- > SO_4^{2-}$. The difference might be attributed to the preparation conditions. Special precautions have to be taken when other anions than CO_3^{2-} are desired between the brucite-like sheets. Atmospheric CO_2 must be excluded from the reaction mixture, and the value of pH level at which the precipitation is performed must be sufficiently low, approximately 7. The low pH is explained by the ionization equilibria of carboxylic acid in water, viz., the concentration of CO_3^{2-} in water decreases at lower pH levels (equations. 4 and 5) (Kruissink et al., 1981) :

$$H_2CO_3 \text{ --> } H^+ + HCO_3^- \qquad \text{with } pK_1 = 6.4 \qquad (2)$$

$$HCO_3^- \text{ --> } H^+ + CO_3^{2-} \qquad \text{with } pK_2 = 10.3 \qquad (3)$$

Carbonate can be removed from the interlayer by calcination at 380° C. A reversible intercalation can be performed by dispersion of the calcined product in water, in which the specific anion has dissolved (Tagaya et al., 1992; Misra and Perrotta, 1992). The last mentioned method enables the preparation of hydrotalcite with specific anions other than carbonate.

The incorporation of anions with large radii in the hydrotalcite structure tends to increase the disorder of the brucite sheet (Miyata, 1983), because its thickness decreases in the order CO_3^{2-}, 7.65-2.72=4.93, F^-, 7.66-(2*1.33)=5, Cl^-, 7.86-(2*1.81)=4.24, Br^-, 7.95-(2*1.95)=4.05, I^-, 8.16-(2*2.16)=3.84 Å.

MATERIALS AND METHODS

Sample preparation

The nomenclature of the hydrotalcite samples is based on the molecular structure of the specific anions incorporated in hydrotalcite. The code of the bicarboxylic acid samples is based on the length of the carbon chain, for example C2 for oxalate with two C-atoms. The hydrotalcite with chloride samples are denoted as Cl- in combination with the preparation pH of, for example, 7 as Cl-7.

- C1, ratio Mg/Al = 2/1, hydrothermally aged hydrotalcite with carbonate.

An aliquot of 2 l of a hydrotalcite suspension containing 0.5 M Mg^{2+}, 0.25 M Al^{3+}, 1.75 M NaOH, and 0.47 M CO_3^{2-} (sample 1) is prepared from $MgCl_2.6H_2O$, $AlCl_3.6H_2O$, NaOH, and $Na_2CO_3.10H_2O$, according to the procedure of Reichle (1985). An amount of 24 g of the hydrotalcite suspension is aged for 24 h at 200° C in a Teflon coated steel pressure vessel of 48 ml. After hydrothermal treatment, the suspension is cooled, centrifuged for 10 minutes at 10000 rpm, and the resulting anionic clay is dried at room temperature.

- C1, ratio Mg/Al = 3/1, pH-statically prepared hydrotalcite with carbonate at pH 10.

An amount of 40.6 g (0.2 mole) $MgCl_2.6H_2O$ and 16.1 g (0.067 mole) $AlCl_3.6H2O$ dissolved in 270 ml H_2O is added at a rate of 14.4 ml*h^{-1} to 800 ml H_2O of pH 10 ± 0.01 contained in a double walled precipitation vessel of 3.5 l kept at 25° C by a thermostat. The pH of the suspension formed during the addition is kept at a constant level of 10 ± 0.01 by computer controlled addition of 40 g (1 mole) NaOH and 18.0 g (0.063 mole) $Na_2CO_3.10H_2O$ in 500 ml H_2O. After the addition of the Al-Mg solution has completed, 300 ml of the hydrotalcite suspension is centrifuged for 10 minutes at 3000 rpm, separated from the fluid, re-suspended in water, and washed and centrifuged additionally three times at 3000 rpm. Finally, the solid is dried at 120° C for a period of time of 18 h.

- C2-C10, ratio Mg/Al = 2/1, bicarboxylic acid anion ($C_nH_{2n-4}O_4^{2-}$) analogues of hydrotalcite, with carbon numbers n of 2 (oxalate), 3 (malonate), 4 (succinate), 6 (adipate), and 10 (sebasate)

A solution of 22.7 g (0.1117 mole) $MgCl_2.6H_2O$ and 12.7 g (0.0527 mole) $AlCl_3.6H_2O$ in 70 ml H_2O is brought into a 250 ml two-neck round bottom flask fitted with a N_2 inlet and stop (solution A), and is evacuated three times and kept under nitrogen. A second solution (B) of 2.24 g (0.0178 mole) oxalic acid dihydrate ($C_2H_2O_4.2H_2O$) in 200 ml H_2O is prepared in a three-neck round bottom flask of 500 ml fitted with a mechanical stirrer, N_2 inlet, and stop. Solid KOH (22.5 g, 0.401 mole) is added, and the white solution is three times evacuated and stored under nitrogen. A third solution (C) of 6.34 g (0.050 mole) oxalic acid dihydrate and 5.71 g (0.1018 mole) KOH in 200 ml H_2O is stored also under nitrogen.

The clear solution (A) is heated to 45° C on a water bath, and subsequently transferred into 100 ml dropping funnel with care being taken to expose the solution exclusively to nitrogen. The dropping funnel with (A) is attached to a 500 ml round bottom flask containing solution (B) again preventing contact with atmospheric air. Solution (A) is subsequently added to (B) in a period of 1 h, and (B) is stirred for 30 minutes. Centrifugation at 3700 rpm for 10 minutes results in a white anionic clay, which is added

to solution (C) under nitrogen. After the addition is complete, the mechanical stirrer fitted to the round bottom flask containing solution (C) is replaced by a reflux cooler under nitrogen. The suspension is refluxed at 101° C for 16 h, cooled, and centrifuged for 10 minutes at 3700 rpm. After three washings with evacuated water and centrifugations at 3700 rpm for 10 minutes, the anionic clay is dried at 125° C. An aliquot of 80 ml of the anionic clay suspension is stored for thermoporometric purpose.

Hydrotalcite anionic clays with malonate (n = 3), succinate (n = 4), adipate (n = 6), and sebasate (n = 10) as interstitial anions are prepared analogously according to the above procedure , with the difference that the solutions (B) contain 0.0252 mole of the bicarboxylic acids.

- Cl-10 to Cl-7, ratio Mg/Al = 3/1, pH-static prepared chloride analogues of hydrotalcite at pH 10 to 7.

The chloride analogues are prepared according to the same procedure as the hydrotalcite prepared at the fixed pH level of 10, except for the fact that a carbonate-free 2 M NaOH solution is added to the Mg-Al solution in a 3.5 l precipitation vessel, kept under nitrogen. The water has previously been boiled to remove CO_2. The pH of the Mg-Al solution is kept at a constant level of 10 ± 0.01, 9 ± 0.01, 8 ± 0.01, and 7 ± 0.01 by a computer controlled addition of the NaOH solution. An aliquot of 300 ml of the suspension is centrifuged for 10 minutes at 3000 rpm, washed with CO_2-free water, and centrifuged again. The procedure is repeated twice. Finally, the anionic clay is dried at 120° C for 20 h. A small amount of the wet anionic clay is stored for examination by thermoporometry.

Measurement of the amount of shrinkage and swelling by thermoporometry

The heat flux accompanying freezing of water and melting of ice within hydrothermally aged C1 (ratio Mg/Al = 2/1) is measured as a function of temperature within a Setaram DSC 111. Differential Scanning Calorimeter (DSC). 140 mg H_2O is added to 125 mg C1 (ratio Mg/Al = 2/1) before examination by thermoporometry.

An amount of 31.6 mg of the centrifuged wet anionic clay samples C1 (pH statically prepared Mg/Al = 3), C2 to C10, and Cl-10 to Cl-7 (series W) is measured, containing about 5.5 mg dry solid and 26.1 mg water. The samples hydrothermally aged C1, pH statically prepared C1, and C10 are dried first, rewetted by addition of 17.5 mg water to 15.9 mg solid, and measured after several weeks by thermoporometry (series D).

The anionic clay suspensions (series W and D) are inserted into an aluminum sample pan, and the heat-fluxes at temperatures below 0° C are measured with a Netzsch 200 DSC and a model 43 measuring cell (Selb, Germany). The following measuring sequence is applied 1) cooling from 20 to -60° C at a rate of -2 $°C*min^{-1}$, 2) heating from -60 to -2.5° C at a rate of 1 $°C*min^{-1}$, measuring the melting peak of pore ice, 3) cooling from -

2.5° C to -60° C at a rate of -1 °C*min^{-1}, measuring the freezing peak of pore water, and, finally, 4) heating from -60 to 20° C at a rate of 1 °C*min^{-1}, measuring the melting peak of both pore and bulk ice outside the pores of the solid.

The crystal radius R_n (in nm) of ice formed in the pores of the anionic clay is a function of the freezing point depression dT (in °C) by $R_n = 64.67*dT^{-1} - 0.23$. The specific pore volume V_n (in ml*g^{-1}) is the division of the amount frozen water, $\int P*dt/(H*D)$, by the weight of the solid, W, by $V_n = \int P*dt/(H*D*W)$, where P is the heat-flux (J/s), dt the time interval (min), H the ice-water transformation enthalpy (J/g), D the density of ice (g/ml).

Characterization of the dried anionic clays

XRD patterns are recorded on a Guinier-Johansson camera ($CuK_{\alpha,1}$ of 1.5406 Å). TEM micrographs and electron diffraction patterns are recorded with a Philips EM 420 transmission electron microscope. A suspension of the anionic clay in ethanol is, therefore, ultrasonically treated. A droplet of the suspension is brought upon a holey carbon film supported on a copper grid, and air dried. The TEM is operated at a voltage of 120 kV. The reflections against the lattice planes of a spacing d (in Å) are inversely proportional to the radial distances, l, of the diffraction maxima on the film (in mm) with a constant of $11.9*10^{-13}$ m^2 as calibrated with a gold film. The diffraction points are indexed using equation 4 of hydrotalcite, and equation 5 of the hexagonal supercell of hydrotalcite with a molar ratio Mg/Al of 2/1 (Figure 2a).

$$1/d^2 = <1/d,1/d> = 4(h^2+h*k+k^2)/3a^2 + l^2/c^2 \qquad (Å^{-2}) \qquad (4)$$

where a = 3.102 Å, and c = 23.404 Å

$$1/d^2 = 4(h^{*2}+h^**k^*+k^{*2})/3a^{*2} + l^{*2}/c^2 \qquad (Å^{-2}) \qquad (5)$$

where $a^* = \sqrt{3}*a = 5.37$ Å.

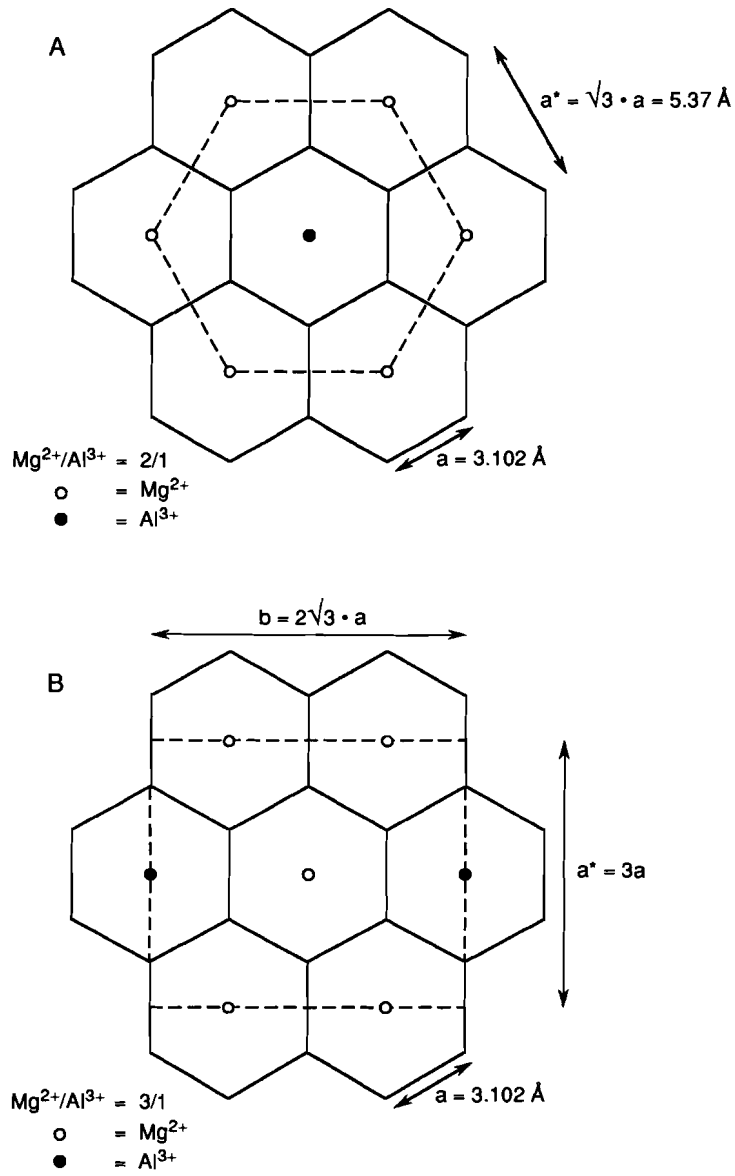

Figure 2 Supercells of hydrotalcite due to cation ordering among the octahedral sites, (a) molar ratio Mg/Al=2/1, hexagonal with $a^* = \sqrt{3}a = 5.73$ Å, and c=23.404 Å, (b) molar ratio Mg/Al=3/1, orthorhombic with $a^* = 3a = 9.31$ Å, $b = 2\sqrt{3}a = 10.75$ Å, and c=23.404 Å.

-stoichiometry

The molar ratio Mg/Al in the precipitates and the amount of bonded water expressed as wH_2O in $Mg_{8-8x}Al_{8x}(OH)_{16}(CO_3)_{8x/2}.wH_2O$ is assessed by ICP-AES and TGA. For ICP-AES measurements, amounts of 50 mg of each anionic clay, viz., the samples C1 (Mg/Al = 3), C2 to C10, and Cl-10 to Cl-7, except of hydrothermally aged C1 (Mg/Al = 2) are suspended in 100 ml 0.1 M HNO_3, forming clear solutions (except of the samples C10 and Cl-7 forming suspensions). An aliquot of 10 ml of the solution thus obtained is diluted to 100 ml with 0.1 M HNO_3. The concentrations of [Mg] and [Al] (in mg metal*l^{-1}) are measured within a 34000 Applied Research Laboratories instrument (Valencia, U.S.A.). From the concentrations [Mg] and [Al] the amount water, w, in the initial 50 mg hydrotalcite is calculated. The molar ratio Mg/Al is calculated from the measured concentrations [Mg] and [Al] according to molar ratio Mg/Al = ([Mg]/[Al])*1.11.

TGA-DTA profiles of about 32 mg of the dried samples in a nitrogen flow of 50 ml*min^{-1} are measured from 20° to 713° C at a rate of 5 °C*min^{-1} within a Dupont 951 thermogravimetric analyzer (Wilmington, U.S.A.), and a Dupont 1200 DTA cell, respectively. The data of TGA and DTA experiments are collected by a Dupont 1090 thermal analyzer.

RESULTS

Structure of hydrotalcite precipitates investigated by XRD, TEM, and IR

-XRD

The XRD reflections of the differently pillared hydrotalcite samples are recorded in Table 2. The two d(003) reflections, viz., 7.7 and 7.89 Å, of the samples C1 are typical for hydrotalcite with carbonate in the interlayer but with different Mg/Al ratios of 2/1 and 3/1. The d(003) spacing is increasing with a decreasing amount of Al.

Incorporation of large bicarboxylic acids, as in samples C2 to C6, causes the d(003) reflections to increase from 10.04 Å of C2, oxalate, to ±10 Å of C3, malonate, to 12.40 Å of C4, succinate, to 13.15 Å of C6, adipate. A layer distance of 18.84 Å is calculated from the d(006) reflection of C10, sebasate, by 2*d(006). Additional d(003) reflections, respectively, 8.32, 9.27, and 11.78 Å are measured with the hydrotalcite samples incorporated with C3, malonate, C4, succinate, and C6, adipate (Table 2). The additional reflection d(003) of 7.85 Å of the hydrotalcite sample incorporated with C6, adipate, is explained by contamination of the C6 sample with carbonate.

Table 2 X-ray diffraction diffraction values d(Å) of synthetic pillared hydrotalcite clay minerals with interstitial bicarboxylic anions with carbon numbers, varying from 1 to 10.

Hydrotalcite, hexagonal a = 3.102 Å, c = 23.404 Å (JCPDS file No 22-700 and 14-191)

C1(Mg/Al = 2)	I/I_0	C1(Mg/Al = 3)	I/I_0	C2	I/I_0	Ref.	I/I_0	hkl
7.7	-	7.89	100	10.04	100	7.84	100	003
5.5	-	-	-	-	-	-	-	-
3.85	-	3.95	60	4.98	60	3.90	60	006
-	-	-	-	-	-	2.62	-	012
2.61	-	2.61	70	3.30	10	2.60	40	009
2.55*	-	-	-	2.56	5	-	-	103*?
2.34	-	2.33	55	-	-	2.33	25	015
1.99	-	1.98	50	-	-	1.99	30	018
1.95	-	-	-	-	-	1.95	6	$00\underline{12}$
-	-	1.74	10	-	-	1.75	10	$10\underline{10}$
-	-	1.67	10	-	-	1.65	10	$01\underline{11}$
1.525	-	1.54	50	1.52	35	1.541	35	$11\underline{0}$
1.496	-	1.51	50	1.50	20	1.498	25	113 $10\underline{13}$
1.418	-	1.43	10	1.41	5	1.419	8	$01\underline{14}$
1.32*	-	1.33	5	-	-	-	-	$20\underline{3}$*?
1.31	-	-	-	-	-	1.302	6	$00\underline{18}$
1.276	-	1.28	20	-	-	1.265	10	-

C3	I/I_0	C4	I/I_0	C6	I/I_0	C10	I/I_0	hkl
±10 ±8.32	100	12.40 9.27	70 100	13.15 11.78 7.85	100 80 25	-	-	003
5.06	30	6.15	10	6.55	10	9.42	-	006
4.58	20	4.59	35	4.99	3			
3.60	5	4.09	5	4.56	10	6.42	-	009
3.17	15	-	-	-	-	-	-	-
2.57*	55	-	-	-	-	-	-	103*?
2.34	15	2.28	5	-	-	-	-	015
2.15	10	2.14	5	-	-	-	-	-
-	-	1.97	10	-	-	-	-	018
1.85	10	1.89	10	-	-	-	-	-
-	-	1.62	5	-	-	-	-	$01\underline{11}$
1.53	95	1.52	55	1.52	85	1.52	-	$11\underline{0}$
1.51	60	1.48	30	-	-	-	-	113 $10\underline{13}$
		1.31	10	1.31	10	-	-	$00\underline{18}$
1.24	15							

* hexagonal supercell a* = 5.37 Å, c = 23.404 Å (Fig. 2)

In Figure 3, a linear curve results when the measured d(003) spacings are plotted against the carbon numbers n of Cn, intersecting the y-axis at 6.9 Å. The spacing of 2*d(006) plotted against the carbon numbers yield an identical line. The data set of Miyata (1973) has also been plotted in Figure 3. A second curve is constructed with the additional d(003) reflections, respectively, 8.32, 9.27, and 11.78 Å of the hydrotalcite samples incorporated with C3, malonate, C4, succinate, and C6, adipate. The second curve represented in Figure 3 is not observed by Miyata, and is situated below the upper curve. The curve is intersecting the y-axis at a relative low value of 4.7 Å. The slope of the upper and lower curve is equal. The difference in d(003) spacing between the upper and the lower curve is, therefore, consequently constant on 2.2 Å.

The slope of the upper and lower line in Figure 3 corresponding to 1.16 and 1.17 Å/C-number, respectively, is close to that of the product of the C-C distance with the sinus of the valence angle, which is 1.54*sin(110/2) = 1.26 Å/C-number. The intersection of the lower line with the y-axis, representing the d(003) spacing, is close to the thickness of the brucite sheet of 4.8 Å, calculated with the ionic radius 1.32 Å of oxygen. The upper line evidently represents more than the thickness of the brucite sheet. Maybe, the bicarboxylic acids are present together with one carbonate ion or a water molecule at the interlayer. The existence of carbonate in sample C6 is demonstrated by the reflection at 7.85 Å measured by XRD, but carbonate is not incorporated in every crystallite.

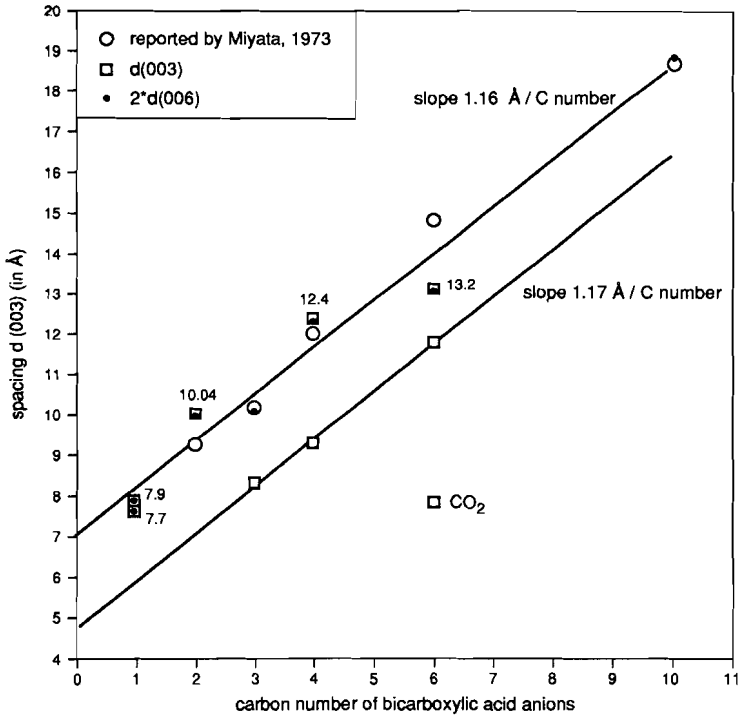

Figure 3 Sheet distance d(003) and 2*d(006) as a function of the carbon number of the bicarboxylic acids with two lines of the layer distances (brucite sheet + interlayer) against the carbon numbers with the same slopes of 1.17 Å/C-number, but cutting the y-axis at 6.9 and 4.7 Å, respectively.

In table 3, the chloride samples prepared at the different pH levels of 10, 9, 8, and 7 have a d(003) reflection decreasing from 8.08 to 7.82 Å at a pH level decreasing from 10 to 7. An exception is sample Cl-8, which has a relative large d(003) spacing of 8.20 Å.

Some XRD reflections marked with an asterisk in Table 2 and Table 3 cannot readily be explained and are attributed to superlattice reflections (Figure 2a and 2b). The reflection at 2.56 Å of the hydrothermally aged carbonate C1, the oxalate C2, and the malonate C3 is ascribed to a reflection from a hexagonal supercell, while the reflections 4.51, 4.49, and 4.41 Å of the chloride samples Cl-9, Cl-8, and Cl-7, respectively, are attributed to reflections from an orthorhombic supercell (Figure 2b).

Table 3 X-ray diffraction values d(Å) of synthetic pillared hydrotalcite clay minerals with interstitial chloride prepared at different static pH values of 10 to 7.

Hydrotalcite, hexagonal a = 3.102 Å, c = 23.404 Å (JCPDS file No 22-700 and 14-191)

Cl-10	I/I_0	Cl-9	I/I_0	Cl-8	I/I_0	Cl-7	I/I_0	hkl
8.08	100	8.04	100	8.20	100	7.82	100	003
-	-	-	-	4.97	30	-	-	-
*	-	4.51	10	4.49	30	4.41	60	⌐023*? | 121*? └201*?
4.03	20	3.97	35	4.06	10	-	-	006
-	-	-	-	3.60	5	-	-	-
2.61	10	2.61	30	2.61	20	2.58	15	009
-	-	-	-	2.43	5	-	-	-
-	-	2.34	30	-	-	-	-	015
-	-	2.14	25	-	-	2.13	70	-
-	-	1.99	15	2.04	5	-	-	018
-	-	-	-	1.77	20	1.76	15	$10\underline{1}0$
-	-	-	-	1.67	20	-	-	$10\underline{1}\underline{1}$
1.53	20	1.54	45	1.54	25	1.52	15	$11\underline{0}$
1.51	10	1.51	30	1.51	15	-	-	⌐113
-	-	-	-	-	-	-	-	$\underline{1}01\underline{3}$
-	-	1.44	5	-	-	-	-	-
-	-	1.32	10	-	-	-	-	-

* orthorombic supercell a* = 9.31 Å, b = 10.75 Å, c = 23.404 Å (Fig. 2)

-TEM

In Figure 4a-c the TEM micrographs of the hydrothermally aged carbonate sample C1 with a ratio Mg/Al of 2 show the hexagonal platelike crystals of a dimension between 300 and 900 nm. In the electron diffraction patterns of hydrotalcite, strange indices, such as, (-1/3,2/3,0), (-2/3,1/3,0) appear (Figure 4c). The TEM reflections (-1/3,2/3,0), (-2/3,1/3,0) can be ascribed to (1,0,0), (0,1,0) reflections of a hexagonal supercell using equation (5). TEM micrographs of hydrotalcite with the interstitial succinate C4 (Figure 4d and e) show lattice fringes when the electron beam is approximately perpendicular to the c-axis. The

distance between the fringes is 20.7 Å. The distance of 20.7 Å is about equal to d(002) of hydrotalcite with the anion succinate, which is 37.2/2=18.6 Å (Table 2). The interlamellar distance of 37.1 Å of adipate (C6) (Figure 4f and g) is close to the 3*d(003) of 3*13.15=39.5 Å. The fringes of the sample with adipate are irregular with respect to those of the sample with succinate. No fringes can be seen in the micrographs of the sample with sebasate. A TEM micrograph of the hydrotalcite C1 prepared at pH 10 displays thin flakes of material (Figure 4h).

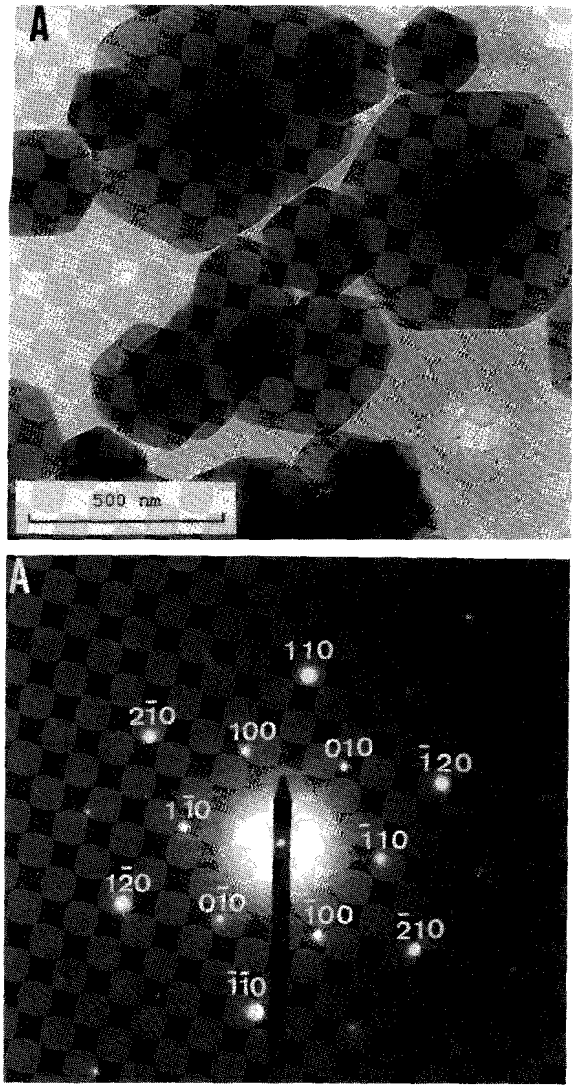

Figure 4

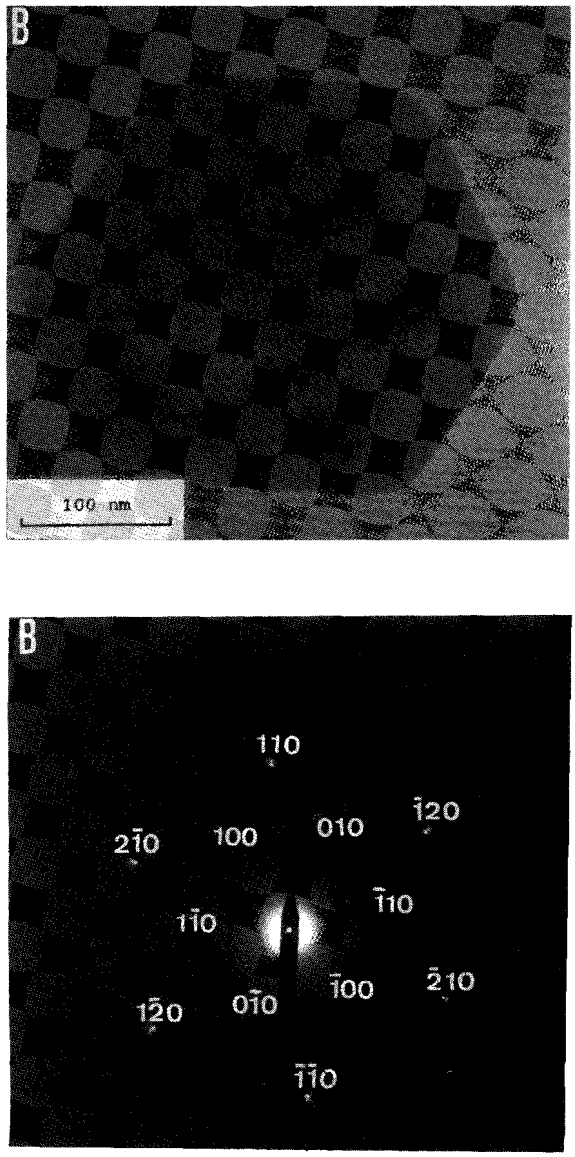

Figure 4 TEM micrographs and electron diffraction patterns of hydrotalcite samples : a) hydrothermally aged 24 h at 200° C with carbonate, magnification to the film 18000 times, b) 70000 times, c) 18000 times.

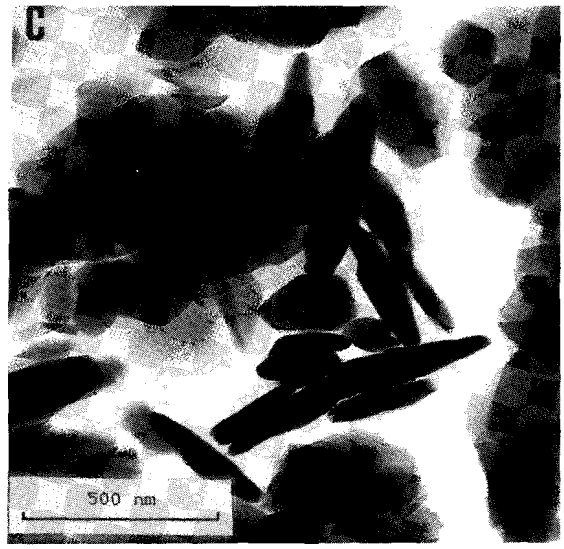

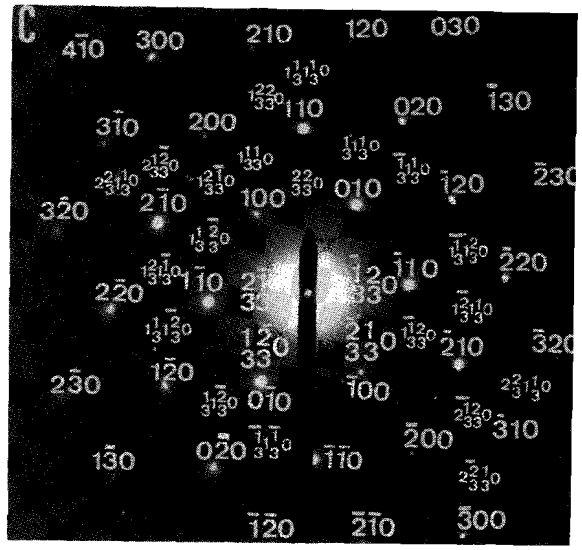

Figure 4 (continued) C1 hydrothermally aged.

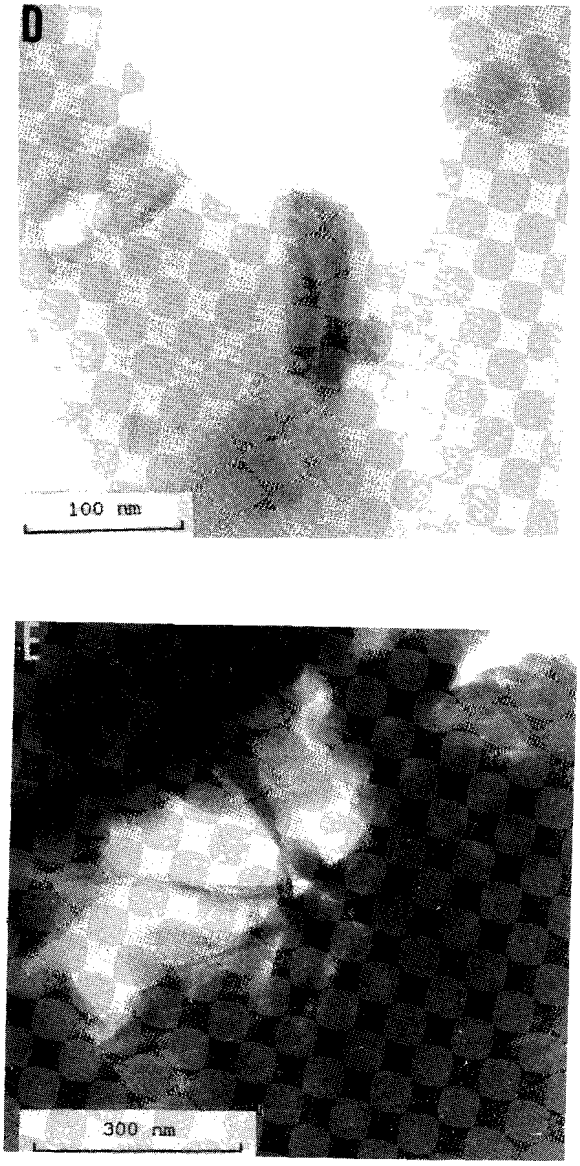

Figure 4 (continued) hydrotalcite d) with succinate (C4) 70000 times, e) C4, 32000 times.

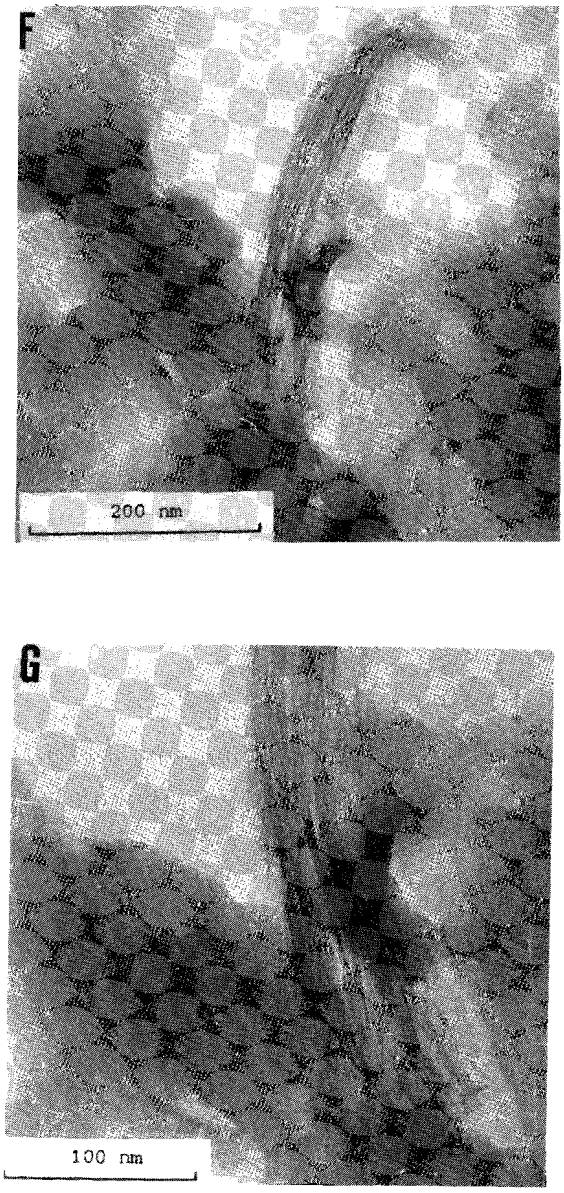

Figure 4 hydrotalcite with interlayer f) adipate (C6) 54000 times, g) C6, 92000 times.

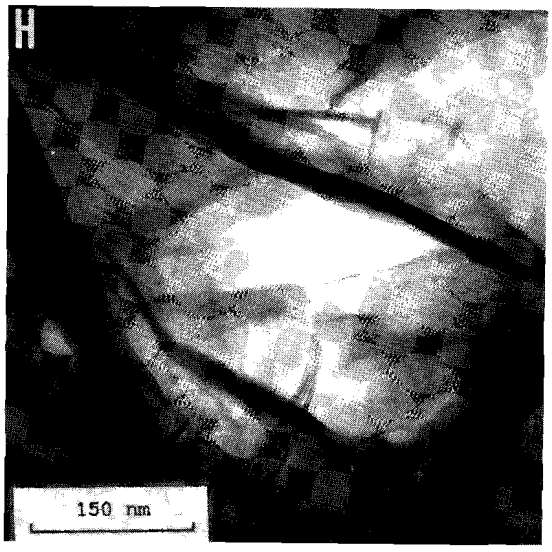

Figure 4 h) hydrotalcite with interlayer carbonate at pH 10, 54000 times.

-IR

The IR spectra of the samples (25 wt% in KBr) of hydrotalcite containing the anions oxalate, malonate, succinate, sebasate, and chloride at pH 10 and at pH 8 (C2-4, C6, Cl-10, Cl-8) are shown in Figure 5. The peaks and the relative intensities of the hydrotalcite with bicarboxylic acid samples are interpreted in Table 4, and that of the hydrotalcite with chloride samples in Table 5. The maximum of the broad OH stretching vibration band of the brucite sheet is slightly shifted from 3550 to 3450 cm^{-1} from carbonate (C1) to sebasate (C10) (Table 4). Water is present in the anionic clays, as shown by the H_2O bending vibration at 1650 cm^{-1} of the bicarboxylic acid samples, and at 1635 cm^{-1} of the chloride samples (Tables 4 and 5). The vibrations of the carboxylic groups in the region 1505 to 920 cm^{-1} are seen in the spectra of the series from carbonate to sebasate, and, remarkably, also in the spectra of the chloride samples. Some carbonate is, therefore, incorporated in the chloride samples, but not sufficiently to observe the CO_3^{2-} to H_2O bridging band at 3050 cm^{-1}. The CO_3^{2-} to H_2O bridging band at 3050 cm^{-1} is visible in the carbonate (C1) spectrum, but not in the spectra of the chloride samples Cl-10 to Cl-7 and also not in the spectra of oxalate to sebasate (C2 to C10). The C-H stretching vibrations at 2922 and 2865 cm^{-1} of the carbon chains of the carboxylic acids is detectable in the

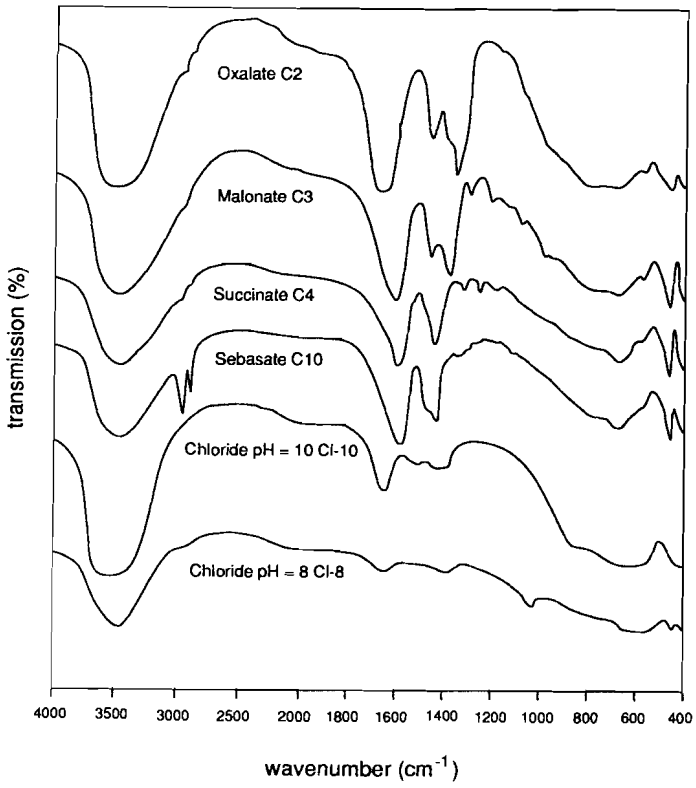

Figure 5 IR spectra of the samples containing oxalate, malonate, succinate, sebasate, and chloride at pH 10 and 8.

spectra of the samples C1 to C10. The very weak C-H vibrations at 2922 and 2865 cm^{-1} of carbonate C1 is attributed to carbonate in the proximity of hydroxyls of the double hydroxide sheet. In contrast, the C-H stretching vibrations at 2922 and 2865 cm^{-1} of hydrotalcite with sebasate is especially strong due to the length of the carbon chain (Figure 5). The C-C vibrations of the carbon chains range from 1625 cm^{-1} of oxalate (C2) to 1572 cm^{-1} of sebasate (C10). The C-C vibration is, as to be expected, absent in the spectra of the carbonate sample C1 and the chloride samples Cl-10 to Cl-7.

In Figure 5, the Mg-O stretching vibration at 660 cm^{-1} and Al-O stretching vibration at 450 cm^{-1} of the brucite-like layer are strong with the anion carbonate to sebasate samples 2 to 7, but weak for the chloride samples 8 to 11, which indicates a poor crystallinity of the chloride samples. The poor crystallinity may be due to the reduced thickness of the brucite sheet of 4.24 Å against a value of 4.8 Å for hydrotalcite with carbonate (Miyata, 1983).

Table 4 Infrared spectroscopy of hydrotalcite samples with interstitial carbonate prepared at the static pH of 10 (C1), oxalate (C2), malonate (C3), succinate (C4), adipate (C6), sebasate (C10) (Kruissink et al., 1981; Bish, 1980; Miyata, 1975).

	wavenumber (cm^{-1})					
sample	2 C1	3 C2	4 C3	5 C4	6 C6	7 C10
OH-stretch.	3550^{b}	3500^{b}	3460^{b}	3450^{b}	3440^{b}	3450^{b}
CO_3^{2-} to H_2O bridging	3050^{sh}	-	-	-	-	-
C-H (CH_2)	2922^{vw} 2865^{vw}	2940^{w} 2865^{w}	2940^{vw} 2865^{vw}	2995^{w} 2940^{w} 2865^{w}	2960^{w} 2870^{w}	2950^{s} 2865^{s}
	2000^{sh}	2075^{sh} 1920^{sh}	2100^{sh}	$2180^{w\text{-}sh}$	2200^{sh} $2000^{w\text{-}sh}$	-
H_2O bending	1650^{s}	1650^{b}	1650^{sh}	1650^{sh}	1650^{sh}	-
C-C	-	1625^{b}	1592^{s}	1575^{s}	1565^{s}	1572^{s}
CO_3^{2-} stretching	1505^{sh} 1440^{s}	1440^{s}	1440^{sh}	1460^{sh}	1450^{sh}	
CO_3^{2-} (n_3) stretching	1378^{s}	1380^{sh} 1339^{s}	1363^{s}	1425^{s} 1328^{w}	1415^{s} 1340^{w}	1420^{s} 1340^{w}
		1315^{sh}	1280^{m}	1300^{m}		1320^{w}
		1160^{w}	1190^{m}	1235^{m}	1265^{w} 1218^{w}	1265^{w}
			1180^{sh}			1110^{w}
			1120^{sh}	1160^{sh}		1148^{w}
	1050^{sh}	1065^{sh} 958^{sh}	1070^{sh} 970^{sh} 935^{sh}		1060^{sh} 960^{sh} 920^{sh}	
CO_3^{2-} (n_2)	850^{sh}	810^{sh}	780^{sh}	-	775^{m}	775^{sh}
Mg-O stretching	650^{s}	675^{sh} 565^{m} 500^{sh}	670^{sh} 565^{m} 500^{sh}	660^{m} 565^{m} 490^{sh}	670^{s} 560^{m}	670^{m} 560^{w} 470^{sh}
Al-O stretching	out of range	450^{m}	455^{s}	450^{s}	out of range	450^{s}

^{s} strong, ^{m} medium, ^{w} weak, ^{vw} very weak, ^{sh} shoulder, ^{b} broad

Table 5 Infrared spectroscopy of hydrotalcite samples with interstitial chloride prepared at the static pH of 10 (Cl-10), 9 (Cl-9), 8 (Cl-8), and 7 (Cl-7) (Kruissink et al., 1981; Bish, 1980; Miyata, 1975)..

	wavenumber (cm^{-1})			
sample	8 Cl-10	9 Cl-9	10 Cl-8	11 Cl-7
OH-stretching	3510^{b}	3440^{b}	3475^{b}	3490^{b}
CO_3^{2-} to H_2O bridging	-	-	-	-
C-H	2932^{w}	2926^{w}	3937^{w}	2935^{w}
(CH_2)	2865^{w}	2856^{w}	2865^{w}	2865^{w}
	2000^{sh}	2000^{sh}	2050^{sh}	
H_2O bending	1635^{m}	1635^{m}	1640^{m}	1635^{sh}
C-C	-	-	-	-
CO_3^{2-}	1495^{sh}	1500^{sh} 1400^{sh}	1500^{sh}	1500^{sh}
CO_3^{2-} (n_3)	1380^{sh}	1370^{m}	1380^{m}	1380^{sh} 1160^{sh}
			1030^{m}	1030^{sh} 975^{sh}
CO_3^{2-} (n_2)	860^{sh}	850^{sh}	860^{sh}	
Mg-O stretching	650^{b}	620^{s}		
			560^{sh}	550^{sh}
Al-O stretching	420^{b}	out of range	452^{m}	455^{m}

^{s} strong, ^{m} medium, ^{w} weak, ^{vw} very weak, ^{sh} shoulder, ^{b} broad

Stoichiometry investigated by ICP-AES, TGA, and DTA

The molar ratios of Mg/Al of the anionic clay precipitates dissolved in acid solution and measured by ICP-AES are listed in Table 6. The molar ratios of Mg/Al of the precipitates are compared with those of the initial solutions. The molar ratio Mg/Al of 2.99 of the pH static prepared hydrotalcite with carbonate sample C1 is equal to that of the initial solution, which is 3. The molar ratio Mg/Al of 3.07 of hydrotalcite with chloride Cl-10 is also equal to that of the suspension, but decreases at lower levels of the pH during preparation to a value of 1.42 of hydrotalcite with chloride Cl-7. The hydrotalcite with chloride sample prepared at a pH level of 7, Cl-7, contains an excess of aluminum. Excess aluminum is also measured for hydrotalcite with malonate C3 to adipate C6 (Table 6). The mean value of Mg/Al of 1.8 of the solid is low with respect to that of 2 of the suspension. In contrast, the molar ratio Mg/Al of 2.13 of hydrotalcite with oxalate C2 is high with respect to the molar ratio of 2 of the initial solution. An excess of Mg is measured.

After determination of the ratio Mg/Al, the stoichiometric amount of water, w, in the interlayer of $Mg_{8-8x}Al_{8x}(OH)_{16}(A_{8x/n}).wH_2O$ is calculated. The value of w scatters between 1.5 and 12.8 (see table 6 and 8). The relative high value of 17.8 of the insoluble hydrotalcite with chloride sample Cl-7 is unreliable.

Table 6 Reconstructed stoichiometry of pillared clay samples from ICP-AES data of a solutions of 50 mg clay in 1 l 0.1 M HNO_3.

	solid (mg/l)	[Mg][1] (mg/l)	[Al][2] (mg/l)	molar ratio Mg/Al theor.	exp[3].	stoichiometry with assumption that solid is clay
C1	54	12.35	4.58	3	2.99	$Mg_6Al_2(OH)_{16}CO_3.5.8H_2O$
C2	48	8.65	4.53	2	2.13	$Mg_{5.44}Al_{2.56}(OH)_{16}(C_2O_4)_{1.18}.8.2H_2O$
C3	56	8.15	5.15	2	1.76	$Mg_{5.10}Al_{2.90}(OH)_{16}(C_3H_2O_4)_{1.45}.12.8H_2O$
C4	51	9.04	5.59	2	1.80	$Mg_{5.14}Al_{2.86}(OH)_{16}(C_4H_4O_4)_{1.43}.4.0H_2O$
C6	61	9.25	5.46	2	1.88	$Mg_{5.24}Al_{2.76}(OH)_{16}(C_6H_8O_4)_{1.38}.9.3H_2O$
Cl-10	63	14.30	5.17	3	3.07	$Mg_{6.04}Al_{1.96}(OH)_{16}Cl_{1.96}.5.8H_2O$
Cl-9	58	12.44	5.23	3	2.64	$Mg_{5.80}Al_{2.20}(OH)_{16}Cl_{2.20}.6.0H_2O$
Cl-8	51	7.36	8.74	3	0.94	$Mg_{3.87}Al_{4.13}(OH)_{16}Cl_{4.13}.1.5H_2O$
Cl-7[4]	(53)	6.65	5.17	3	(1.42)	$(Mg_{4.71}Al_{3.29}(OH)_{16}Cl_{3.29}.17.8H_2O)$

1) Mw Mg = 24.3 g/mole 2) Mw Al = 27.0 g/mole 3) exp. molar ratio = ([Mg]/[Al]) * 1.11
4) qualitative

Figure 6 shows the temperatures of four TGA and DTA peaks exhibited by the samples, viz., the loss of interstitial water (endotherm) at about 215° C for the carboxylic samples C1, C3, and C6, and at about 270° C for the chloride samples Cl-8 to Cl-7, an endothermic dehydroxylation step of OH bound to Al (gibbsite) at about 330° C of the carboxylic samples, and at about 360° C of the chloride samples, an endothermic dehydroxylation step of OH bound to Mg (brucite) at about 405° C of the carboxylic and chloride samples, about 60° C above the dehydroxylation step of OH bound to gibbsite, and an exothermic oxidation step of the carbon chain of the carboxylic acid samples C3, C4, and C10. The dashed lines in Figure 6 assume a constant difference of the temperatures of the four TGA and DTA peaks.

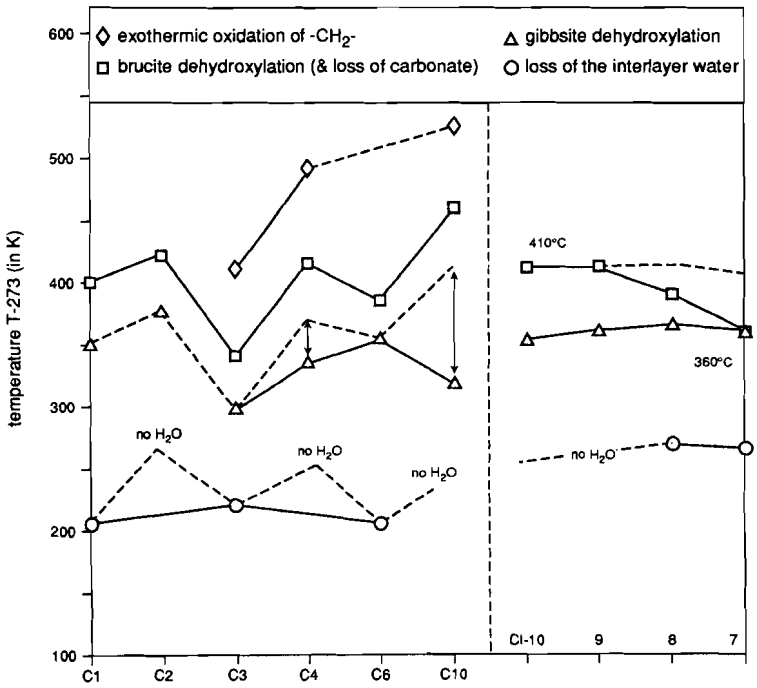

Figure 6 TGA and DTA analysis of the samples carbonate to sebasate and chloride at a pH level of 10 to 7.

-hydrotalcite with bicarboxylic acid anions

The brucite dehydroxylation temperature for the samples C2, C4, and C10 is relatively high when no loss of interlayer water is measured (squares in Figure 6). As mentioned, the temperature of dehydroxylation of gibbsite (triangles in Figure 6) is situated about 60° C under the temperature of dehydroxylation of brucite, except with the samples C4 and C10 that exhibit an even lower temperature of dehydroxylation of gibbsite as displayed by the arrows in Figure 6. The oxidation temperature of the carbon chain increases with increasing chain length from C3 to C10. The oxidation of C6 is not observed.

-hydrotalcite with chloride anions

The temperature of dehydroxylation of brucite of Cl-10 at 410° C is 50° C above the temperature of dehydroxylation of gibbsite, but decreases when the pH level during low preparation pH from 10 to 7 (Cl-10 to Cl-7), where the gibbsite dehydroxylation temperature at about 350° C is slightly increasing with 10° C.

The experimental weight losses of both the bicarboxylic and chloride anionic clays (in %) due to the loss of interlayer water (W1), dehydroxylation gibbsite (W2) and brucite (W3), and oxidation of the carbon chain (W4) are presented in Table 7. The theoretical weight losses are calculated using the proposed stoichiometric reactions under Table 7. For the sake of simplicity, the stoichiometric amounts of Mg and Al are those of the initial solutions, and not those of ICP-AES.

In table 8, the DTA-TGA analysis yields values, w, of bonded water in $Mg_6Al_2(OH)_{16}(A_{x/n}).wH_2O$ between 0 and 5. The amounts of water are different from the ICP-AES results and seem to be restricted to 1,3, or 5 H_2O, while the values calculated from the ICP-AES data results in values between 1.5 and 12.8 (Table 8), clearly measuring interlayer water as well as the amount of water adhering to the anionic clays.

Shrinkage and swelling as a function of the hydrotalcite anions

The thermoporometry results of the wet (W) samples show values of R_n, ranging from 0.9 to 3.1 nm, and values of V_n from 0.013 to 0.58 $ml*g^{-1}$. The mean value V_n of 0.36 $ml*g^{-1}$ of the wet (W) samples C1 to Cl-7 (2 to 11 in Table 9) is high as compared to that of the dried samples. The mean value of the shape factor F of both the wet (W) and dried (D) samples is 1.7, which is between that of a purely cylindrical (F = 2) and spherical (F = 1) pore shape.

The dried (D) samples exhibit values of R_n from 1.4 to 2.2 nm, and values of V_n from 0.025 to 0.44 $ml*g^{-1}$ (Table 9). The mean value V_n of the dried pH statically prepared sample C1 (D) and the sample C10 (D) dried at 120° C is 0.026 $ml*g^{-1}$.

Table 7 TGA and DTA analysis of pillared hydrotalcite clay minerals with (i) interstitial bicarboxylic anions with carbon numbers, varying from 1 to 10, C1 to C10, and (ii) chloride prepared at static pH values of 10 to 7, Cl-10 to Cl-**7**.

	sample									
	C1	C2	C3	C4	C6	C10	Cl-10	Cl-9	Cl-8	Cl-**7**
	experimental weight loss (%)									
W1	10	-	3	-	4	-	-	-	11	16
W2	28	37		10	32		31	31	15	14
W3			37	14 | 39		49				
W4	-	-		15	-		-	-	-	-
	theoretical weight loss (%) calculated with quoted formula									
W1	9[1]	-	3[4]	-	4[7]	-	-	-	10[11]	16[12]
W2	32[2]	41[3]	41[5]		43[8]		37[10]	37[10] ?	?	
W3				41[6]		53[9]				
W4	-	-	-		-		-	-	-	-

W1 loss of interlayer water, W2 structural water bound to Al (gibbsite), W3 structural water bound to Mg (brucite), W4 oxidation of CH_2 chain.

Mw = molar weight

1) $Mw(3H_2O)/Mw(Mg_6Al_2(OH)_{16}CO_3.3H_2O) * 100$ (%)
2) $Mw(8H_2O+CO_2)/Mw(Mg_6Al_2(OH)_{16}CO_3.3H_2O) * 100$ (%)
3) $Mw(8H_2O+1.33CO+1.33CO_2)/Mw(Mg_{5.32}Al_{2.66}(OH)_{16}(C_2O_4)_{1.33}) * 100$ (%)
4) $Mw(H_2O)/Mw(Mg_{5.33}Al_{2.66}(OH)_{16}(C_3H_2O_4)_{1.33}.H_2O) * 100$ (%)
5) $Mw(8H_2O+4CO)/Mw(Mg_{5.32}Al_{2.66}(OH)_{16}(C_3H_2O_4)_{1.33}.H_2O) * 100$ (%)
6) $Mw(10.6H_2O+1.33CO+4C)/Mw(Mg_{5.32}Al_{2.66}(OH)_{16}(C_4H_4O_4)_{1.33}) * 100$ (%)
7) $Mw(1.5H_2O)/Mw(Mg_{5.33}Al_{2.66}(OH)_{16}(C_6H_8O_4)_{1.33}.1.5H_2O) * 100$ (%)
8) $Mw(10.6H_2O+5.32C+1.33CH_4+1.33CO)/Mw(Mg_{5.32}Al_{2.66}(OH)_{16}(C_6H_8O_4)_{1.33}.1.5H_2O) * 100$ (%)
9) $Mw(12H_2O+6.6C+6.6CH_4)/Mw(Mg_{5.32}Al_{2.66}(OH)_{16}(C_{10}H_{16}O_4)_{1.33}) * 100$ (%)
10) $Mw(7H_2O+2HCl)/Mw(Mg_6Al_2(OH)_{16}Cl_2) * 100$ (%)
11) $Mw(5H_2O)/Mw(Mg_6Al_2(OH)_{16}Cl_2.5H_2O) * 100$ (%)
12) $Mw(3H_2O)/Mw(Mg_6Al_2(OH)_{16}Cl_2.3H_2O) * 100$ (%)

DISCUSSION

Assignment of thermoporometric R_n values to pores containing specific anions

It is proved by XRD and IR spectroscopy, that the anions carbonate, malonate, succinate, sebasate, and chloride are incorporated with minor contaminations in hydrotalcite. The layer distances d(003) and 2*d(006) increase with the carbon number of the bicarboxylic acid anions. Also the layer distances of the chloride containing samples (ionic radius 1.81 Å) are larger than that of that of the carbonate (ionic radius O^{2-} 1.46 Å) containing hydrotalcites.

The values of R_n in the wet anionic clays are attributed to water in interlayer pores containing a specific anion. The peaks in the thermograms are attributed to the ice crystal radii, R_n, indicative for the sheet distances in water ($\approx 2R_n$). The effect of a possible non-freezing layer appearing at the hydrotalcite-water interface is not considered here. The values of R_n of hydrothermally aged C1 with a molar ratio Mg/Al of 2/1, containing carbonate, which is dried at room temperature (D) and rewetted, are 1.9 and 2.2 nm (Table 9). The mean value of 2.05 nm is ascribed to water in the pores containing carbonate. The sheet distance in water is, therefore, 2*2.05 $\approx$ 4 nm.

A second ice crystal radius R_n of 1.0 nm of C1 (W) in water prepared at the statically pH level of 10 (Mg/Al = 3/1) points to a second, smaller anion present in the pores, and is assigned to pores containing OH^-.

Ice crystal radii, R_n, of values of 3 nm are measured with the wet (W) hydrotalcite samples containing bicarboxylic acid anions, C2 to C10. The value of R_n is surprisingly constant with increasing carbon chain of 2 to 10. The carbon chains, originally perpendicular to the basal layers in dried hydrotalcite, are assumed to rotate into flat positions between the sheets in water.

For the chloride samples, two sets of values of R_n are observed for Cl-10 to Cl-7, viz., 1) a decreasing R_n of 1.6 to 1.3 nm from pH 9 to 7, with a mean value of 1.43 nm, and 2) a small R_n of 1.0 $\pm$ 0.1 nm, not observed for sample Cl-9. The R_n of 1.43 nm is ascribed to ice nuclei in the pores containing chloride. The R_n of 1.0 nm is again ascribed to ice in the pores containing OH^-. The decrease of d(003) from 8.08 to 7.82 Å with declining pH from 10 to 7, indicates that chloride is incorporated at high pH and hydroxyls at low pH. This is in agreement with the loss of interlayer water (hydroxyls) of the samples prepared at the low pH values of 7 and 8 determined by DTA and TGA analysis (Figure 6).

Table 8 Comparison between the stoichiometry of the clays obtained by ICP-AES and TGA/DTA analysis

sample	technique	stoichiometry	w.H_2O w =
C1	ICP-AES	$Mg_6Al_2(OH)_{16}CO_3$	5.8
	TGA/DTA	$Mg_6Al_2(OH)_{16}CO_3$	3
C2	ICP-AES	$Mg_{5.44}Al_{2.56}(OH)_{16}(C_2O_4)_{1.18}$	8.2
	TGA/DTA	$Mg_{5.32}Al_{2.66}(OH)_{16}(C_2O_4)_{1.33}$	0
C3	ICP-AES	$Mg_{5.10}Al_{2.90}(OH)_{16}(C_3H_2O_4)_{1.45}$	12.8
	TGA/DTA	$Mg_{5.33}Al_{2.66}(OH)_{16}(C_3H_2O_4)_{1.33}$	1
C4	ICP-AES	$Mg_{5.14}Al_{2.86}(OH)_{16}(C_4H_4O_4)_{1.43}$	4.0
	TGA/DTA	$Mg_{5.32}Al_{2.66}(OH)_{16}(C_4H_4O_4)_{1.33}$	0
C6	ICP-AES	$Mg_{5.24}Al_{2.76}(OH)_{16}(C_6H_8O_4)_{1.38}$	9.3
	TGA/DTA	$Mg_{5.33}Al_{2.66}(OH)_{16}(C_6H_8O_4)_{1.33}$	1.5
C10	ICP-AES	-	-
	TGA/DTA	$Mg_{5.32}Al_{2.66}(OH)_{16}(C_{10}H_{16}O_4)_{1.33}$	0
Cl-10	ICP-AES	$Mg_{6.04}Al_{1.96}(OH)_{16}Cl_{1.96}$	5.8
	TGA/DTA	$Mg_6Al_2(OH)_{16}Cl_2$	0
Cl-9	ICP-AES	$Mg_{5.80}Al_{2.20}(OH)_{16}Cl_{2.20}$	6.0
	TGA/DTA	$Mg_6Al_2(OH)_{16}Cl_2$	0
Cl-8	ICP-AES	$Mg_{3.87}Al_{4.13}(OH)_{16}Cl_{4.13}$	1.5
	TGA/DTA	$Mg_6Al_2(OH)_{16}Cl_2$	5
Cl-7	ICP-AES	$(Mg_{4.71}Al_{3.29}(OH)_{16}Cl_{3.29}$	17.8
	TGA/DTA	$Mg_6Al_2(OH)_{16}Cl_2$	3

A plot of the experimental values of R_n against the ionic radii of the anions is represented in Figure 7. The ionic radii of O^{2-} in vacuum and of Cl^- are taken for hydroxyls and chloride, the sum of the atomic radii of C and O, 1.31 + 0.73 = 2.04 Å, respectively, is taken for carbonate. For carbonate it is taken into account that the molecule can rotate from a flat towards a tilted position, with the negative charge of the oxygens as near as possible to the positive brucite-like sheets. The radius is assumed to be in direction of the C-O valence bond, perpendicular to the three fold axis of carbonate. The radius of oxalate is taken perpendicular to the two fold axis, which measures 2.51 Å. The regression points to a successful measurement of the interlayer spacing by thermoporometry.

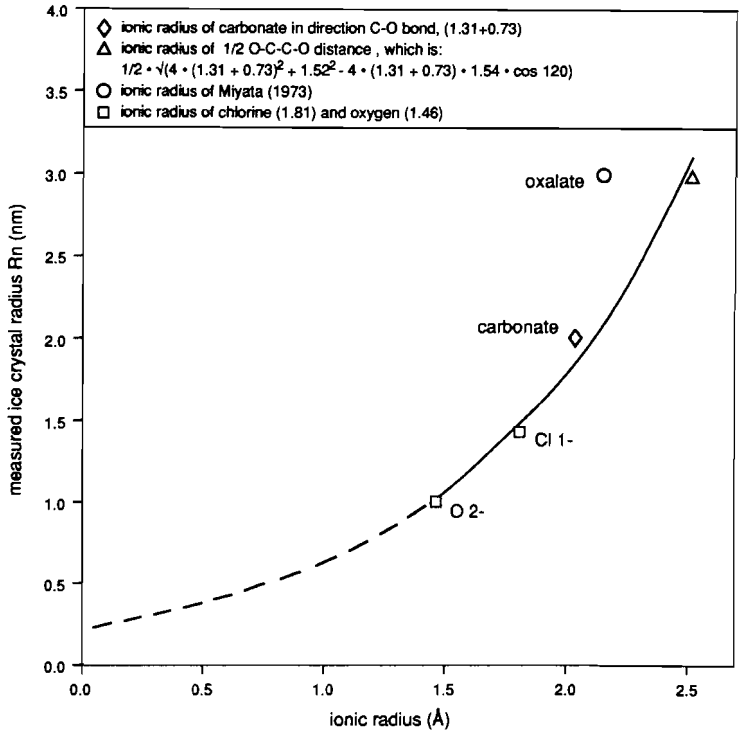

Figure 7 Plot of the ice crystal radius R_n measure by thermoporometry against the radius of the anions incorporated in the clays as determined by XRD and IR.

Extent of shrinkage and swelling calculated from the R_n and d(003) values

The radius, R_n, of 2.0 nm of the wet (W) carbonate sample C1 prepared at a static pH level of 10 is remarkably identical to that of the rewetted C1 sample, firstly dried (D) at room temperature, which has a mean value of (2.2 + 1.9)/2 = 2.05 nm (Table 9). Firstly drying at room temperature and subsequently rewetting thus leads to an equal ice-crystal radius, indicating that the swelling of the anionic clay reversible.

The value of V_n of 0.44 $ml*g^{-1}$ the firstly dried at room temperature and subsequently rewetted C1 sample (D) is equal to the mean value of 0.48 $ml*g^{-1}$ of the not dried hydrotalcite with bicarboxylic acid anions C2 to C10 (W) (Table 9). This is a second prove that the swelling of C1 is reversible after drying at room temperature, and leads to an equal pore dimension. This was established before with the measured ice-crystal radii.

Table 9 Thermoporometric ice crystal radii R_n, pore volumes V_n, and shape factors F measured on a Netzsch DSC 200 and model 43 measuring cell of pillared hydrotalcite clay minerals with (i) interstitial bicarboxylic anions with carbon numbers, varying from 1 to 10, and (ii) chloride prepared at static pH values of 10 to 7.

anion	pH	Dry/Wet[1]		R_n (nm)		V_n (ml/g)		F	
1 C1[2]	-	D	2.2[b]	1.9[a]		0.44[ab]		1.4[ab]	
2 C1[3]	10	W		2.0[a]	1.0[b]	0.06[a]	0.013[b]	-	
		D		1.4		0.025		-	
3 C2	-	W	3.6[b]	3.1[a]		0.52		1.7	
4 C3	-	W		2.9		0.58		1.9	
5 C4	-	W		2.9		0.44		1.6	
6 C6	-	W		3.1		0.54		1.6	
7 C10	-	W		2.9		0.31		1.8	
		D		1.4		0.026		-	
8 Cl^-	10	W		1.1		0.22		2.1	
9 Cl^-	9	W		1.6		0.26		1.5	
10 Cl^-	8	W		1.4[a]	0.9[b]	0.51[a]	0.30[b]	1.6[a]	1.7[b]
11 Cl^-	7	W		1.3[a]	1.1[b]	0.46[a]	0.49[b]	1.6[a]	1.5[b]

1) Wet (W) means that the clay suspension is 10 minutes centrifuged at 3000 rpm and not dried (5.5 mg clay + 26.1 mg H_2O), Dry (D) means that the centrifuged suspension is dried at 120° C (except of hydrothermally aged sample C1) and 17.5 mg H_2O is added to 15.9 mg dried clay.

2) sample C1 (Mg/Al = 2) is measured on a Setaram DSC 111, clay is centrifuged 10 minutes at 10000 rpm dried at room temperature, and 140 mg H_2O is added to 125 mg dried clay.

3) pH-static prepared sample C1 at pH = 10 (Mg/Al = 3)

a) main peak

b) secondary peak

ab) main peak + secondary peak together

In contrast, the ice crystal radius, R_n, in the pH statically prepared carbonate sample C1 (D) (Mg/Al = 3/1) dried at a high temperature of 120° C and rewetted is 1.4 nm, which is 70% of the radius, R_n, of 2.0 nm before drying. The drop in the radius, R_n, demonstrates that the shrinkage during drying at high temperature is irreversible.

The extent of shrinkage upon drying of the anionic clay samples can be evaluated from the ice crystal radii, R_n, of the anionic clays before drying as compared to the interlayer spacing obtained by XRD after drying. The amount of shrinkage is calculated by the division of sheet distance in water by the interlayer distance after drying :

$$\text{shrinkage} = 2*R_n/(d(003)-4.8) \qquad (6)$$

where $2R_n$ (Å) is sheet distance of hydrotalcite in water, which is equal to the diameter of the ice-crystal in the wet clay (Table 9), and d(003)-4.8 (Å) is the interlayer spacing of the dried clay, which is the subtraction of the d(003) reflections (Å) (Tables 2 and 3) by the thickness of the brucite-like layer of 4.8 Å.

The measured values of shrinkage are $2*20/(7.89-4.8) \approx 13$ times of hydrotalcite with the anion carbonate, $2*30/(10.04-4.8) \approx 12$ times of hydrotalcite with oxalate, $2*29/(10-4.8) \approx 11$ times of hydrotalcite with malonate, $2*29/(12.4-4.8) \approx 8$ times of hydrotalcite with succinate, $2*31/(13.15-4.8) \approx 7$ times of hydrotalcite with adipate, $2*29/(18.84-4.8) \approx 4$ times of hydrotalcite with sebasate, and, finally, $2*14.3/(8-4.8) \approx 9$ times of hydrotalcite with chloride.

CONCLUSIONS

1) Hydrotalcite anionic clay minerals with carbonate anions, various bicarboxylic acid anions with increasing carbon numbers of 2 to 10, and chloride anions have been successfully prepared. Two linear curves of the XRD reflections d(003) are fitted against the carbon number of the bicarboxylic acid samples with identical slopes. One curve is intersecting the y-axis at a value relatively high at 6.9 Å, which is equal to the value reported earlier in the literature, and the other curve reconstructed with additional d(003) reflections at 4.8 Å, which is equal to the thickness of the brucite-like sheet.

2) Carbonate-free chloride samples (Cl-10 to Cl-7) have been successfully prepared at pH values of 10 to 7 as shown by XRD and IR. Hydroxyl contamination of the samples prepared at a static pH of 8 and 7 is additionally demonstrated by XRD and TGA/DTA measurements.

3) After drying at room temperature, the swelling of the hydrotalcite anionic clays in water as measured by thermoporometry is reversible with a hydrothermally prepared hydrotalcite sample with carbonate at the interlayer, but irreversible with a pH-statically prepared hydrotalcite sample with carbonate at the interlayer and dried at an elevated temperature of 120 °C. Drying at a higher temperature and subsequent rewetting leads to a reduction of 70% of the original sheet distance in water.

4) The ice crystal radius R_n of 2 nm measured with thermoporometry in the wet (W) carbonate sample is attributed to pores containing carbonate. The R_n values of 3.1, 1.42, and 1.0 nm measured on samples containing oxalate, chloride, and hydroxyl, respectively, are attributed to pores containing the corresponding anions.

5) A plot of the ice crystal radius, R_n, against the ionic radius of the anion O^{2-}, Cl^-, CO_3^{2-}, $C_2O_4^{2-}$ incorporated in the anionic clay mineral points to a successful measurement of the interlayer spacing by thermoporometry. The effect of a non-freezing layer normally occurring at the solid-water interface is not considered.

6) The amount of shrinkage of the anionic clays is calculated by a simple formula, viz., shrinkage = $2*R_n/(d(003)-4.8)$, where $2R_n$ (Å) is the diameter of the ice-crystal of the wet clay before drying, and the subtraction d(003)-4.8 (Å) the interlayer spacing of the dried clay after drying as determined by XRD. The amount shrinkage of hydrotalcite with the anions recorded in the R_n against the ionic radius plot, respectively, is assessed on 13, 11, and 9 times for the anions carbonate, oxalate, and chloride, respectively. An amount of shrinkage of 11, 8, 7, 4 times is measured for hydrotalcite with malonate, succinate, adipate, sebasate, which are not recorded in the plot.

ACKNOWLEDGMENTS

The authors thank J.A.L.M. van Dorst and W.P.A. van de Noort for their experimental work, concerning the preparation and characterization of the clay minerals, and J.T. Kloprogge for the critical review of the paper.

REFERENCES

Allmann, R. (1968) The crystal structure of pyroaurite: *Acta Cryst.* **B24**, 972-977

Bish, D.L. (1980) Anion-exchange in takovite, application to other hydroxide minerals: *Bull. Minéral.* **103**, 170-175

Block, C., Breuer, W., Endres, H., and Hackgenei, J. (1992) Deutsches Patentamt, Offenlegungsschrift DE 4040679 A1

Bunte, R., Rats, H-C., Müller, R. (1992) Deutsches Patentamt, Offenlegungsschrift DE 4025925 A1

Endres, H., Loeffelholtz, F., Wedl, P., Worscheck, K., Hansen, A., Geismar, G. (1992) Deutsches Patentamt, Offenlegungsschrift DE 4031818 A1

Feitknecht, W. (1942) Zur kenntnis der Doppelhydroxide und basischen doppelsalze III (Über magnesium-aluminium doppelhydroxyd, experimentell bearbeitet von M. Gerber) : *Helv. Chim. Acta* **25**, 131-137

Geismar, G., Endres, H. (1992) Deutsches Patentamt, Offenlegungsschrift DE 4033730 A1

Iida, Y., Shimoyama, N., Oka, Y. (1992) Filler-containing expandable vinyl chloride polymer compositions: *Chem. Abstr.* **117**, 49906y, 49

Iizuka, S., Nishimura, M. (1992) Powdered stabilizers for chlorine-containing resins: *Chem. Abstr.* **117**, 49957r, 53

Kruissink, E.C., van Reijen, L.L., and Ross, J.R.H. (1981) Coprecipitated Nickel-Alumina catalysts for methanation at high temperature, part 1.-Chemical composition and structure of the precipitates: *J. Chem. Soc., Faraday Trans.* (1) **77**, 649-663

Kumagai, J., Tan, R., Ikeda, T., Fujii, T., Okada, C., Higashida, O. (1992) Electrostatographic toner and developer: *Chem. Abstr.* **117**, 58859n, 709

Misra, C., and Perrotta, A.J. (1992) Composition and properties of synthetic hydrotalcite : *Clays and Clay Minerals* **40** (2) 145-150

Miyata, S., and Kumura, T. (1973) Synthesis of new hydrotalcite-like compounds and their physico-chemical properties: *Chemistry Letters*, 843-848

Miyata, S. (1975) The synthesis of hydrotalcite-like compounds and their structures and physico-chemical properties-I, the systems Mg^{2+}-Al^{3+}-NO_3^-, Mg^{2+}-Al^{3+}-Cl^-, Mg^{2+}-Al^{3+}-ClO_4^-, Ni^{2+}-Al^{3+}-Cl^-, Zn^{2+}-Al^{3+}-Cl^-: *Clays and Clay Minerals* **23**, 369-375

Miyata, S. (1980) Physico-chemical properties of synthetic hydrotalcites in relation to composition: *Clays and Clay Minerals* **28**, 50-56

Miyata, S. (1983) Anion-exchange properties of hydrotalcite-like compounds: *Clays and Clay Minerals* **31**, 305-311

Ogawa, T. (1992) Fire-resistant vinyl chloride resin compositions: *Chem. Abstr.* **117**, 28122z, 73

Reichle, W.T. (1985) Catalytic reactions by thermally activated, synthetic, anionic clay minerals: *J. of Catalysis* **94**, 547-557

Reichle, W.T. (1986) Synthesis of anionic clay minerals (mixed metal hydroxides, hydrotalcite): *Solid States Ionics* **22**, 135-141

Ross, G.J., Kodama, H. (1967) Properties of a synthetic magnesium-aluminium carbonate hydroxide and its relationship to magnesium-aluminium double hydroxide, manasseite and hydrotalcite: *Am. Mineral.* **52**, 1036-1047

Schutz, A., and Biloen, P. (1987) Interlamellar chemistry of hydrotalcites, I. Polymerization of silicate anions: *J. of Solid State Chemistry* **68**, 360-368

Serna, C.J., Rendon, J.L., and Iglesias, J.E. (1982) Crystal-chemical study of layered $[Al_2Li(OH)_6]^+X^-.nH_2O$: *Clays and Clay Minerals* **30**, 180-184

Suzuki, S., Okamoto, M., and Ono Y., Catalysis by synthetic hydrotalcite-like materials in halide exchange between alkyl halides: *J. of Molecular Catalysis* **61**, 283-294

Tagaya, H., Tsunaki, K., Hasegawa, M., Karasu, M., Chiba, K. (1992) Adsorption of carbondioxide into hydrotalcite-like compounds: *Chem. Abstr.* **117**, 56712k

Tatsumi, T., Yamamoto, K., Tajima, H., Tominaga, H. (1992) Shape selective epoxidation of alkenes catalyzed by polyoxometalates intercalated hydrotalcite: *Chem. Lett.* **1992**, 815-818

Taylor, H.F.W. (1973) Crystal structures of some double hydroxide minerals: *Mineralogical Magazine* **39**, 377-389

Twu, J., and Dutta, P.K. (1990) Decavanadate ion-pillared hydrotalcite, spectroscopic studies of the thermal decomposition process: *J. of Catalysis* **124**, 503-510

Valim, J., Kariuki, B.M., King, J., and Jones, W. (1992) Photoactivity of cinnamate intercalates of layered double hydroxides, *Chem. Abstr.* **117**, 58585v, 686

Chapter 10

The quantity of reduced nickel in synthetic takovite ; effects of preparation conditions and calcination temperature*

M.K. Titulaer[1], J.B.H. Jansen[1], and J.W. Geus[2]

[1]Department of Geochemistry, Institute for Earth Sciences, University of Utrecht, Budapestlaan 4, P.O. Box 80.021, 3508 TA Utrecht, The Netherlands.
[2]Department of Inorganic Chemistry, University of Utrecht, Sorbonnelaan 16, P.O. Box 80.083, 3508 TB Utrecht, The Netherlands.
*This paper is a contribution of the Debye Institute, University of Utrecht, The Netherlands.

ABSTRACT

Takovite, $Ni_6Al_2(OH)_{16}CO_3.5H_2O$, with molar Ni/Al ratios of 2.5 and 3 is prepared by precipitation at pH-levels of 7 and 10, periods of reaction of 3 and 20 h, and calcination temperatures varying between 120 and 853° C. The quantity of reduced nickel is determined as a function of the calcination temperature, and the solid phases remaining after reduction are determined with XRD. The ratio Ni/Al, pH of precipitation, and calcination temperature are important preparation conditions. A precursor of a Ni/Al ratio of 2.5 precipitated at a pH-level of 10 exhibits on reduction metallic nickel particles of about 15 nm irrespective of the drying or calcination temperature. After reduction a considerable amount of $NaAlO_2$ is present. Metallic nickel particles of 6 nm are present in a reduced precursor of Ni/Al ratio of 2.5 precipitated at a pH-level of 7. The size of the nickel particles present in a reduced precursor of Ni/Al ratio of 3 precipitated at a pH-level of 10 rises from 4-8 nm to 16 nm after calcination at temperatures increasing from 120 to 853 °C. The last precursor contain much less sodium, and show after reduction a disordered NiO phase containing some alumina.

INTRODUCTION

Thermostable nickel-on-alumina catalysts of high loadings of nickel are useful as liquid-phase hydrogenation catalysts, currently used for carbon monoxide-hydrogen gas flows

by steam reforming of methane and naphtas. Recently, Kruissink and Van Reijen [1] have investigated the use of reduced nickelhydroxide / aluminumhydroxide coprecipitates for the reaction of H_2/CO flows to methane. Since steam is produced at high temperatures with methanation sinter-stable alumina is preferred as support. Silica is liable to react with steam at high temperatures to volatile species.

Ni-Al coprecipitates, reacting to the mineral takovite, can be prepared from nickel and aluminum salts with molar ratios Ni/Al between 1 and 5.6 with fresh precipitates (and between 2 and 3 with hydrothermally aged samples [2]). Takovite belonging to the group of Feitknecht clays, is build up of mixed positively charged nickel and aluminum double hydroxide layers, separated by layers of carbonate and crystal water. The morphology of the clays consists of rod shaped sponge-like clusters of dimensions of 100x200 nm. Surprisingly, the external morphology is not changed with calcination of the takovite to the corresponding oxides and even after reduction of the NiO present after calcination to Ni [3]. The calcination of takovite (with Ni/Al = 3), and the reduction to the Ni-on-alumina catalyst involve the following steps :

$$Ni_6Al_2(OH)_{16}CO_3.5H_2O \xrightarrow{T} 6\,NiO + Al_2O_3 + 13H_2O + CO_2 \qquad (1)$$

$$6\,NiO + 6\,H_2 \longrightarrow 6\,Ni + 6\,H_2O \qquad (2)$$

For the sample with Ni/Al = 2.5 the steps are :

$$Ni_{5.7}Al_{2.3}(OH)_{16}(CO_3)_{1.15}.4.55H_2O \xrightarrow{T} 5.7NiO + 1.15Al_2O_3 + 12.55H_2O + 1.15CO_2 \qquad (3)$$

$$5.7\,NiO + 5.7H_2 \longrightarrow 5.7\,Ni + 5.7\,H_2O \qquad (4)$$

In Eqs. 1 and 2 it is assumed that the nickel present in takovite is completely calcined to the NiO and that the resulting NiO is completely reduced to metallic Ni. However, calcination actually leads to different oxide phases, besides nickeloxide. Oxide phases mentioned in the literature are a DOSI (disordered oxide spinel intermediate) phase, which comprises NiO containing some aluminum ions with a characteristic XRD reflection at 1.464 Å, and a NCA (nickel containing alumina) phase, which is a very poorly crystallized nickel deficient spinel $Ni_{1-\delta}Al_{2+2\delta/3}O_4$ phase, of which the characteristic reflection is 1.415 Å. The DOSI reflection by XRD is situated between the d(110) of NiO of 1.476 Å [4a] and the d(440) of $NiAl_2O_4$ of 1.423 Å [4b]. The NCA reflection is situated between the d(440) of $NiAl_2O_4$ of 1.423 Å [4b] and the d(440) of Al_2O_3 of 1.400 [4c]

In the spinel structure ($NiAl_2O_4$) the oxygen ions are arranged to a ccp structure. 50 % of the octahedral sites is occupied by the aluminum ions and 50 % is vacant. 12.5 % of the tetrahedral sites is filled by the nickel ions and 87.5 % of the sites empty.

De Korte et al. [2] usually observed three maxima at 450, 550, and 750° C in the TPR profiles of takovite of Ni/Al ratio of two being calcined at 900° C. The first reduction peak displaying an activation energy of 130 kJ/mole is attributed to NiO dispersed on a supporting phase, the second peak, of an activation energy of 150 kJ/mole, to reduction of the DOSI phase, and the third peak of an activation energy of 320 kJ/mole, to reduction of the NCA phase. The rate-determining step in the reduction of the NiO or DOSI phase is probably the formation of Ni-nuclei in the individual takovite crystals. The rate determining step in the reduction of the NCA phase is assumed to be cation diffusion.

Calcination is an important procedure in the preparation of the catalysts. With high calcination temperatures, it is observed that the maximum in the reduction of NiO to Ni is shifted to high temperatures [2]. Less attention has been paid to the effect on the calcination temperature on the fraction nickel present in the catalyst being reduced to metallic nickel.

To investigate the effect of the Ni/Al ratios on the behavior of the catalyst precursors during thermal treatment, nickel-on-alumina precursors exhibiting the takovite structure are prepared of a Ni/Al ratio of 2.5 and 3.

When the takovites are prepared from solutions of soda, nickel nitrate and aluminum nitrate, the anions taken up into the interlayer depend on the pH during the precipitation. At a pH-level of 7 more nitrate will be taken up, while after precipitation at a pH-level of 10 carbonate ions will be present in this interlayer. To study the effect of the anions in the interlayer on the behavior of the catalyst precursor during calcination, takovite is precipitated at pH-levels of 7 and 10. The temperature of the liquid during precipitation and the period of time involved in the precipitation can affect the crystallinity of the takovite, and, hence, the reactions during calcination. To assess the effect of the crystallinity, precipitations of takovite are carried out at 20 and 50 °C with precipitation times of 3 and of 20 h. Sodium ions remaining in the takovite precursors are difficult to remove by washing. A sample containing an appreciable amount of sodium is studied too.

EXPERIMENTAL

Synthesis

The preparation conditions of the different samples are listed in Tab. 1. Five takovite samples are prepared of Ni/Al molar ratios of 2.5 and 3, pH-levels of 7 and 10, synthesis time of 3 h with one sample of 20 h, and temperatures of 20 and 50° C.

A 0.2 M Al-containing solution is prepared by dissolving 18.7 g (0.05 mole) $Al(NO_3)_3.9H_2O$ in 250 ml H_2O. Subsequently, 36.3 or 43.6 g $Ni(NO_3)_2.6H_2O$ is added to establish molar ratios Ni/Al of 2.5 or 3. A second solution containing 0.26 M CO_3^{2-} is prepared by dissolving 36.25 g $Na_2CO_3.2H_2O$ in 1 l water. The 1 l carbonate solution is

prepared in a 3.5 l double walled precipitation vessel kept at 20 or 50° C by a thermostat bath.

The 250 ml Ni and Al containing solution is added at a rate of 1.4 ml/min to the carbonate solution within a period of time of 3 h, except of sample 4 in which the solution is added within 20 h. The amount of carbonate is in a 2*0.26/0.05 = 10.4 fold excess as compared to the stoichiometrically required quantity. The pH is kept at a constant level of 10 ± 0.01 and 7 ± 0.01 by computer-controlled addition of 3 M NaOH. After completion of the addition of the Ni-Al solution, the suspensions are centrifuged at 3000 rpm for 5 minutes, and the clays are dried at 120° C (samples 1A-5A).

Table 1 Preparation conditions of the takovite minerals.

sample No.	Ni/Al	T(°C)	time(h)	pH	d(003) Å XRD
1	2.5	50	3	┌10	7.72
5	2.5	50	3	└7	7.69
1	┌2.5	50	3	10	7.72
2	└3	┌50	3	10	7.82
3	3	└20	┌3	10	7.82
4	3	20	└20	10	7.74

Sample codes

Sample 1 is divided in 6 fractions, of which 1A is only dried at 120° C, and 1B to 1F, are additionally calcined at 260, 399, 493, 585, and 850° C, respectively, for a period of time of 1 h in an Ar flow of 63 ml/min. Samples 2A to 2F are kept at 120, 260, 395, 499, 586, and 853° C under identical conditions. Finally, samples 3A, 4A, and 5A are dried at 120° C for XRD and TGA investigations, and 3B, 4B, and 5B are calcined at 260° C with TPR measurements.

TPR

Amounts of 0.5 g of the sieve fraction between 0.7 and 2 mm of the takovite sample 1A-F, 2A-F, 3B, 4B, and 5B is placed in a vertical quartz reactor tube of 8.4 mm diameter. The volume of the catalyst bed is 1 ml with a height of 1.8 cm. The H_2 consumption is measured from 20 to 850° C from an upstream 10%H_2/90%Ar flow at a flow rate of 70 ml/min. The space velocity is 4200 h^{-1} and the linear gas rate 2.1 cm/s. The temperature is increased by an Eurotherm controlled furnace at a rate of 9.6° C/min,

and measured with a nickel-chromium/aluminum-chromium type K thermocouple. The H_2 consumption is measured with a four filament thermal conductivity cell kept at 20° C (10-077 wx T/C detector, Gow Mac). Each filament has a resistance of 30 Ohm, while a current of 85 mA is applied to the Wheatstone bridge. The hot wire detector (HWD) signal (in mV) is amplified and registered on a recorder. The total H_2 consumption due to reduction of nickel is measured by the integral of the HWD signal :

$$\text{mmole } H_2 = \int \text{HWD} * dT/387*sr = \int \text{HWD} * dT/3715 \qquad (5)$$

where HWD is the HWD signal (in mV), dT the increment of the temperature (in °C), 387 a constant (mV*min/mmole), and sr the scan rate of 9.6 °C/min.

XRD

X-ray diffraction profiles of the dried samples 1A-5A are recorded on a Guinier-De Wolff camera (Cu $K_{\alpha,1} = 1.5406$ Å).

Nickel particle sizes of the reduced samples 1A-F, 2A-F, 3B, 4B, and 5B are derived from the broadening of the reflections (200) (25,923 θ) and (220) (38.186 θ) of the cubic cell (a = 3.524 Å, JCPDS 4-850) with the Scherrer equation :

$$L = 0.94*\lambda / 2HW(\theta)*\cos(2\pi\theta/360) \qquad \text{(nm)} \qquad (6)$$

where L is the particle size (in nm), λ is 0.154 nm, $HW(\theta)$ the width in θ of the reflection peak at half maximum intensity, θ the diffraction angle. The halfwidth is corrected for the spectral line width of the instrument by $HW(\theta)_{corr} = \sqrt{(HW^2(\theta)_{meas} - HW^2(\theta)_{instr})}$, with $HW(\theta)_{instr}$ is 0.0008 rad θ at (200) and 0.0012 rad θ at (220).

TGA

The weight loss of the samples 1A, 2A, 4A, and 5A, which have been dried at 120 °C is measured in a 50 ml/min N_2-flow as a function of the temperature, which increases from 20 to 900° C at a heating rate of 10 °C/min. The weight loss comprises removal of carbonate and interlayer water at 215° C (W1 in wt%). Water of the double hydroxide sheet near Al (W2 in wt%) is lost at 320° C, denoted as gibbsite dehydration. The water

Table 2 X-ray diffraction of synthetic takovite samples dried at 120° C and not reduced by H_2 (JCPDS 15-87).

1A	10 pH	2A	10 pH	3A	10 pH	4A	10 pH	5A	7 pH	ref. [1]		
d(Å)	I/I_1	d(Å)	I/I_1	d(Å)	I/I_1	d(Å)	I/I_1	d(Å)	I/I_1	d(Å)	I/I_1	hkl
7.72	100	7.82	100	7.82	100	7.74	100	7.69	100	7.72	100	003
4.92	w	4.87	w	4.87	w	4.92	w	4.87	w	-	-	-
4.48	w	4.87	w	4.52	w	4.48	w	-	-	-	-	-
3.85	w	3.88	27	-	-	3.86	11	3.85	21	3.85	90	006
2.57	45	2.59	32	2.59	34	2.59	26	2.57	42	2.57	40	012
-	-	-	-	-	-	-	-	2.30	20	2.29	80	015
-	-	-	-	-	-	-	-	1.95	21	1.95	-	018
1.524	47	1.527	32	1.527	25	1.524	23	1.52	23	1.520	80	110
1.496	40	1.500	27	1.521	25	1.496	18	1.49	20	1.492	80	113
1.420	8	1.422	5	-	-	1.40	w	1.39	w	1.414	30	116
1.311	9	-	-	1.28	w	1.29	w	1.29	w	1.308	50	119

w = weak

of the double hydroxide sheet near Ni (W3 in wt%) is lost at 350° C, denoted as $Ni(OH)_2$ dehydration. The temperature of dehydration of $Ni(OH)_2$ in the presence of Al_2O_3 is about two times as high as the temperature normally observed with purely $Ni(OH)_2$, viz., 180° C (in a reducing flow). Stabilization of $Ni(OH)_2$ by remaining Al_2O_3 is assumed.

Of 0.5 g of samples used in the TPR reactor experiments, the weight loss involved in the reaction of $(NiO + Al_2O_3)$ to $(Ni + Al_2O_3)$ (W4 in %) is reconstructed by measurement of the total weight loss (Wtotal in %). The weight loss W4 due to reduction of NiO to Ni is the subtraction of the total weight loss Wtotal by the combined weight losses W1 + W2 + W3, by W4 = Wtotal - (W1 + W2 + W3). The amount of H_2 needed for reduction of nickeloxide is calculated with W4 by :

$$\text{mmole } H_2 = 10^3 * W4(\%) * 0.5 / 16*100 \qquad (7)$$

RESULTS

X-Ray Diffraction

The XRD reflections of the samples 1A to 5A, which have been dried, but not reduced are those of takovite (Tab. 2). Samples 2A and 3A of a high molar ratio Ni/Al of 3 have a large layer spacing with the reflection d(003) of 7.82 Å. Sample 1A of a molar ratio 2.5 and sample 4A of a long reaction time of 20 h have intermediate d(003) values of 7.72 and 7.74 Å. Sample 5A prepared at a low pH of 7 exhibits the smallest d(003) value of 7.69 Å.

Reduction of the samples

-sample 1

Sample 1 contains a fair amount of sodium. The reduction profiles of the samples 1A to 1F having a Ni/Al ratio of 2.5, as measured by the hydrogen consumption in a TPR experiment, show different maxima, viz., 1. at 300° C (1C and 1D); 2. at 350° C (1A); 3. at 450° C (1C); 4. at 520° C (1A and 1B); 5. at 550° C (1D); and 6. at 600-700° C(1E and 1F) (Fig. 1a). As can be seen in Fig. 1a, calcination at a temperature higher than about 500° C causes the reduction to shift to levels above about 500° C. Apparently decomposition of the takovites leads to a mixed nickeloxide / aluminumoxide phase in which the nickel is difficult to reduce. The reduced samples 1A-F are identified as to contain metallic Ni by XRD of a mean particle size L of 15 nm (Tab. 3). There is, hence, no effect of the calcination temperature on the Ni particle size. The samples calcined above 493° C (1D-F) show an additional gamma $NaAlO_2$ phase.

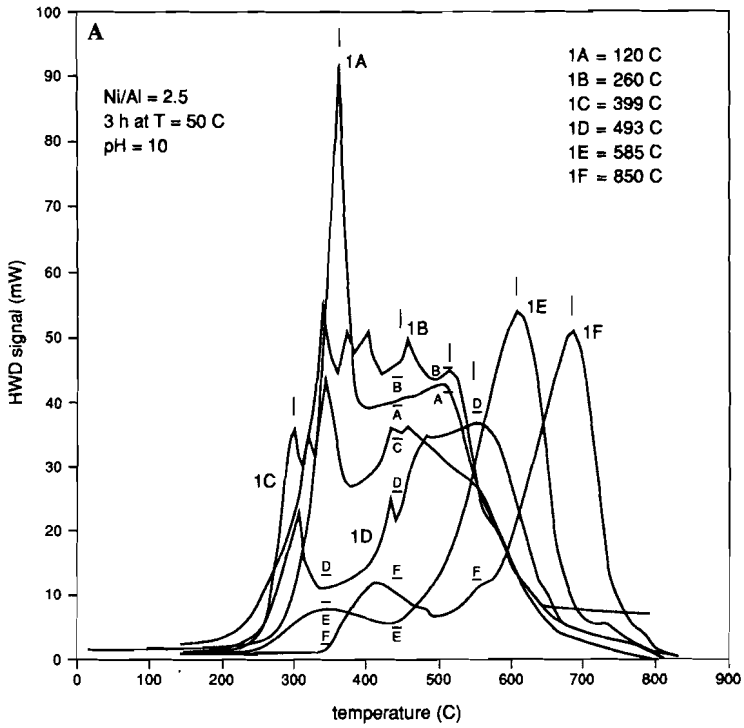

Figure 1 TPR profiles of takovite after calcination at increasing temperature ; (a) Ni/Al=2.5, pH=10, 3 h at T=50° C, calcined from 120 to 850° C (1A-F), (b) Ni/Al=3, pH=10, 3 h at T=50° C, calcined from 120 to 853° C (2A-F), (c) samples 1B to 5B prepared at various conditions but calcined at 260° C before reduction at a temperature above the loss of carbonate and interstitial water at 215° C.

-sample 2

The reduction profiles of the samples 2A-F of a higher molar ratio Ni/Al of 3 (Fig. 1b) show a gradual shift of the reduction maximum to higher temperatures from 450 to 700° C at a calcination temperature increasing from 120 to 853° C. The shift in the reduction temperature proceeds more continuously with the precursor having a higher Ni/Al ratio of 3 and containing less sodium. Shoulders at 300 and 350° C are seen with sample 2A (and 2B), but less strong than with 1A (Fig. 1a). The smooth curved TPR maxima of 2A-F are different from those of 1A-F, which show sharp peaks and submaxima. The exception is sample 2F calcined at 853° C, which exhibits a sharp peak at 730° C

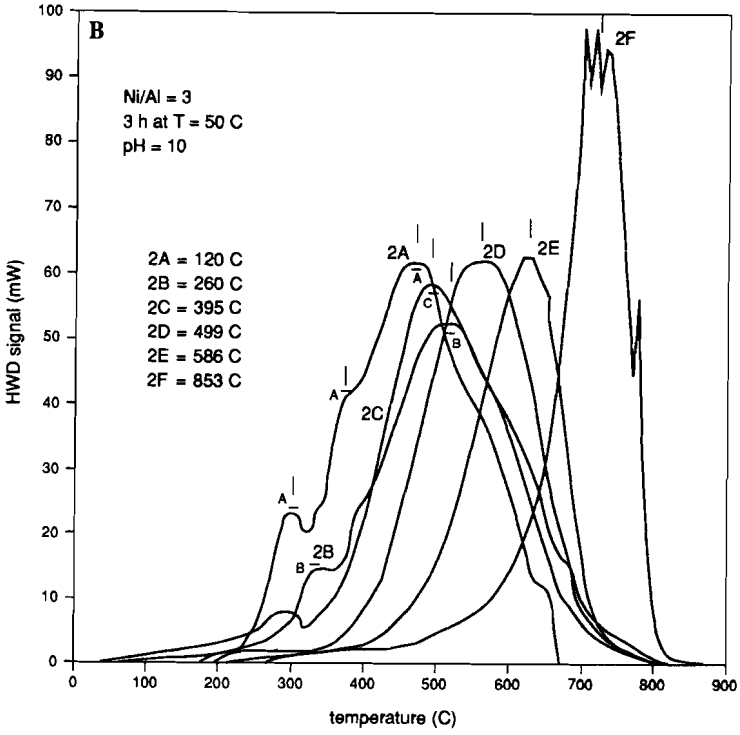

Figure 1 (continued) (b) Ni/Al=3, pH=10, 3h at T=50°C

The samples 2A-F after reduction show only XRD reflections of Ni and of a not entirely reduced DOSI phase (reflection 1.45 Å, Tab. 4). The nickel particle size of sample 2 increases from 4-8 to 16 nm with calcination temperatures raising from 120 to 853° C.

-samples 3-5

In Fig. 1c, the samples 3B and 4B with Ni/Al = 3, synthesized at a temperature of 20° C for 3 and 20 h, respectively, and calcined at 260° C display an identical TPR profile as 2B. Apparently, neither the temperature of the liquid during the preparation nor the duration of the precipitation strongly affect the reducibility of the catalyst precursor. The curves display maxima at 500-550° C with shoulders at 350° C. Reflections of metallic Ni and a not entirely reduced DOSI phase are observed with XRD (reflection 1.46 Å, Tab. 5). Furthermore, the nickel particle size is small, viz., 6 and 7 nm for 3B and 4B, and equal to that of 2B calcined at 260° C. The reduction profiles of sample 1B and 5B with the same Ni/Al ratio of 2.5, produced at pH of 10 and 7, respectively, are remarkably different (Fig. 1c). Presumably the difference is due to the sodium content. The shape of the TPR curve of 5B is equal to that of 2B-4B and similar phase reflections are determined, but the TPR maximum is at a relatively high temperature of 600° C. Evidently the reduction proceeds more difficult at a lower Ni/Al ratio. The nickel particle size is 6 nm.

Table 3 X-ray diffraction of takovite samples 1 A-F, Ni/Al = 2.5, with calcination temperatures of 120 to 850° C and reduced with H_2 .

1A 120°C		1B 260°C		1C 399°C		1D 493°C		1E 585°C		1F 850°C		Ni (JCPDS 4-850)		
d(Å)	I/I_1	d(Å)	I/I_1	d(Å)	I/I_1	d(Å)	I/I_1	d(Å)	I/I_1	d(Å)	I/I_1	d(Å)	I/I_1	hkl
2.01	100	2.02	100	2.02	100	2.02	100	2.02	w	2.12	w	2.03	100	111
1.74	52	1.74	w	1.75	57	1.75	60	1.74	w	1.76	w	1.76	42	200
1.23	37	1.23	w	1.22	45	1.22	45	1.23	w	1.24	w	1.24	21	220
												gamma $NaAlO_2$ (JCPDS 19-1179)		
-	-	-	-	-	-	4.23	57	4.23	38	4.22	44	4.25	90	101
3.53	w	-	-	-	-	3.52	12	3.52	9	3.53	11	3.78	30	110
-	-	-	-	-	-	3.32	6	3.31	6	3.32	8	3.32	70	111
-	-	2.94	w	-	-	2.93	79	2.93	87	2.94	70	2.94	100	102
-	-	2.64	w	-	-	2.65	100	2.65	100	2.64	100	2.65	100	200
-	-	2.60	w	-	-	-	-	-	-	-	-	-	-	-
2.58	w	2.56	w	-	-	2.56	79	2.56	95	2.57	53	2.59	95	112
-	-	-	-	-	-	2.49	56	-	-	-	-	2.49	30	201
-	-	-	-	-	-	2.36	35	-	-	-	-	2.38	20	210
-	-	-	-	-	-	1.93	w	-	-	1.97	w	1.97	85	212
1.67	w	-	-	-	-	1.65	7	-	-	1.66	w	1.66	10	222
-	-	-	-	-	-	1.57	25	1.57	23	1.58	39	1.59	95	302
-	-	-	-	-	-	1.50	25	1.50	15	1.52	22	1.52	80	312
-	-	-	-	1.48	w	1.48	21	1.48	18	1.47	20	1.47	90	204
-	-	-	-	-	-	1.45	29	1.46	31	1.44	22	1.44	6	321
-	-	1.40	w	-	-	1.40	23	1.40	33	1.40	25	1.42	55	303
1.38	w	1.38	w	1.37	w	1.38	25	1.38	38	1.36	22	1.37	40	313
-	-	1.34	w	-	-	1.34	27	1.34	31	-	-	1.36	90	322
-	-	-	-	-	-	1.27	10	1.27	21	1.26	w	-	-	-
16		13		15		15		16		17		Nickel particle size L(nm)		

w = weak

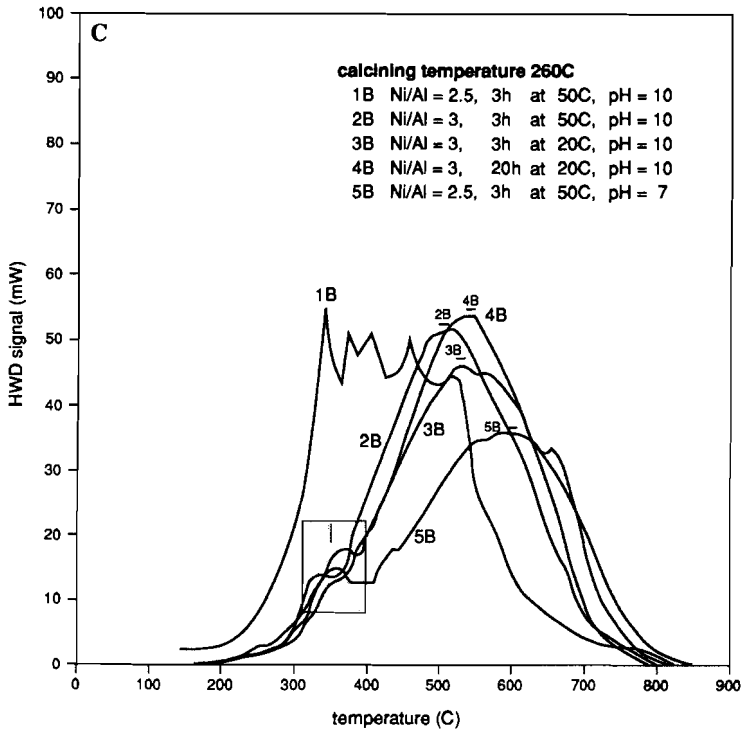

Figure 1 (continued) (c) samples 1B to 5B calcined at 260°C

Quantity of reduced nickel

The theoretical amount of H_2 consumed during reduction of nickel is calculated from the theoretical weight loss W4 (in %) of 0.5 g takovite (Tab. 6). The theoretical amount H_2 is 3.44 mmole for the reduction of takovite with a molar ratio Ni/Al of 2.5, and 3.75 mmole for takovites with ratio Ni/Al of 3 (Tab. 6). In Tab. 6 also the extends of reduction calculated by integration of the of the hydrogen consumption measured in the TPR experiments are mentioned. It is apparent that the accuracy of the extent of reduction calculated from the TPR results is higher than calculated from the weight loss. Since desorption of water vapor produced during the reduction out of the generally highly porous dehydrated and reduced sample proceeds slowly, a lower extent of reduction of the calculated from the weight loss has to be expected. The weight loss measured with sample 2A suggests a very low extent of reduction in contrast with the TPR measurement of sample 2A. The relatively low weight loss during the reduction might be due to the

Table 4 X-ray diffraction of takovite samples 2 A-F, Ni/Al = 3, with calcination temperatures of 120 to 853° C and reduced with H_2.

2A 120°C		2B 260°C		2C 393°C		2D 585°C		2E 585°C		2F 850°C		Ni (JCPDS 4-850)		
d(Å)	I/I_1	d(Å)	I/I_1	d(Å)	I/I_1	d(Å)	I/I_1	d(Å)	I/I_1	d(Å)	I/I_1	d(Å)	I/I_1	hkl
2.01	w	2.04	w	2.03	100	2.02	w	2.02	100	2.02	100	2.03	100	111
1.73	w	1.75	w	1.75	57	1.75	w	1.75	63	1.74	93	1.76	42	200
1.21	w	1.23	w	1.23	58	1.23	w	1.23	50	1.23	78	1.24	21	220
												NiO (JCPDS 22-1189)		
-	-	-	-	-	-	-	-	-	-	3.36[1]	w			
-	-	-	-	-	-	-	-	2.82	w	-	-			
-	-	-	-	-	-	2.60[1]	w	-	-	-	-			
2.39	68	2.4	w	2.39	74	2.40	w	-	-	-	-	2.41	60	003
2.06	100	2.07	w	2.06	100	-	-	-	-	-	-	2.09	100	012
-	-	-	-	-	-	1.60[1]	w	-	-	-	-			
1.44	65	1.45	w	1.46	74	1.45	w	1.45	w	1.46	w	1.48	35	110
1.37	15	-	-	1.38	9	1.38	w	1.37	w	1.38[1]	w			
1.18	26	1.18	w	1.18	34	-	-	-	-	-	-			
4-8		4-9		6		10		16		16		Nickel particle size L(nm)		

1) evt $NaAlO_2$
w = weak

presence of more narrow pores in the decomposed takovite prepared at 50° C. However sample 1A, which differs only in the Ni/Al ratio, exhibits a much higher weight loss during reduction.

It is interesting to study the effect of the temperature of the previous calcination on the reducibility of the nickel. Figure 2 shows the experimental hydrogen consumption calculated by integration of the HWD signal recorded during the TPR experiment. The hydrogen consumption is plotted as a function of the calcination temperature in Fig. 2.

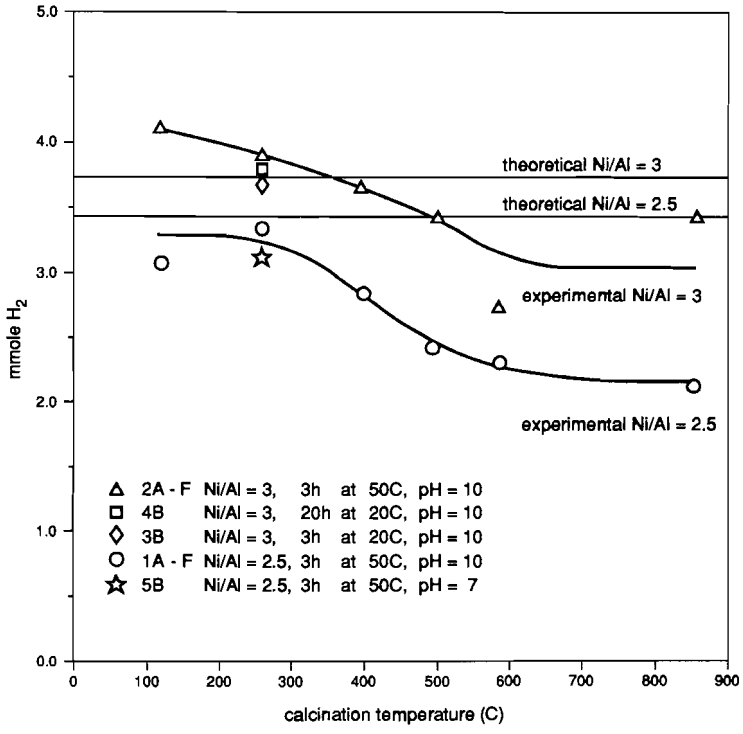

Figure 2 Integrated H_2 consumption upon reduction of synthetic takovite of different Ni/Al ratios of 3 and 2.5 as a function of the calcination temperature. The horizontal lines represent the theoretical H_2 consumption based on the stoichiometric amount of Ni in 0.5 g takovite. The curves of sample 1 with Ni/Al=2.5 and sample 2 with Ni/Al=3, represent the experimental H_2 consumption calculated from the surface integrals under the TPR profiles.

Table 5 X-ray diffraction of takovite samples 3B-5B,dried at a temperature of 120°C, calcined at 260° C and reduced with H_2.

3B 260°C		4B 260°C		5B 260°C		Ni (JCPDS 4-850)		
d(Å)	I/I_1	d(Å)	I/I_1	d(Å)	I/I_1	d(Å)	I/I_1	hkl
2.03	100	2.01	100	2.02	100	2.03	100	111
1.75	38	1.74	53	1.75	58	1.76	42	200
1.22	29	1.22	39	1.22	46	1.24	21	220
						NiO (JCPDS 22-1189)		
2.41	w	-	w	2.41	w	2.41	60	003
2.09[1]	-	2.09[1]	-	2.09[1]	-	2.09	100	012
1.46	w	-	-	1.47	w	1.48	35	110
-	-	-	-	7.56	w	takovite ?		
-	-	4.46	w	-	-	takovite ?		
3.56	w	3.58	w	3.58	w	evt. $NaAlO_2$		
1.38	w	1.38	w	1.39	w	evt. $NaAlO_2$		
1.34	w	-	-	-	-	evt. $NaAlO_2$		
6		7		6		Nickel particle size L (nm)		

1) partly under the 2.03 reflection of Ni
w = weak

It can be seen that the samples with molar Ni/Al ratio of 3 exhibit a reduction higher than calculated for the amount of NiO. The theoretical amounts of H_2 of 3,75 and 3,44 mmole needed for reduction of samples with molar ratios Ni/Al of 3 and 2.5 are plotted as horizontal lines in Fig. 2. Presumably the apparently higher extents of reduction of the sample with Ni/Al = 3 are due to the formation NiO_{1+x}, where x is significantly higher than 0.01. It is well known that finely divided NiO takes up additional oxygen due to the oxidation to Ni(III). At higher calcination temperatures the non-stoichiometric oxygen is released and NiO assumes the green color of stoichiometric NiO. At still higher calcination temperatures some Ni present as nickelaluminate cannot be reduced. After a first large consumption of H_2 at calcination temperatures between 100 and 200° C, the values decline at temperatures between 700 and 750° C.

The extent of reduction of the samples with a molar ratio of 2.5 is at all calcination temperatures below the theoretically calculated level. Evidently reaction to a non-reducible Ni-Al compound proceeds to a relatively higher extent. After calcination at temperature above 500° C an appreciable amount of badly reducible nickel results. It is likely that the sodium present in the samples 1A to 1F promotes reaction of Ni(II) with the alumina.

DISCUSSION

In ref. [5] analogously precipitated compounds are described, that are hydrothermally treated to improve the crystallinity of the precipitates. The catalyst precursors prepared by Kruissink et al. [5] exhibit a layer spacing of 7.58 Å after precipitation at a pH-level of 10, and of about 7.5 Å after precipitation at a pH-level of 7. The above authors showed that the incorporation of nitrate ions, also on precipitation at pH 7, remains low, viz., about 10% of the amount of carbonate incorporated. Substantially higher contents of nitrate are obtained when the precipitation is performed at a pH-level of 5, or when sodium hydroxide is exclusively used in the precipitation. The layer spacings of Tab. 2 indicate accordingly no significant effect of the uptake of nitrate ions ; the spacings vary from 7.82 to 7.69 Å. The lowest spacing is exhibited by sample 5A, which is precipitated at a pH level of 7, which leads to the most nitrate being incorporated. Kruissink et al. [5] observed layer spacings of 8.92 and 9.0 Å only when much more nitrate ions were incorporated. The nickel particle size after reduction increased from 6 nm of the takovite with carbonate samples to 50 nm of the takovite with nitrate samples.

The size of the metallic nickel particles obtained after reduction also agrees well with the size of the nickel particles mentioned by Kruissink et al. [5], viz., 4 nm. Kruissink et al. [5] also mentioned that precursors containing sodium exhibit lower activities. We have confirmed the lower activity and established that the lower activity is due to the presence of large nickel particles.

Reduction of NiO by atomic hydrogen proceeds already at room temperature. The dissociation of molecular hydrogen therefore is likely to be the rate-determining step with the reduction of nickel(II)oxide. Since the reduction of nickeloxide to metallic nickel has been shown to initiate on a small number of sites at the surface of nickeloxide, the dissociation of hydrogen will proceed on lattice defects at the surface. Dissociation of the di-hydrogen and desorption of water from the surface proceed at a significantly rate above 150° C as can be concluded from the onset of the reduction at temperatures around 150° C. Once metallic nickel has resulted from the reduction, the dissociative adsorption of hydrogen proceeds rapidly, and also the reduction.

Bulk $Ni(OH)_2$ looses water at temperatures of about 200° C. When bulk $Ni(OH)_2$ is heated in a flow of nitrogen, reduction immediately follows the dehydration of $Ni(OH)_2$. The defect rich NiO resulting from the dehydration dissociates rapidly to molecular hydrogen and, hence, is reduced readily. If $Ni(OH)_2$ is dehydrated in flow of a non-reducing gas, defects in the resulting NiO are annealed. Subsequent reduction therefore proceeds less rapidly. Reduction of well annealed NiO calls for temperatures as high as 450° C to be initiated.

Lattice defects present in takovite will not be able to dissociate molecular hydrogen in contrast to defects present in the surface of NiO, where nickel ions of a valency different from that present in the defect-free lattice are involved. Consequently reduction of the nickel ions will proceed only after decomposition of the takovite, which provides NiO, analogously to the behavior of $Ni(OH)_2$ being heated in a reducing gas flow.

Table 6 Thermogravimetric analysis (TGA) of synthetic takovite, dried at 120°C, with W1 loss of carbonate and interstitial water at 215° C, W2+W3 dehydration of water bound to Gibbsite and $Ni(OH)_2$ at 320 and 350° C, and W4 loss of weight by reduction of NiO. W1-W4 are expressed in % of the initial weight of 0.5 g takovite

	sample	W1(%)		W2+W3(%)		W4(%)		W4(mmole H_2)		TPR (mmole H_2)	
	Ni/Al	exp.	theor.	exp.	theor.	exp.	theor.	exp.	theor.	exp.A	exp.B series
1A[1]	2.5	15	18	16	17	9	11	2.81	3.44	3.1	3.3
2A[2]	3	13	18	17	17	3	12	0.94	3.75	4.1	4.0
4A[2]	3	13	18	16	17	7	12	2.19	3.75	-	3.9
5A[1]	2.5	15	18	16	17	13	11	4.06	3.44	-	3.2

exp. and theor. mean loss of weight obtained either by the experiment or by the theoretical loss by the stoichiometry of ; 1) $Ni_{0.72}Al_{0.28}(OH)_2(CO_3)_{0.14}.\ 0.57H_2O$ interstitial, and 2) $Ni_{0.75}Al_{0.25}(OH)_2(CO_3)_{0.12}.\ 0.63H_2O$ interstitial

The higher stability of takovite as compared to that of $Ni(OH)_2$ causes the decomposition and the subsequent reduction to occur at temperatures around 350° C, which is at appreciable higher temperatures than that of $Ni(OH)_2$.

The reduction profiles of sample 2, which does not contain much sodium can be explained smoothly. After drying at 120° C the dehydration of nickel-rich takovite sets on at a temperature of about 220° C. Apparently the precipitate produced at a pH level of 10 contains also takovites of a lower nickel-to-alumina ratio, which decompose to nickeloxide at higher temperatures. The reduction of the nickeloxide thus formed also proceeds at higher temperatures. A second shoulder to the main peak is shown at a temperature of about 350° C, while the main peak is at 460° C. We feel that the three different peaks at 300, 350, and 460° C are due to the presence of takovites of different nickel-to-alumina ratio. The first maximum at 300° C coincides with the $Al(OH)_3$ (gibbsite) dehydration, perhaps catalyzing some $Ni(OH)_2$ decomposition, and the second as mentioned before $Ni(OH)_2$ decomposition. Since metallic nickel accelerates the reduction, the width of the reduction profile and the presence of the shoulders indicate a finely divided nickel containing species resulting from the decomposition of sample 1 dried at 120° C. Migration of atomic hydrogen spilling over from initially formed metallic nickel cannot proceed over a large distance. Intimate contact of takovites of a different nickel-to-alumina ratio therefore does not agree with the experimentally observed three reduction peaks.

Calcination at 260° C of sample 2 prior to the reduction leads to the formation of nickeloxide slightly more difficult to reduce. When the previous calcination is performed at 395° C, more nickeloxide results, which take up additional oxygen to NiO_{1+x} during cooling to room temperature. Due to the overstoichiometric amount of oxygen the reduction sets on already at an extremely low temperature of 70° C (Fig. 1b), but due to the small amount of defects, the hydrogen consumption below 310° C remains low. With sample 1B, calcined at 260° C the amount of NiO_{1+x} is too small to become distinctly apparent by hydrogen consumption at low temperatures (Fig. 1a).

Previous calcination at temperatures of 499° C or higher leads to reaction of nickeloxide and aluminumoxide resulting from the decomposition of the takovite to nickelaluminate or to a DOSI (disordered oxide spinel intermediate) phase. It is well known that reduction of nickel spinel only proceeds at high temperatures. The reaction to a spinel phase becoming more complete at higher temperatures is apparent from the gradual shift of the maxima of the reduction profile. Defects in the surface of the spinel easily dissociating hydrogen do not exist.

Sample 1 contains a substantial amount of sodium. It is assumed that the presence of sodium promotes the reaction of nickeloxide with alumina to nickelaluminate. Drying at 120° C and calcination at 260 and 399° C lead to reduction profiles exhibiting a significant hydrogen consumption over a broad temperature range. After calcination at 585 and 850° C formation of nickelaluminate or a DOSI phase is apparent. Reduction of these phases is fairly difficult.

Reduction of nickel ions present in nickelaluminate or in a DOSI phase leads to relatively large nickel particles. At the more elevated temperatures required for the reduction of the

nickel ions in nickelaluminate or a DOSI phase, the resulting nickel atoms are highly mobile over the aluminate or alumina. As a result the nickel atoms agglomerate to nickel particles of a size of about 16 nm [6].

At lower temperatures nickel atoms and small clusters of nickel atoms are less mobile, which result in smaller nickel particles. Accordingly reduction at lower temperatures leads to smaller particles of a size of 4 to 10 nm, which do not migrate or coalescence rapidly at higher temperatures. It is interesting that also reduction at relatively low temperature leads with sample 1, which contains sodium, to large nickel particles. We attribute the formation of relatively large nickel particles to a high mobility of nickel metal atoms over spinel surfaces. The mobility of nickel metal atoms over nickeloxide is lower than over spinel surfaces, since the interaction of metallic nickel with nickeloxide is higher than with a spinel surface.

CONCLUSIONS

1) With the reduction of nickel in takovite, the molar ratio Ni/Al, the pH level during precipitation, and the calcination most significantly affect the shape of the TPR-profile, the solid phases after reduction, and the metallic nickel particle size. Less important are the temperature of the liquid during the precipitation and the period of time involved in the precipitation.

2) The main peak in the TPR profile of samples with a molar ratio Ni/Al of 3 shifts to higher temperatures when previous calcination is performed at higher temperatures, while the sample with a molar ratio Ni/Al of 2.5 containing Na shows a relatively broad TPR profile after previous calcination at temperatures up to 500° C.

3) Raising the temperature of the previous calcination from 120 to 853° C leads to an increase of the size of the nickel particles from 4-8 nm to 16 nm due to reaction to nickel aluminate at higher temperatures. The high mobility of nickel metal atoms over sodiumaluminate causes the size of the nickel metal particles to be 15 nm irrespective of the temperature of the previous calcination.

4) After calcination of the takovite precursors below 400° C, the nickel can be completely be reduced to metallic nickel; calcination at higher temperatures produces nickel aluminate a fraction of which cannot be reduced to metallic nickel. The presence of sodium promotes formation of aluminates thus appreciably decreases the reducibility of nickel.

ACKNOWLEDGMENTS

The authors thank Tonny de Beer and Guido Mul for their contribution to the experimental work, and dr.J.T. Kloprogge for the critical review of the paper.

REFERENCES

1 E.C. Kruissink, L.L. van Reyen, *J. Chem. Soc., Faraday Trans.*, (1) **77** (1981) 649
2 P.H.M. de Korte, E.B.M. Doesburg, C.P.J. de Winter, and L.L. van Reyen, *Solid State Ionics*, **16** (1985) 73-80
3 E.B.M. Doesburg, G. Hakvoort, H. Schaper, and L.L. van Reyen, *Applied Catalysis*, **7** (1983) 85
4 Joint Committee of the Powder Diffraction file Standards (JCPDS) a) NiO 22-1189, b) $NiAl_2O_4$ 10-0339, c) Al_2O_3 29-0063
5 E.C. Kruissink, L.E. Alzamora, S. Orb, E.B.M. Doesburg, L.L. van Reijen, J.H.R. Ross, and G. van Veen, Studies in Surface Science and Catalysis 3, Preparation of Catalysts 2, Proceedings of the Second International Symposium, Louvain-la-Neuve, September 4-7 (1978), Ed. B. Delmon, P. Grange, P. Jacobs, and G, Poncelet, Elsevier (1979) Amsterdam, 143
6 E.B.M. Doesburg, P.H.M. de Korte, H. Schaper, and L.L. van Reyen, *Applied Catalysis* **11** (1984) 155

SAMENVATTING

Een probleem dat bij de katalysator bereiding altijd aan de orde is geweest is de vorming van actieve plaatsen voor de te katalyseren reactie en de rol van deze plaatsen in het katalytisch proces. Het antwoord moet vaak gezocht worden in de structuur van de katalysator. De actieve plaatsen zijn juist in die omgeving aanwezig waarbij de gewenste reactie gekatalyseerd wordt. Soms is de zeer directe omgeving van de actieve plaatsen van belang, maar vaak speelt ook de drager waarop de katalyserende verbinding is aangebracht een belangrijke rol. De drager is meestal een inert materiaal die er voor zorgt dat de katalyserende deeltjes, bijvoorbeeld metaal deeltjes, niet met elkaar grotere deeltjes gaan vormen, waardoor het gezamenlijk oppervlak van de deeltjes en dus ook de katalytische activiteit afneemt. Een gevolg kan ook zijn dat de grotere metaal deeltjes, bijvoorbeeld nikkel deeltjes, een andere katalytische werking hebben. De separatie van de deeltjes van de actieve fase is echter niet de enige rol van de drager. De drager kan door zijn porie afmetingen een rol spelen in de selectiviteit voor een bepaalde reactie. De afmeting van de bij de katalytische reactie ontstane verbinding kan immers niet groter zijn dan van de poriën in de drager. Daarnaast kan de drager door zijn eigen actieve oppervlakte groepen participeren in de werking van de katalysator. Voorbeelden van poreuze dragermaterialen zijn aluminiumoxide (alumina) en siliciumdioxide (silica). Een veelbelovende groep van dragermaterialen zijn de gepilaarde kleien. Deze materialen bezitten een plaatvormige structuur, waarbij de platen door middel van pilaarverbindingen gescheiden worden gehouden. In de spleetvormige poriën bevinden zich dan de katalytisch actieve pilaren. De plaatvormige kleideeltjes zijn op hun beurt klein hetgeen voor een snelle aanvoer van reactanten en afvoer van het gewenste produkt zorgt.

Belangrijk voor de goede werking van de katalysator is de synthese stap die reproduceerbaar moet kunnen worden uitgevoerd. Verbindingen met dezelfde chemische samenstelling kunnen verschillende reacties katalyseren. Een praktijk voorbeeld is de selectieve oxydatie van zwavelwaterstof naar zwavel over gedragen ijzeroxide katalysatoren. De werking van deze katalysatoren wordt in sterke mate bepaald door de structuur van de aluminiumoxide drager.

De dragermaterialen die in dit proefschrift zijn bestudeerd zijn poreus sol-gel silica, een basisch aluminium-magnesium coprecipitaat (hydrotalciet), en een aluminium-nikkel coprecipitaat (takoviet). Een silica gel is een zeer ijle drie-dimensionale structuur van silica sol deeltjes van enkele nanometers. De silica gelen zijn bereid uit basisch silicium houdend waterglas en een sterk zuur. De gebruikte waterglas oplossing bevat naast een hoge concentratie silicaat anionen ook een hoge concentratie natrium ionen. Er zijn drie bereidingsmethoden onderzocht om de poreuze silica gel structuur te produceren. De drie methoden verschillen in de manier waarop de waterglas oplossing wordt aangezuurd. De eerste methode behelst de additie van waterglas aan een sterk zuur, waarbij de silica sol deeltjes die bij deze additie gevormd worden zich vertakken tot een silica gel, de klassieke methode. Bij de tweede, pH-statische, methode worden de

waterglas en zuur oplossing gelijktijdig aan een oplossing van een constante pH toegevoegd. De derde methode, de electrodialyse, verschilt van de eerste twee methoden, in het feit dat de pH van de waterglas oplossing niet met een sterk zuur, maar met aan een platina anode gegenereerde H^+ ionen wordt verlaagd. Het gevolg van de laatste methode is dat gedurende de vorming van de silica sol deeltjes de natrium ionen uit de waterglas oplossing worden gedialyseerd. Interessant is het dan ook de vorming van de silica sol deeltjes en de gelering van het sol tot een silica gel bij de afwezigheid van natrium ionen te vergelijken met die van de eerste twee methoden.

De porie structuur van de silica gel drager wordt in een belangrijke mate bepaald door de kinetiek van de precipitatie reacties van de silicaat anionen. De kinetiek van de reacties by lage vormingstemperatuur kunnen worden afgeleid uit de kinetiek van de reacties onder hydrothermale condities, waar de reacties als gevolg van de hoge temperatuur vele malen sneller verlopen. Als gevolg van de precipitatie reactie reageren reeds aanwezige kiemen van ongeveer 2 nm in de waterglas oplossing tot silica sol deeltjes van enkele nanometers. De grootte van deze deeltjes kan worden bepaald met behulp van een elektronen microscoop.

De op klassieke wijze door additie van waterglas aan sterk zuur bereide silica gelen zijn gegeleerd bij een pH van 5 en gedroogd bij een temperatuur van 393 K. De gelen bevatten sol deeltjes van ongeveer 5 nm, hebben een porie volume van 0.8 ml/g, en hebben een intern oppervlak van ongeveer 457 m^2/g. De diameter van de poriën tussen de deeltjes is ongeveer gelijk aan die van de afmeting van de deeltjes, namelijk 4.8 nm gemeten met N_2 adsorptie en 8.8 nm gemeten met thermoporometrie.

De pH statische bereidingsmethode leidt bij een lage pH waarde van 2 tot zeer kleine deeltjes van 2 tot 3 nm met diameter van de poriën van 6.2 nm tussen de deeltjes. Bij een hogere statische pH van 4 en 5 worden deeltjes met een diameter van 5 à 8 nm gevormd met afmetingen van de poriën van 5.6 en 13.6 nm, en bij een nog hogere pH waarde van 9 en 10 worden deeltjes gevormd met een deeltjes afmeting van 21 à 26 nm. De porie diameter van de laatsgenoemde gelen is onbekend. De gelen die bij een lage pH van 1 à 2 gevormd zijn, hebben een porie volume van 0.4 ml/g en een intern oppervlak van 286 m^2/g. Deze waarden voor het porie volume en intern oppervlak zijn lager dan die zijn gemeten bij de klassieke zuur-base gelen, die bij een pH van 5 gegeleerd zijn. De pH statische silica gelen die bij een pH van 4 en 5 zijn bereid hebben een gemiddeld porie volume van 0.9 ml/g en een gemiddeld intern oppervlak van 476 m^2/g, vergelijkbaar met die van de klassieke zuur-base bereidings methode. Bij de klassieke bereidingsmethode loopt de pH door een traject van een zeer lage pH kleiner dan nul naar een pH van 5. Beneden een pH van 2 worden slechts kleine deeltjes van 2 à 3 nm gevormd. Kennelijk treedt in het pH traject vanaf 2 tot 5 een reactie op waarbij uit de deeltjes van 2 nm de deeltjes van 5 nm worden gevormd. De deeltjes van 5 nm zouden opgebouwd kunnen zijn uit de deeltjes van 2 à 3 nm, hetgeen een aanwijzing zou kunnen zijn voor de fractale structuur van silica. Een dergelijke fractale structuur kan echter niet uit de poriestraal verdelingen van de silica gelen worden waargenomen.

Interessant is de vergelijking van de porie structuur van de op electrochemische wijze

verkregen silica gelen, enerzijds, met de pH-statisch en klassiek gesynthetiseerde gelen, anderzijds. De pH van de op electrochemische wijze gesynthetiseerde gelen loopt door een traject van pH waarden van 11.3 tot 2.8. In het pH gebied 9 à 10 wordt een deeltjes grootte van 21 tot 26 nm verwacht, terwijl deeltjes van 5 nm worden gemeten. Dit verschil kan worden toegeschreven aan de geringe hoeveelheid natrium die door de dialyse in het traject pH 11.3 tot 2.8 in de waterglas oplossing aanwezig is. Natrium heeft namelijk een katalytisch effect op aangroei van de sol deeltjes en op de gelering. Bij afwezigheid van natrium worden dus kleinere deeltjes verwacht.

Natrium is in staat om het proton van een oppervlakte silanol groep te verwijderen en veroorzaakt daardoor een negatieve lading op het silica deeltje, die slechts ten dele door het natrium kan worden afgeschermd. De negatieve lading van het SiO^{-}-Na^{+} complex heeft een katalytisch effect op de vorming van siloxaan bindingen tussen de silica sol en het monosilicium zuur (aangroei) en op de vorming van bindingen tussen de sol deeltjes onderling (gelering). Uit titratie experimenten is gebleken dat de negatieve logaritme van de ionisatie constante van de oppervlakte silanol groepen in de aanwezigheid van natrium gelijk is aan 6.2. Tot een pH van 6 neemt het porie volume van pH-statisch bereide gelen en hydrothermaal behandelde zuur-base silica gelen dan ook toe door een toename van siloxaan bindingen tussen de deeltjes, waarvan de vorming door geïoniseerde silanol groepen gekatalyseerd wordt. Wellicht neemt het porie volume ook toe door de afstotende werking tussen de sol deeltjes onderling. Uit hydrothermale experimenten is gebleken dat het porie volume van zuur-base hydrogelen bij een pH van 6 door een maximum van 1.4 ml/g loopt. Bij de pH-statische silica gelen bereikt het porie volume een maximum van 0.8 ml/g bij een pH van 6. Duidelijk is dat bij een pH waarde boven 6 de electrostatische repulsie tussen de deeltjes van 5 nm te sterk toeneemt en een geringer aantal siloxaan bindingen tussen deeltjes wordt gevormd. Het geringere aantal vertakte deeltjes verzwakt de gel structuur en de gelen zijn meer onderhevig aan krimp.

De electrochemisch gesynthetiseerde silica gelen hebben een minimum in de geleertijd van 279 minuten bij een pH waarde van 5.9. De geleertijd neemt beneden een pH waarde van 5.9 toe door een gering aantal geïoniseerde silanol groepen en boven de pH van 5.9 door electrostatische repulsie tussen de sol deeltjes. De toename van de oppervlakte lading heeft nog een ander effect. Door de afstotende werking worden kortere strengen van silica sol deeltjes gevormd, die verder uit elkaar liggen. Het gevolg is dat bij de verhoging van de gelerings pH van 2.8 tot 6.5 de porie diameter toeneemt van 4.8 tot 8.4 nm, terwijl het porie volume gelijk blijft met 0.6 ml/g.

Het krimp gedrag van de op drie manieren gesynthetiseerde gelen is onderzocht met behulp van thermoporometrie. Met thermoporometrie wordt het warmte effect gemeten dat gepaard gaat met de vorming van ijs in de poriën van de silica gel. Het warmte effect wordt als functie van de temperatuur gemeten op een differentiële scanning calorimeter. De afmeting van de gevormde ijs kristallen is een maat voor de porie grootte, de hoeveelheid ijs voor het porie volume, en de oppervlakte van het ijs kristal is een maat voor het intern oppervlak van de silica gel. De met thermoporometrie gemeten waarden voor de ijskristallen moeten daarbij gecorrigeerd worden voor een niet

bevriesbare laag water van 0.9 nm, die bij de overgang silica-ijs aanwezig is. Informatie over de aanwezigheid van de niet bevriesbare laag van 0.9 nm bij toepassen van thermoporometrie wordt verkregen door de afmeting en het volume van het gevormde ijs in de porie te vergelijken met de porie afmeting en porie volume die door de traditionele karakteriseringstechnieken stikstof adsorptie bij 77 K en kwik penetratie worden verkregen. Daarnaast kan de deeltjes afmeting van het gehydrateerde sol in water bepaald met dynamische lichtverstrooiing vergeleken worden met de elektronen microscopisch vastgestelde waarde.

De aanwezigheid van de niet bevriesbare laag is vergeleken bij een hydrofiel silica oppervlak en in holle chrysotiel naalden met een hydrofoob oppervlak. Uit dynamische lichtverstrooiings metingen (DLS) is gemeten dat aan het silica oppervlak inderdaad een sterk gebonden laag water aanwezig is. De waarde van het gehydrateerde silica deeltje in water is met DLS bepaald op 7.3 nm en is groter dan de deeltjes grootte van 5 nm bepaald met behulp van elektronen microscopie, hetgeen resulteert in een niet bevriesbare laag dikte ter grootte van ongeveer (7.3-5)/2 $\approx$ 1 nm. De afmeting van het ijs dat in de holle hydrofobe chrysotiel naalden gemeten wordt, is echter gelijk aan de afmeting van de porie. Kennelijk is in de hydrofobe holle chrysotiel buizen de sterk gebonden water laag afwezig. Het hydrofobe karakter van de chrysotiel buizen en de afwezigheid van de niet bevriesbare laag heeft echter geen gevolg voor de penetratie van water in de buizen en voor de vorming van ijs.

Met thermoporometrie kan de verandering in de porie structuur worden gemeten die gepaard gaat met de overgang ongedroogd silica gel (hydrogel) naar gedroogd gel (xerogel). Voor de metingen aan de xerogelen moeten de monsters eerst weer geïmpregneerd worden met water. De silica gelen die op klassieke wijze zijn bereid en bij een pH van 5 zijn gegeleerd en gedroogd zijn bij 393 K vertonen een afname van de porie diameter ter grootte van 59 % en van het porie volume ter grootte van 44 %. Een vergelijkbare afname van het porie volume van 40 % wordt ook waargenomen bij de pH-statisch bereide gelen die bij een pH van 1 en 2 gesynthetiseerd worden. Hydrothermale behandeling van de klassiek bereide gelen leidt tot een toename van de sol deeltjes grootte en dus ook tot een toename van de door de deeltjes omsloten porie diameter. De porie diameter van het xerogel kan zo gevarieerd worden tussen 4.8 en 40 nm. Bij de laatstgenoemde porie afmeting van 40 nm wordt slechts een krimp van de porie diameter waargenomen van 26 %, terwijl de krimp van het porie volume nog tamelijk hoog is, namelijk 43 %. Hieruit blijkt dat door de hydrothermale behandeling de krimp van de porie diameter aanzienlijk lager wordt, maar dat de afname van het porie volume nauwelijks door de hydrothermale behandeling beïnvloed wordt.

Totaal verschillend is het gedrag bij drogen van electrochemisch gesynthetiseerde silica gelen met silica sol deeltjes van 5 nm. De porie diameter en het porie volume blijken bij drogen niet af te nemen. De porie diameter van een bij pH 5 gegeleerd gel blijft gelijk aan 5.6 nm en het porie volume blijft gelijk aan 0.6 ml/g na drogen bij 393 K. De afwezigheid van krimp is waarschijnlijk te wijten aan de geringe hoeveelheid natrium die bij het geleren aanwezig is. Dit blijkt uit een vergelijking met de krimp van de op klassieke wijze gesynthetiseerde zuur-base silica gelen. Na drogen bij 393 K van

een bij een pH van 5 gegeleerde zuur-base silica gel met een zelfde deeltjes afmeting wordt een afname van de porie diameter gemeten van 19 tot 8.8 nm en in het porie volume van 1.1 tot 0.8 ml/g. Hieruit blijkt dat de door natrium geïnduceerde negatieve oppervlakte lading van de sol deeltjes leidt tot een grotere porie afmeting en een iets hoger porie volume. De deeltjes zin derhalve iets minder sterk vertakt en zijn meer onderhevig aan krimp.

De op de drie, klassieke, pH-statische, en electrochemische, methode gesynthetiseerde gelen vertonen geen afname van het intern oppervlak bij drogen.

Tenslotte is de plaatafstand van gepilaard hydrotalciet in water onderzocht met thermoporometrie. Deze plaatafstand is belangrijk omdat onder hydrothermale condities de pilaren tussen de kleiplaten wordt aangebracht en in water de pilaren kunnen worden uitgewisseld, zodat een katalysator met de juiste selectiviteit voor de te katalyseren reactie wordt gesynthetiseerd. Hydrotalciet mineralen zijn hydrothermaal gesynthetiseerd met plaat afstanden in gedroogd klei variërend tussen 3 en 14 Å. De porie afmetingen in water zijn onderzocht met thermoporometrie en vergeleken met de plaatafstand in gedroogde toestand. De met thermoporometrie bepaalde afname van de plaat afstand bij drogen is geschat op waarden variërend tussen 4 en 13 maal de originele porie afmeting in water.

Curriculum Vitae

Mark Kurt Titulaer werd op 29 juli 1964 geboren in Hilversum. In juni 1982 behaalde hij het VWO diploma aan het Alberdingk Thijm College in Hilversum, en begon hij datzelfde jaar met de studie scheikunde aan de Rijksuniversiteit Utrecht. Het propaedeuse examen werd afgelegd in augustus 1983 en het doctoraal examen in juni 1987. In het hoofdvakonderzoek is meegewerkt aan de ontwikkeling van een ijzeroxide gedragen katalysator voor de selectieve oxydatie van zwavelwaterstof naar zwavel. De katalysator is onder de naam SuperClaus katalysator geoctrooieerd en wordt thans gebruikt als Claus tialgas katalysator. De keuzevakken waren Biochemie en Voedingsmiddelenchemie van Dierlijke Oorsprong. Het laatste onderzoek betrof de ontwikkeling van een methode om een zeer geringe hoeveelheid tetracycline in vlees aan te tonen. Van juli 1987 tot augustus 1991 was hij als wetenschappelijk assistent verbonden aan de vakgroep Anorganische Chemie in samenwerking met de vakgroep Geochemie van het Instituut voor Aardwetenschappen, waar het in dit proefschrift beschreven onderzoek werd uitgevoerd. Vanaf augustus 1991 werd gedurende een jaar de militaire dienstplicht vervuld als ziekenverzorger/ambulance chauffeur.